

AD-A114 389

PHYSICAL SCIENCES INC WOBURN MA
LABCEDE STUDIES.(U)

F/G 20/7

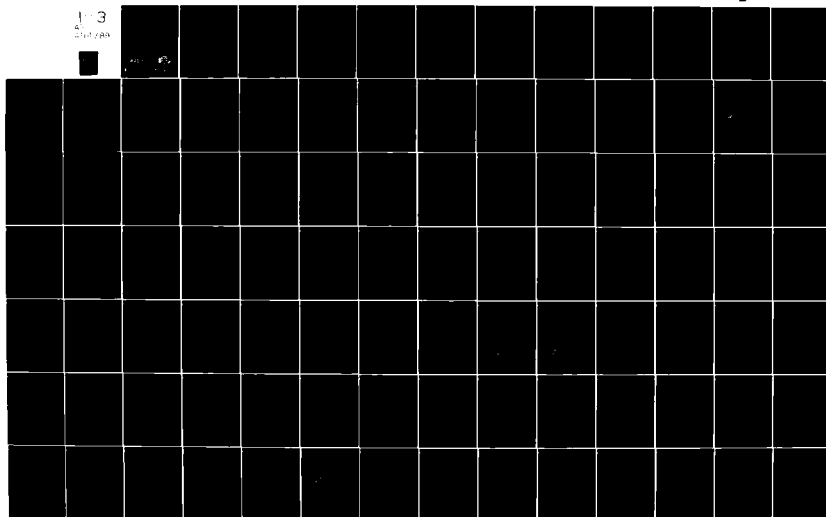
UNCLASSIFIED SEP 81 B D GREEN, G E CALEDONIA, L G PIPER
PSI-TR-261

F1962A-78-C-0115

AFGL-TR-82-0060

NL

1-3
4-100



AFGL-TR-82-0000

LABCEDE STUDIES

B.D. Green
G.E. Caledonia
L.G. Piper
J.S. Goetz
A. Fairbairn
R.E. Murphy

Physical Sciences Inc.
30 Commerce Way
Woburn, Massachusetts 01801

Final Report
30 April 1978 - 30 April 1981

September 1981

Approved for public release; distribution unlimited

AFGL-TR-82-0000
AFGL-TR-82-0000
AFGL-TR-82-0000
AFGL-TR-82-0000
AFGL-TR-82-0000

AFGL-TR-82-0000
AFGL-TR-82-0000
AFGL-TR-82-0000
AFGL-TR-82-0000
AFGL-TR-82-0000

UNCLASSIFIED

SECURITY CLASSIFICATION OF THIS PAGE (When Data Entered)

REPORT DOCUMENTATION PAGE		READ INSTRUCTIONS BEFORE COMPLETING FORM
1. REPORT NUMBER AFGL-TR-82-0060	2. GOVT ACCESSION NO. AD A114 384	3. RECIPIENT'S CATALOG NUMBER
4. TITLE (and Subtitle) LABCEDE Studies	5. TYPE OF REPORT & PERIOD COVERED Final Scientific Report 30 April 1978-30 April 1981	
6. AUTHOR(s) B. D. Green, G. E. Caledonia, L. G. Piper, J. S. Goela, A. Fairbairn*, R. E. Murphy*	7. PERFORMING ORG. REPORT NUMBER PSI TR-261	
8. PERFORMING ORGANIZATION NAME AND ADDRESS Physical Sciences Inc. 30 Commerce Way Woburn, MA 01801	9. CONTRACT OR GRANT NUMBER(s) F19628-78-C-0115	
10. CONTROLLING OFFICE NAME AND ADDRESS Monitor/Alastair Fairbairn/OPR Air Force Geophysics Laboratory Hanscom Air Force Base, MA 01731	11. PROGRAM ELEMENT, PROJECT, TASK AREA & WORK UNIT NUMBERS 61102F 2310G4AJ	
12. MONITORING AGENCY NAME & ADDRESS (if different from Controlling Office)	13. REPORT DATE September 1981	
	14. NUMBER OF PAGES 284	
	15. SECURITY CLASS. (of this report) UNCLASSIFIED	
	16. DECLASSIFICATION/DOWNGRADING SCHEDULE	
17. DISTRIBUTION STATEMENT (of this Report) Approved for public release; distribution unlimited.		
18. DISTRIBUTION STATEMENT (of the abstract entered in Block 20, if different from Report)		
19. SUPPLEMENTARY NOTES *AFGL, Hanscom AFB, Massachusetts 01731		
20. KEY WORDS (Continue on reverse side if necessary and identify by block number) Infrared radiation Vibrational kinetics Chemiluminescence Electron irradiation Einstein coefficients NO Interferometers NH Nitrogen metastables CO Cryogenics		
21. ABSTRACT (Continue on reverse side if necessary and identify by block number) → This report describes the research efforts of the past three years centered around measurements made on the LABCEDE Facility at the Air Force Geophysics Laboratory. Chapters 2 and 3 are concerned with fluorescence arising from beam created CO in irradiated CO ₂ /Ar mixtures. The two dominant sources of radiation observed in these mixtures are the CO ₂ (v ₂) band at 4.3 μ m and the fundamental vibration/rotation band of CO. The CO emission arises from highly vibrationally excited levels (up to v = 19)		

DD FORM 1 JAN 73 1473

EDITION OF 1 NOV 65 IS OBSOLETE

UNCLASSIFIED

SECURITY CLASSIFICATION OF THIS PAGE (When Data Entered)

UNCLASSIFIED

SECURITY CLASSIFICATION OF THIS PAGE (When Data Entered)

occurring in an extremely non-Boltzmann vibrational distribution. The relaxation of excited vibrational levels ($v \leq 16$) by CO_2 and bounds on the radiative lifetimes for several of the levels are presented.

→ From a related kinetic analysis, predictions of the efficiency of creating vibrationally excited CO in these mixtures is discussed in Chapter 3. These predictions are based on modeling of the energy deposition in the gas by the beam and beam growth coupled with the accurately measured non-uniform field of view of the detector.

→ Chapters 4 and 5 deal with NO fluorescence arising from electron irradiated N_2/O_2 mixtures. Fluorescence from both bands of NO were simultaneously detected using the interferometer with an indium antimonide detector. As a result, the ratios of the radiative lifetimes of each level have been determined, and are presented in Chapter 4.

→ The relaxation of NO in N_2/O_2 mixtures is described in Chapter 5. Relaxation rate constants have been measured for quenching of $\text{NO}(v=7)$ by O_2 . Although the role of atomic quenchers has not been quantified, supporting studies of O-NO afterglow and computer modeling have permitted a qualitative understanding of their contribution to the observed relaxation.

→ A study of the cryogenic LABCEDE facility is found in Chapter 6. This study establishes facility capabilities and recommends key design goals for system performance improvement to permit the determination of absolute intensities and excitation efficiencies of uncontaminated gases. A preliminary survey of the emission from N_2 , O_2 , and N/O_2 gas mixtures in the spectral region 0.6-3.0 μm has been completed using both the interferometer and a 1/4 meter spectrometer and these findings are given in Chapter 7. A variety of gas mixtures were irradiated in search of a strong radiation in the 3-4 μm region. The results of this survey are presented in Chapter 8. The magnitude of various noise sources and their effect on the transformed spectra are discussed in Chapter 9, along with our findings of the effects of interferometer alignment on spectral intensities.

Experimental improvements; a computer code which was developed to predict the fractional response of the system due to field of view non-uniformities and beam growth; the effects of radiation trapping of argon excited states; O + NO afterglow experiments used to qualitatively determine O-atom concentrations as a function of O_2 pressure; and a detailed spectral intensity code of the nitrogen first positive system are presented in Appendixes.

UNCLASSIFIED

SECURITY CLASSIFICATION OF THIS PAGE (When Data Entered)

TABLE OF CONTENTS

<u>Section</u>	<u>Page</u>
1. INTRODUCTION	1
REFERENCES	4
2. VIBRATIONAL RELAXATION OF CO(v)	5
2.1 Introduction	5
2.2 Experimental Operating Conditions	7
2.3 Data Reduction and Analysis	11
2.4 Kinetic Interpretation	16
2.5 Summary and Conclusions	35
REFERENCES	36
3. EXCITATION EFFICIENCY OF CO(v) IN IRRADIATED CO ₂ /Ar MIXTURES	39
3.1 Introduction	39
3.2 Absolute Calibration	39
3.3 Kinetic Analysis	43
3.4 Formation Mechanisms	54
3.5 Summary	62
REFERENCES	63
4. NITRIC OXIDE EINSTEIN COEFFICIENT RATIOS DETERMINATION	65
4.1 Introduction	65
4.2 Experimental Measurements Program	68
4.3 Analysis	71
4.4 Summary and Conclusions	78
REFERENCES	80
5. THE VIBRATIONAL RELAXATION OF NO(v=1-7) BY O ₂	83
5.1 Introduction	83
5.2 Experimental and Data Analysis	86
5.3 Kinetic Analysis	91
5.4 Global Kinetic Effects/Computer Modeling	105
5.5 Summary	122
REFERENCES	123

TABLE OF CONTENTS (Continued)

<u>Section</u>	<u>Page</u>
6. CRYOGENIC LABCEDE SYSTEMS STUDY	129
6.1 Introduction	129
6.2 Present System Capabilities	131
6.3 System Study Recommendation	133
6.4 System Performance Maps for Refurbished LABCEDE	135
REFERENCES	152
7. NEAR IR EMISSION OF N ₂ /O ₂ MIXTURES	153
7.1 Introduction	153
7.2 Experimental	154
7.3 Results and Discussion	157
7.3.1 Nitrogen First Positive Emission Features	157
7.3.2 Metastable N(² P) Decay	159
7.3.3 Fluorescence from O ₂ and N ₂ /O ₂ Mixtures	161
7.4 Summary and Future Plans	162
REFERENCES	164
8. SURVEYS OF 3-4 μM EMITTERS	165
REFERENCES	175
9. INTERFEROMETRIC NOISE SOURCES	177
9.1 Introduction	177
9.2 Noise Sources	178
9.2.1 Detector Noise	178
9.2.2 Source Noise	179
9.2.3 Digitizing Noise	189
9.2.4 Photon Noise	190
9.2.5 Sampling Errors	190
9.2.6 Summary of LABCEDE Interferometric Noise Source	192
9.3 Interferometer Optical Misalignment	193
REFERENCES	198

TABLE OF CONTENTS (Continued)

<u>Section</u>	<u>Page</u>
APPENDIX I EXPERIMENTAL APPARATUS MODIFICATION	199
APPENDIX II FIELD OF VIEW CALCULATIONS	205
REFERENCES	214
APPENDIX III RADIATIVE TRAPPING OF ELECTRONICALLY EXCITED ARGON	215
REFERENCES	219
APPENDIX IV NO + O AFTERGLOW STUDIES	221
IV.1 Introduction	221
IV.2 Basic Technique of Air Afterglow Calibration	222
IV.3 Air Afterglow Calibration in LABCEDE	224
IV.3.1 Experimental Set Up	224
IV.3.2 Identification of O/NO Afterglow	227
IV.3.3 Kinetic Model for Analyzing Air Afterglow Calibration Experiments	230
IV.3.4 Results of O/NO Calibration with N ₂ /NO Mixtures	236
IV.4 Air Afterglow Measurements in N ₂ /O ₂ /NO Mixtures	236
IV.4.1 Kinetic Model for N ₂ /O ₂ /NO Mixtures	236
IV.4.2 Results of Studies in N ₂ /O ₂ /NO Mixtures	241
IV.5 Observations in N ₂ /O ₂ Mixtures	247
IV.5.1 N ₂ /O ₂ Mixtures with O ₂ > 1.5 Torr	247
IV.5.2 N ₂ /O ₂ Mixtures with PO ₂ < 0.75 Torr	249
IV.6 Summary	253
REFERENCES	257
APPENDIX V NITROGEN FIRST POSITIVE SPECTRUM SYNTHESIS	259
V.1 Theory	259
V.2 Computer Program	263
REFERENCES	268



Accession For	
NTIS GRA&I	<input checked="" type="checkbox"/>
DTIC TAB	<input type="checkbox"/>
Unannounced	<input type="checkbox"/>
Justification	
By	
Distribution/	
Availability Codes	
Avail and/or	
Dist	Special
A	

LIST OF ILLUSTRATIONS

Figure		Page
2.1	Time sequencing of data acquisition during an experiment.	10
2.2	The time and frequency resolved fluorescence from a 0.15 torr CO ₂ /9.0 torr Ar mixture at 0.2 ms intervals after beam termination.	13
2.3	A fit of a synthetic CO spectrum to data taken 0.5 ms after beam termination as in Fig. 2.2.	17
2.4	The relative populations of levels 1-13 at three times after beam termination.	18
2.5a	The populations of levels 1-6 calculated from the fluorescence spectra of Fig. 2.3 between 0.1-4.9 ms after beam termination.	19
2.5b	The populations calculated from the fluorescent spectra of Fig. 2.3 between 0.1-4.9 ms after beam termination for levels 7-12.	20
2.6	The relaxation rates deduced for the 0.15 torr CO ₂ /9.0 torr Ar case.	27
2.7	Some representative Stern-Volmer plots for levels 4, 6, 8 and 10.	29
2.8	The deduced rate constants for the reaction CO(v) + CO ₂ + CO(v-1) + CO ₂ * for v = 1,16.	30
2.9	The values of the intercepts for two series of runs taken at different times as a function of vibrational level.	32
2.10	The differences between the intercepts as plotted in Fig. 2.9 and the theoretical Einstein coefficient predictions as a function of vibrational level.	33
3.1	Schematic of beam current distribution within field of view.	42
3.2	Calculated populations in each level within the field of view at three times during beam pulse.	46
3.3	Deduced CO(v) creation rates within the field of view as a function of vibrational level.	47
3.4a	Normalized CO(v) created per ion pair vs. vibrational level.	49

LIST OF ILLUSTRATIONS (Cont.)

<u>Figure</u>		<u>Page</u>
3.4b	Normalized CO(v) created per ion pair vs. vibrational level.	50
3.5	Total vibrationally excited CO created per ion pair vs. CO ₂ pressure.	52
3.6	Fraction of deposited electron beam energy partitioned to CO vibrational excitation as a function of CO ₂ pressure.	53
3.7	Argon excitation efficiencies as a function of primary electron energy for a 1% CO ₂ /99% Ar mixture.	57
3.8	CO ₂ excitation efficiencies as a function of primary electron energy for a 1% CO ₂ /99% Ar mixture	58
4.1	Theoretical values of Einstein coefficients for the NO fundamental and overtone transitions, from Michels ⁷ and Billingsley. ⁶	67
4.2a	Least-squares fits to NO fundamental data from a 0.3 torr CO ₂ , 10 torr N ₂ mixture at beam termination using a lead selenide detector.	75
4.2b	Least-squares fit to NO overtone data from 0.3 torr O ₂ , 10 torr N ₂ mixture at beam termination using a lead sulfide detector.	76
4.3	Experimentally determined Einstein coefficient ratios for first overtone/fundamental bands of NO.	77
5.1	The time and spectrally resolved fluorescence from NO($\Delta v=1$) transitions at 0.1 ms intervals after beam termination.	88
5.2	Fit of a synthetic NO spectrum to data taken at beam termination from a 50 torr N ₂ , 1.5 torr O ₂ mixture.	89
5.3	NO vibrational population histories for levels 1-5 for P _{N2} = 50 torr, P _{O2} = 1.5 torr.	90
5.4	Bounds on the relaxation rate constants for the reaction NO(v) + O ₂ → NO(v-1) + O ₂ for v = 1-7.	98
5.5	Stern-Volmer plots for vibrational levels 1 and 3.	99
5.6	Intercepts of Stern-Volmer plots with expected N ₂ relaxation for v = 1 and radiative decay rates shown for comparison.	104

LIST OF ILLUSTRATIONS (Cont.)

<u>Figure</u>		<u>Page</u>
5.7	Predicted relative production/electron-ion pair of N_2^+ , $N_2(A)$, N^+ , N , O_2^+ , O^+ , O for various O_2/N_2 mixtures.	108
5.8	Monte Carlo prediction of electron energy deposition in nitrogen.	114
5.9	Predicted electron-ion pair production rate vs. pressure for several distances downstream.	116
5.10	Fraction of oxygen atoms which have not diffused out of a cylinder of radius 2.2 cm.	118
5.11	Predicted species mole fraction vs. time for the tenth pulse.	119
5.12	Predicted mole fraction vs. time.	121
6.1	Schematic of cryogenic LABCEDE facility in its present configuration.	132
6.2	Possible electron beam improvements.	136
6.3	Possible gas flow changes.	137
6.4	Summary of suggested LABCEDE system changes.	138
6.5	The time scales for diffusion and quenching to occur are plotted as a function of pressure in the cryogenic LABCEDE facility.	139
6.6	The time scales for diffusion and quenching as in Fig. 6.5 Also shown are the radiative lifetimes of some transitions of interest.	141
6.7	The theoretical blackbody emission curves for several temperatures as a function of wavelength.	143
6.8	LABCEDE extrapolated beam growth at 30 μ pressure from the two measurements (see text).	144
6.9	The expected signal and background intensities assuming one photon per ion pair for short lived transitions when diffusion and quenching are unimportant.	146
6.10	The expected intensities for one photon per ion pair for 2 keV electrons assuming quenching occurs at 10^{-2} gas kinetic and a radiative lifetime of 10 ms for a 15 cm field of view.	147

LIST OF ILLUSTRATIONS (Cont.)

<u>Figure</u>		<u>Page</u>
6.11	Expected signal and background levels on the refurbished LABCEDE facility.	149
7.1	System spectral response of the three detectors when used with the 1/4 m spectrometer.	155
7.2	Comparison of interferometric data and N ₂ (1P) code prediction.	158
8.1	Relative spectral responses of detectors available on LABCEDE for survey runs.	166
8.2	Spectrum from N ₂ /O ₂ mixture at 100 torr/2 torr viewed by an InSb detector.	167
8.3	Uncorrected spectrum from 20 torr N ₂ , 4 torr NO using a PbSe detector at 77 K.	169
8.4	Uncorrected spectrum of 5 torr N ₂ O/90 torr N ₂ mixture using the PbSe detector at 77 K showing N ₂ O bands ν_3 , $\nu_1 + 2\nu_2$, and $2\nu_1$ as well as weak NO fundamental.	170
8.5	Uncorrected spectrum from N ₂ (20 torr)/H ₂ (1 torr) mixture using PbS detector at 77 K.	172
8.6	Emission from 0.3 torr CH ₄ , 20 torr N ₂ mixture.	173
9.1	Spectrum from transformed interferogram at beam termination from 0.14 torr CO ₂ /8.9 torr Ar mixture.	183
9.2	Spectrum from transformed interferogram with 1% noise added.	184
9.3	Spectrum from transformed interferogram with 3% noise added.	185
9.4	Spectrum from transformed interferogram with 10% noise added.	186
9.5	Vibrational populations calculated from previous spectra with varying amounts of noise added to the original interferogram.	188
9.6	Spectrum of blackbody (1173 K) viewed through a filter with a PbSe detector at 77 K.	195

LIST OF ILLUSTRATIONS (Cont.)

Figure		Page
9.7	Spectrum of blackbody viewed under the same conditions as Fig. 9.6, except interferometer was poorly optically aligned for this run.	196
II.1	Beam growth parameters A and B.	208
IV.1	Block diagram of experimental system.	255
IV.2	N_2 1 π spectrum from N-atom recombination in 50 torr of N_2 6 ms after termination of e-beam pulse, $\Delta\lambda = 5.2$ nm.	228
IV.3	Air afterglow spectrum in N_2/NO mixtures, 4 ms after e-beam termination.	229
IV.4	Decay of emission at 700 nm in $N_2/O_2/NO$ mixtures.	231
IV.5	Decay rates of 700 nm emission as a function of $[NO]$ at two different total pressures in $N_2/O_2/NO$ gas mixtures.	232
IV.6	Decay of emission at 700 nm as a function of time for N_2/NO mixtures.	237
IV.7	Decay rates of 700 nm emission as a function of $[NO]$ for N_2/NO mixtures.	238
IV.8	Air afterglow calibration plot after Eq. (IV.19).	239
IV.9	Decay of emission at 700 nm as a function of time.	243
IV.10	Decay of emission at 700 nm as a function of time for $N_2/O_2/NO$ mixtures.	244
IV.11	Decay rates at 700 nm as a function of $[O_2]$ for different $[NO]$ in $N_2/O_2/NO$ mixtures.	345
IV.12	O production rates as a function of $[O_2]$ for different values of $[NO]$ in $N_2/O_2/NO$ mixtures.	246
IV.13	Decay rates of emission at 700 nm as a function of $[O_2]$ in N_2/O_2 mixtures.	248
IV.14	700 nm emission zero-time intercepts as a function of $[O_2]$ for N_2/O_2 mixtures.	250
IV.15	Variation in emission intensity at 700 nm with time in N_2/O_2 mixtures.	251

LIST OF ILLUSTRATIONS (Cont.)

Figure		Page
IV.16	Beam growth as a function of λ for N_2/O_2 mixtures.	101
IV.17	Beam intensity percent of last decay component as a function of λ for N_2/O_2 mixtures at low λ .	101
IV.18	Intensity of slow decay component as a function of λ for N_2/O_2 mixtures at low λ .	101

LIST OF TABLES

Table		Page
5.1	Rate constants for processes $NO(v) + O_2 \rightarrow NO(v-1) + O_2$	101
5.2	Neutral chemistry for N_2/O_2 mixtures	112
6.1	Quenching rates by N_2, O_2	116
9.1	Comparison of spectral intensities	124
II.1/II.2	Beam growth parameters	202
II.3	Field-of-view function	211
II.4	Field-of-view computer code	212/213
V.1	Input data (cm^{-1})	265
V.2	Rotational constants (cm^{-1})	266
V.3	Absolute transition probabilities for the N_2 First Positive System	267

1. INTRODUCTION

This report describes the research efforts of the past three years which are primarily centered around measurements made on the warm LABCEDE Facility at the Air Force Geophysics Laboratory. In this apparatus a constant pressure, continuously flowing gas is irradiated by a pulsed electron beam. As the electrons pass through the gas mixture, they undergo inelastic collisions with the molecules and deposit energy. The energy lost by the beam goes into creation of free radicals and excited atomic and molecular states, and a fraction of that amount is emitted as fluorescence. This emission can be interpreted in terms of the chemical kinetic mechanisms occurring in the irradiated gases. Various fundamental quantities can be deduced from the temporal behavior of the fluorescence including relaxation rate constants, excitation rates, and radiative lifetimes.

Several of the projects described were undertaken simultaneously, and frequently provided mutual insight. As an example, Chapters 2 and 3 are concerned with fluorescence arising from beam created CO in irradiated CO₂/Ar mixtures. The emission is monitored with a lead selenide detector (through a Michelson interferometer). In the detector's bandpass the two dominant sources of radiation observed in these mixtures are the CO₂(ν_2) band at 4.3 μm) and the fundamental vibration/rotation band of CO. The CO emission arises from highly vibrationally excited levels (up to $v = 19$) occurring in an extremely non-Boltzmann vibrational distribution. The relaxation of excited vibrational levels ($v \leq 16$) by CO₂ and bounds on the radiative lifetimes for several of the levels are presented in Chapter 2.^{1,1}

From a related kinetic analysis, predictions of the efficiency of creating vibrationally excited CO in these mixtures is discussed in Chapter 3. These predictions are based on modeling of the energy deposition in the gas by the beam and beam growth coupled with the accurately measured non-uniform field of view of the detector.

Chapters 4 and 5 deal with NO fluorescence arising from electron irradiated N₂/O₂ mixtures. Although several theoretical predictions of the Einstein coefficients for NO($\Delta v=1$) and ($\Delta v=2$) exist, there are no experimental

measurements of these quantities for $v=2$. Fluorescence from both bands of NO were simultaneously detected using the interferometer with an indium antimonide detector. As a result, the ratios of the radiative lifetimes of each level have been determined, and are presented in Chapter 4.^{1,2}

The relaxation of NO in N_2/O_2 mixtures is described in Chapter 5. Relaxation rate constants have been measured for quenching of $NO(v=7)$ by O_2 .^{1,3} Although the role of atomic quenchers has not been quantified, supporting studies of O-NO afterglow and computer modeling have permitted a qualitative understanding of their contribution to the observed relaxation.

A study of the cryogenic LABCEDE facility is found in Chapter 6. This study establishes facility capabilities and recommends key design goals for system performance improvement to permit the determination of absolute intensities and excitation efficiencies of uncontaminated gases.

A preliminary survey of the emission from N_2, O_2 , and N_2/O_2 gas mixtures in the spectral region 0.6-3.0 μm has been completed using both the interferometer and a 1/4 meter spectrometer. Emission from N_2 (B-A) First Positive, $O_2(b-x)$ and $O_2(b-a)$ bands was observed among others. These findings are given in Chapter 7.

Chapters 8 and 9 are an outgrowth of the NO Einstein coefficient ratios studies. Before the indium antimonide detector was utilized, both bands could not be observed with the same detector and two detectors were required. A variety of gas mixtures were irradiated in search of a strong radiator in the 3-4 μm region which would be detectable by both detectors and could be used as a cross calibration. The results of this survey are presented in Chapter 8. An alternate approach was to try to reduce the spectral noise levels to permit simultaneous detection of both NO bands. The magnitude of various noise sources and their effect on the transformed spectra are discussed in Chapter 9, along with our findings of the effects of interferometer alignment on spectral intensities.

Experimental improvements and technique refinement have resulted in over an order of magnitude improvement in signal-to-noise during this reporting period and briefly described in Appendix I. A computer code which was developed to predict the fractional response of the system due to field of view nonuniformities and beam growth is discussed in Appendix II. Appendix III deals with the effects of radiation trapping of argon excited states leading to increased CO production in CO₂/Ar mixtures. Appendix IV describes in more detail the O + NO afterglow experiments used to qualitatively determine O-atom concentrations as a function of O₂ pressure in support of the measurements of Chapter 5. A detailed spectral intensity code of the nitrogen First Positive system was developed as part of this program and is described in Appendix V.

REFERENCES

- 1.1 G. E. Caledonia, B. D. Green, and R. E. Murmphy, "A Study of the Vibrational Level Dependent Quenching of CO($v=1-16$) by CO₂," J. Chem. Phys. 71 (11), 4369 (1979).
- 1.2 B. D. Green, G. E. Caledonia, and R. E. Murphy, "A Determination of the Nitric Oxide Einstein Coefficient Ratios," JQSRT 26, 215 (1981).
- 1.3 B. D. Green, G. E. Caledonia, and R. E. Murphy, "Vibrational relaxation of NO($v=1-7$) by O₂," submitted to J. Chem. Phys.

2. VIBRATIONAL RELAXATION OF CO(v)

2.1 Introduction

The phenomenon of vibrational relaxation of gas phase molecules has been the subject of a considerable amount of research in the last few decades because of its importance in a number of disparate areas such as gas laser physics, sound propagation, energy conversion and infrared radiation physics. The most prominent diagnostic used for these studies has been the radiative infrared emission or absorption of the relaxing states, although alternate techniques such as ultrasonic absorption, Raman scattering, electronic state excitation and Schlieren photographs have also been utilized successfully. A variety of excitation techniques such as optical and electron pumping, chemiluminescent reactions and shock wave heating have also been employed. The multiplicity of experimental techniques, as well as the data base for vibrational relaxation and exchange, has been the subject of several review articles^{2.1-2.4} and will not be discussed in detail here. In the majority of cases, only the relaxation of the lowest vibrational level, or possibly, the lowest two levels, have been studied. Indeed, in many cases, the upper levels are assumed to be in Boltzmann equilibrium with the first level.

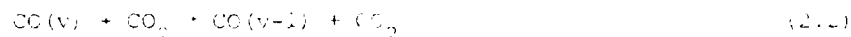
Perhaps the most prominent examples of multi-level relaxation studies are those of Smith and co-workers.^{2.5-2.8} In these experiments, highly vibrationally excited species are created via chemiluminescent reactions and the steady state, spectrally resolved emission from the fundamental or first overtone vibration-rotation band of the excited molecules is monitored as a function of the quenchant partial pressure. The observed spectra are interpreted to determine appropriate vibrational population distributions which are then analyzed with modified Stern-Volmer^{2.9} relationships to deduce the vibrational level dependent quenching rate constants. This technique has been successfully employed to determine the single quantum deactivation rate constants for a large number of vibrational levels of molecules such as CO, HF and DF.

Chemi-excitation reactions are also used in the present approach to produce the highly vibrationally excited molecules; however, the precursors of the chemi-excitation process are now produced through irradiation of the test gas by a pulsed electron beam. The spectrally resolved temporal histories of the vibrational band emission from the excited states is monitored both during and after pulse irradiation via time resolved Fourier spectroscopic techniques.^{2.10,2.11} These spectra are then interpreted to deduce the temporal histories of the vibrational population distribution which may then be used in conjunction with the master equations for vibrational relaxation to deduce the quenchant rate constants of interest.

The specific case considered in this section of the report involves the relaxation of highly vibrationally excited CO produced during the electron irradiation of mixtures of CO₂/Ar. The predominant mechanism producing CO is believed to be the electron-ion recombination reaction



The spectrally resolved fluorescence of the fundamental vibration-rotation bands of CO has been monitored as a function of time with a spectral resolution of 10 cm⁻¹ which permits discrimination of the fluorescence contributions from individual vibrational levels; fluorescence from levels as high as v = 19 has been observed. The primary quenchant in the system is CO₂ and rate constants for the reaction



have been obtained for vibrational levels v = 1-10.

A general description of the experimental apparatus including the details of the computer-interfaced interferometer system is presented in Part 2.2 of this section. A description of the fluorescence data base and its reduction to vibrational populations is given in subsection 2.3, and

the details of the kinetic analysis used to deduce the relevant rate constants are provided in Part 2.4. The summary and conclusions of this section may be found in the last part.

2.3 Experimental Operating Conditions

For these measurements a constant pressure, continuously flowing gas is irradiated by the pulsed, collimated electron beam of known current and voltage. As the electron beam passes through the gas, the beam electrons undergo collisions with the gas molecules which result in beam energy loss and spreading. Some fraction of the energy lost by the electron beam will, either directly or indirectly, appear as fluorescence in the gas. This fluorescence can be interpreted in terms of the chemical kinetic mechanism of the gas and the irradiated test gases.

The electron beam is accelerated through a series of seven electrodes which provide a total potential drop of 30 kV and is then focused through a series of lenses and nozzles into the target chamber. A differential pumping system maintains the target chamber at pressures between 10^{-7} torr and 10^{-8} torr while maintaining the gun filament at a pressure of 10^{-7} torr. The electron beam current is attained by a combination of meter screw adjustment of the position of the pinhole nozzles and magnetic beam deflection. A solid state pulser network accurately controls beam pulse width and timing. The measured current rise and decay times ($1/e$) are six nanoseconds. Because the target chamber is electrically insulated from the rest of the apparatus, it acts as a Faraday cup and is utilized to measure the beam current at reaching the target chamber. The experiments were performed with a 9% duty cycle (2.5 ms on, 25 ms off) and typical current of 100 nA.

The gases used in these experiments were ultrahigh purity argon (99.9998%) and carbon dioxide (99.99%). These test gases were further purified through use of a dry ice-acetone trap before admission into the test chamber. The relative flows of the two gases are measured using flowmeters with the flow controlled by a Granville-Phillips variable leak valve. The two flows are mixed just prior to entering the target chamber. Total

chamber pressure is monitored using a Baratron capacitance manometer (MKS) referenced to the low pressure filament chamber. An alphasatron gauge monitored the pressure in the last nozzle chamber. Both pressure monitors were calibrated against a Wallace-Tiernan diaphragm pressure gauge, and the flowmeters were calibrated for their respective gases using the Wallace-Tiernan gauge and the accurately known system volume.

It is desirable to flow the gases through the test chamber as quickly as possible in order to minimize the buildup of electron beam created species (see Part 2.4). The measurements discussed here were all performed at total chamber pressures between 9 and 10 torr with flow rates of order 5-6 standard liters per minute (CO_2 flow rates were varied between 8-500 standard cubic centimeters per minute). For these conditions the gas residence time within the test chamber is estimated to be 1.3 seconds.

The fluorescence from the irradiated gases is viewed through a calcium fluoride window by the Michelson interferometer having its optical axis perpendicular to the beam axis. The central fringe pattern of the interferometer is focused on to a lead selenide detector (cooled to 77 K) which has an intrinsic response time of 75 μs . The detector is 3 mm square masked to 3 mm circular diameter to match the spectral resolution, and forms the limiting aperture of the system providing a circular field of view 8 cm in diameter centered on the electron beam axis at a position 8 cm downstream of the beam entrance into the target chamber. System improvements and technique refinement during this measurement program resulted in over an order of magnitude improvement in signal to noise. Further details are given in Appendix I.

The detector signal, after processing by computer, can be used to obtain both spectral and temporal resolution of the fluorescence. The general techniques employed in time-resolved Fourier spectroscopy have been described previously^{2.10,2.11} and only a brief account of the system specifics will be provided here. The signal from the biased detector is band-pass amplified (PARC model 113) and then the amplified signal is fed into a sample and hold network, which samples the detector signal at times determined by a digital delay network. The sampled signal is converted to

digital form by an A/D converter and stored in the memory of a Digital Equipment Corp. PDP 15 computer which is dedicated to the experiment. The digital delay network timing is referenced just prior to the onset of the electron beam. A clock internal to the delay network initiates sampling of the detector signal at intervals of 0.2 milliseconds corresponding to a total of 137 consecutive sampling times during the beam period.

The interferometer scanning mirror is moved continuously during the data acquisition. Changes in the mirror position are followed by monitoring the central interference fringe of a helium-neon laser ($\lambda = 632.8$ nm) spatially offset from the interferometer optical axis. These fringes are detected by a separate silicon diode. This reference fringe pattern repeats itself as the mirror is moved $0.3164 \mu\text{m}$ ($\lambda/2$ for the monochromatic laser source). An assumption is made in the signal processing that all electron beam pulses occurring between laser fringe maxima have the same mirror position, i.e., that the mirror steps. For these experiments, the mirror was scanned at a speed such that fringes occurred about once a second, and the beam was pulsed about forty times during each fringe. The stored signals at each sampled time during the beam period are recorded on a peripheral magnetic tape, and the next sampling started. The time sequence of the data acquisition is shown in Fig. 2.1. In this manner, the time history of the decay of the total signal on the detector at each mirror position is stored. In any experimental run the movable mirror is scanned from the maximum optical path difference through zero optical path difference to a similar maximum displacement on the opposite side of zero (double-sided interferogram). For these experiments, the maximum path difference (0.05 cm) is chosen so that a resolution of 10 cm^{-1} is obtained in the recovered spectra.

The data stored on the magnetic tape during the experiment is an array of time ordered signals for each consecutive mirror position. The array is re-ordered to provide the signal at a given time during the pulse for all mirror positions for each of the consecutively sampled times, i.e., the interferogram of the signal at every 0.2 milliseconds during the pulse. The change in signal caused by the electron beam pulse is obtained by comparison of the averaged signal just prior to beam onset with the averaged

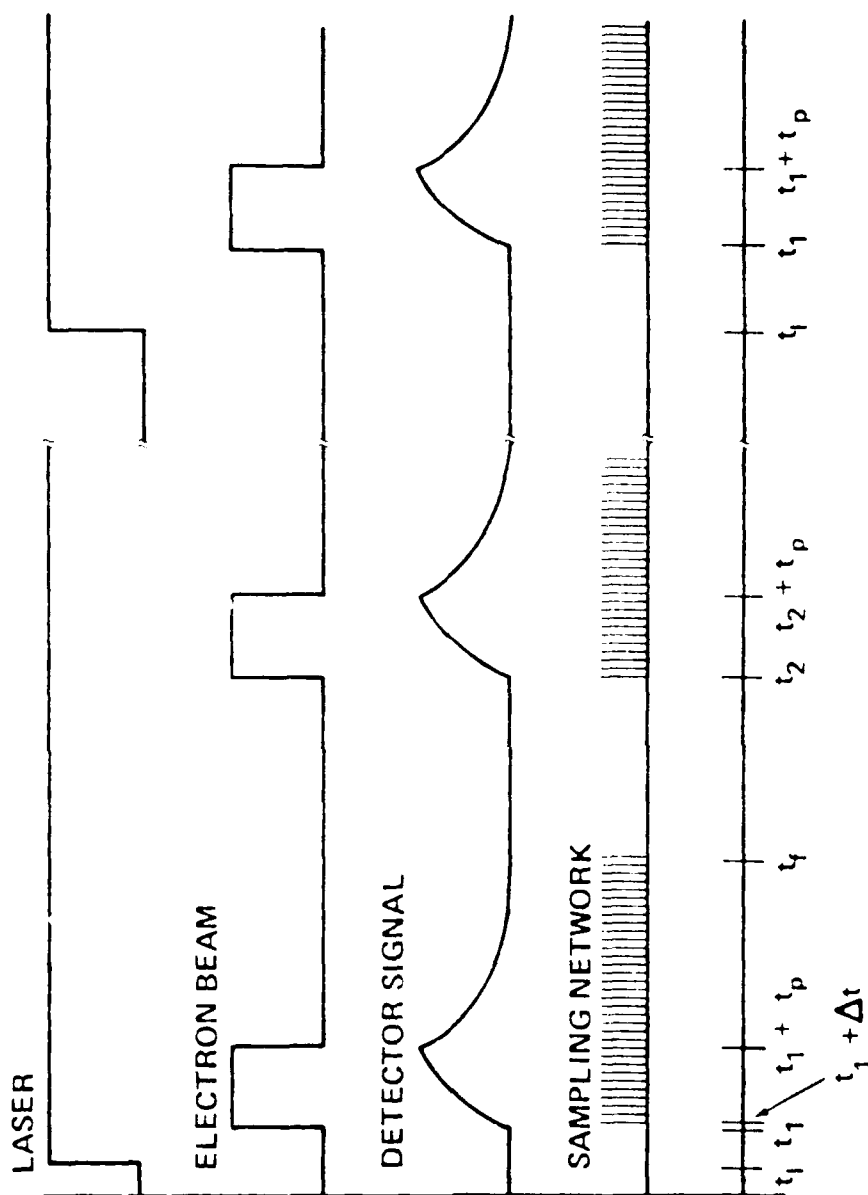


Fig. 2.1 Time sequencing of data acquisition during an experiment. The HeNe laser reference channel logic goes high and new arrays are opened for data storage. The next electron beam pulse at time t_1 , starts the sampling of the fluorescence signal at 0.2 ms intervals both during the pulse and after termination. During the next pulse at t_2 the signal from each interval is stored by adding it to the signal from the same interval during the first pulse. After about 40 electron beam pulses the next laser logic signal occurs, causing the summed signals for all the intervals to be stored on magnetic tape and the arrays for the next mirror position to be initialized.

signal at each specific time during the pulse period for each individual mirror position. This subtraction is performed during the sorting of the data.

A series of such measurements were performed in electron irradiated mixtures of Ar/CO₂. The argon bath was maintained at a pressure near 9 torr while the CO₂ partial pressure was varied between 0.008 - 1.0 torr. These conditions were chosen in order to maximize energy deposition while maintaining a thin target gas and keeping residence time short, minimizing the build-up of beam created species. Carbon dioxide pressures were found to be sufficiently high so that measurable CO vibrational relaxation occurred on the 20 millisecond time scale of the experiment. Cases in which the fluctuations of the electron beam current were greater than 5% were discarded.

Measurements were performed over a period of several months. Several runs with increasing CO₂ pressure were made on individual days in order to allow determination of the effects of background quenchers and to provide a range of values for the observed level dependent relaxation of CO(v) by CO₂. Because CO₂ tends to absorb on the walls, runs were made with increasing CO₂ partial pressure during a given day. At least once a day the interferometer was rotated to view a 1173 K calibrated blackbody source and a relative spectral response curve was obtained. The blackbody source was positioned at a distance equal to the distance of the center of the target chamber from the interferometer. Day to day overall system response was reproducible to 1%.

2.3 Data Reduction and Analysis

For each case, the basic experimental data are a set of interferograms representative of the infrared fluorescence generated at 0.2 ms intervals during the beam period. These interferograms are then transformed into spectra using the fast Fourier transform algorithms.^{2,12} Recovered spectra are correlated for detector spectral response using spectral calibrations from a standard blackbody source. The spectral range spanned by the interferometer is constrained by the response curve of the PbSe detector which peaks at 1100 cm⁻¹ and falls to one-third maximum response at 1560 cm⁻¹ and at 3300 cm⁻¹.

Careful measurements of the field of view of the interferometer have permitted the determination of an absolute spectral calibration; details of this calibration will be presented in the next section of this report which discusses absolute electron excitation efficiencies. Only the relative changes in the signal levels are required for the relaxation kinetics studies here; however, absolute intensities and concentrations were necessary for estimation of typical chemiluminescence product densities.

In all measurements the dominant features observed in the 1700-2500 cm^{-1} spectral region are due to radiation from the $\text{CO}_2(\nu_3)$ and CO fundamental vibration-rotation bands. A typical time history of the observed spectra is shown in Fig. 2.2; the spectra are plotted with time increasing out of the page so as to emphasize the vibrational relaxation occurring after beam termination at 2.5 ms. The $\text{CO}_2(\nu_3)$ band radiation centered near 2330 cm^{-1} , is strongly self-absorbed and much of the observed spectral structure is the result of hot band and isotopic species transitions. This radiation is caused primarily by direct electron excitation of CO_2 . This radiation has been analyzed previously^{2.13,2.14} and will not be discussed further here. The CO fluorescence, falling between 1700-2200 cm^{-1} is due to radiation from highly vibrationally excited CO, with levels up to $v = 19$ in evidence. Since CO is not present in the unperturbed test gases, it must be formed during electron beam irradiation. Dissociative recombination of CO_2^+ , reaction (2.1), appears to be the primary production mechanism for CO in the present system although other kinetic processes may also play some role. Possible CO production mechanisms are discussed more fully in Sec. 3.

The emphasis of this section is not to determine the appropriate creation processes for the vibrationally excited CO, but rather in interpreting the kinetic mechanisms responsible for the subsequent vibrational relaxation occurring upon beam termination. The first step in such an interpretation involves the determination of the vibrational population distributions responsible for the vibro-luminescence. This is accomplished by a curve fitting procedure wherein the spectrally resolved fluorescence is compared with synthetic computer-generated CO spectra obtained as the

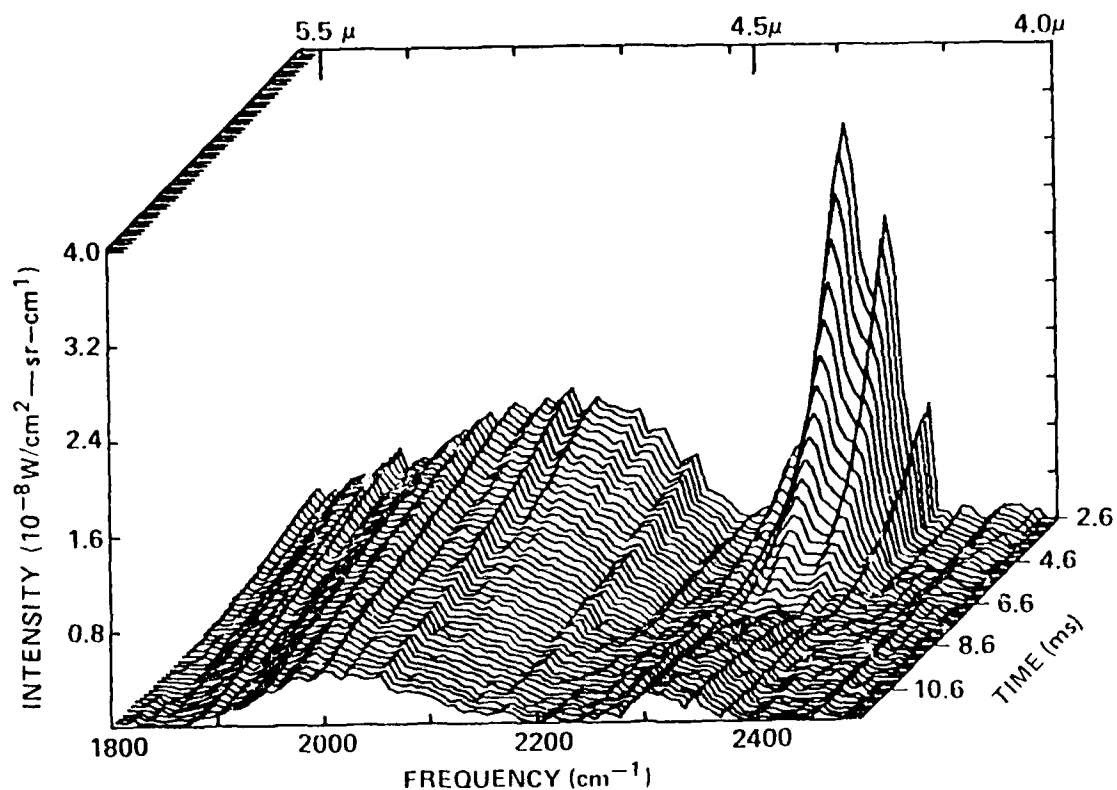


Fig. 2.2 The time and frequency resolved fluorescence from a 0.15 torr $\text{CO}_2/9.0$ torr Ar mixture at 0.2 ms intervals after beam termination. The CO fundamental ($\nu < 19$) and $\text{CO}_2(\nu_3)$ features are observed. Time is plotted as increasing toward the front of the figure. The rear scan corresponds to the spectrum 0.1 ms after beam termination (2.6 ms after onset), and the front scan to 9.3 ms after termination. The CO_2 fluorescence has essentially disappeared by 4.5 ms after beam termination. These spectra have been corrected for detector response.

sum of the contributions of the radiation per unit population in each vibrational level. Details of this fitting procedure have been discussed previously for the case of NO radiation;^{2,15} similar methods have also been used in earlier studies of CO relaxation.^{2,5,2,16} A brief description of the technique is provided below.

The integrated intensity of a given rotational transition in the vibrational band may be specified by

$$I_{J \rightarrow J+1}^{v \rightarrow v+1}(\nu_T) = \frac{hc}{T} \frac{4}{(2J+1)} \frac{S_J^{P,R}}{3} \frac{A_{v \rightarrow v+1}}{\nu_{v \rightarrow v+1}} \frac{N_{v,J}}{\nu_{v \rightarrow v+1}} \quad (2.3)$$

where $A_{v \rightarrow v+1}$ is the Einstein coefficient, $\nu_{v \rightarrow v+1}$ is the band origin in cm^{-1} , ν_T is the frequency of the individual transition, $S_J^{P,R}$ is the Hönl-London factor, h and c are Planck's constant and the speed of light, respectively. $N_{v,J}$ is the population of the radiating state which for a Boltzmann rotational distribution is

$$N_{v,J} = N_v \frac{hcB_v}{kT} (2J+1) \exp(-F(v,J) hc/kT) \quad (2.4)$$

where

$$B_v = B_0 - \epsilon_0 (v + 1/2) \quad (2.5)$$

and

$$F(v,J) = B_v J(J+1) - D_v J^2 (J+1)^2 \quad (2.6)$$

The frequency of each transition, ν_T is defined as the energy difference between upper and lower states of the transition, whose energies are calculated from the formula:

$$E_{v,v'} = \left[\left(v + \frac{1}{2} \right) - \frac{1}{2} x_{11} \left(v + \frac{1}{2} \right)^2 \right] \left(\frac{1}{2} \right) \left(v + \frac{1}{2} \right)$$

$$+ \frac{1}{2} x_{12} \left(v + \frac{1}{2} \right) + E_{v,v'}^0 \left(v + \frac{1}{2} \right)^2$$

The values of the spectroscopic constants, in cm^{-1} , used in the present work taken from Hamilton and Klemm^{11,12}

$$x_{11} = 0.0001, \quad x_{12} = 0.0001, \quad x_{22} = 0.0001$$

$$E_{0,0}^0 = 0, \quad E_{1,0}^0 = 17150, \quad \text{and } E_{2,0}^0 = 34300 \text{ cm}^{-1}$$

Using the constants and combining Eq. (1.1) and (2.1), the intensity of a given vibrational level transition for vibrationally excited molecules, $I_{v,v'}^{\text{vib}}$, can be found once the harmonic coefficients are known. The intensity is defined for the fundamental and first overtone band for the $v=0$ and $v=1$ levels. The present work is based on work of Rabinovich and Rabinovich¹³ and Rabinovich¹⁴. Agreement between the two sets of values is good; in Figure 2 the values of $I_{v,v'}^{\text{vib}}$ used in the present analysis.

The calculated line spectrum per vibrationally excited molecule is then convolved with a sinc slit function representative of the interferometer's instrument function:

$$g(\nu, \nu_0) = \frac{0.82}{\pi} \frac{\sin \left(\frac{\pi}{0.82} (\nu - \nu_0) \right)}{(\nu - \nu_0)} \quad (2.2)$$

where ν_0 is the center of the instrument function, and π is the spectral resolution, 10 cm^{-1} . The resultant spectra per vibrationally excited molecule (basis function) for each of the vibrational levels are used in generating the synthetic spectrum. The best fit to the data is obtained by a routine which minimizes the squares of the differences between the data and the sum of the weighted vibrational basis functions. The weighting factor is the relative population of each vibration level.

An example of the results of this fitting procedure is shown in Fig. 2.3. Both the experimental data of the CO fundamental fluorescence and synthetic spectrum fit to it are shown in the figure. A rotational temperature of 300 K was used in generating the synthetic spectra. The computed spectrum matches the vibrational structure exhibited in the fluorescence very well over the entire spectral band. The standard deviation of the fit is only 1.5%. Several of the contributing basis functions, appropriately weighted, are also displayed. The basis functions overlap greatly, necessitating the least squares fitting procedure: for example, note that the P branch transition of molecules with seven vibrational quanta occurs at the same frequency as the $v = 9$, R branch transitions. In fact, only in the wing of the $v = 1$, R branch is there an absence of overlap with radiation from other vibrational bands.

The relative populations determined from such fits are shown in Fig. 2.4 at three times after beam termination. The populations of the majority of the excited states continually decrease with increasing time after beam termination. It can be seen however, that the populations of some of the levels decrease more slowly than others and in a few instances actually increase temporarily. This may be attributed to the interplay between the source term (due to relaxation from the level above) and the loss term (due to relaxation by all pathways into the level below) of the particular level. In the figure, levels 5 through 8 are seen to change less rapidly in time than the levels above and below. In fact, at later times, a population inversion occurs between level 5 and levels 2 through 4. The change in the population of each vibrational level as a function of time is shown more clearly in Fig. 2.5, where the calculated populations from fits to spectra at 0.2 ms intervals are plotted. The calculated populations are seen to be relatively smoothly varying. With small temporal and spectral fluctuations, data such as this can be used directly to deduce the coupled vibrational-level dependent relaxation rates, as discussed in subsection 2.4.

2.4 Kinetic Interpretation

As mentioned previously, CO fluorescence measurements have been performed in room temperature mixtures of CO_2/Ar having CO_2 partial pressures

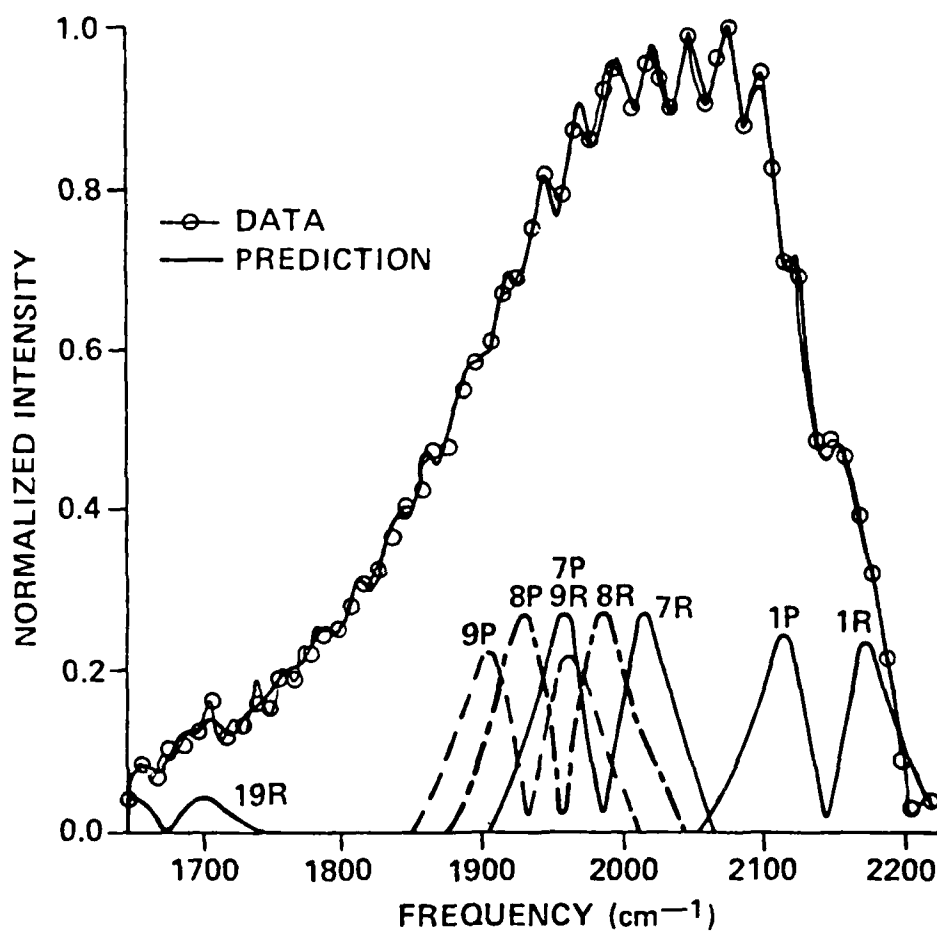


Fig. 2.3 A fit of a synthetic CO spectrum to data taken 0.5 ms after beam termination as in Fig. 2.2. The standard deviation of the fit is 1.5%. Basis functions for $v = 1, 7, 8, 9$, and 19 are shown with intensities representative of their contribution to the total synthetic spectrum. Only the $v = 1$ R branch is not overlapped by radiation from other levels. In particular, the $v = n$ P branches and the $v = n + 2$ R branches fall on top of each other (7P and 9R shown). See text for details of basis function generation.

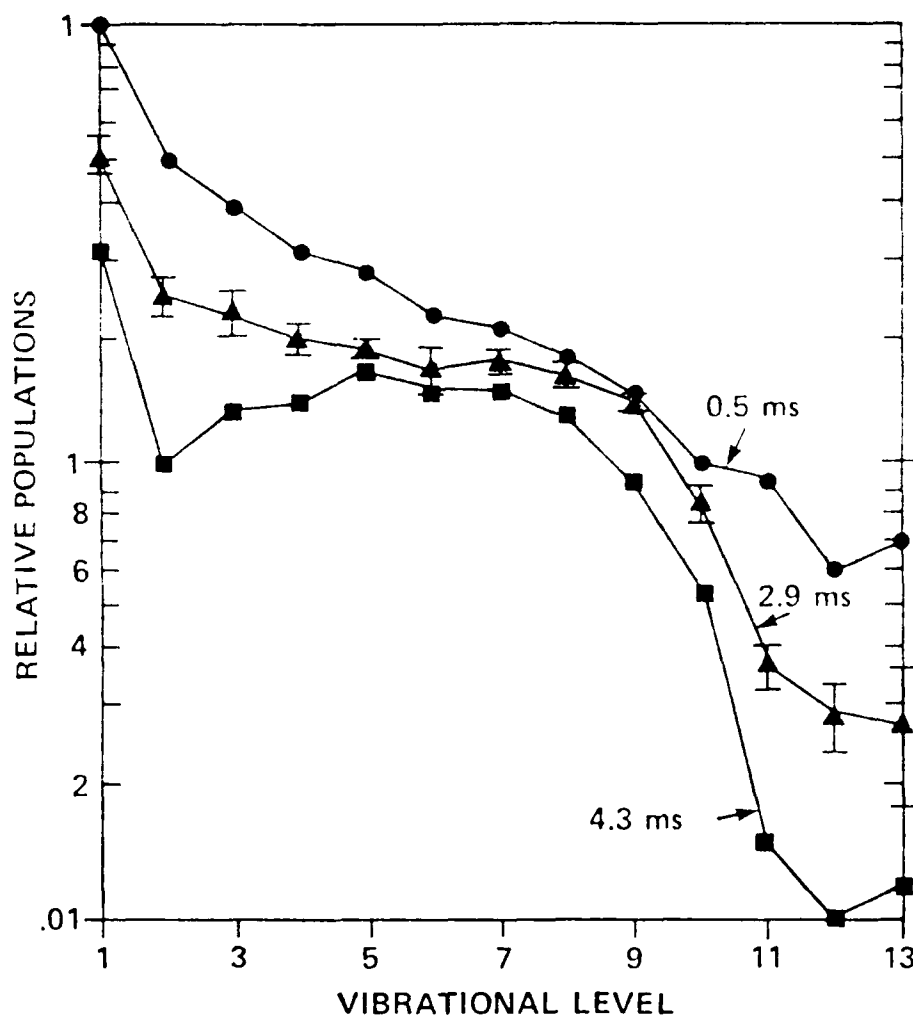


Fig. 2.4 The relative populations of levels 1-13 at three times after beam termination. These populations are an average of three runs at 0.2 torr CO₂/9.0 torr Ar taken at different times. Error bars of 1 standard deviation are presented only for the 2.9 ms trace, but are representative of all the times. The high vibrational levels and levels 2-4 relax more rapidly than levels 5-9, and the bottleneck at these levels results in a population inversion of the lower levels at long times.

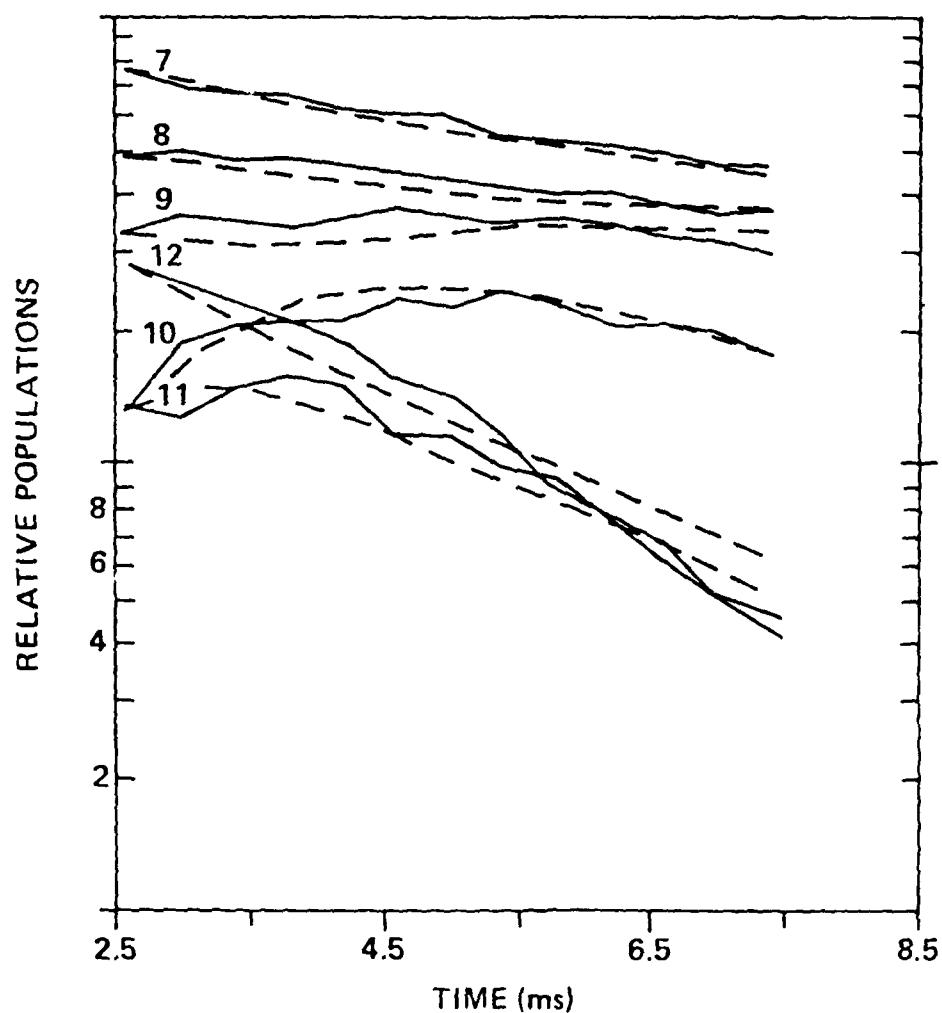


Fig. 2.5a The populations of levels 1-6 calculated from the fluorescence spectra of Fig. 2.3 between 0.1-4.9 ms after beam termination. The dashed lines are the predicted vibrational population decay histories based on the deduced rates and master equations for relaxation. The good agreement between the data and the prediction serves to validate the analysis and demonstrate that a single quantum collisional transfer treatment is adequate. The smooth variation of the calculated populations reflects the small experimental uncertainty due to noise in the spectrum.

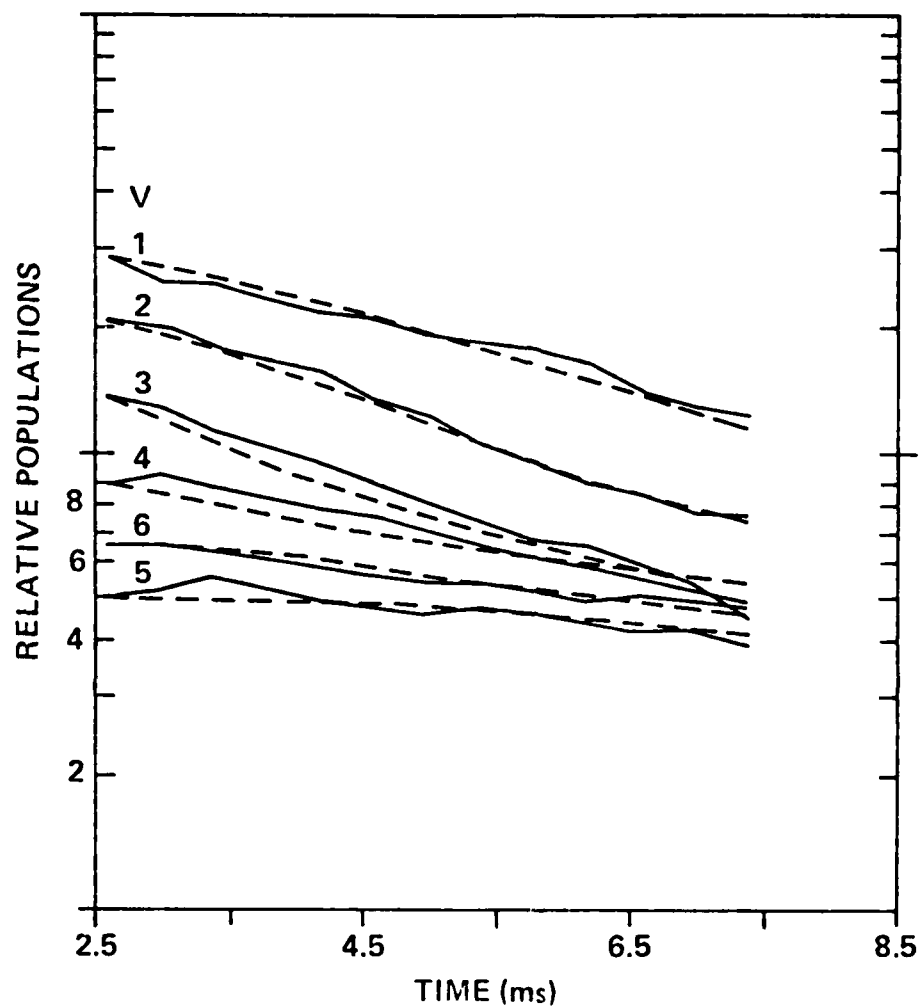


Fig. 2.5b The populations calculated from the fluorescent spectra of Fig. 2.3 between 0.1-4.9 ms after beam termination for levels 7-12. The dashed lines are the predicted vibrational population decay histories based on the deduced rates and master equations for relaxation.

varying between 0.008 - 1.0 torr and a total pressure of approximately 9 torr. Population histories for vibration levels as high as $v = 17$ have been deduced from this fluorescence data. Typical population relaxation times are of order 10 ms and are found to scale inversely with CO_2 pressure, suggesting that CO_2 plays an important role in the relaxation process. The purpose of the present analysis is to deduce rate constants for the processes



from the data. Care must be taken, however, to ensure that all other important kinetic mechanisms are included in the analysis.

The two most obvious additional mechanisms to be considered are CO radiative decay and collisional quenching by Ar. For the present experimental conditions both fundamental band and first overtone transitions, i.e.,

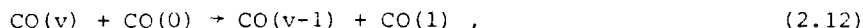


can provide a significant contribution to the total decay of high vibrational levels of CO (the CO concentrations are sufficiently low so that self-absorption is negligible). Although only the lowest level Einstein coefficients have been measured, they together with the higher levels have been calculated theoretically.^{2.18,2.19} Indeed, recent measurements^{2.20} of the ratio of $A_{v \rightarrow v-2}/A_{v \rightarrow v-3}$ for CO have been found to be in excellent agreement with the theoretical predictions. The potential importance of quenching by Ar, i.e.,

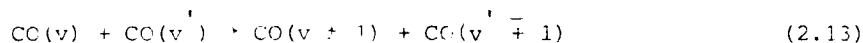


is less clear. The room temperature rate constant for process (2.11) $v = 1$, is negligibly small.^{2.21} Furthermore, scaling of the $v = 1$ rate to higher vibrational levels using a modified SSH theory,^{2.22} see for example CO-CO predictions by Caledonia and Center,^{2.23} would suggest that process (2.11) is unimportant for all vibrational levels of interest. Nonetheless, given the lack of experimental data, the possible importance of the quenching of high vibrational levels by Ar cannot be excluded a priori.

Beam created species can provide an additional source of quenchant molecules. There are two basic advantages in using a chemical reaction to produce the excited state distribution. The first, and primary one, is that the species to be studied need not be present in the ambient gas. Because of this, the effect of undesirable collisions with ground state molecules, for example in the present case reactions of the form



may be minimized. Secondly, the population of excited vibrational levels may be kept sufficiently low so that complicating intra-mode vibrational exchange reactions, i.e.,



are negligible.

These advantages are also achieved when an electron beam is used as a precursor to the chemi-excitation reaction. For example, in the case at hand CO is not present in the ambient gas, and for the electron beam currents and voltage applied, peak concentrations of $\text{CO}(v)$ are $\leq 10^{13} \text{ cm}^{-3}$ minimizing any effects due to reactions (2.13). However, an additional complication arises when multiple beam pulses are used for measuring fluorescence time histories. Specifically, a finite amount of CO and O is created during each pulse of the electron beam and, although the vibrationally excited CO completely relaxes between pulses, any given parcel of gas will be subject to irradiation by several pulses before being cleared from the system field

of view. The net result of multi-pulse irradiation of the test gas is that the gas sample within the field of view will exhibit finite steady state concentrations of CO and O in as much as the characteristic times for chemical removal of these species are much longer than the gas residence time within the field of view.

It can be deduced from electron beam energy deposition calculations that the steady state concentrations of CO and O will be of order 10^{14} cm^{-3} , sufficiently large to be of concern. Indeed, the room temperature rate constants for processes (2.12) have been found to be as large as $2-3 \times 10^{-12} \text{ cm}^3/\text{s}$ at low vibrational levels^{2.5,2.16,2.24}; thus characteristic reaction times for these processes can be of the same order as the observed fluorescence decay time. The potential role of quenching by oxygen atoms, i.e.,



is less apparent. The room temperature rate constant for reaction (2.14), $v = 1$, has been measured^{2.25} to be $2.7 \times 10^{-14} \text{ cm}^3/\text{s}$, sufficiently small so that this reaction will be unimportant. There are no reported measurements for the rate constants for oxygen atom quenching of higher vibrational levels; theoretical estimates^{2.26} suggest that these will be larger than that for $v = 1$.

Thus, it appears that the beam created species CO (and possibly O) can provide a significant contribution to the observed relaxation rate of the CO fluorescence. Fortunately, it will be shown in Sec. 3 that CO and O are not formed primarily by direct electron impact dissociation of CO_2 , but rather are formed indirectly by such mechanisms as electron/ion recombination and quenching of metastable states of Ar. This allows for a great simplification in the analysis in as much as the CO/O production rates will scale with total pressure rather than the partial pressure of CO_2 . Specifically, the rate of CO/O production will scale linearly with the rate of beam energy deposition within the field of view; since all measurements were performed at similar beam current/voltage conditions and at near constant pressure the background concentration of CO/O will be approximately the same for all the

measurements. This observation is supported by the fact that the observed peak CO fluorescent intensity varies only slightly over the whole of the CO₂ pressure range of interest.

Therefore, it follows that the temporal histories of the vibrational population may be interpreted in terms of the radiative mechanisms (2.9) and (2.10), the collisional deactivation processes (2.2) and (2.12) and an overall collisional loss mechanism



where X is representative of all potential deactivating species such as Ar and O (as well as any impurities in the Ar test gas) which will scale with the total pressure. The master equations which describe the time rate of change of the vibrational populations in terms of these mechanisms may be written as:

$$\begin{aligned} \frac{dn_1}{dt} &= -R_1 n_1 + R_2 n_2 + A_{3 \rightarrow 1} n_3 + \sum_{v=2}^N R'_v n_v (1 + \delta_{v,2}) \\ \frac{dn_2}{dt} &= -R_2 n_2 - A_{2 \rightarrow 0} n_2 + R_3 n_3 + A_{4 \rightarrow 2} n_4 \\ \frac{dn_m}{dt} &= -R_m n_m - A_{m, m-2} n_m + R_{m+1} n_{m+1} + A_{m+2 \rightarrow m} n_{m+2} \\ \frac{dn_N}{dt} &= -R_N n_N - A_{N \rightarrow N-2} n_N \end{aligned} \quad (2.16)$$

where N represents the highest vibrational level excited and where for vibrational level m, n_m is the relative population, and R'_m is the rate of deactivation due to collisions with ground state CO, i.e., reaction (2.12). The quantity R_m is the total rate of decay due to processes (2.2), (2.9), (2.12), and (2.15) and is defined by

$$R_m = k_2(m) [\text{CO}_2] + A_{m \rightarrow m-1} + R'_m + R''_m \quad (2.17)$$

where $k_2(m)$ is the rate constant for process (2.2), $v = m$, $[CO_2]$ is the CO_2 number density, and R_m is the deactivation rate due to process (2.15), $v = m$.

From examination of Eq. (2.16), it may be seen that if values for the Einstein coefficients $A_{m \rightarrow m-2}$ are specified, the quantities R_m should be readily deducible from the measured time histories $n_m(t)$. In practice, such an analysis is complicated by numerical inaccuracies introduced upon evaluating the slopes, dn_m/dt , of the experimental data. This complication may be circumvented by working with the time integrated forms of the master equations, i.e.,

$$\begin{aligned} \Delta n_m = & - R_m a_m - A_{m \rightarrow m-2} a_m + R_{m+1} a_{m+1} \\ & + A_{m+2 \rightarrow m} a_{m+2} \end{aligned} \quad (2.18)$$

where Eq. (2.18) is the integral of the general form of Eq. (2.16) taken over the time interval (t_1, t_2) and

$$\Delta n_m = n_m(t_2) - n_m(t_1) \quad (2.19)$$

$$a_m = \int_{t_1}^{t_2} n_m dt \quad (2.20)$$

The integral form of the master equations is particularly useful in that it not only eliminates the need for derivative values, but also allows determination of the best value of R_m over a specified time interval, effectively filtering any random fluctuations in the population histories introduced through the curve fitting process.

The Eq. (2.18) can be readily rearranged to allow direct specification of the rates R_m in terms of measured quantities. The resulting relationships are

$$R_m = - \sum_{v=m}^N \left(\ln a_{v,m} - A_{m+m-2} - A_{m+1+m-1} \frac{a_{m+1}}{a_m} \right) + a_{1,m}^{-1} \sum_{v=2}^N R_v a_{v,v} (1 + \tau_{v,2}) \quad (2.21)$$

where $\delta_{m,1}$ is the Kronecker delta and the quantity $A_{1,-1}$ is defined to be zero. Note that R_1 cannot be determined directly from the data inasmuch as the quantities R_v are undefined; all other values of R_m are, however, directly accessible from the data.

The deactivation rates R_v have been deduced from the measured vibrational population histories through use of the Eq. (2.21). In deducing these rates the populations were typically integrated over the time range of 2.6 to 8.2 ms (beam termination is at 2.5 ms); it has been found that rates evaluated from the same set of data but over different time intervals varied by no more than 10 to 15%. The populations of the highest vibrational levels tended to be the least accurate both because of the lower concentrations at high v and because of the decreased infrared detector sensitivity at the higher wavelengths. Because of this, rates were generally only evaluated for the lowest twelve vibrational levels; however, there were a few measurements of sufficiently high quality to allow evaluation of rates up to $v = 16$. In either event, it was found that the inclusion of a few of the poorer quality high vibrational level histories in the analysis produced only 5 to 15% changes in the values of the rates determined for the lower levels.

A typical set of CO deactivation rates, those deduced from the population histories shown in Fig. 2.5 are shown in Fig. 2.6. The general trend of the rates, a distribution peaking at the highest and lowest vibrational levels and exhibiting a minimum near $v = 8$, is common to the observations at all CO_2 pressures. Note that although the measurements of the magnitude of the rate for level 12 vary, it is typically larger than that for level 11.

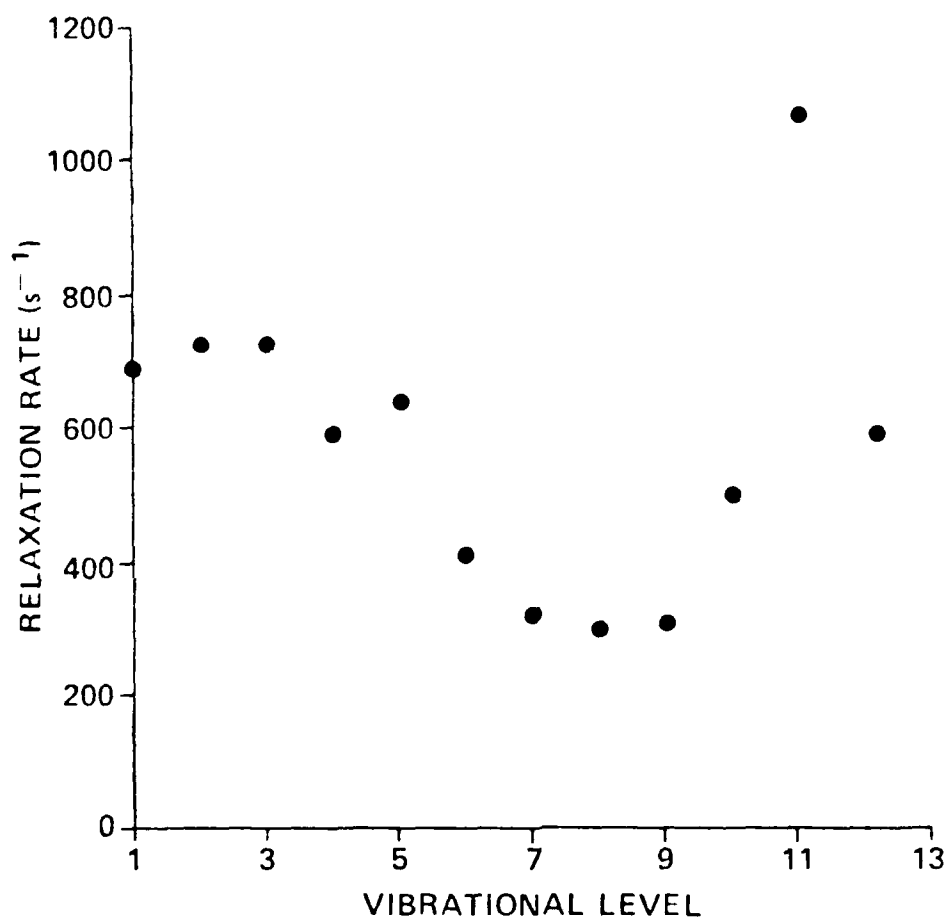


Fig. 2.6 The relaxation rates deduced for the 0.15 torr CO_2 /9.0 torr Ar case. As suggested by Figs. 2.4 and 2.5, relaxation is slowest for levels 5-9. The rate for level 1 is small due to the cold CO collisional deactivation source term for $v = 1$.

As a cross check on the data analysis, these rates have been used in conjunction with the master equations (2.16) to predict the vibrational population decay histories. These predictions are shown in Fig. 2.5 and can be seen to be in quite good agreement with the data. This comparison not only demonstrates the quality of the "rate fit" to the data but also shows that the data can be adequately interpreted in terms of the single quantum collisional transfer reactions used in the analysis; i.e., if the relaxation mechanism were different than assumed, the rates determined from the integral form of the master equations would not properly reproduce the population time histories.

The ultimate goal of the analysis is not to deduce the rates R_v but rather the rate constants for process (2.2). These rate constants can be determined using a Stern-Volmer^{2.9} type analysis inasmuch as, for constant total pressure and beam conditions, a plot of R_v vs. CO_2 partial pressure should fall along a straight line having slope $k_2(v)$ as indicated by Eq. (2.17). The rates R_v have been determined over a range of two orders of magnitude in CO_2 partial pressure and resulting Stern-Volmer plots for several typical vibrational levels are shown in Fig. 2.7. This data is very well fit by a linear representation as can be seen from the straight line least squares curve fits shown on the figure.

Several sets of data, taken at different times, were fit in this manner and the resultant rate constants determined from the least squares data fits are shown in Fig. 2.8. The error bars shown represent only the standard deviations of the data from several different sets of runs and not the ultimate uncertainty in the rate constants. The error bars on the rate constants for levels $v > 12$ are larger because they correspond to the fitting of only a few measurements. The rate constant for deactivation of the first vibrational levels cannot be determined by this technique as illustrated in Eq. (2.21), and determination of this rate constant will be discussed later. The rate constant measurements of Hancock and Smith^{2.5} deduced for levels $v = 4 - 12$ from steady state observations are also shown in Fig. 2.8 and can be seen to be in reasonably good agreement with the present results. In particular the unusual variation of rate constant with

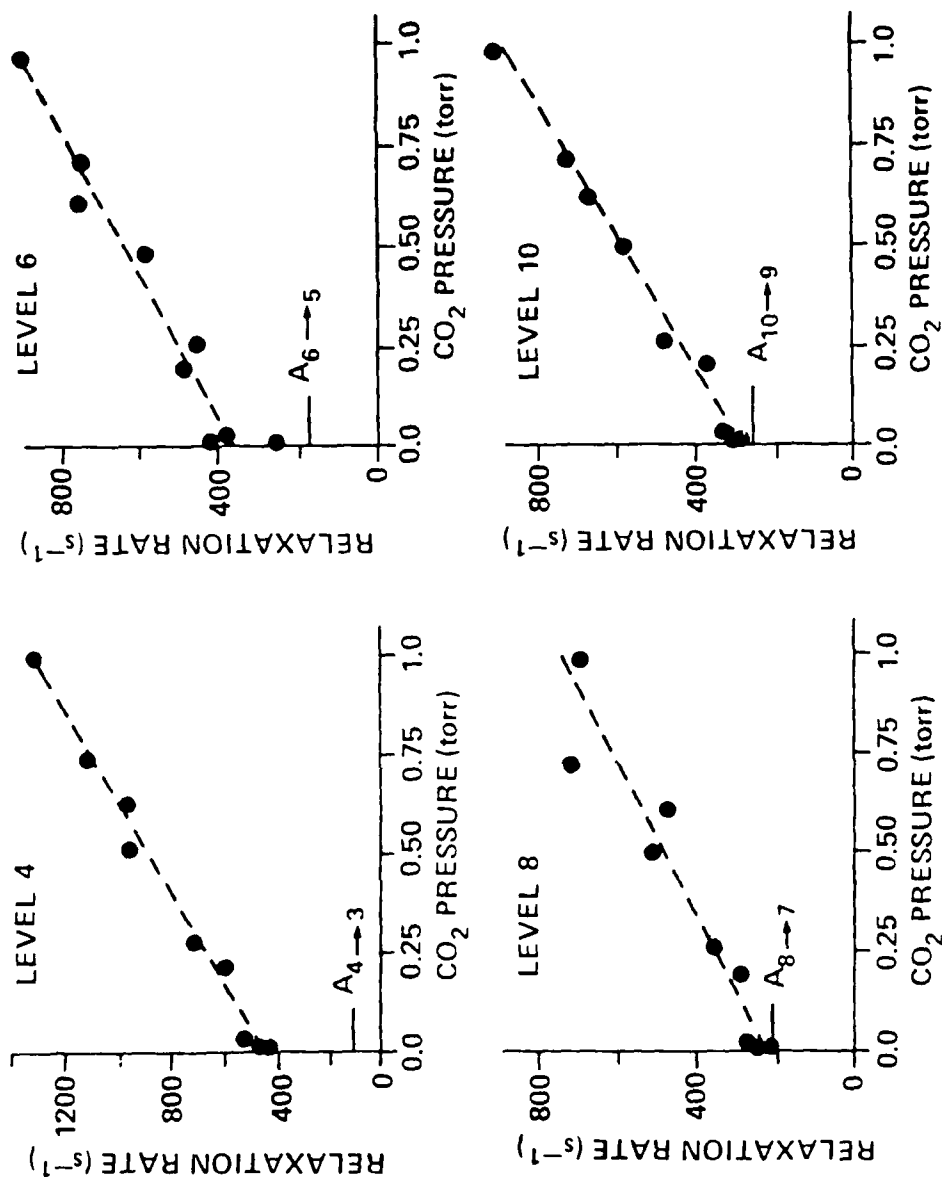


Fig. 2.7 Some representative Stern-Volmer plots for levels 4, 6, 8, and 10. The relaxation is linear with CO₂ pressure over a factor of 100 in pressure. The relaxation rates vary widely for the levels shown. Level 4 even at the highest CO₂ pressures has an observed decay of 0.83 ms which is much slower than the time resolution of the experiment (0.2 ms). The A_{v, v-1} values are shown for comparison.

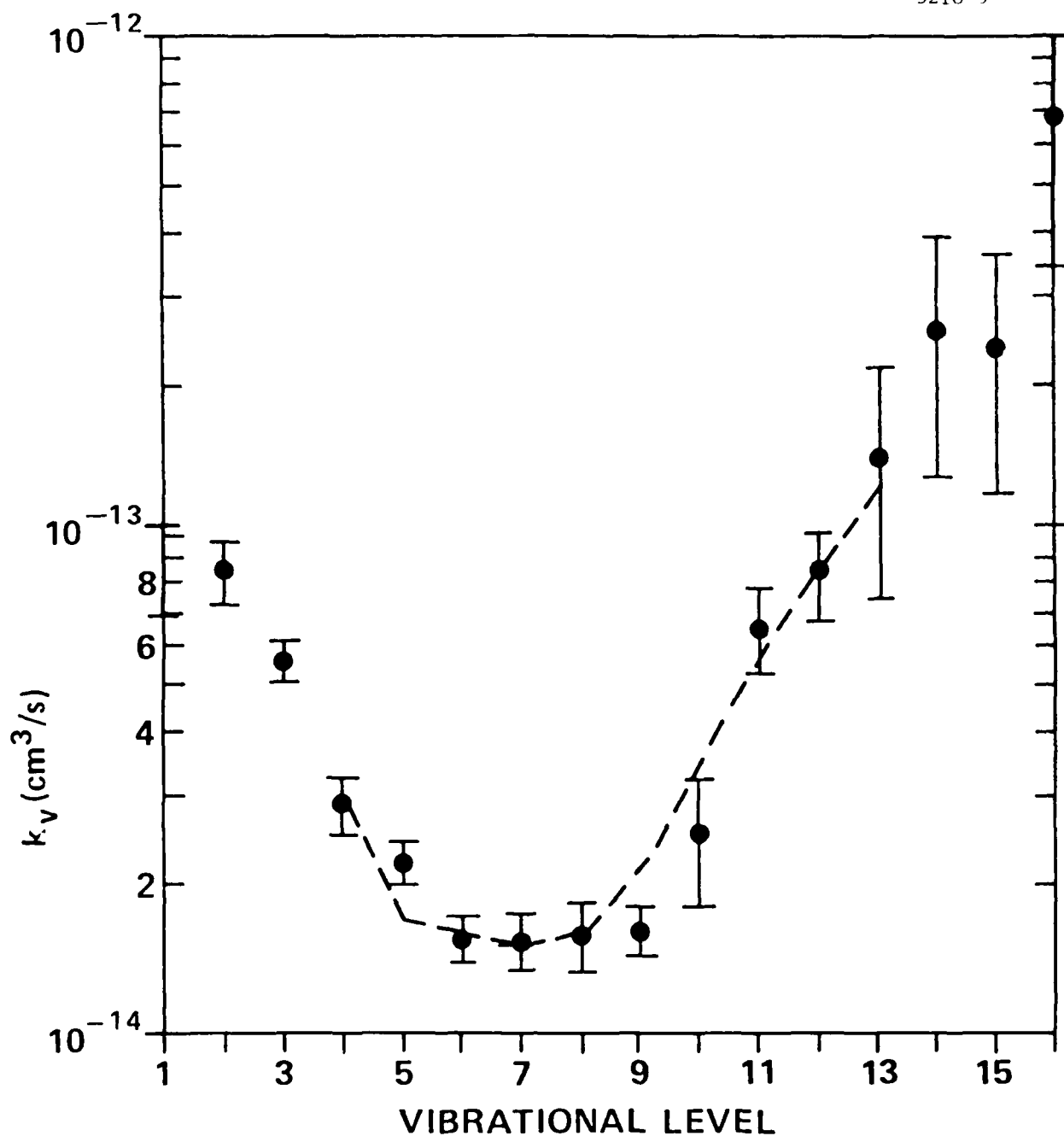


Fig. 2.8 The deduced rate constants for the reaction $\text{CO}(v) + \text{CO}_2 \rightarrow \text{CO}(v-1) + \text{CO}_2^*$ for $v = 1-16$. The error bars represent a standard deviation of the data deduced from several different sets of runs. The errors for levels 13-16 are large due to a smaller data base. Previous values measured by Hancock and Smith (Ref. 2.5) are shown for comparison. The unusual variation with vibrational level they reported is confirmed and found to extend to higher and lower levels.

vibrational level observed in this earlier work has been verified and found to extend to higher levels. This behavior strongly suggests that reaction (2.2) is a vibration-vibration exchange process which, perhaps, requires a vibrationally excited state of CO_2 to provide an efficient exchange at higher vibrational levels of CO .^{2.5}

It is also of some interest to examine the zero CO_2 pressure intercepts of the rates inasmuch as these should represent the cumulative effect of fundamental band radiative transitions, process (2.9), and the quenching reactions (2.12) and (2.15). The intercept values are shown as a function of vibrational level in Fig. 2.9. The results of Stern-Volmer analysis performed on two different sets of data are displayed and these can be seen to differ only slightly. The theoretical predictions for the Einstein coefficients $A_{v \rightarrow v-1}$ are also shown in this figure for comparison; it can be seen that these quantities asymptote into the deduced values of the intercepts at high vibrational levels. The intercepts represent upper bounds for the Einstein coefficients and the close agreement between measurement and prediction suggest that collisional quenching by species other than CO_2 is unimportant at higher vibrational levels. Alternately these high v intercepts may be interpreted as the first experimental verification of predicted high vibrational level Einstein coefficients for CO . (Note that there are symbiotic effects in this determination in that the relative values of the fundamental band Einstein coefficients are utilized in determining the rates R_v . On the other hand, the absolute magnitude of the Einstein coefficients are not input to the data analysis.)

It is clear from Fig. 2.9 that additional deactivation processes do affect the relaxation of the lower vibrational levels of CO . In order to isolate the effect of such processes, the predicted Einstein coefficients have been subtracted from the intercept values providing the set of zero CO_2 pressure collisional deactivation rates shown in Fig. 2.10. These rates exhibit a peak near $v = 4$ and fall to near zero by $v = 8$. Shown for comparison are the arbitrarily normalized rate constants for CO deactivation by vibrationally cold CO ,^{2.5, 2.16, 2.24} reaction (2.12). Note that the data

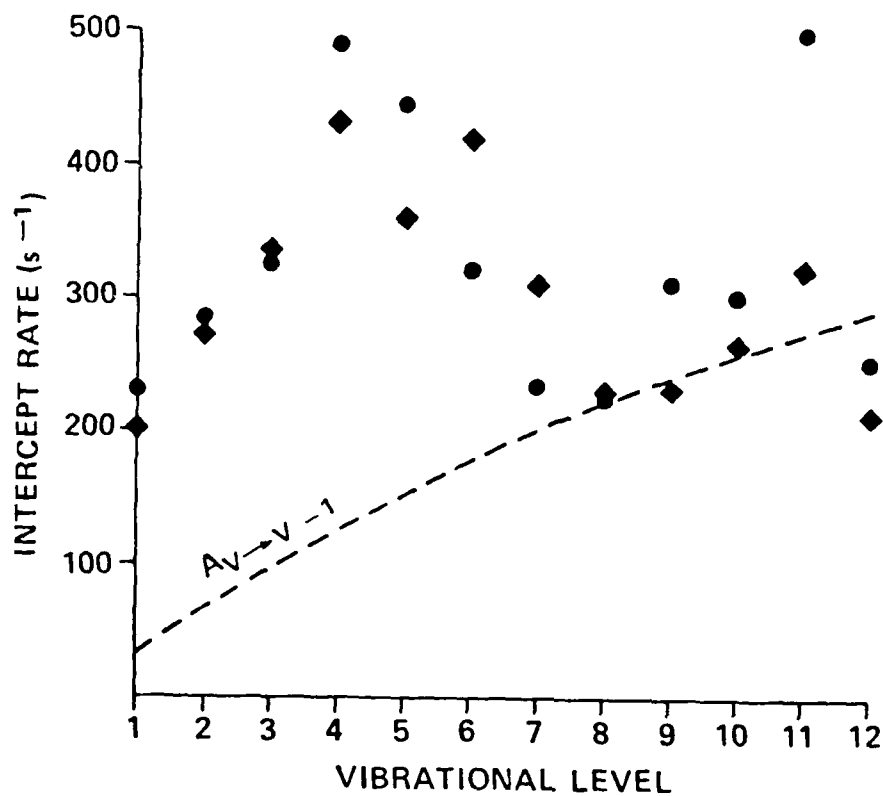


Fig. 2.9 The values of the intercepts for two series of runs taken at different times as a function of vibrational level. Theoretical predictions for the Einstein coefficients are shown. The intercepts asymptote to the predictions for $v \geq 7$ and form an upper bound measurement of the Einstein coefficients for these levels. At lower v molecular quenching by CO or X dominates the intercept residual quenching.

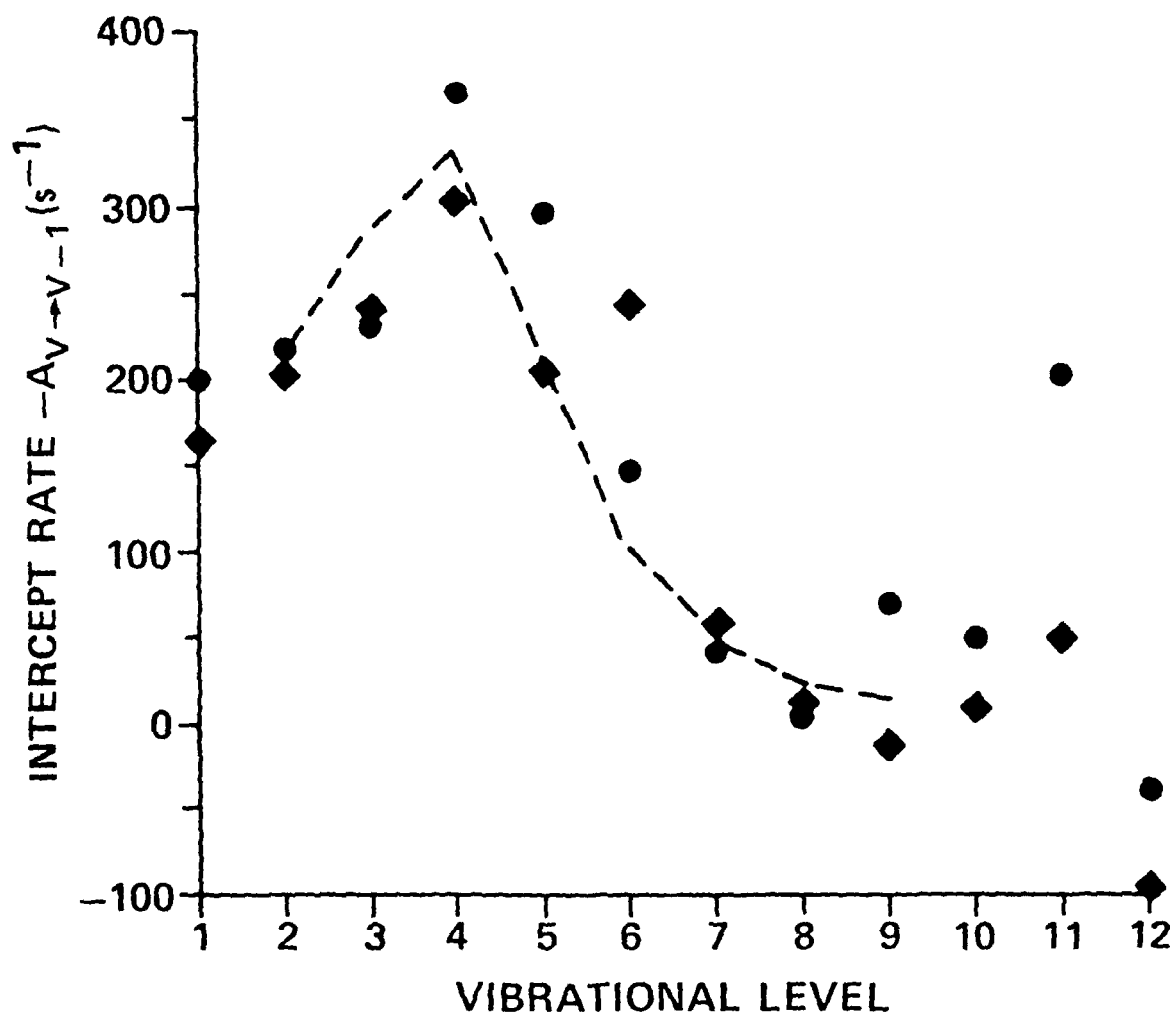


Fig. 2.10 The differences between the intercepts as plotted in Fig. 2.9 and the theoretical Einstein coefficient predictions as a function of vibrational level. Shown for comparison are the arbitrarily normalized relaxation rates for the $\text{CO}(v) + \text{CO}(0) \rightarrow \text{CO}(v-1) + \text{CO}(1)$ reaction. The cold CO required to produce these rates is 10^{14} cm^{-3} , which is reasonable based on estimates of gas residence time and electron beam energy deposition rates.

closely follows the vibrational level dependence of these rate constants. Furthermore, the cold CO concentration required along with these rate constants to produce the observed rates is found to be $\sim 10^{14} \text{ cm}^{-3}$, a value in line with estimates made upon the basis of gas residence time, electron beam energy deposition rates and the absolute fluorescence intensity calibration.

It may be concluded on the basis of these comparisons, that the only important processes controlling the observed relaxation of CO vibro-fluorescence are collisions with CO_2 and vibrationally cold CO and radiative decay. Any losses due to collisions with argon or oxygen atoms or gas impurities appear to be negligibly small except, perhaps, at the lowest vibrational levels. As a last consistency check, the measured rates for $\text{CO}(v = 1)$ deactivation at high CO_2 pressures have been used to evaluate the rate constant $k_2(1)$ in the two limits where either all or none of the excess collisional deactivation for $v \geq 2$ is assumed to be by process (2.12). The resulting rate constants are displayed in Fig. 2.8 and can be seen to nicely bracket the measured room temperature value of $k_2(1) = 8 \times 10^{-14} \text{ cm}^3/\text{s}$.^{2.27-2.30}

No attempt has been made to provide a detailed statistical study of error propagation in the data analysis. It has been found that the fluorescence data and subsequently deduced population histories are quite reproducible, exhibiting minimal variance when fitting parameters were widely varied. Furthermore, changes in the number of levels or time interval used in the analysis caused only small variations in the deduced rates. Lastly, as seen in Figs. 2.7 through 2.10, the statistical uncertainties of the least square fits to the rate data were also found to be quite small. Nonetheless, as seen from the master equations, the relaxation of any one level is affected by the behavior of all higher levels; thus the analysis can allow for a significant degree of error propagation. The potential cumulative uncertainty has not been gauged in any detailed manner; however, the various tests performed as well as the comparisons with other measurements suggest that the deduced rate constants are most probably accurate to well within 50% (with, of course, the exception of the highest levels which exhibit a larger uncertainty because of the limited data base).

2.5 Summary and Conclusions

The technique of time-resolved Fourier transform spectroscopy has been used to monitor the simultaneous relaxation of the total ensemble of vibrational states of a highly excited molecule. Carbon monoxide is found to be created upon electron irradiation of mixtures of CO_2/Ar and CO fundamental vibration/rotation band emission originating from vibrational levels as high as $v = 19$ has been observed. This spectrally resolved fluorescence has been analyzed to determine the time histories of the vibrational population distribution. The resulting population histories were interpreted in terms of a kinetic model which included radiative transitions and single quantum deactivation collisions with CO_2 , vibrationally cold CO and impurity species. This analysis allowed for determination of the room temperature rate constants for process (2.2), $v = 1-16$, and establish reasonable upper bounds for the fundamental band Einstein coefficients for levels $v = 7-12$. It is seen that time dependent Fourier transform spectroscopy can be a very powerful tool in the analysis of multilevel systems. Specifically, the ability of this technique to provide simultaneous spectral and temporal information removes any susceptibility to fluctuations in experimental conditions which may be experienced in sequential measurement techniques. Furthermore, the ability to monitor the fluorescence data both during and after beam irradiation allows one to analyze each set of data independently, without the requirements that the chemical source remain invariant as the quenchant concentration is varied.

REFERENCES

- 2.1 R. L. Taylor and S. Bitterman, "Survey of Vibrational Relaxation Data for Processes Important in the CO₂-N₂ Laser System," Rev. Mod. Phys. 41, 26 (1969).
- 2.2 C. B. Moore, "Vibration-Vibration Energy Transfer," in Advances in Chemical Physics, (John Wiley and Sons, New York, 1973), pp. 41-83.
- 2.3 R. L. Taylor, "Energy Transfer Processes in the Stratosphere," Can. J. Chem. 52, 1436 (1974).
- 2.4 S. Ormonde, Rev. Mod. Phys. 47, 193 (1975).
- 2.5 G. Hancock and I. W. M. Smith, "Quenching of Infrared Chemiluminescence 1. The Rates of De-Excitation of CO(4 < v < 13) by He, CO, NO, N₂, O₂, OCS, N₂O, and CO₂," Appl. Opt. 10, 1827 (1971).
- 2.6 J. R. Airey and I. W. M. Smith, J. Chem. Phys. 57, 1669 (1972).
- 2.7 P. R. Poole and I. W. M. Smith, J. Chem. Soc. Far. Trans. II, 73, 1434 (1977).
- 2.8 P. R. Poole and I. W. M. Smith, J. Chem. Soc. Far. Trans. II, 73, 1447 (1977).
- 2.9 O. Stern and M. Volmer, Phys. Zeits. 20, 183 (1919).
- 2.10 R. E. Murphy, F. H. Cook and H. Sakai, "Time Resolved Fourier Spectroscopy," J. Opt. Soc. Amer. 65, 600 (1975).
- 2.11 H. Sakai and R. E. Murphy, Appl. Opt. 17, 1342 (1978).
- 2.12 M. Forman, J. Opt. Soc. Am. 56, 908 (1966).
- 2.13 R. E. Murphy, F. M. Cook, G. E. Caledonia, and B. D. Green, "Infrared Fluorescence of Electron Irradiated CO₂ in the Presence of N₂, Ar, and He," Air Force Geophysics Laboratory TR-77-0205, Environmental Research Papers, No. 609, 15 Sept. 1977.
- 2.14 B. D. Green and G. E. Caledonia, "LABCEDE and COCHISE Analysis II, Vol. II: LABCEDE Studies," Physical Sciences Inc. TR-117, February 1978.
- 2.15 J. P. Kennealy, F. P. DelGreco, G. E. Caledonia and B. D. Green, "Nitric Oxide Chemiexcitation Occurring in the Reaction Between Metastable Nitrogen Atoms and Oxygen Molecules," J. Chem. Phys. 69, 1574 (1978).

REFERENCES (Continued)

- 2.16 Y. Fushiki and S. Tsuchiya, "Vibration-Vibration Energy Transfer from CO in States $v = 2-9$," Jap. J. Appl. Phys. 13, 1043 (1974).
- 2.17 G. Schiffner and E. Klement, "Calculation of Improved $^{12}\text{C}^{16}\text{O}$ Molecular Constants and Rotational-Vibrational Transition Frequencies," Appl. Phys. 6, 199 (1975).
- 2.18 L. A. Young and W. J. Eachus, J. Chem. Phys. 44, 4195 (1966).
- 2.19 K. Kirby-Docken, "Theoretical Study of Molecular Dipole Moment Functions I. The $X^1\Sigma^+$ State of CO," J. Chem. Phys. 66, 4309 (1977).
- 2.20 A. J. Lightman and E. R. Fisher, "A Coefficient for Spontaneous Emission in CO," Appl. Phys. Lett. 29, 593 (1976).
- 2.21 R. C. Millikan and D. R. White, "Systematics of Vibrational Relaxation," J. Chem. Phys. 39, 3209 (1963).
- 2.22 R. N. Schwartz, Z. Salwsky and K. F. Herzfeld, J. Chem. Phys. 20, 1591 (1952).
- 2.23 G. E. Caledonia and R. E. Center, J. Chem. Phys. 55, 552 (1971).
- 2.24 Y. S. Liu, R. A. McFarlane and G. J. Wolga, "A Study of the Dynamic Behavior of the Vibrational Population Relaxation in Carbon Monoxide," J. Chem. Phys. 63, 228 (1975).
- 2.25 M. E. Lewittes, C. C. Davis and R. A. McFarlane, J. Chem. Phys. 69, 1952 (1978).
- 2.26 J. D. Kelley and R. L. Thommarson, "Vibrational Deactivation and Atom Exchange in $\text{O}(^3\text{P}) + \text{CO}(X^1\Sigma^+)$ Collisions," J. Chem. Phys. 66, 1953 (1977).
- 2.27 W. A. Rosser, Jr., R. D. Sharma and E. T. Gerry, "Deactivation of Vibrationally Excited Carbon Dioxide (V_3) by Collisions with Carbon Dioxide or with Nitrogen," J. Chem. Phys. 54, 1196 (1971).
- 2.28 J. C. Stephenson and C. B. Moore, "Temperature Dependence of Nearly Resonant Vibration-Vibration Energy Transfer in CO_2 Mixtures," J. Chem. Phys. 56, 1295 (1972).
- 2.29 D. J. Miller and R. C. Millikan, "Vibration-Vibration Energy Exchange Between Carbon Monoxide and Carbon Dioxide," Chem. Phys. 6, 317 (1974).
- 2.30 D. F. Starr and J. K. Hancock, "Vibrational Energy Transfer in CO_2 -CO Mixtures from 163 to 406 K," J. Chem. Phys. 63, 4730 (1975).

3. EXCITATION EFFICIENCY OF CO(v) IN IRRADIATED CO₂/Ar MIXTURES

3.1 Introduction

Fluorescence from vibrationally excited CO created by electron irradiation of CO₂/Ar mixtures was analyzed in Chapter 2 to determine the rate of relaxation of CO(v) by CO₂. The same data (while the beam is on) can be further analyzed to determine the rates at which CO(v) is formed. In this chapter we will quantify the fraction of the electron energy deposited in the gas which appears as CO vibrational excitation. In addition to the kinetic analysis, this requires 1) an understanding of direct electron excitation cross-sections and the energy transfer pathways to estimate the energy deposited, and 2) an absolute calibration of the fluorescent intensities to permit excited state density determination. Details of the calibration which involve corrections for electron beam growth are presented in Section 3.2. Corrections for non-uniform detector response across the field of view (as discussed in Appendix II), and interferometer alignment and calibration (as discussed in Chapter 9) are also essential for accurate calibration. The kinetic analysis leading to creation rates and average vibrational excitation is given in part 3. The kinetic mechanisms which may be responsible for CO(v) formation are discussed in Section 3.4, and a summary is given in the last section.

3.2 Absolute Calibration

The determination of an absolute spectral calibration for the LABCEDE experiment is complicated by the fact that the radiation source does not fill the field of view, i.e., is not an extended source, and indeed varies continuously across the field of view. The observed fluorescence is due to vibrationally excited CO created directly or indirectly by reactions with secondary electrons which, in turn, are formed through the energy deposition of the primary electron beam. In the present system, the time between formation and fluorescence is sufficiently small so that diffusion is relatively unimportant and, therefore, the spatial variation in fluorescence may be taken to be nearly the same as that of the electron beam energy deposition. Thus, this latter quantity must be defined in order to develop an absolute calibration.

As the electron beam propagates through the test chamber, it undergoes collisions with the ambient gas. These collisions lead both to a loss in beam energy and a spreading of the beam profile about the axis of propagation. The phenomenology of electron energy degradation in gas targets is well understood and the rate of energy loss is found to depend upon both the composition of the ambient gas and the beam voltage. The energy loss per unit pathlength, typically written as $\rho^{-1} dE/ds$ where ρ is the gas density, E is electron energy and s is electron pathlength, has been tabulated for a number of gases^{3.1} and, for example, would be 6.5 MeV-cm²/gm for the present case of 30 keV electrons in argon. Unfortunately, the relationship between electron pathlength and distance along the axis of beam propagation, x , is not so readily specified and generally requires evaluation via computer analysis. Two different computer models have been used to predict the axial profile of beam energy deposition within the test chamber. The first of these is ELTRAN,^{3.2} a standard one-dimensional Monte Carlo transport code, which describes the electron multiple scattering in terms of the Moliere^{3.2} distribution. The second is the Transport Electron Program,^{3.3} which utilizes various analytic approximations to develop an integral solution of the transport equation. These codes have been exercised for injection of 30 keV electrons into argon and the axial energy depositions predicted by the two models were found to be in excellent agreement. For the present case of nine torr of argon held at room temperature, the energy loss per unit axial distance, $\rho^{-1} dE/dx$, is predicted by these models to increase monotonically between 13-16 MeV-cm²/gm across the field of view. It is to be noted that this is more than twice the energy loss per unit pathlength tabulated by Berger and Seltzer.^{3.1}

The radial distribution of the beam energy loss at any axial position is linearly proportional to the radial current density profile of the beam at that position. The electron beam spreads as it traverses the field of view as the result of scattering collisions with the test gases and detailed evaluation of the beam spreading can require an involved modeling effort. Fortunately Center^{3.4} has measured radial beam current density profiles under experimental conditions very similar to those of the present study. His observation, for the case of thin N₂ and Ar targets, was that the beam current dis-

tribution was apparently Gaussian about the beam axis. Center defined a parameter, $\theta_{1/2}$, which is the angle, as measured from beam origin, at which one half of the total beam current is encompassed. He found that this quantity could be adequately represented by a relationship of the form:

$$\theta_{1/2} = \frac{A(N\ell)^{3/2}}{1 + B(N\ell)} \quad (3.1)$$

where N is gas number density, ℓ is the distance from beam origin and the quantities A and B are both gas and beam voltage specific. (For the case of 30 keV electrons in Ar, it was found that $A = 4.2 \times 10^{-28} \text{ cm}^3$ and $B = 2.7 \times 10^{-18} \text{ cm}^2$.) As discussed earlier, the radial distribution of fluorescent intensity will be functionally the same as the current distribution. Predicted profiles of beam growth within the field of view are shown in Fig. 3.1. Fifty percent of the beam-induced fluorescence will fall within the $r_{1/2}$ boundaries shown, whereas 90% will fall within the boundaries labeled $2r_{1/2}$.

The absolute calibration is affected by the non-uniformity of the source because the interferometric detection system does not provide a constant response across the field of view. The latter result is due to several effects; (a) aberrations introduced by the optical train, (b) non-uniform detectivity along the IR detector surface, (c) vignetting, and (d) interferometer misalignment. The variation in system response across the field of view has been carefully mapped out utilizing a standard black body "point" source. The Gaussian beam current (fluorescence) distribution has been convolved over this field of view response function in order to determine a correction factor to account for the system response non-uniformities (see Appendix II). This correction factor was found to be ~ 2 , i.e., the measured response to the beam fluorescence is a factor of two lower than it would have been if the system response had been uniform across the field of view. (This correction factor does not vary grossly for other choices of beam shape; for example for the

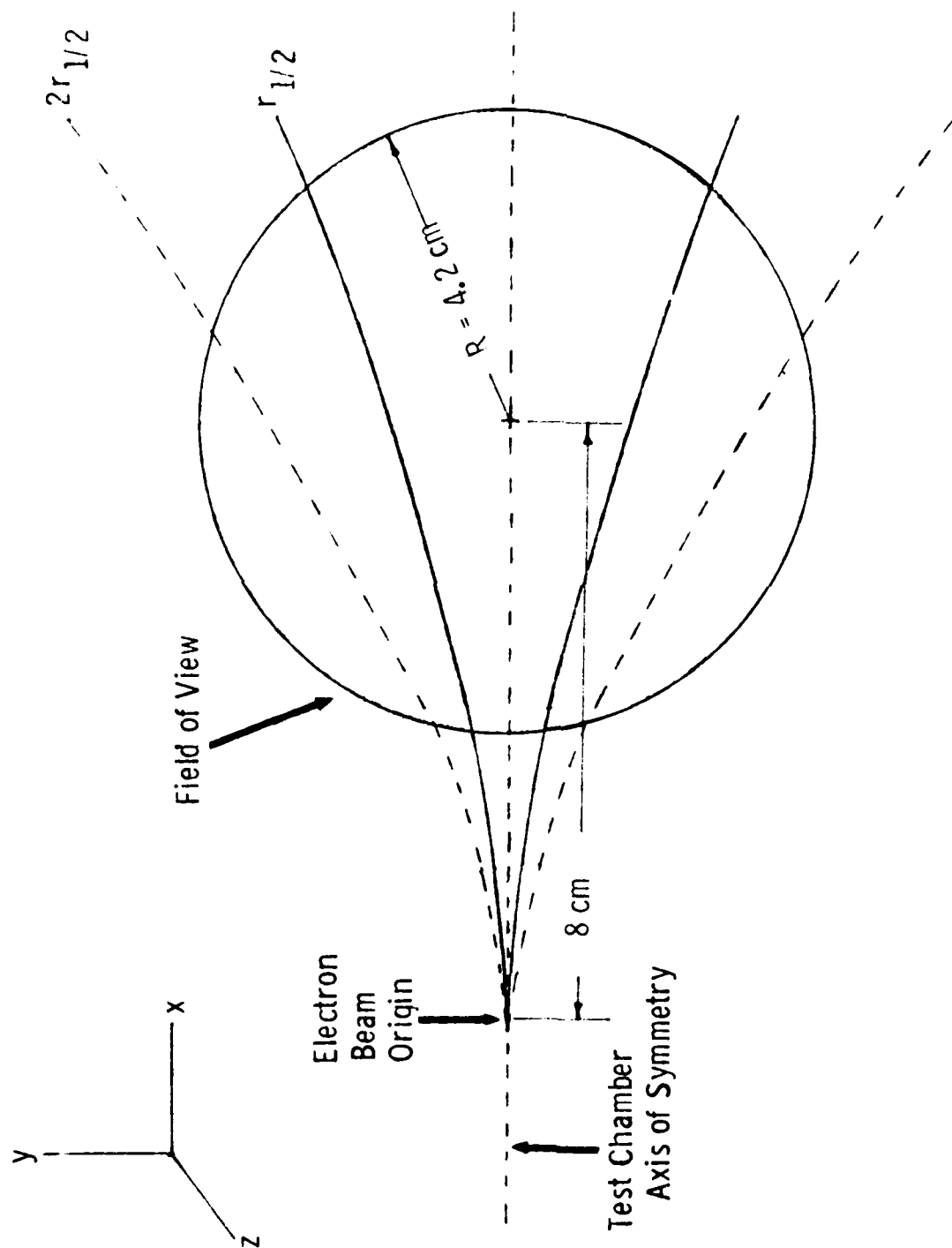


Fig. 3.1 Schematic of beam current distribution within field of view.

case of a line source, i.e., no spread of the electron beam, the correction factor would be ~ 1.7.) All intensity measurements have been adjusted by this factor. Additionally, the intensities have been corrected after the fact for interferometer misalignment (see Chapter 9) as inferred from black body integrated intensities.

3.3 Kinetic Analysis

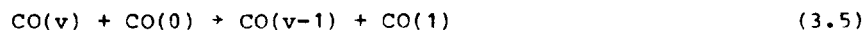
The rates for creation of vibrationally excited CO may be determined directly from the deduced vibrational population histories if the competing effects of vibrational relaxation are properly accounted for. As discussed in Section 2, the vibrational kinetics can be described in terms of five processes. These are vibrational de-activation by CO₂:



radiative decay in fundamental and first overtone vibrational band transitions,



vibrational exchange with beam created, vibrationally cold, CO



and quenching by Ar, impurities or beam-created species such as oxygen atoms,



The only source term acting to balance those losses is the creation rate for vibrationally excited CO, $Re(v)$, which can represent the cumulative result of several processes induced by beam irradiation. The master equations which describe the vibrational population histories in terms of these processes may be written as:

$$\begin{aligned} \frac{dn_v}{dt} = & Re(v) - R_v n_v + R_{v+1} n_{v+1} - A_{v+v-2} n_v + A_{v+2+v} n_{v+2} \\ & + \delta_{v,1} \sum_{m=2}^N (\delta_{m,2} + 1) R_m n_m; \quad v = 1, N \end{aligned} \quad (3.7)$$

where N is the highest level created and $A_{1,-1}$ and $n_{v>N}$ are identically zero. The quantity R_v is the rate of deactivation of level v due to processes (3.5) and R_v is the decay rate due to processes (3.2), (3.3), (3.5) and (3.6). Once again, it is more convenient to deal with the time integrated form of the master equations,

$$\begin{aligned} n_v(t_p) = & Re(v)t_p - R_v a_v + R_{v+1} a_{v+1} - A_{v+v-2} a_v \\ & + A_{v+2+v} a_{v+2} + \delta_{v,1} \sum_{m=2}^N (\delta_{m,2} + 1) R_m a_m \end{aligned} \quad (3.8)$$

where the quantities a_v are defined by:

$$a_v = \int_0^{t_p} n_v dt \quad (3.9)$$

and t_p is the electron beam pulse time. Note that the quantities a_v are defined directly from the data and the rates R_v , with the exception of R_1 , have been determined from an analysis of the relaxation data taken after beam termination.

All the available fluorescence data taken during beam irradiation for the conditions $p_{Ar} = 9$ torr, $p_{CO_2} = 0.1-1.0$ torr and $V = 30$ keV have been reduced in the manner described previously. Vibrational population histories were deduced via least squares fits to the spectral data and typical deduced population distributions at three times after beam onset are shown in Fig.

3.2. Note that a population inversion is apparent at early times, suggesting that this phenomena is source specific, rather than being a result of the relaxation process. Similar vibrational distributions have been observed at all CO_2 pressures considered.

The time integrals of these population histories were used to evaluate the quantities $Re(v)$. This evaluation was performed utilizing Eq. (3.8) and the case-specific relaxation rates R_v which were deduced from the data after beam termination. The resulting values of $Re(v)$ for the data of Fig. 3.2 are shown in Fig. 3.3. The value shown for level one should be considered as an upper bound in that it includes the effect of excitation due to de-activation of higher vibrational levels of CO by cold CO, i.e., reaction (3.5). Note that the excitation rates tend to decrease with increasing vibrational level although a secondary maxima is apparent about $v=7$. Rates are only shown for the first thirteen levels inasmuch as the data was of insufficient quality to allow evaluation of the excitation rates for higher levels. Nonetheless the major fraction of CO vibrational energy is found to reside in those lower levels.

The magnitudes of the rates shown in Fig. 3.3 are not very instructive inasmuch as they represent the total rate of excitation within the field of view and thus are both specific to the experimental configuration and to the beam current and voltage. All the data can be collapsed to a common scale by normalizing by the total rate of beam energy deposition within the field of view. This deposition "power" is defined by:

$$P = \int \rho_i (\rho^{-1} dE/dx) dV \quad (3.10)$$

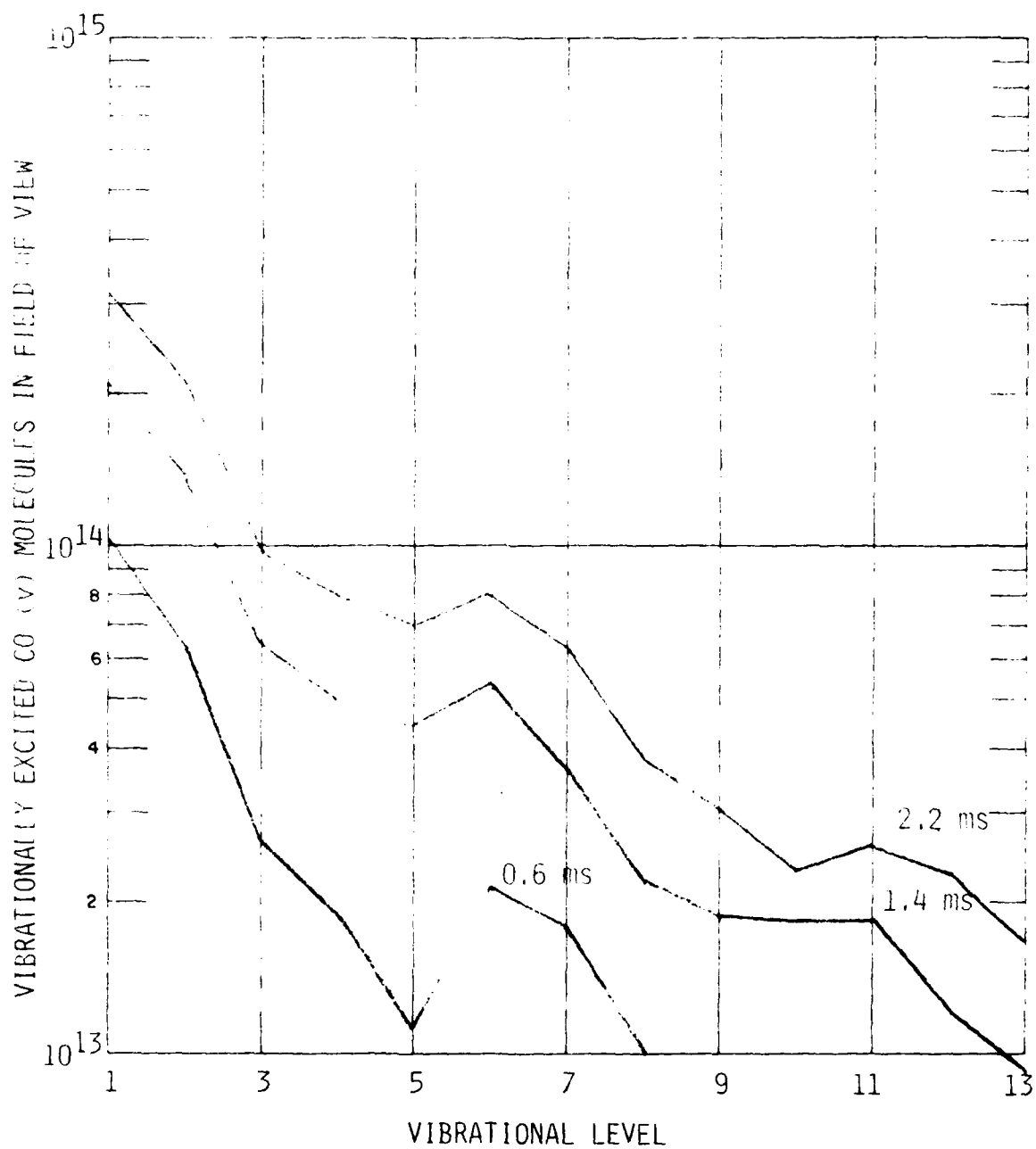


Fig. 3.2 Calculated populations in each level within the field of view at three times during beam pulse. $P_{Ar} = 9$ Torr, $P_{CO_2} = 0.1$ Torr, $V = 30$ keV.

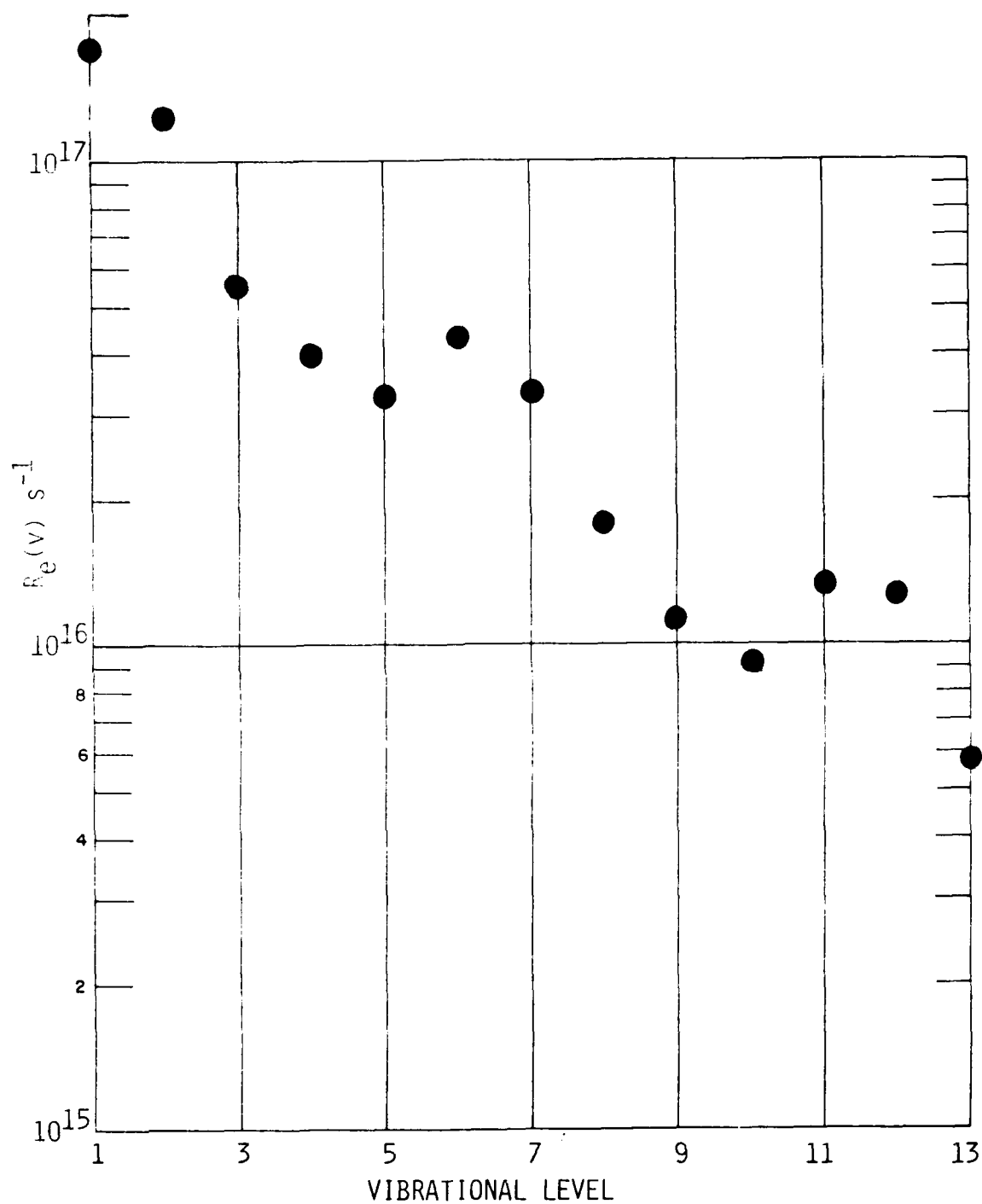


Fig. 3.3 Deduced CO(v) creation rates within the field of view as a function of vibrational level. $P_{\text{Ar}} = 9 \text{ Torr}$, $P_{\text{CO}_2} = 0.1 \text{ Torr}$, $V = 30 \text{ keV}$.

where ρ is gas density, i is the local current density as defined by Center's Gaussian distribution,^{3,4} $\rho^{-1} dE/dx$ is the previously defined energy loss per unit axial distance for a 30 keV electron and the integral is over the beam volume falling within the field of view. For a thin gas target, Eq. (3.10) may be more simply represented as

$$P = \rho \bar{I} L (\rho^{-1} dE/dx) \quad (3.11)$$

where I is total beam current, L is the effective diameter of the field of view (incorporating corrections due to finite beam size and the circular form of the field of view) and the bracketed quantity is meant to represent the average energy loss per unit distance across the field of view. The quantity L has been evaluated numerically and found to be only slightly smaller than the actual diameter of the field of view for all cases considered. For convenience, the excitation rates have been normalized by the creation rate for ion pairs within the field of view, rather than the deposition power. These two quantities are related by the expression:

$$\dot{X}^+ = P/ew \quad (3.12)$$

where e is the electron charge and w is energy required to produce an ion pair in the test gas (26.1 eV in argon).

Excitation rates have been deduced from 16 separate measurements spanning the CO₂ pressure range from 0.1-1.0 torr and the full data base, properly normalized by their respective ion pair creation rates, are shown -vs- vibrational level in Figs. 3.4A and 3.4B. As can be seen the run-to-run variation in the rates is small and furthermore, there is no apparent dependence upon CO₂ pressure with the exception of the rates for $v = 1$. This latter variation is due to the previously alluded to effects of cold CO; the rates determined at the higher CO₂ pressures are the least affected by this correction.

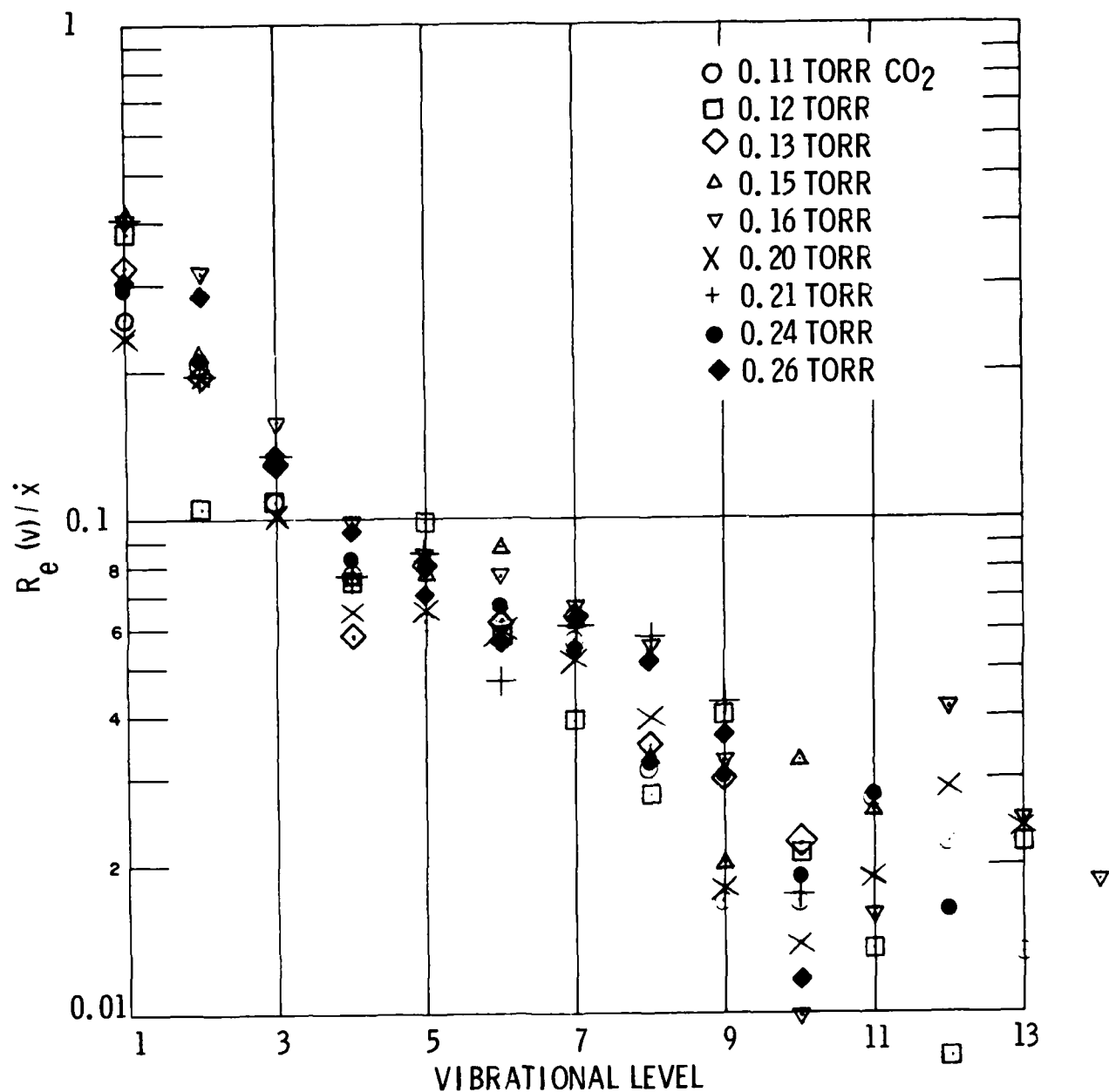


Fig. 3.4a Normalized CO(v) created per ion pair vs. vibrational level. $P_{Ar} = 9$ Torr, $V = 30$ keV, $P_{CO_2} = 0.11-0.26$ Torr. Absolute levels are 2.2 times greater.

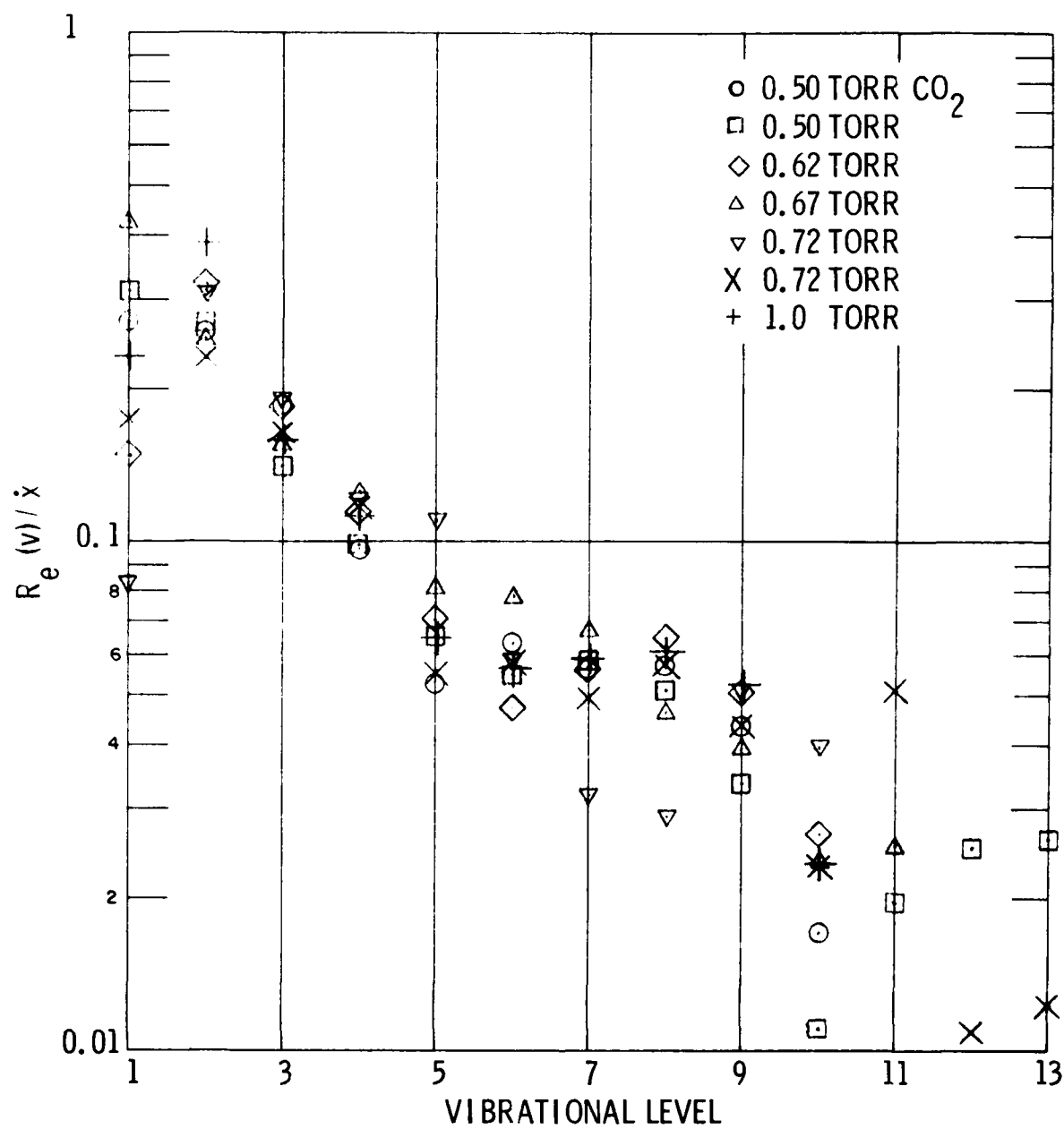


Fig. 3.4b Normalized $\text{CO}(v)$ created per ion pair vs. vibrational level.
 $P_{\text{Ar}} = 9 \text{ Torr}$, $V = 30 \text{ keV}$, $P_{\text{CO}_2} = 0.5\text{-}1.0 \text{ Torr}$. Absolute values
 are 2.2 times greater.

The prediction of the total creation rate per ion pair for producing vibrationally excited CO is also of interest. This quantity is defined by:

$$\dot{CO}^* = \sum_{v=1}^{\infty} RE(v)/\dot{X}^+ \quad (3.13)$$

It is known from the fluorescence data that CO vibrational levels as high as $v = 19$ are formed during electron irradiation, however it appears that CO is predominantly formed in the lower vibration levels. It is estimated that the evaluation of Eq. (3.13) using only the data on the first 13 vibrational levels should be accurate to within ten percent. The resulting total excitation rate per ion pair is shown in Fig. 3.5 as a function of CO₂ partial pressure. As can be seen the number of vibrationally excited CO per ion pair is approximately 2.2 ($\pm 2\%$ r.m.s.), independent of CO₂ pressure.

The fraction of deposited beam energy which is converted to CO vibrational energy is defined by:

$$\epsilon = \sum_{v=1}^{\infty} E_v Re(v)/P \quad (3.14)$$

where E_v is the energy difference between level v and the ground state defined by:

$$E_v = v\omega_e - v(v+1)\omega_e x_e \quad (3.15)$$

where $\omega_e = 2169.8 \text{ cm}^{-1}$ and $\omega_e x_e = 13.29 \text{ cm}^{-1}$ for CO. This quantity has also been evaluated from the data again truncating the sum at $v = 13$, and is shown in Fig. 3.6 as a function of CO₂ pressure. The average energy efficiency is seen to be about 7.7% and does exhibit a slight variation with pressure which may be within the scatter of the data. Note that in this case the truncation of the sum can produce a larger error because the higher vibrational levels

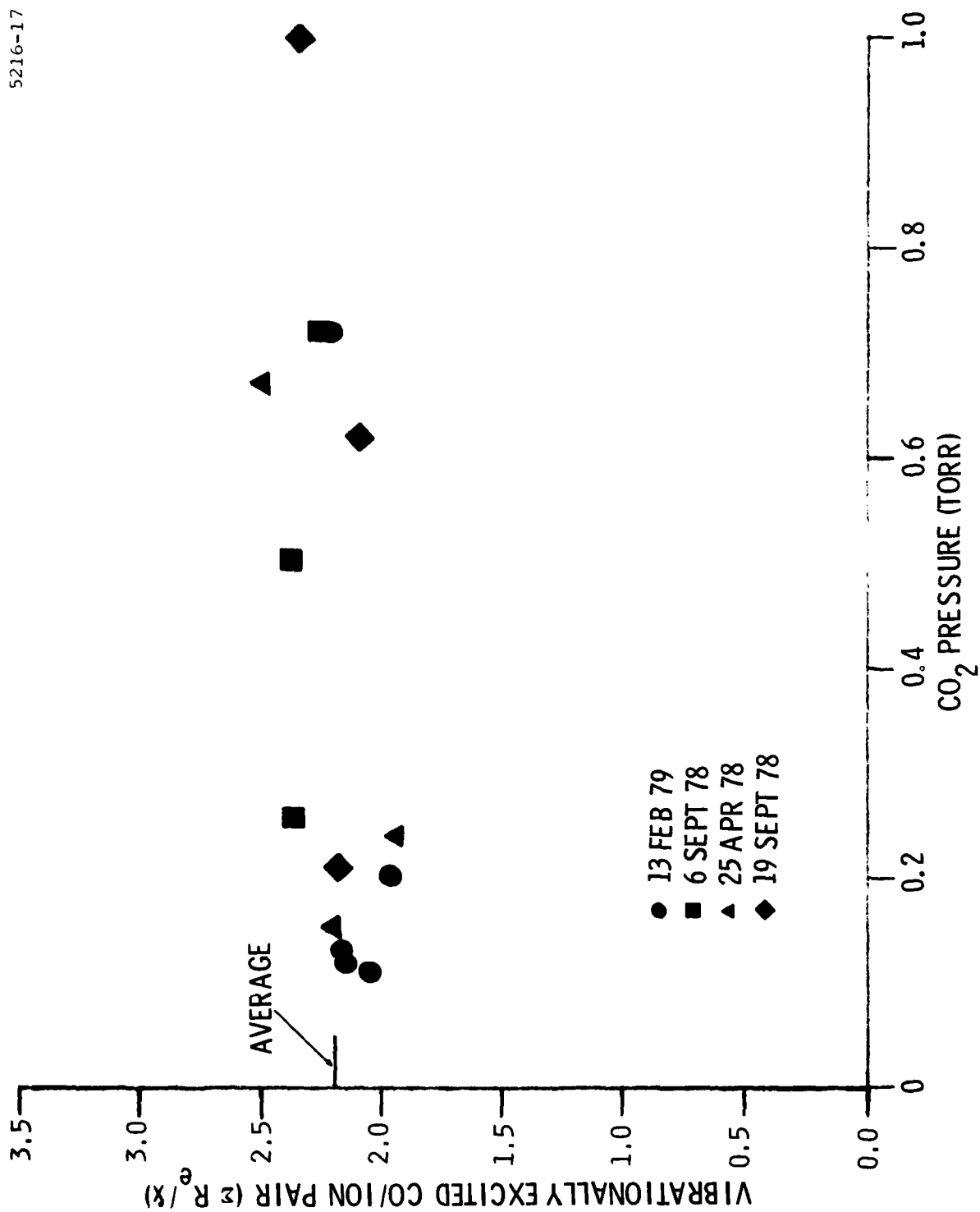


Fig. 3.5 Total vibrationally excited CO created per ion pair vs. CO₂ pressure. Conditions as in Fig. 3.4.

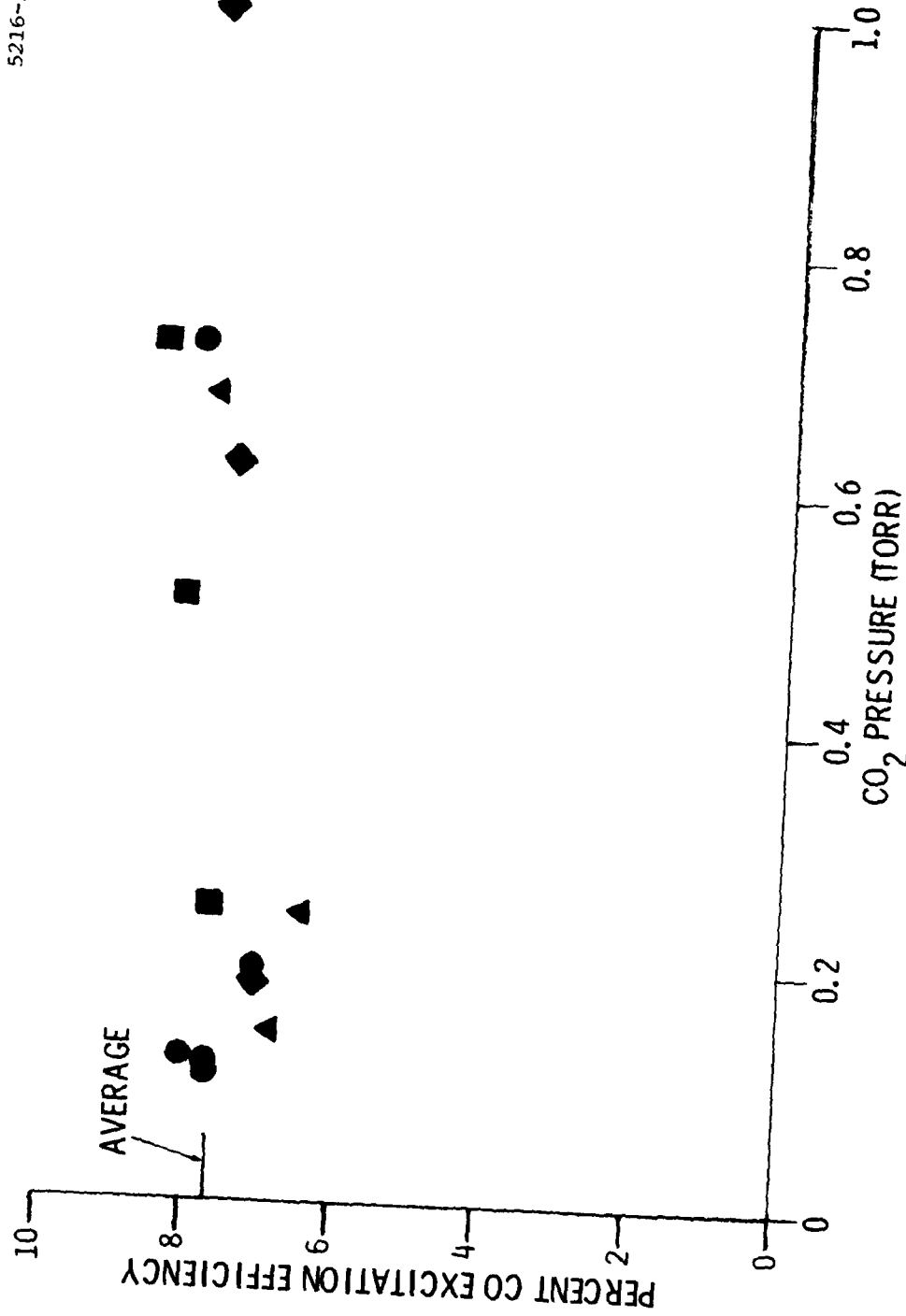


Fig. 3.6 Fraction of deposited electron beam energy partitioned to CO vibrational excitation as a function of CO₂ pressure. Conditions as in Fig. 3.5.

are weighted by the quantity E_v . It is estimated that the true efficiency could be as much as 25% higher than the values shown in Fig. 3.6 (i.e., 9.6%).

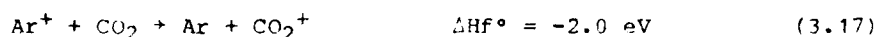
The average level of vibrational excitation may also be readily deduced from the data. The average number of vibrational quanta per excited CO molecule is defined by:

$$v = \frac{\sum_{v=1}^{\infty} v \text{Re}(v)}{\sum_{v=1}^{\infty} \text{Re}(v)} \quad (3.16)$$

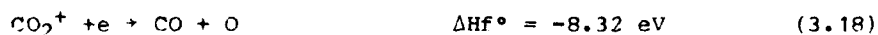
and is found to be ~ 3.5 varying only slightly with CO_2 pressure (this quantity is also a lower bound because of the truncation of the sums at $v = 13$). It is to be noted that v is dependent only upon the relative vibrational distribution and not the absolute calibration.

3.4 Formation Mechanisms

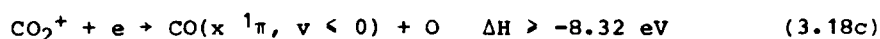
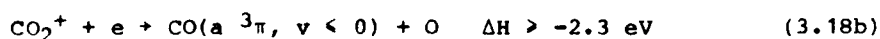
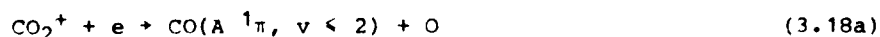
The actual kinetic mechanism responsible for the formation of the vibrationally excited CO is not well defined. The process does not involve a direct interaction between CO_2 and the primary electrons inasmuch as the $\text{CO}(v)$ production rate is found to be invariant over a factor of ten range in CO_2 pressure. The dominant species created by the electron beam are ionic and electronically excited argon. The Ar^+ will rapidly charge exchange with CO_2 ,



and the CO_2^+ will then recombine forming CO, i.e.,

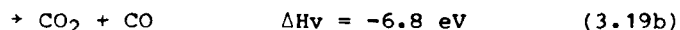
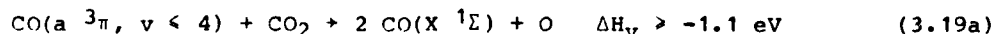


where reaction (3.18) has a room temperature rate constant of $4 \times 10^{-7} \text{ cm}^3/\text{s}^{3.5,3.6}$. Reaction (3.18) has at least three branches.



Gutcheck and Zipf^{3.5} have studied the recombination of CO_2^+ ions produced via charge exchange from Ar^+ , as in the present system, and found that $\approx 5\%$ of the recombining molecules form the $\text{CO}(A^1\pi)$ state will radiatively decay to vibrationally excited ground state CO with a lifetime of $\sim 10^{-8} \text{ s}$.^{3.7}

$\text{CO}(a^3\pi)$ formation has also been observed in CO_2^+ recombination. Wauchop and Broida^{3.8} created CO_2^+ through Penning ionization collisions of CO_2 with $\text{He}(2^3S)$ metastables and found that 55% of the CO_2^+ formed in this manner recombined to form $\text{CO}(a^3\pi)$. (Extrapolation of these results to the present conditions is speculative since the ions produced in the experiment of Wauchop and Broida^{3.8} could have been both electronically and vibrationally excited.) Reaction (3.18b) is sufficiently exothermic to produce $\text{CO}(a^3\pi)$ in vibrational states as high as $v = 11$; however, states higher than $v = 4$ will rapidly convert to the CO triplet states $a^3\Sigma$, $d^3\Delta$, etc., through radiationless curve crossings, and these states will then radiatively cascade back to the $a^3\pi$ state. The $\text{CO}(a^3\pi)$ state has a radiative lifetime of several ms ^{3.8} but it can be rapidly quenched by collisions with CO_2 , i.e.,



Reaction (3.19) has a rate constant of $\sim 2 \times 10^{-11} \text{ cm}^3/\text{s}$ ^{3.9} and thus for the CO_2 pressures of the present study $\text{CO}(a^3\pi)$ will be quenched prior to radiating (note the rate constant for quenching $\text{CO}(a^3\pi)$ by Ar is many orders

of magnitude smaller than that for quenching by CO_2 .^{3.9} The products of reaction (3.19) have not been measured; however both branches of the reaction can lead to vibrationally excited CO. The dissociative branch can also produce a second CO molecule. This reaction path has only enough excess energy to produce ground state CO in levels $v < 4$ and thus by itself is not sufficient to explain the present observations. The direct quenching branch (3.19b) is highly exothermic but the lowest triplet state of CO_2 is not energetically accessible from this reaction.

One last source for CO production in the present system is quenching by excited electronic states of Argon. The relative fraction of deposited beam energy converted to Ar electronic states may be specified using a computer model developed for the determination of the relative allocation of electron energy deposited in gas mixtures. This code uses a set of parameterized cross sections for each gas to determine the apportionment of absorbed electron energy among the various possible paths of atomic and molecular excitations and ionizations. The calculations are performed using the continuous slowing down approximation and include the effect of the total decay (to thermalization) in primary electron energy as well as the effect of all additional excitations/ionizations caused by secondary and higher order electrons. This computer model is well documented^{3.10} and has been previously used to provide electron energy allocation predictions in pure Ar^{3.11} and pure CO_2 ^{3.12} among other gases. Furthermore, the parameterized cross sections required as input to the model are now available^{3.13} for nine gases: Ar, H_2 , H_2O , O_2 , N_2 , O, CO, CO_2 and He.

Energy allocation predictions have been made with this code for several mixtures of CO_2/Ar ; typical results are shown in Figs. 3.7 and 3.8 for the case of one percent CO_2 in Ar. The predicted excitation efficiencies for various inelastic processes in Ar are shown in Fig. 3.7 as a function of primary electron energy. Similar results for CO_2 are presented in Fig. 3.8. (Notation is as in Refs. 3.11 and 3.12.) These excitation efficiencies, which

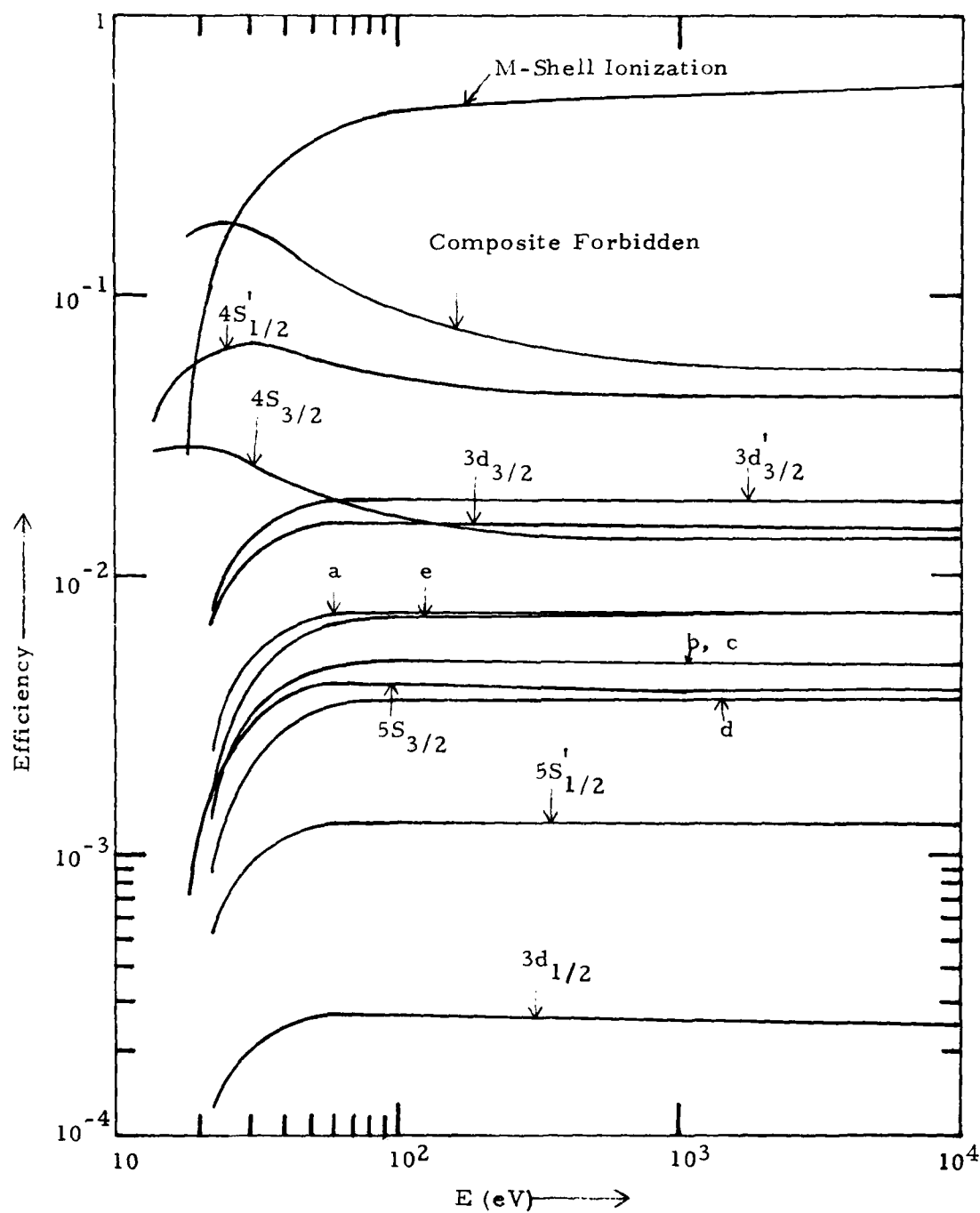


Fig. 3.7 Argon excitation efficiencies as a function of primary electron energy for a 1% CO_2 /99% Ar mixture.

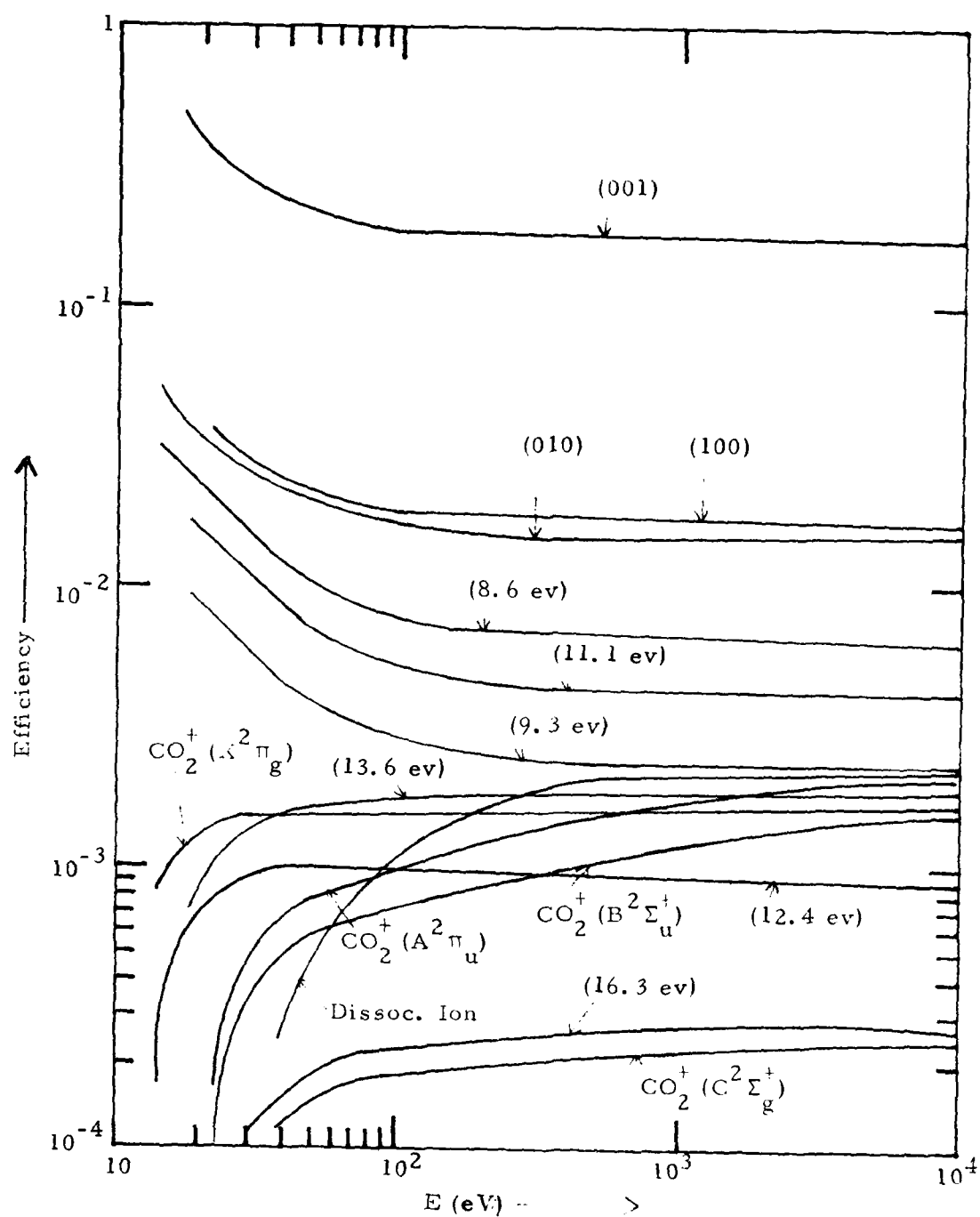
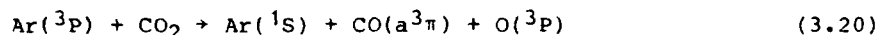


Fig. 3.8 CO₂ excitation efficiencies as a function of primary electron energy for a 1% CO₂/99% Ar mixture.

are the fraction of primary electron energy partitioned into all relevant ionization, electronic state and vibrational excitation processes, are seen to asymptote for primary electron energies greater than 1 keV and thus the efficiencies for 30 keV primaries will be the same as those shown for 10 keV primaries.

It can be seen from Figs. 3.7 and 3.8 that approximately 0.4 electronically excited Ar atoms are created per ion pair. This fraction changes only slightly as the CO₂ concentration is varied between one and ten percent. Although only a fraction of the Ar* are metastable states, those electronic states which do have optically allowed transitions to the ground will be optically trapped for the present experimental conditions (see Appendix III). Thus they will either radiatively cascade to metastable states or be quenched by CO₂. In either case the ultimate quenching can be dissociative. For example, it has been observed^{3,14} that quenching of Ar metastables by CO₂ can lead to production of CO(a ³π) state, i.e.,



It should be noted however that the relative efficiencies for the various reaction paths of such quenching processes have not been defined. Taylor and Setser^{3,15} have noted that the quantum efficiency for reaction (3.20) is low.

In conclusion then at least one CO molecule per ion pair will be created in electron irradiated mixtures of CO₂/Ar by means of the dissociative recombination of CO₂⁺. As many as 2.2 CO per ion pair could be created if the other reaction paths identified above all occurred with unit quantum efficiency; this appears to be an unlikely upper bound, however. The experimental observation that 2.2 vibrationally excited CO are created per ion pair is in disagreement with these kinetic estimates, both because some ground state CO must be created along with the excited molecules and because 2.2 CO per ion pair estimate is an extreme upper bound. Recent measurements by Golde^{3,16} tend to reduce this upper bound even further. Furthermore, the observed

vibrational level dependence of the CO(v) creation rate precludes dissociative quenching of CO(a $^3\pi$) by CO₂ (which accounts for half of the 2.2 per ion pair estimate) as the dominant formation mechanism.

The final issue to address is the potential importance of beam created species in the formation of CO(v). As pointed out in Chapter 2, the steady state number densities of CO and O are expected to be $\sim 10^{14}/\text{cm}^3$. These species will not compete with CO₂ in electron transfer from Ar⁺. The reaction:



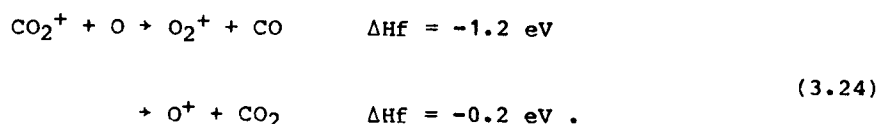
is rapid but it will be immediately followed by



The charge exchange reaction



does not appear to have been studied but is most probably slow. Oxygen atoms can, however, react with CO₂⁺,



The molecular ion O₂⁺ cannot react further with any of the neutral species present and will ultimately dissociatively recombine.

The net effect of reaction (3.24) is to destroy CO_2^+ molecules more rapidly than reaction (3.18). Note that the reactions (3.24) and (3.25) still result in the formation of CO molecules. However, the exothermicities of these reactions only allow excitation up to levels 4-5. Thus if the concentration of oxygen atoms builds up to levels sufficient for reaction (3.24) to dominate (3.18), a distinct change in the CO radiation profiles could occur. The ratio of the rates of these two reactions is given by:

$$R = k_1 [e] / k_{24} [O] \quad (3.26)$$

It can be readily shown that the steady state electron density may be specified by:

$$e = (\alpha / k_1)^{1/2} \quad (3.27)$$

where α is the local ion pair creation rate per unit volume. It has been assumed that the average electron/ion recombination rate constant in the gas may be approximated by k_1 . (This is certainly true when CO_2^+ is the dominant ion.) The local value of α may be defined in terms of the electron beam half-radius via the relationship:

$$\alpha \approx \frac{\dot{X}^+}{2L \pi r^2_{1/2}} \quad (3.28)$$

Where \dot{X}^+ was defined by Eq. (3.12). For a current of 1 mA the value of α at the center of the field of view is found to be $\sim 10^{16}$ ions/cm³s. Ferguson^{3.17} gives k_{24} as 2.6×10^{-10} cm³/s, and with a beam created species [O] concentration of 10^{14} atoms/cm³, Eq. (3.26) becomes:

$$R \approx 2, \quad (3.29)$$

This implies that reaction (3.24) could indeed play a role in the present measurements.

In order to examine this possibility several measurements were performed at decreased beam current and/or duty cycle in order to vary the concentrations of beam created species. No significant change in the efficiency or CO(v) creation rates were observed in these cases which should have spanned up to a factor of six decrease in O-atom density. In an additional set of measurements O₂ was added to CO₂/Ar mixtures in an attempt to see if increased O-atom concentrations would change the CO fluorescence. No change in either intensity or in the level dependent creation rates of CO(v) was observed. These data are taken as evidence that reaction (3.24) is an unimportant loss mechanism for CO₂⁺ in contradiction to the previous estimate, Eq. (3.29). This contradiction could result from uncertainties in the rate constants and densities used in evaluating Eq. (3.26). Alternately there may be unidentified loss mechanisms for oxygen atoms in the system.

3.5 Summary

The mechanics of producing vibrationally excited CO in electron irradiated mixtures of Ar/CO₂ has been examined. CO(v) excitation rates per ion pair have been deduced for vibrational levels 1-13 and the average level of excitation has been found to be 3.5 vibrational quanta. It has been determined that approximately 2.2 vibrationally excited CO created per ion pair and that some 7.7% of the deposited beam energy is allocated to CO vibrational energy. These observations cannot be reconciled with the potential kinetic mechanisms considered for CO(v) in this system, additional mechanisms or systematic errors must be found before these results can be understood.

REFERENCES

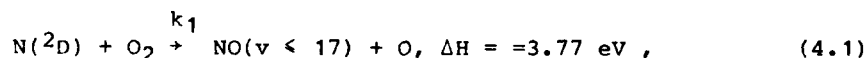
- 3.1 M. J. Berger and S. M. Seltzer, "Tables of Energy Losses and Ranges of Electrons and Positrons," NASA SP-3012, (1964).
- 3.2 F. H. Brittain, "A Description of ELTRAN; An Electron Deposition Code," Sandia Report SC-TM-68-713, January 1979.
- 3.3 'ARPA-NRL Laser Program - Semi-annual Technical Report to Defense Advanced Research Projects Agency," 1 July 1974 to 31 December 1974, NRL Mem. Rpt. 3084, July 1975, pp. 76-99.
- 3.4 R. E. Center, "Plural and Multiple Scattering of Fast Electrons in Gases," Phys. Fluids 13, 79 (1970).
- 3.5 R. A. Gutcheck and E. C. Zipf, "Excitation of the CO Fourth Positive System by the Dissociative Recombination of CO_2^+ Ions," J. Geophys. Res. 78, 5429 (1973).
- 3.6 C. S. Weller and M. A. Biondi, "Measurements of the Dissociative Recombination of CO_2^+ Ions with Electrons," Phys. Rev. Lett. 19, 59 (1967).
- 3.7 P. H. Krupenie, "The Band Spectrum of Carbon Monoxide," National Standard Reference Data Series-NBS5, (1966).
- 3.8 T. S. Wauchop and H. P. Broida, "Lifetime and Quenching of $\text{CO}(a^3\Pi)$ Produced by Recombination of CO_2 Ions in a Helium Afterglow," J. Chem. Phys. 56, 330 (1972).
- 3.9 G. W. Taylor and D. W. Setser, "Quenching Rate Constants for $\text{CO}(a^3\Pi; v = 0, 1, 2)$," J. Chem. Phys. 58, 4840 (1973).
- 3.10 L. R. Peterson, T. Sawada, J. N. Bass and A. E. S. Green, "Electron Energy Deposition in a Gaseous Mixture," Comp. Phys. Comm. 5, 239 (1973).

- 3.11 L. R. Peterson and J. E. Allen, Jr., "Electron Impact Cross-Sections for Argon," J. Chem. Phys. 56, 6068 (1972).
- 3.12 T. Sawada, D. J. Strickland and A. E. S. Green, "Electron Energy Deposition of CO₂," J. Geophys. Res. 77, 4812 (1972).
- 3.13 C. H. Jackman, R. H. Garvey and A. E. S. Green, "Electron Impact on Atmospheric Gases I. Updated Cross-Sections," J. Geophys. Res. 82, 5081 (1977).
- 3.14 W. L. Starr, "Dissociation-Excitation Reactions of Argon Metastables with Carbon Dioxide," J. Chem. Phys. 55, 5419 (1971).
- 3.15 G. W. Taylor and D. W. Setser, "Chemical Applications of Metastable Argon Atoms. V. Generation, Identification and Characterization of CO(a³Π)," Chem. Phys. Lett. 8, 51 (1971).
- 3.16 M. Golde, Private Communication.
- 3.17 E. E. Ferguson, "Rate Constants of Thermal Energy Binary Ion-Molecule Reactions of Aeronomic Interest," Atom. Data Nucl. Data Tables 12, 159 (1973).

4. NITRIC OXIDE EINSTEIN COEFFICIENT RATIOS DETERMINATION

4.1 Introduction

A determination of the radiative lifetimes of high vibrational levels of molecules is of fundamental interest, providing information on the dipole moment function and indirect evidence about the molecular potential energy surfaces. Data on the Einstein coefficients of high vibrational levels is very limited. One example of such measurements is provided by the recently evaluated Einstein coefficient ratios of CO $\Delta v = 2/\Delta v = 3.4$.¹ Previous work by the authors provides a bound to the absolute $\Delta v = 1$ Einstein coefficients for CO $v = 7-12$.^{4,2} The present work presents measurements of the ratios $A_{v \rightarrow v-2}/A_{v \rightarrow v-1}$ for NO ($v = 2-9$). The radiative properties of nitric oxide are of fundamental interest in a wide variety of fields such as combustion, laser and upper atmospheric modeling. Additionally, vibrational fluorescence from the fundamental and first overtone bands of NO ($X^2\Pi$) is an important source of infrared radiation in the disturbed upper atmosphere. The dominant mechanism for formation of vibrationally excited NO in aurorally disturbed atmospheres can be the reaction:^{4,3,4,4}



where the $N(^2D)$ atoms are produced as a result of the auroral electron dosing. The unrelaxed vibrational distribution created by this reaction has been experimentally observed previously.^{4,5} The distribution shows a uniform creation rate for molecules with one to eight vibrational quanta of excitation, with decreasing rates for the higher levels up to 12 quanta (which was the highest level from which emission was observed). The distribution for aurorally induced NO fluorescence may be determined by coupling the distribution, which is taken as the initial distribution created in the upper atmosphere, with a relaxation model that includes the Einstein coefficients.

In order to relate (atmospheric) emission quantitatively to a molecular vibrational population distribution, the absolute thermally-averaged vibrational emission rates or Einstein coefficients must be known for all levels of interest ($v < 12$). Several theoretical models of the NO $\Delta v = 1, 2$ coefficients exist.^{4.6-4.9} Billingsley, in a rigorous treatment,^{4.6} develops a theoretical electronic dipole moment function for the ground state and, in addition, takes into account vibration-rotation coupling and spin-uncoupling effects. Michels' theory,^{4.7} which is based on a less sophisticated dipole moment function, was intended for prediction of the Einstein coefficients of the lowest vibrational levels and is not expected to be as accurate for large v . The thermally averaged Einstein coefficients for $\Delta v = 1, 2$ transitions of NO based on these two theoretical models are presented in Fig. 4.1 for $v < 13$. It is seen from the figure that the two calculations track well at low v . Michel's predictions for the fundamental and first overtone Einstein coefficients cross above level 7, i.e., the overtone band emission would be more intense than the fundamental for all levels above 7. In contrast, based on Billingsley's theory, the fundamental emission would be more intense for all levels plotted. The differences between the theories are most evident in the ratios of the overtone to fundamental Einstein coefficients, A_{v+v-2}/A_{v+v-1} . The two models would provide significantly different ratios of fundamental to first overtone emission intensities at elevated NO vibrational temperatures.

Although Billingsley's model appears to be preferred, there are as yet no experimental data available for verification of his theory. Only integrated band intensity measurements have been made^{4.10-4.12} and these can not be scaled to provide high vibrational level information because of vibrational anharmonicity and limited dipole moment function knowledge. As a result, only A_{1+0} and A_{2+0} are accurately measured. Elementary scaling of the fundamental and overtone Einstein coefficients, according to the relation:

$$A_{v+v-1} = v A_{1+0} , \quad (4.2)$$

is found to disagree with both theoretical predictions with increasing v .

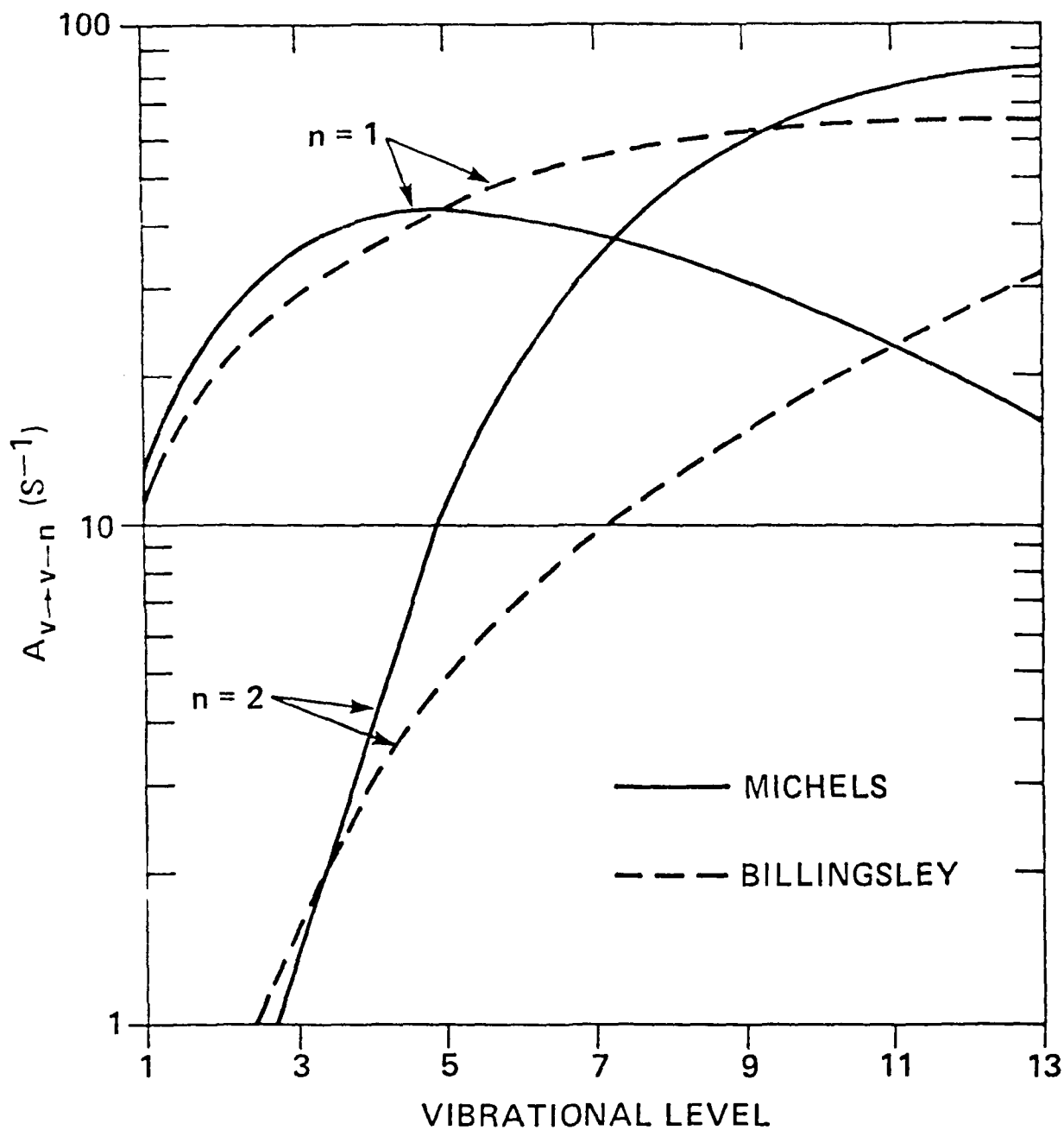


Fig. 4.1 Theoretical values of Einstein coefficients for the NO fundamental and overtone transitions, from Michels⁷ and Billingsley.⁶

We report here the first experimental determination of the ratio of these vibrational-level dependent Einstein coefficients for the fundamental and first overtone bands. The present results yield the necessary data for theoretical evaluation and provide support for theoretical predictions of absolute radiative decay rates. These experiments were performed on the LABCEDE facility at the Air Force Geophysics Laboratory. This apparatus has been described previously^{4.2,4.13} and only a brief description will be presented here. For this study, N_2 /trace O_2 mixtures were irradiated by a 36 keV electron beam to form highly vibrationally excited NO. The high energy primary electrons undergo inelastic collisions with the molecular nitrogen which can result in electronic excitation (forming $N^2(A)$), dissociation (yielding $N(^2D)$, $N(^4S)$), or ionization (N_2^+ , N^+), of the bath gas. Subsequent ionic reactions can result in additional formation of $N(^2D)$ or $N(^4S)$. The $N(^2D)$ so created reacts with the molecular oxygen (Reaction 1) to form vibrationally excited NO. A small fraction of the electron-beam energy deposited in the gas mixture appears as infrared fluorescence and this fluorescence is dominated by NO fundamental ($\Delta v=1$) and overtone ($\Delta v=2$) emission. Because a Michelson interferometer is used to resolve the emission, both bands can be observed simultaneously using an indium antimonide detector. Geometric and temporal intensity fluctuations cancel and thus an absolute determination of the relative intensities of the two bands can be obtained. Spectral curve fitting techniques utilizing synthetic NO spectra permit determination of the relative emission rates for the fundamental and first overtone transitions out of each vibrational level observed. Ratios for levels 2-9 are presented.

A brief description of the experiment and operating conditions is given in the next section of this chapter. The spectral curve fitting and analysis are presented in Part 4.3, with the summary and conclusions appearing in the last section.

4.2 Experimental Measurements Program

A detailed description of the LABCEDE operating conditions has been given in Section II of the report for CO_2/Ar mixtures, and only the modifications made for these measurements will be mentioned here. The gases used in

these experiments were ultrahigh purity nitrogen and oxygen, further purified using a dry ice-acetone trap to remove H_2O . The two gas flows were monitored using calibrated flowmeters. In a previous set of measurements^{4,14} it was observed that the NO fundamental band fluorescence was nearly two orders of magnitude weaker than the CO fluorescence for similar operating conditions. In order to improve the NO signal level the electron beam acceleration potential was increased to 36 kV. As a result the current in the beam increased significantly, increasing energy deposition and the total fluorescent signal level. In addition, it was found that when the concentration of oxygen was varied from 20% to a trace of the nitrogen pressure, signal levels increased drastically. With the present gas mixture only NO fundamental band fluorescence is observed in the band pass of the lead selenide detector, and the total detector signal may be used as an indicator of NO fundamental band intensity. The signal was observed to peak when the O_2 concentration was low, around 0.3 torr, and decreased fairly rapidly on either side of this maximum. Molecular oxygen quenching of NO has been measured to be rapid (see Chapter 5), and clearly a balance exists between providing sufficient oxygen for NO formation and an excess causing NO fluorescence quenching.

The optical path between the detector and the experiment was strongly purged and dried to attempt to minimize the ambient H_2O . The Lorentzian water vapor absorption lines are much narrower than the experimental spectral resolution but can coincidentally overlap NO emission lines both in the fundamental and overtone regions. The blackbody calibration cannot properly correct for this effect because of the 10 cm^{-1} resolution and thus water vapor absorption could result in a distortion of the deduced Einstein coefficients. The magnitude of the effect of atmospheric H_2O will be discussed in the analysis.

Three different detectors were utilized during these measurements. An indium antimonide detector (77 K, response time $< 1\text{ }\mu\text{s}$) was used to observe both bands simultaneously. Unfortunately, its spectral response decreases drastically at wavelengths corresponding to $v > 4$ transitions of the NO

fundamental band. Consequently, a lead selenide detector (77 K, $\tau \approx 70$ ps) was used to observe emission out to $v = 11$ in the fundamental band. The overtone emission was weaker than the fundamental and, in order to measure less intense emission features in that band better, a lead sulfide detector (193 K, $\tau \approx 2.4$ ms) was employed. The data acquired with the indium antimonide detector were used to provide a common reference between the two bands; the individual band data were used to determine the relative variation of the Einstein coefficient ratios out to high vibrational levels. Experimental conditions were closely duplicated between runs with different detectors. A variable bandpass amplifier (PARC Model 113) was used to reduce the high frequency response of the signal from each detector to about 2.5 ms, which is sufficiently fast to follow the 10 ms beam pulse.

The detector signal is sampled by an A/D converter and stored in the memory of a PDP/15 computer dedicated to the experiment. The interferogram signal is referenced relative to the mirror position and electron beam pulse onset. Signals from about 50 consecutive pulses are averaged for each mirror sampling position. About one-half hour was required to scan the interferometer for each run and obtain spectra with 10 cm^{-1} resolution. If the experimental pressure or beam current varied by more than 3% during this time, the data were discarded.

Interferograms were acquired at 0.5 ms intervals during and after the pulse. The spectrally resolved data were found to reach steady-state values (for all three detectors) over the entire emission band within 5 or 6 ms after beam onset. This is primarily determined by the detection system response time and is governed primarily by the bandpass amplifier. When not limited by the bandpass amplifier, the fluorescence is observed to reach a constant value in less than a millisecond with the fast PbSe detector. After the spectra reach their steady-state distribution, fluctuations of the data are less than 5%, as is expected from the constancy of the total fluorescent intensities. The small magnitudes of these fluctuations indicate excellent data reproducibility. Time resolved spectra are only needed for comparison of data from

different detectors. The emission from all vibrational levels must reach steady-state during the pulse in order to permit the ratio of the radiative emission rates for each level to be determined. Temporally resolved data are required for a companion set of measurements of the relaxation of NO in these mixtures reported in Chapter 5.

The present series of measurements was made at both 10 and 20 torr N₂ with flow rates of 5 standard liters/min. The oxygen pressure was kept constant at about 3% of the N₂ pressure. This concentration gives the maximum fluorescent intensity at these pressures, illustrating the balance between sufficient O₂ to form NO by reaction (1) and O₂ quenching of vibrationally excited NO. As the final part of the calibration, the interferometer was rotated to view a 1123 K blackbody standard in order to obtain the relative spectral response curve for each detector.

4.3 Analysis

The interferograms were Fourier-transformed into spectra, each corresponding to a time interval during the electron beam pulse. These spectra were then corrected for detector spectral response to give calibrated intensities in watts/cm². The long wavelength spectral responses of the lead sulfide and lead selenide detectors were sufficient to allow the respective overtone and fundamental fluorescence from all emitting vibrational levels to be observed.

The observed emission intensity from each vibrational band may be written as:

$$I_v = \frac{N_v A_{v \rightarrow v-n} h c \nu}{4\pi} \quad (4.3)$$

where N_v is the total number of molecules within the field of view which are in vibrational state v , $A_{v \rightarrow v-n}$ is the Einstein coefficient, and $h\nu$ is the energy of the emitted photon. The observed fluorescence is composed of emission arising from up to 10 vibrational levels. Because the emission from these levels is spectrally overlapped, a curve fitting procedure has been developed to match computer generated NO spectra from different vibrational levels to the observed emission.

The method for generating the spectrally resolved emission predictions and curve fitting has been given previously,^{4.2,4.3} and only a brief description will be given here. The total intensity in a rotational line of a vibrational band may be written

$$I_{J \rightarrow J, J \pm 1}^{v \rightarrow v-n} = \frac{h^2 c^2 \nu^4 S^{P,Q,R}_J}{3 k T \nu_{v \rightarrow v-n}} A_{v \rightarrow v-n} N_v \exp(-B_v J(J+1)hc/kT) \quad (4.4)$$

$$= C(\nu, T, v, J) A_{v \rightarrow v-n} N_v,$$

where $A_{v \rightarrow v-n}$ is the fundamental ($n=1$) or overtone ($n=2$) Einstein coefficient, $\nu_{v \rightarrow v-1}$ is the band origin (cm^{-1}), ν is the frequency of the individual line, h , c , and k are Planck's constant, the speed of light, and Boltzmann's constant respectively, B_v is the rotational constant for level v , $S^{P,Q,R}$ is the Honl-London factor, T is the rotational temperature, and J is the rotational quantum number. The heating of the gas by the electron beam has been measured as only a few degrees, and the NO rotational temperature is assumed to be in equilibrium with the gas translational temperature at 300 K. This assumption is verified through a spectral comparison. The values for the

spectroscopic constants used in the present analysis which are taken from Goldman and Schmidt,^{4,15} are (in cm^{-1}) $\omega_e = 1903.937$, $\omega_e x_e = 13.97$, $\omega_e y_e = -0.0037$, and $B_v = 1.705 - 0.0176 (v + 1/2)$.

Calculation of the intensity for each rotational line within the vibrational band and subsequent convolution with the instrument function (resolution = 10 cm^{-1}) permits creation of a unit intensity basis function, $\xi_v(v)$ for each vibrational transition. The calculated intensity at any frequency is the sum of the overlapped basis functions at that frequency, viz.

$$I_n(v) = \sum_v N_v A_{v \rightarrow v-n} \xi_v(v). \quad (4.5)$$

The quantities $N_v A_{v \rightarrow v-n}$ are adjusted by the least-squares fitting routine so that the square of the differences between the data $I(v)$ and fit $I_n(v)$ is minimized. Because the fluorescence from the fundamental and overtone bands is observed simultaneously from the same emitting volume, the fitted quantities $N_v A_{v \rightarrow v-n}$ may be directly ratioed to obtain the Einstein coefficient ratios $A_{v \rightarrow v-2}/A_{v \rightarrow v-1}$.

The above analysis assumes that the gas is optically thin for both fundamental and overtone emission. A great advantage of the LABCEDE experiment is that the radiating species are created in situ by chemiluminescent reactions so that there exists only a small population of the ground state molecule of interest in the observation volume. Upper bound estimates of the NO concentration lead to the conclusion that the fractional reabsorption of the emitted fluorescence is less than 5% even at the line center of the strongest rotational line within a vibrational band; thus, self-absorption may be neglected.

Examples of typical fits of synthetic overtone and fundamental spectra to the experimental data are shown in Fig. 4.2. The data were taken with PbSe and PbS detectors. The contributions from some of the individual basis functions to the total intensity are included along the bottom of the figures. The synthetic spectra match the envelope of the emission very well. The standard deviations of the fits are less than 3%. However, at smaller wave numbers where detector responses are decreasing, spectral noise is significant and the quality of the fits decreases. In the fundamental band, the basis functions are sufficiently overlapped so that no individual vibrational branches are resolvable. For the overtone spectra, the P-branch radiation from the vibrational level v strongly overlaps the R-branch emission from the level $v + 1$; only the $v = 2$ R-branch is not overlapped. Fluorescence from level $v = 10$ is definitely observed in the overtone spectra. Even though great care was taken to remove H_2O from the atmospheric optical path, some residual water vapor remained, as is evidenced by the structure in the fundamental band fluorescence between 1600 and 1800 cm^{-1} . The atmospheric water vapor lines randomly overlap NO rotational emission lines and act to decrease the detected intensity. As a result, the values of $N_v A_{v \rightarrow v-1}$ calculated for those levels which suffer absorption will be slightly lower than the unattenuated values. This absorption has been estimated to have less than a 5% effect on the calculated values for the populations (and consequently the ratios).

Comparison of the $N_v A_{v \rightarrow v-n}$ values calculated from fits to the InSb data permits direct calculation of the quantities $A_{v \rightarrow v-2}/A_{v \rightarrow v-1}$ for $v = 3$ and 4. These values are displayed in Fig. 4.3. The plotted points are the average values of the ratio taken during steady-state of the fluorescence signal. The $N_v A_{v \rightarrow v-n}$ values deduced from fits to similar runs using different detectors will allow $A_{v \rightarrow v-2}/A_{v \rightarrow v-1}$ to be determined only to within an arbitrary constant due to geometry and absolute response uncertainties. Nine sets of data from the PbS and PbSe detectors were used to determine this ratio for levels up to $v=9$. The average values of the ratios obtained from these runs were then normalized to the values at $v=3, 4$ obtained using the InSb detector.

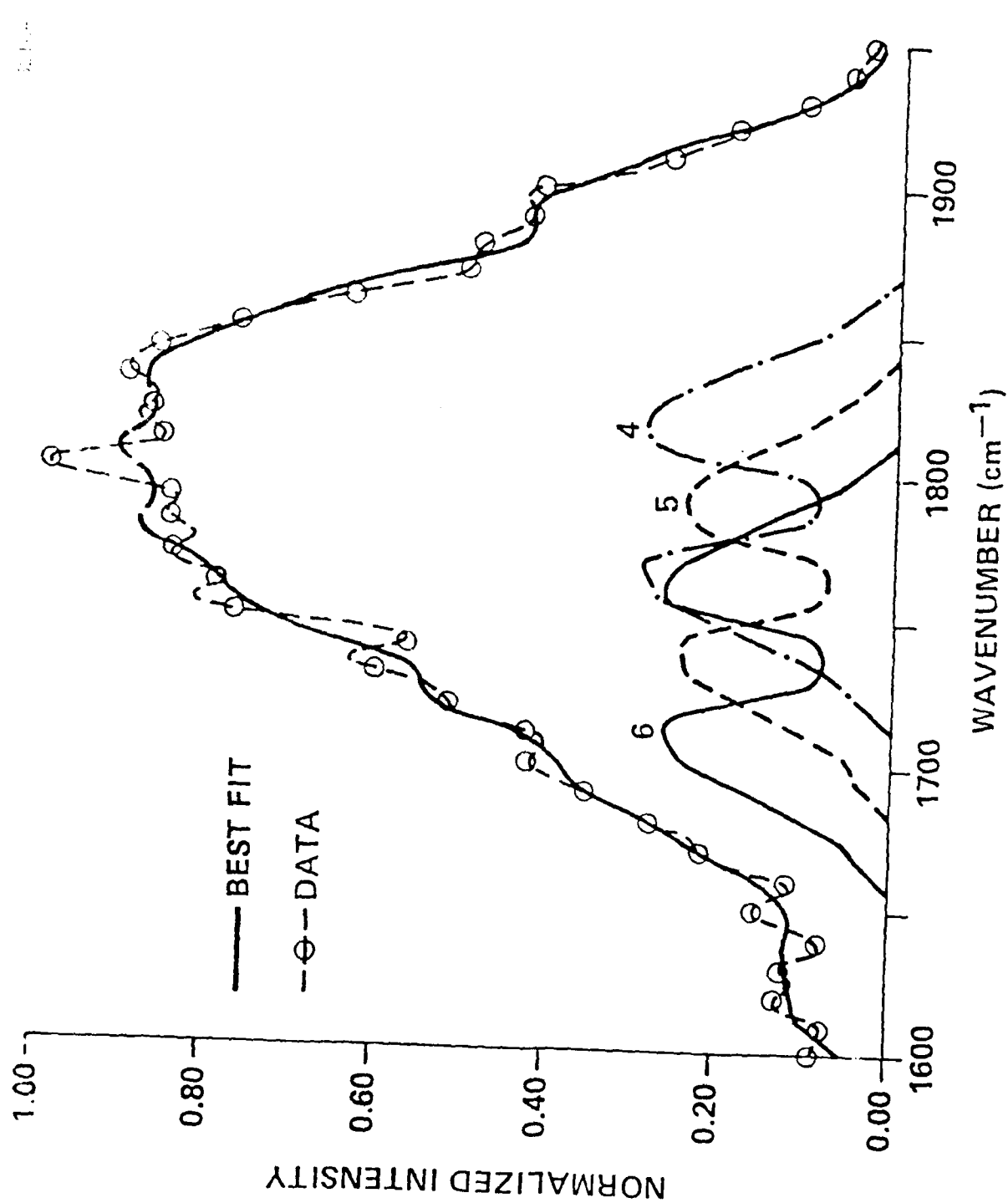


Fig. 4.2a Least-squares fits to NO fundamental data from a 0.3 torr O_2 , 10 torr N_2 mixture at beam termination using a lead selenide detector. Contributions of the emission from individual vibrational levels to the synthetic spectrum are shown.

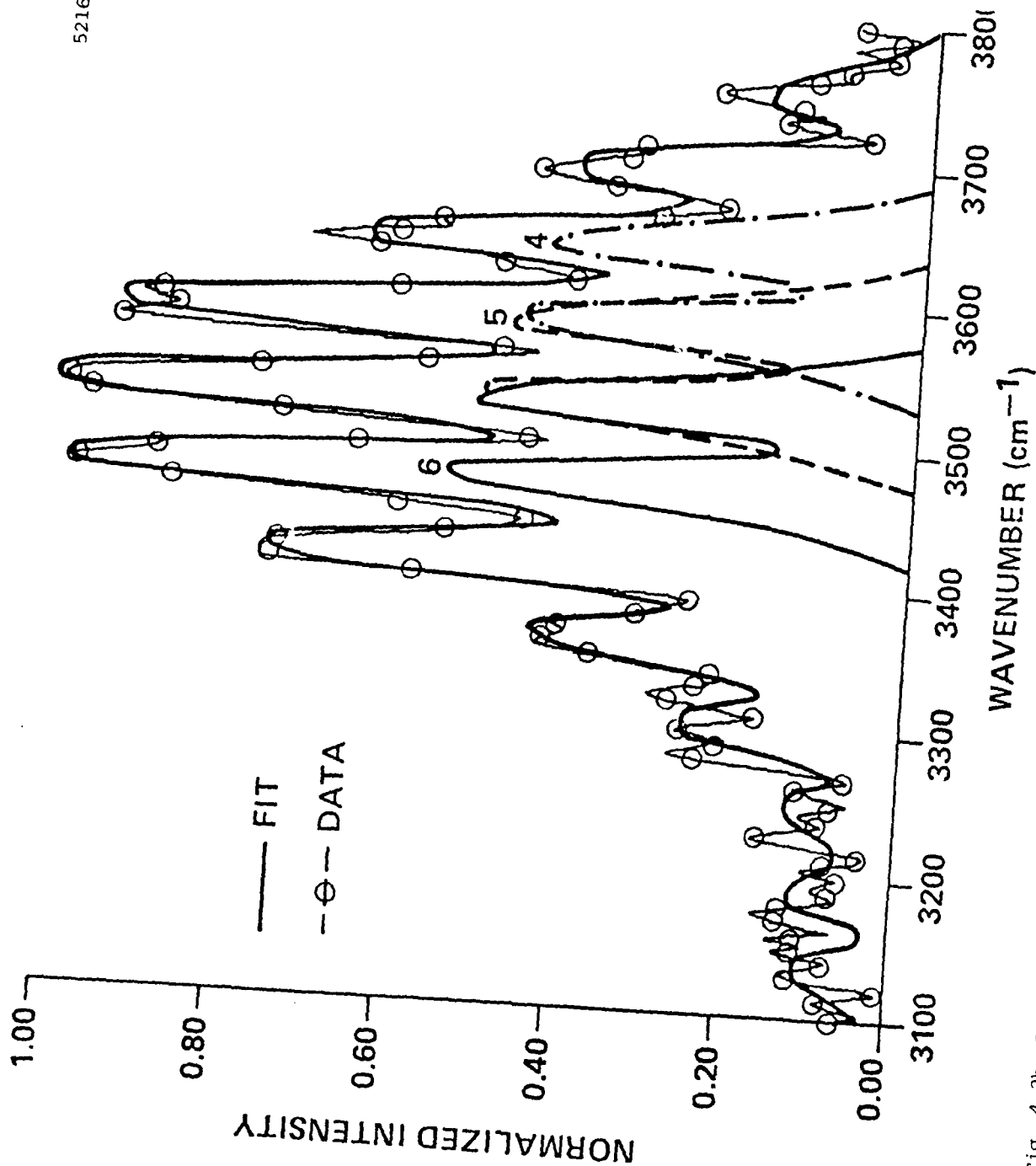


Fig. 4.2b Least-squares fits to NO overtone data from a 0.3 torr O₂, 10 torr N₂ mixture at beam termination using a lead sulfide detector. Contributions of the emission from individual vibrational levels to the synthetic spectrum are shown.

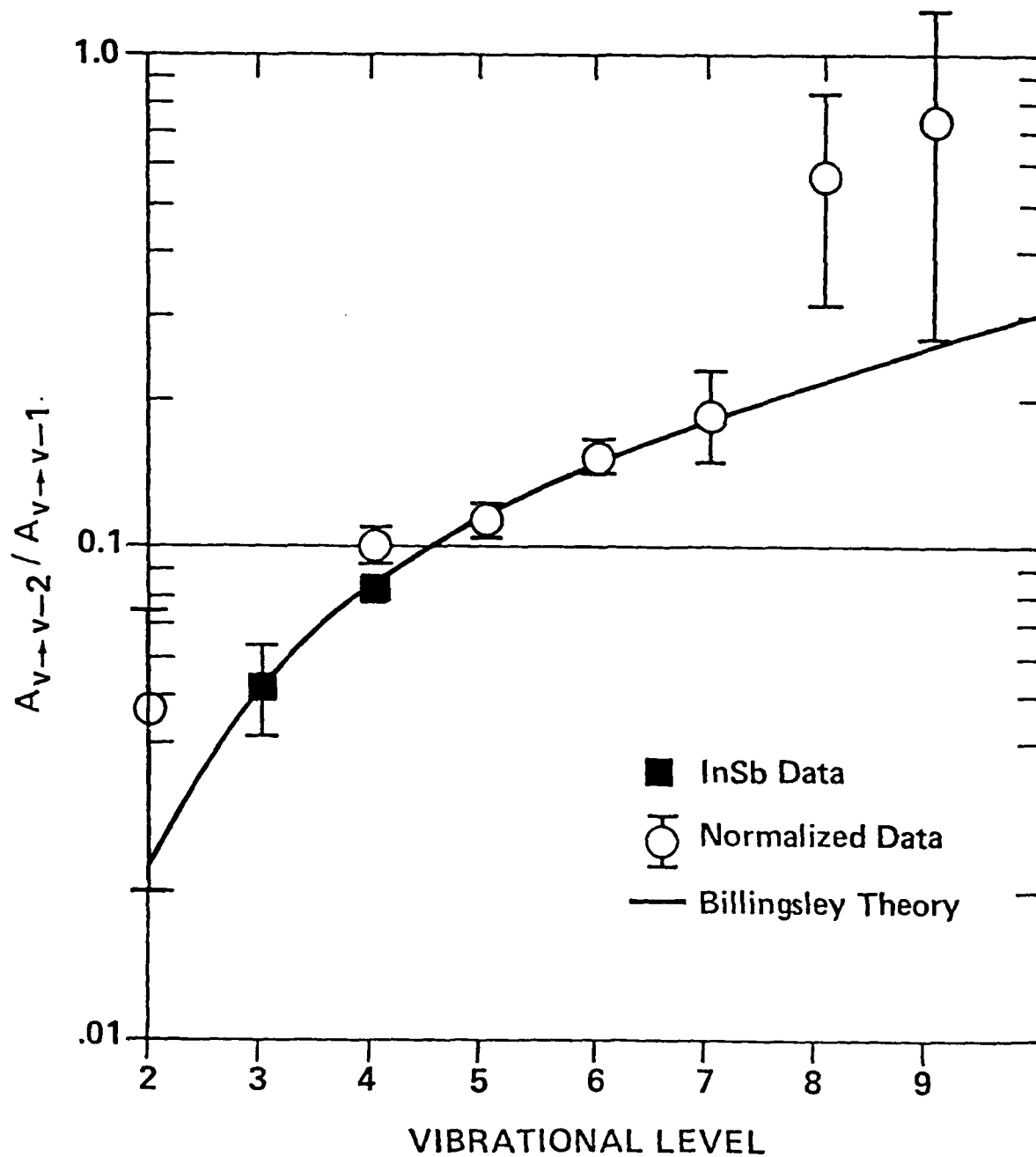


Fig. 4.3 Experimentally determined Einstein coefficient ratios for first overtone/fundamental bands of NO. Billingsley's theoretical prediction is shown for comparison.

These normalized points are presented as circles in Fig. 4.3. Their associated error bars represent the cumulative effect of errors due to uncertainties in the fitting of each vibrational population, variations in the populations due to temporal fluctuations of the fluorescence during the pulses, effects of H_2O , and the statistical deviations of the average values from different runs. These errors are accumulated as the square root of the sum of the squares of all the contributions, and the displayed error bars are thus felt to represent an upper bound for the statistical errors and run-to-run variations. No attempt has been made to include an estimation of the magnitude of systematic experimental errors. The uncertainties in the ratios are greatest for the levels with the weakest emission intensities. The highest levels (8, 9, and 10) are not significantly populated and the fluorescent intensity is close to the noise level. Level 10 can be observed but our analysis predicts a complete uncertainty in its Einstein coefficient ratio. The low overtone intensity of level 2 is a consequence of its long radiative lifetime for overtone emission; $N_2A_{2\rightarrow0}$ is small even though the vibrational population is significant and this emission is close to the noise level. Noise appears as spectral intensity and erroneously increases the N_v values during the fitting. The overtone spectra are noisier than the fundamental band, and as a result the $A_{v\rightarrow v-2}/A_{v\rightarrow v-1}$ ratios for levels 2, 8, and 9 are elevated with the $A_{2\rightarrow0}/A_{2\rightarrow1}$ ratios being most significantly affected. The value of $A_{2\rightarrow0}/A_{2\rightarrow1}$ is reduced to 0.030 for those experiments having the smallest spectral noise level. This value is in much better agreement with Billingsley's predictions, which are also plotted in the figure. The values of the ratios plotted in Fig. 4.3 refer to the entire data base for all levels; however, the large error bars for levels 2, 3, 7, 8, and 9 reflect increased uncertainties produced by decreased signal-to-noise ratios. Billingsley's predictions of the ratios are seen to agree well with the trend of the experimental points out to the highest levels. The absolute values at levels 3 and 4 are seen to agree with the theory to within 3%.

4.4 Summary and Conclusions

The fluorescent emission from electron-irradiated mixtures of N_2 with trace O_2 has been spectrally resolved using a Michelson interferometer. By

using three different detectors, the total fundamental and overtone emission from NO could be observed. Nitric oxide emission dominated the infrared fluorescence and exhibited emission from molecules with up to ten quanta of vibrational excitation. Utilization of an indium antimonide detector permitted the absolute relative intensities in both NO bands to be obtained. Fitting of the data with computer-generated spectra permitted a determination of the quantity $N_v A_{v \rightarrow v-n}$ for all $v \leq 9$ and $n = 1, 2$ as a function of time during electron irradiation. Steady-state values of this quantity were averaged and ratioed to give the first experimental measurements of the ratio of NO Einstein coefficients $A_{v \rightarrow v-2}/A_{v \rightarrow v-1}$. Comparison of these measured ratios with theoretical predictions provides strong support for the calculations of Billingsley.

REFERENCES

- 4.1 A. J. Lightman and E. R. Fisher, "A Coefficients for Spontaneous Emission in CO," Appl. Phys. Lett. 29, 593 (1976).
- 4.2 G. E. Caledonia, B. D. Green, and R. E. Murphy, "A Study of the Vibrational Level Dependent Quenching of CO(v=1-6) by CO₂," J. Chem. Phys. 71 (11) 4369 (1979).
- 4.3 T. Ogawa, Planet and Space Sci. 24, 749 (1976).
- 4.4 T. C. Degges, "Vibrationally Excited Nitric Oxide in the Upper Atmosphere," Appl. Opt. 10, 1856 (1971).
- 4.5 J. P. Kennealy, F. P. DelGreco, G. E. Caledonia, and B. D. Green, "Nitric Oxide Chemiexcitation Occurring in the Reaction Between Metastable Nitrogen Atoms and Oxygen Molecules," J. Chem. Phys. 69 (4) 1574 (1978).
- 4.6 F. P. Billingsley, "Calculated Vibration-Rotation Intensities for NO(X²π)," J. Molec. Spect. 61, 53 (1976).
- 4.7 H. H. Michels, "Calculation of the Integrated Band Intensities of NO," J. Quant. Spect. Radiat. Transfer 11, 1735 (1971).
- 4.8 G. Chandraiah and C. W. Cho, "A Study of the Fundamental and First Overtone Bands of NO in NO-Rare Gas Mixtures at Pressures up to 10,000 PSI," J. Molec. Spect. 47, 134 (1973).
- 4.9 K. Cashion, "A Method of Calculating Vibrational Transition Probabilities," J. Molec. Spect. 10, 182 (1963).
- 4.10 P. Varanasi and S. S. Penner, "Absolute Infrared Intensity Measurements on the Fundamental of NO," J. Quant. Spect. Radiat. Transfer 7, 279 (1967).

REFERENCES (Continued)

- 4.11 R. M. Feinberg and M. Camac, "Band Intensity of NO Fundamental," J. Quant. Spect. Radiat. Transfer 7, 581 (1967).
- 4.12 U. P. Oppenheim, Y. Avir, and A. Goldman, Appl. Opt. 6, 1305 (1967).
- 4.13 R. E. Murphy, F. H. Cook, and H. Sakai, "Time-Resolved Fourier Spectroscopy," J. Opt. Soc. Amer. 65, 600 (1975).
- 4.14 B. D. Green, G. E. Caledonia, and R. E. Murphy, "SWIR-MWIR Electron Fluorescence Measurements in N₂/O₂ and Air," Air Force Geophysics Laboratory TR-78-0083, Environmental Research Papers, No. 629, April 4, 1978.
- 4.15 A. Goldman and S. C. Schmidt, "Infrared Spectral Line Parameters and Absorptance Calculations of NO at Atmospheric and Elevated Temperatures for the $\Delta v=1$ Bands Region," J. Quant. Spect. Radiat. Transfer 15, 127 (1975).

5. THE VIBRATIONAL RELAXATION OF NO(v=1-7) BY O₂

5.1 Introduction

An understanding of the relaxation kinetics of high vibrational levels of molecules is necessary for the proper interpretation of non-equilibrium phenomena which occur in a broad range of applications such as infrared gas lasers, rocket plumes and the disturbed upper atmosphere. In particular, nitric oxide is a prominent infrared radiator in the ionosphere and knowledge of its vibrational energy transfer rates with atmospheric species is needed to properly describe non-equilibrium infrared radiative phenomena in the excited atmosphere, such as during an aurora.

The dominant collisional partners for quenching of vibrationally excited NO in the upper atmosphere are N₂, O₂ and O. There have been several measurements of the relaxation of the first excited vibrational level of NO by O₂ and N₂ and the rate constants for these processes are well established, e.g.:

$$\text{NO}(v=1) + \text{O}_2 \xrightarrow{k_{\text{O}_2}} \text{NO}(v=0) + \text{O}_2; k_{\text{O}_2} = (2.4 \pm 1.5) \times 10^{-14} \text{ cm}^3/\text{s}^{5.1} \quad (5.1)$$

$$= (2.8 \pm 0.25) \times 10^{-14} \text{ cm}^3/\text{s}^{5.2}$$

$$= (2.6 \pm 0.15) \times 10^{-14} \text{ cm}^3/\text{s}^{5.3}$$

$$= (2.9 \pm 0.5) \times 10^{-14} \text{ cm}^3/\text{s}^{5.4}$$

$$\text{and NO}(v=1) + \text{N}_2 \xrightarrow{k_{\text{N}_2}} \text{NO}(v=0) + \text{N}_2; k_{\text{N}_2} = (1.7 \pm 0.7) \times 10^{-16} \text{ cm}^3/\text{s}^{5.1} \quad (5.2)$$

$$= (1.3 \pm 0.1) \times 10^{-16} \text{ cm}^3/\text{s}^{5.3}$$

$$= (1.4 \pm 0.15) \times 10^{-16} \text{ cm}^3/\text{s}^{5.5}.$$

Oxygen atoms become a major atmospheric constituent above 90 km, and relaxation of NO(v=1) by O has been measured^{5,6} to be very efficient ($k_{\text{O}} = 6.5 \pm 0.7 \times 10^{-11} \text{ cm}^3/\text{s}$). All of the above rate constants are specific to 300 K.

Very little data exists for the relaxation of vibrational levels $v > 1$ for these species. Whitson, Darnton and McNeal^{5,7} have placed bounds on the rate constants of the processes:

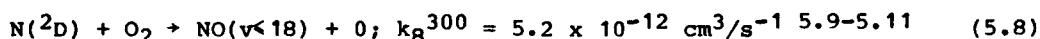
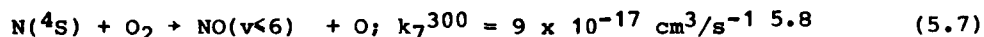


for $v=1-7$ based on Lambert-Salter probability scaling of $v=1$ data using constants based on their experimental data. Their deduced scaling is less than linear with v . However, because their data was acquired in a time-to-steady-state flowing afterglow experiment where relaxation is not actually observed, the analysis required to deduce rate constants is complex.

In this chapter we report a measurement of the relaxation rate constants of $\text{NO}(v=1-7)$ by O_2 on the LABCEDE apparatus, which has been described previously. NO is created vibrationally excited in nitrogen/trace oxygen mixtures irradiated by 36 keV electrons. Energy is deposited in the gas mixture primarily by inelastic collisions of the primary and secondary electrons with N_2 . These collisions are dominantly with N_2 and can result in N_2 electronic excitation (e.g., forming $\text{N}_2(A^3\Sigma_u^+)$, etc.) dissociation (forming $\text{N}(^4\text{S})$, $\text{N}(^2\text{D})$), or ionization N_2^+ , N^+). Subsequent reactions can lead to the formation of additional atomic nitrogen, e.g.:



where e_s is a beam-created secondary electron. (Under the present experimental conditions it is likely that the charge transfer reaction N_2^+ to O_2^+ will dominate over reaction (5.4).) The atomic nitrogen so created will then react to form NO.



From the reaction rates for (5.7) and (5.8) it can be seen that unless $\text{N}(^4\text{S}) > 10^5 \text{ N}(^2\text{D})$, the (^2D) reaction will dominate.

The initial distributions of vibrationally excited NO formed by these reactions have been measured. The two measurements of the $\text{N}(^4\text{S})$ reaction distribution^{5.7,5.12} differ somewhat, but both predict insignificant population of levels above $v=5$. The $\text{N}(^2\text{D})$ reaction nascent product distribution has been measured^{5.13} to have vibrational levels 1-8 essentially equally populated. Population of the higher levels was less probable, but levels up to $v=12$ were observed. The observed NO fluorescence in the present experiment exhibits contributions from levels with $v \leq 10$; thus $\text{N}(^2\text{D})$ is at least partially responsible for the NO formation.

The NO relaxation is studied using time resolved Fourier spectroscopy to deduce the total relaxation history for each level at a given O_2 pressure. Variation of the O_2 pressure then permits isolation of the portion of the relaxation due to O_2 by means of a Stern-Volmer analysis. A similar analysis has been completed previously^{5.14} for CO relaxation by CO_2 . The details of the experiment and spectral fitting will be briefly summarized in the next section. The kinetic analysis and the possible effects of beam-created species will be considered in Part 5.3. Global kinetic effects and the computer modeling effort will be discussed in Subsection 5.4. A summary and discussion are given in the last section.

5.2 Experimental and Data Analysis

Details of the interferometric technique providing simultaneous temporal and spectral resolution has been presented elsewhere.^{5.14-5.16} For these experiments 36 keV electrons were directed into mixtures of N₂ at 20, 50 and 100 torr with trace concentrations of O₂ (0.02-5 torr). The kinetic measurements analyzed below were made with 50 torr N₂ in the tank. Typical electron beam currents were 1.5-1.7 mA during a 1.0 ms pulse. During this pulse, the spectrally integrated intensity on the detector (as observed during data acquisition) nearly reached steady-state, and longer pulses did not substantially improve signal levels. The observed decays were rapid (0.1-3 ms depending on O₂ pressure), but a beam period of 20 ms was used to prevent excessive build-up of beam created species. Nitrogen gas was flowed at five standard liters per minute, which corresponds to a residence time of 2.5s in the field of view. As a result, the gas within the field of view was irradiated by many sequential electron beam pulses. Experimental considerations limit the maximum interpulse time, and thus products of electron induced reactions build up and complicate the relaxation kinetics. Their effects will be discussed in the kinetic analysis section.

The gases used in these experiments were ultrahigh purity nitrogen and oxygen, trapped with a dry ice-acetone bath to remove H₂O. A lead selenide detector was positioned at the exit plane of the interferometer for detection of the NO fundamental band emission. This detector had an intrinsic time response of 75 μ s, but the response of the detection system could be further reduced (to decrease noise levels) using a bandpass amplifier. The PbSe detector used for these experiments had a significant low wavenumber response out to 1430 cm⁻¹. As a result, the detector did not artificially cut off the fundamental band fluorescence - the emission from all populated levels was observed.

Data was acquired at 100 μ s intervals during and after the beam pulse, with the data from 50 consecutive pulses being averaged to improve signal to noise prior to storage on magnetic tape. Subsequent data manipulation permits generation of the interferograms and spectra of the fluorescence at 100 μ s

AD-A114 389 PHYSICAL SCIENCES INC WOBURN MA

F/G 20/7

LABCEDE STUDIES.(U)

SEP 81 B D GREEN, G E CALEDONIA, L G PIPER

F1962R-78-C-0115

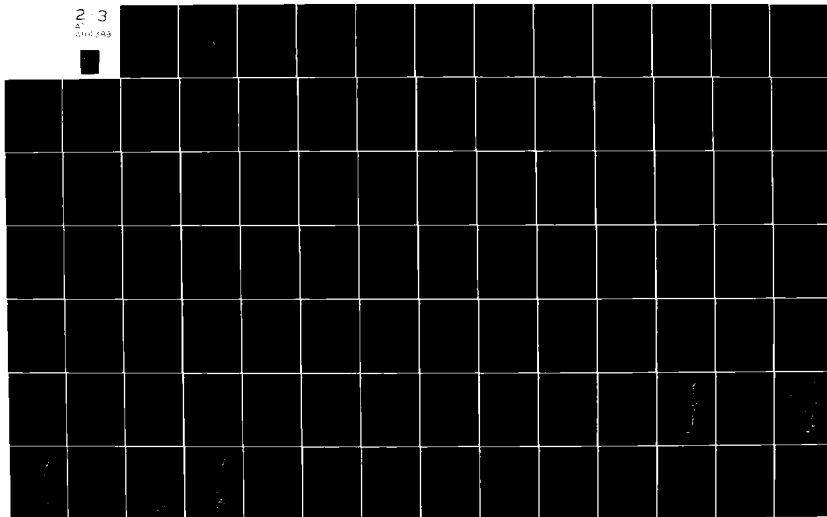
UNCLASSIFIED PSI-TR-261

AFGL-TR-82-0060

NL

2-3

4-100-249



intervals. All signals are referenced to a baseline just before beam onset. In this manner the beam-created portion of the emission is separated from the background radiation. A typical set of fluorescence intensities are plotted in Fig. 5.1 at 100 μ s intervals after beam termination. As the final part of the calibration, the interferometer was rotated to view a 1173 blackbody standard in order to determine the relative spectral response of the detection system.

The experimental NO spectra were corrected for detector response then spectrally fit with synthesized basis functions to determine the relative intensity contribution of each vibrational level to the observed emission. The amount of NO created is sufficiently small so that the gas is optically thin. The NO spectroscopic constants of Goldman and Schmidt^{5,17} were used in this analysis. A fuller description of the fitting procedure is provided in Chapter 4.

A typical fit to the data is presented in Fig. 5.2. The data shown is a spectrum of the fluorescence at beam termination from a mixture of 50 torr N_2 , 1.5 torr O_2 . The contribution of several individual vibrational levels to the total intensity is shown along the bottom of the figure. Emission can be observed from up to 10 excited vibrational levels. Emission from still higher levels may be present at very low levels, but the signal would be buried in the noise beyond 1600 cm^{-1} . The intensity fluctuations in the data between $1650\text{--}1750\text{ cm}^{-1}$ appear to be due to the random overlap of atmospheric H_2O absorption lines with the NO emission lines. Even though H_2O was purged from the optical path, some residual water vapor remained and acted to decrease the detected intensity. This absorption is estimated to have less than a 5% effect on the calculated populations and rates. On the whole, the generated spectrum closely matches the data and the standard deviation of the fit is only 3.5%.

The deduced time histories of the NO vibrational populations during and after an electron beam pulse in 50 torr N_2 , 1.5 torr O_2 are shown in Fig. 5.3 for vibrational levels 1-5. The highest vibrational levels are seen

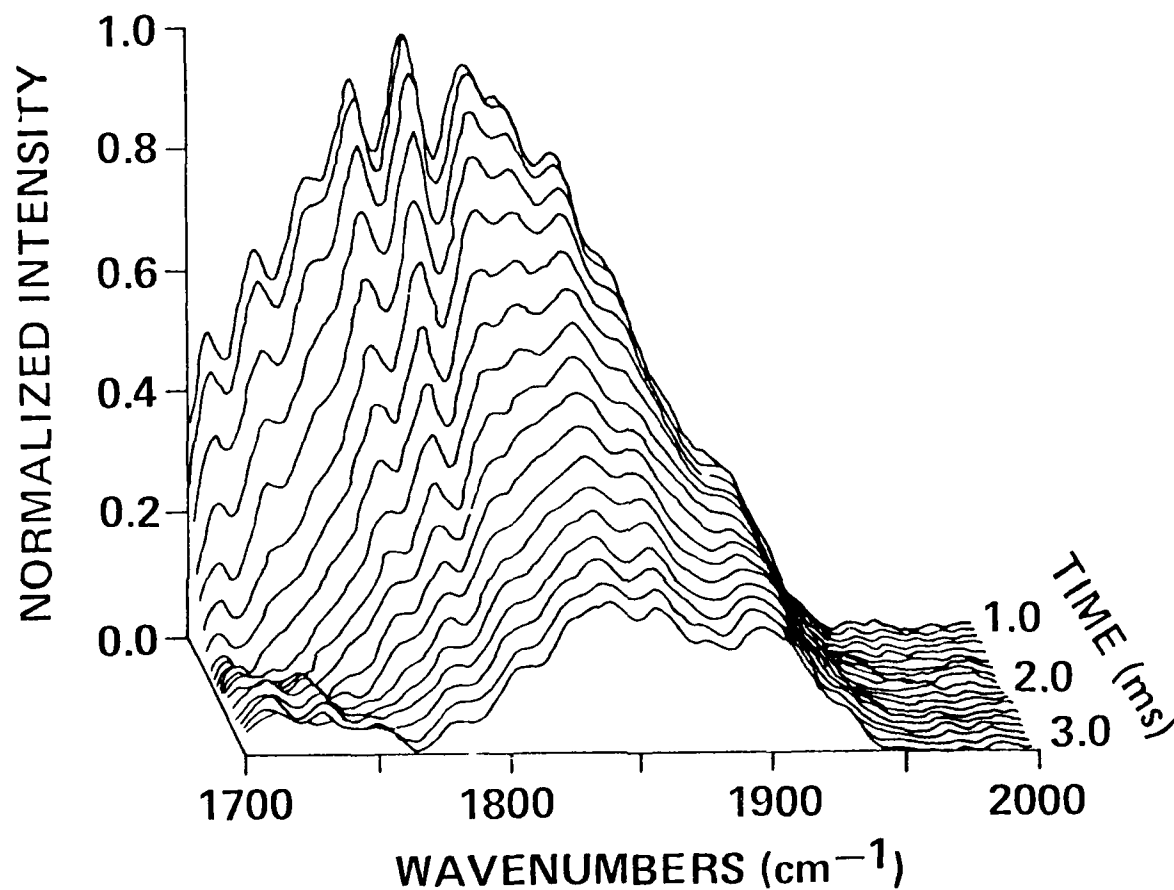


Fig. 5.1 The time and spectrally resolved fluorescence from NO($\Delta v=1$) transitions at 0.1 ms intervals after beam termination. Time is plotted as increasing outward from the plane at the page. The rear spectrum corresponds to the time of beam termination. These spectra have been corrected for detector response.

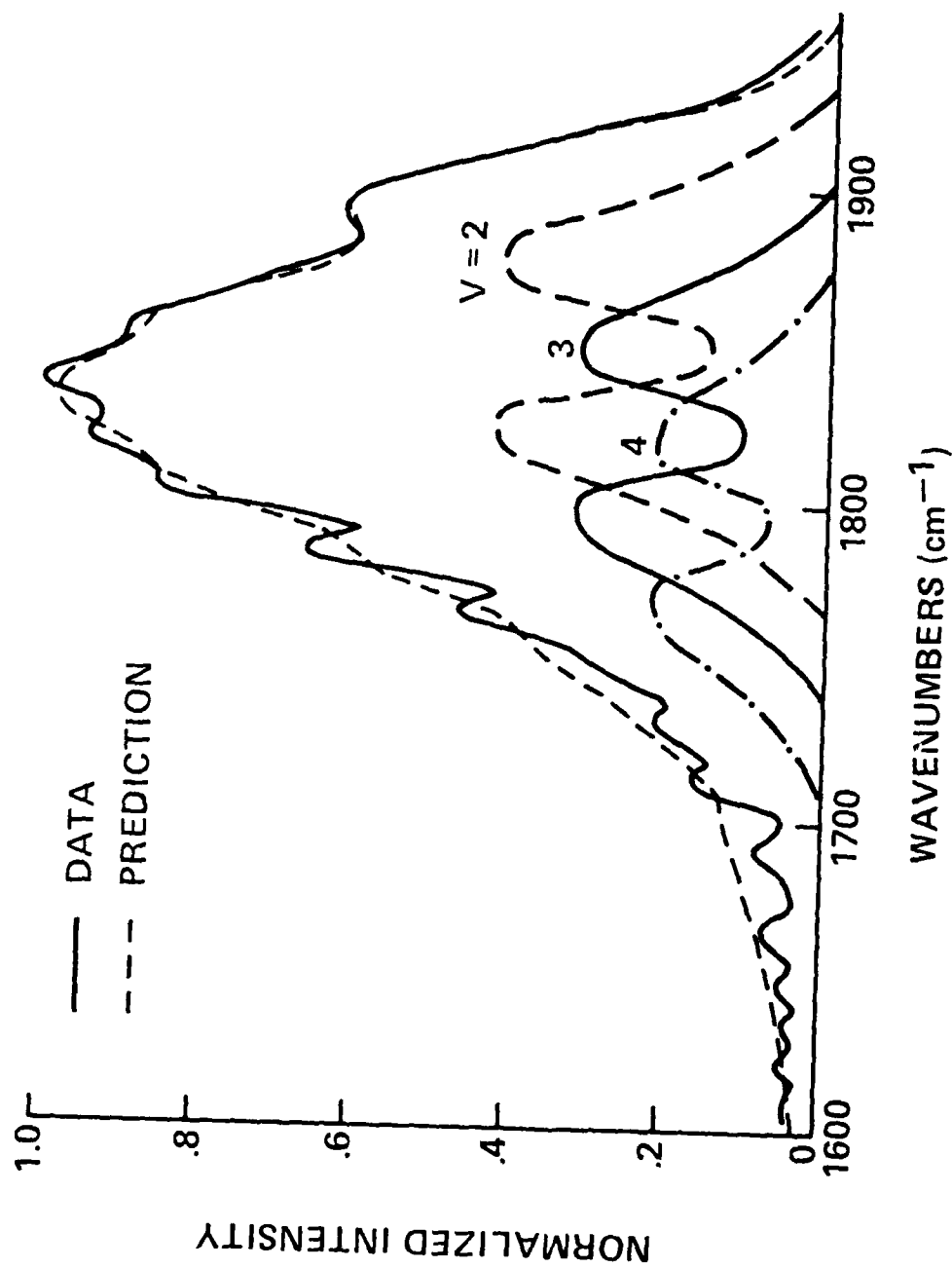


Fig. 5.2 Fit of a synthetic NO spectrum to data taken at beam termination from a 50 torr N₂, 1.5 torr O₂ mixture. The standard deviation of the fit is 3.5%. Emission contributions from individual vibrational levels are also shown.

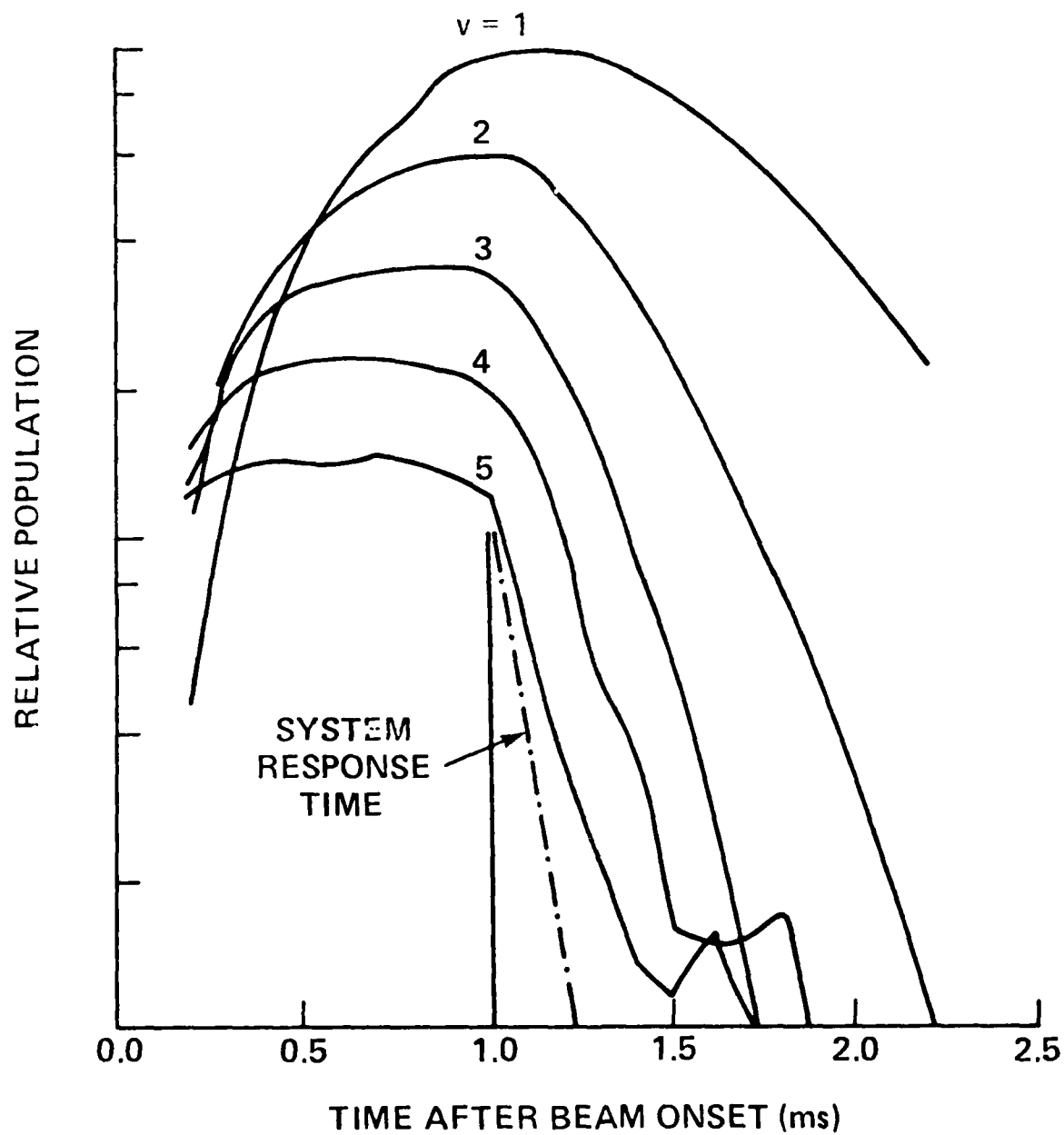


Fig. 5.3 NO vibrational population histories for levels 1-5 for $p_{N_2} = 50$ torr, $p_{O_2} = 1.5$ torr.

to decay most rapidly after beam termination. These decay times approach the system response time for high v especially at the larger O_2 pressures. Nevertheless, the decay in these populations can be followed over more than an order of magnitude due to good signal-to-noise levels. Levels 3-5 are seen to reach steady-state values during the pulse -their rapid decay balancing beam excitation. The temporal behavior of sets of coupled vibrational populations were used to determine level-dependent relaxation rates for each O_2 pressure. Details of this analysis are given in the next section. However, to isolate the effects of O_2 relaxation from other relaxation mechanisms, several series of runs with increasing oxygen concentrations were made. In total, measurements were made at 14 oxygen concentrations between 0.017 and 5.0 torr of N_2 . The populations deduced from this data form the base for the following kinetic analysis.

5.3 Kinetic Analysis

The observed population decays are likely to have contributions from several relaxation processes which can occur simultaneously under LABCEDE conditions. Quenching by the reactant gases is expected to dominate radiative decay, which has rates of $10-60s^{-1}$ for $v \leq 1-7$ of the NO fundamental band.^{5,18} At 50 torr of N_2 the rate of quenching $v=1$ of $NO^{5.1,5.3,5.5}$ by N_2 would be $260s^{-1}$; the N_2 quenching rates are expected to increase with vibrational quantum number. The rate for quenching $NO(v=1)$ by $O_2^{5.1,5.4}$ will vary between $10-4000s^{-1}$ over the experimental range of oxygen concentration. Again the relaxation constant is expected to increase with vibrational level. Thus at oxygen pressures of several torr, relaxation by O_2 can be an order of magnitude faster than N_2 quenching and orders of magnitude faster than radiative decay.

Unfortunately, as a result of the experimental flow conditions, a fresh gas sample was not irradiated with each pulse. Thus reaction products from previous pulses will still be in the irradiated volume and can interact with the vibrationally excited NO. These long-lived beam-created species

are O and N atoms formed by direct electron impact and ionic reactions, and the products of their subsequent reactions which yield O₃, NO, and NO₂. Computer modeling of the relevant neutral kinetics indicates that O atoms will be the dominant beam created species, being removed primarily by diffusion and by its reaction with O₂:^{5.19}



the next most prevalent species will be N and NO, but they destroy each other in the reaction:^{5.19}

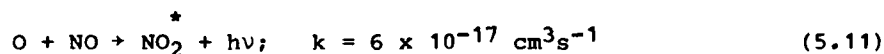


which creates an additional O atom. N atoms are also removed in the creation of NO via reactions (5.7) and (5.8) resulting again in the production of oxygen atoms.

A computer model was used to predict the interactive temporal behavior of the species concentrations during a series of beam pulses. It was found that as the O₂ concentration increases, the NO concentration linearly increases through reaction (5.8). The atomic oxygen concentration is predicted to linearly decrease with increasing O₂ pressure because of reaction (5.9), and the product of [O] [NO] will remain roughly constant. Moreover, the model predicts that at low O₂ pressures (0.2 torr) the NO concentration will quickly decay after beam termination, while O-atoms will be nearly invariant. As the O₂ pressure increases the two decay times should approach each other. This model will be discussed in more detail in Section 5.4.

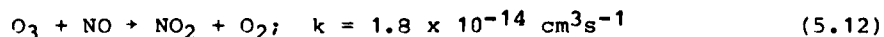
In order to experimentally verify our modeling predictions of beam-created species, a separate measurements program was undertaken to monitor the O + NO afterglow emission. When atomic oxygen and nitric oxide are mixed, a

continuum emission extending from 375 to beyond 3000 nm is observed, the intensity of which is linearly proportional to the product of the number densities of [O] and [NO]. The reaction

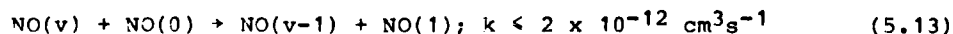


is well studied^{5.20-5.22} and the chemiluminescence spectral distribution is known. The observed NO₂ continuum intensity is nearly invariant over the range of O₂ pressures studied, suggesting that the product of O and NO concentrations is constant in good agreement with modeling predictions. Moreover, at low O₂ pressures, the NO and O afterglow exhibits a biexponential decay which tends to a single exponential as O₂ increases, again as predicted. Unfortunately, the NO concentration in these mixtures is not known and so the absolute O-atom concentration could not be determined. Nevertheless, the qualitative agreement of the modeling with the chemiluminescence experiment temporal and intensity behavior supports the accuracy of the modeling. The afterglow experiments are described more fully in Appendix IV.

At large O₂ concentrations, O₃ is predicted to be the dominant beam created species (from reaction (5.9), with O-atoms an order of magnitude lower in concentration. The reaction of O₃ with NO,



proceeds at a rate which is considerably less efficient than O-atom quenching. Likewise beam created N-atoms rapidly react with NO by reaction (5.10) but are expected to be an order of magnitude down in concentration from O. NO self-quenching proceeds with a slower rate than the atomic processes, i.e.,



for $v=1-8^{5.23}$ and should be negligible for anticipated NO concentrations. Lastly, relaxation by species such as N_2O or NO_2 could not compete with O-atom relaxation even if these processes proceeded at gas kinetic rates. Relaxation by trace impurities introduced with the reactant gases is expected to be negligible. An impurity of several parts per million in the N_2 would have to exhibit a gas kinetic rate for quenching of NO in order to compete with the above processes. Because the gases are trapped to remove H_2O , the most likely candidate, it is concluded that the role of these impurities should be minor.

Thus the observed temporal histories of the vibrational populations may be interpreted in terms of quenching by the reactant gases N_2 , O_2 , and the beam-created species O, and by radiative decay. The total quenching rate for each level v , R_v , may then be written as a sum of these processes:

$$R_v = k_{O_2}(v) [O_2] + k_{N_2}(v) [N_2] + k_O(v) [O] + A_{v,v-1} \quad (5.14)$$

For the case of single quantum relaxation the change in the observed population of a vibrational level as a function of time is a balance between feeding through quenching of the level above and losses by relaxation into the next lower level. The master equations which describe the time rate of change of the coupled vibrational populations may then be written:

$$\begin{aligned} \frac{dn}{dt} &= -R_1 n_1 + R_2 n_2 \\ &\vdots \\ \frac{dn_m}{dt} &= -R_m n_m + R_{m+1} n_{m+1} \\ &\vdots \\ \frac{dn_N}{dt} &= -R_N n_N \end{aligned} \quad (5.15)$$

where N represents the most highly excited vibrational level, and n_m is the relative population of vibrational level m . Determination of the R_m values is complicated by the numerical inaccuracies introduced upon evaluating the slopes, dn_m/dt , of the experimental data. A time integrated approach developed previously for CO relaxation measurements,^{5,14} improves the accuracy of the deduced values of R_m . Integrating Eq. (5.15) over all times between t_1 and t_2 , we obtain:

$$\Delta n_m = n_m(t_1) - n_m(t_2) = R_{m+1} a_{m+1} - R_m a_m \quad (5.16)$$

where

$$a_m = \int_{t_1}^{t_2} n_m dt \quad (5.17)$$

This integral form of the master equations is particularly useful in that it not only eliminates the need for derivative values but also allows determination of the best value of R_m over a specified time interval, effectively filtering random fluctuations in the population histories introduced in the curve fitting process. Rearranging Eq. (5.16) permits direct specification of the rates R_m in terms of measured quantities.

$$R_m = - \sum_{v=m}^N \Delta n_v / a_m \quad (5.18)$$

The deactivation rates R_m have been deduced from the measured vibrational population histories (such as shown in Fig. 5.3) through use of Eq. (5.18). The populations were typically integrated over 1 ms starting

just after beam termination (populations were measured at 0.1 ms intervals). Variation of the time interval chosen for integration has only a small effect on the deduced rates. The populations of the highest vibrational levels tend to be the least accurately determined; primarily because the rapid relaxation out of these levels causes the populations at all times to decrease with increasing v (see Fig. 5.3) thus resulting in signal-to-noise limitations being more important for the higher levels. Accordingly, the rates could generally be evaluated for only the lowest seven vibrational levels even though emission from ten levels was observed under the best conditions. It was found that inclusion of the more poorly determined populations in the analysis produced only 5-10% changes from the rate values determined without the high v data.

The aim of the analysis is not to deduce the rates R_m , but to separate the effects of the competing relaxation processes (the different terms in Eq. (5.14), isolating the contribution of O_2 relaxation to permit deduction of the rate constants, $k_{O_2}(v)$. Although the computer modeling and visible afterglow measurements helped to identify the importance of the various quenching partners, absolute concentrations of beam created species could not be determined and the role of O_2 quenching cannot be completely isolated. However, the O_2 relaxation rate constants can be accurately bounded from the following analysis.

A strong upper bound can be placed on the O_2 rate constants by assuming that the relaxation rates calculated from experiments at high O_2 pressures are entirely due to O_2 quenching. Any contributions to the quenching by other processes will decrease the role of O_2 . Thus, neglecting those processes and setting

$$R_v = k_{O_2}^u(v) [O_2] \quad (5.19)$$

gives the maximum possible values of the rate constants. The upper bound $k_{O_2}^u$ (1) is in excellent agreement with (just slightly above) the previously reported measurements as shown in Fig. 5.4. For higher vibrational levels, the role of other quenchers could be more important, so that the actual rate constants could lie further below $k_{O_2}^u(v)$ for those levels.

A second method of data interpretation is to subject the relaxation rates to a Stern-Volmer type analysis. If the calculated relaxation rates from the different experiments with varying O_2 pressures are plotted versus O_2 concentration as shown in Fig. 5.5, they are observed to fall along straight lines. This behavior can be interpreted as an O_2 quenching contribution varying linearly with pressure and a constant baseline contribution attributable to relaxation by O , N_2 and spontaneous emission. The slope of the line is then the relaxation rate constant for that vibrational level. The rates for $v=1$ and 3 displayed in Fig. 5.5 are seen to exhibit linearity across the entire range of O_2 pressures. Similar results are obtained for the other vibrational levels. The slopes of this data, as deduced from linear least square fits, are also shown in Fig. 5.4.

From the kinetic discussion above N_2 and O are expected to be the other significant terms in Eq. (5.14). These experiments were all performed at constant N_2 pressure so that $k_{N_2}(v)[N_2]$ term will form a constant baseline on the Stern-Volmer plots. However, according to the computer modeling, the O -atom concentration is expected to decrease with increasing O_2 . The observed linear behavior indicates that either the O -atom contribution is insignificant or that it changes roughly linearly with increasing O_2 pressure. In either case, the rate constants for O_2 relaxation found from the slopes of these plots are a lower bound to the true values, inasmuch as both our kinetic modeling and NO_2 continuum measurements imply that the O -atom concentration can only decrease with increasing O_2 concentration. If the baseline is indeed constant, then these $k_{O_2}(v)$ are accurate. If the baseline were not constant but decreasing (due to O -atom decreases), then the rate constant would have to be re-evaluated upward. Obviously as the baseline contribution approaches zero, the rate constant tends to the previous upper bound estimate.

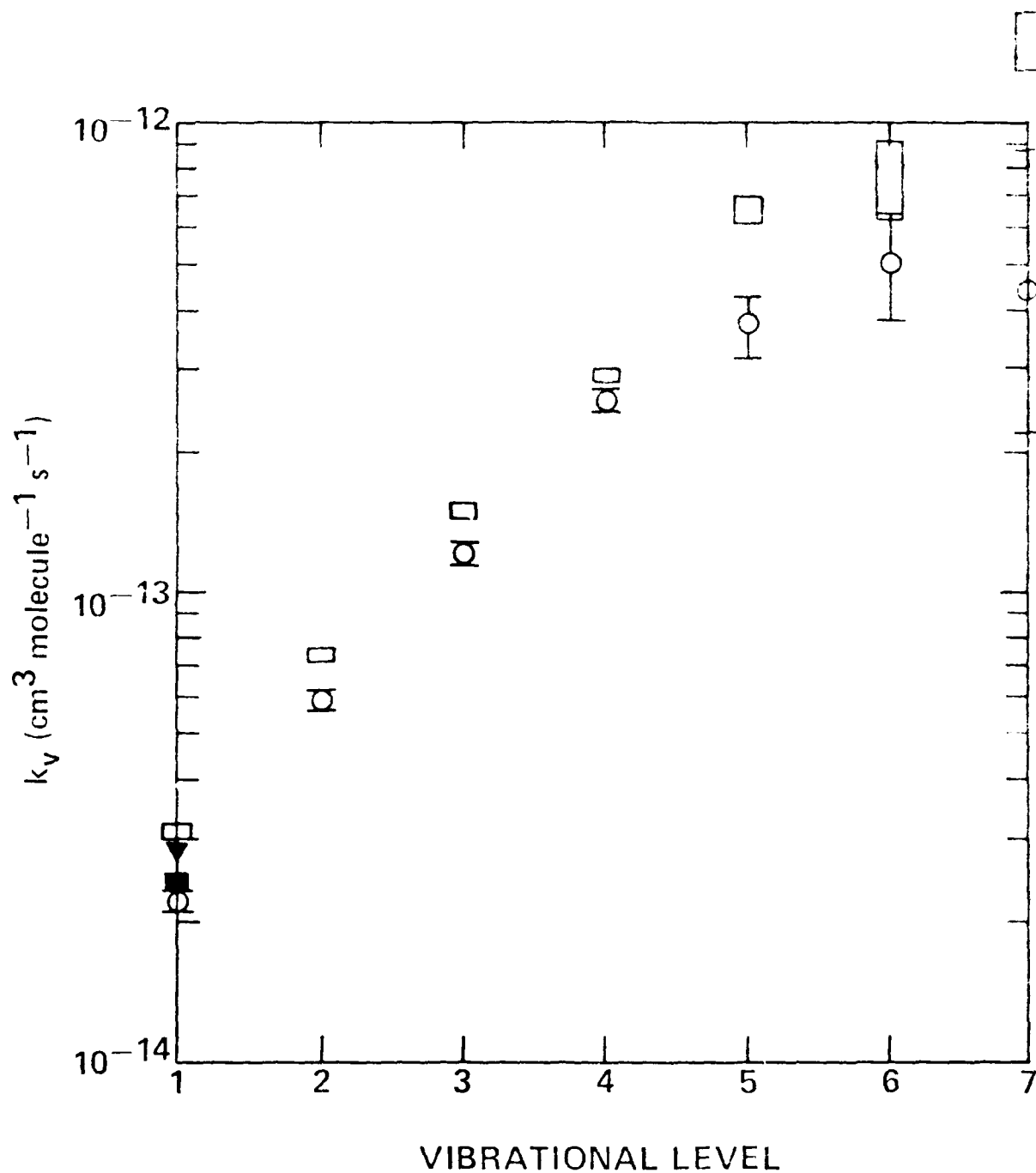
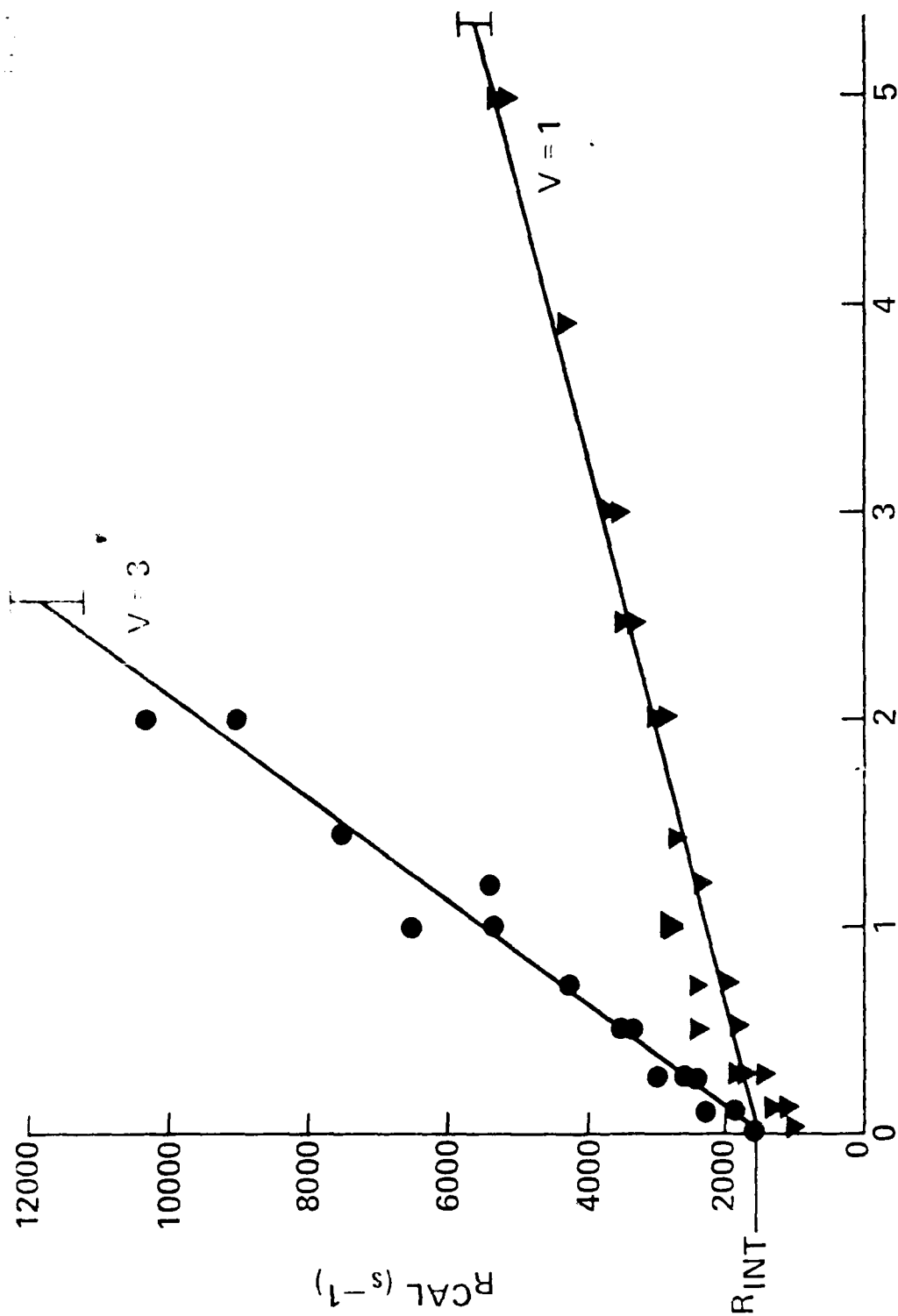


Fig. 5.4 Bounds on the relaxation rate constants for the reaction $\text{NO}(v) + \text{O}_2 \rightarrow \text{NO}(v-1) + \text{O}_2$ for $v = 1-7$. Upper bounds are from total decay rates; lower bounds from a Stern-Volmer analysis. The error bars reflect fitting uncertainties as propagated through the analysis.



OXYGEN CONCENTRATION (TORR)

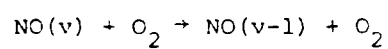
Figure 1. Relationship between R^{CAL} and oxygen concentration. The relationship appears to be linear with R_{INT} as the intercept. The slope of the line is $1.5 \times 10^3 s^{-1} torr^{-1}$.

Thus the actual $k_{O_2}(v)$ values are neatly bounded between limits set by the Stern-Volmer analysis and by considering O_2 to be the exclusive quenching partner of $NO(v)$. Both sets of bounds on the rate constants are plotted in Fig. 5.4 for $v=1-7$ and are also listed in Table 5.1. The bounds are typically separated by less than 40%. The previous measurements of $k_{O_2}(1)$ are also displayed in the figure, and the bounds of the present measurement nicely bracket the literature values.

The magnitude of the errors in the deduced rates can be estimated as the propagation of the uncertainties in the calculated populations. The populations of all levels have an uncertainty arising from fitting of the overlapped basis functions and from spectral noise. The uncertainty in each of the populations is generated as part of the least squares fitting process, and is found to have a typical standard deviation of less than 3% for the lowest four levels. The standard deviation rises to 7% for level 5 and is about 16% for levels 6 and 7. The calculated standard deviations of levels 8, 9 and 10 are 30%, 40%, and 70%, respectively, indicating that the populations of these levels are very poorly determined. In order to determine the effect of these errors on the deduced rates, R_m , random noise in a Gaussian distribution having standard deviation equal to the uncertainties in the populations, was added to the population values. Many sets of these modified population values were then used to deduce new R_m values and statistical trends observed. The changes in the calculated rates were observed to have a statistical standard deviation about the original values which was only slightly greater than the input noise level, i.e., little additional uncertainty was added through the integral R_m calculation.

The error bars displayed in Fig. 5.4 represent the uncertainties in the rates discussed above (for both bounds) and the uncertainties in the slopes of the Stern-Volmer plots (for the lower bound values) added as the square root of the sum of the squares. The upper bound estimates are felt to be very reliable, limited only by uncertainties in the observed relaxation rates. The lower bounds exhibit the additional uncertainty of the kinetic interpretation discussed above.

TABLE 5.1: Rate Constants for Processes



Vibrational Level	Rate Constant ($\text{cm}^3 \text{ molec}^{-1} \text{ s}^{-1}$) Lower Bound - Upper Bound*
1	2.2 - 3.1×10^{-14}
2	5.9 - 7.4×10^{-14}
3	1.2 - 1.5×10^{-13}
4	2.5 - 2.9×10^{-13}
5	3.7 - 6.5×10^{-13}
6	5.1 - 7.7×10^{-13}
7	4.4 - 1.5×10^{-13}

*Error bars on lower bounds shown in Fig. 5.4.

As a cross check on the data analysis, the calculated R_m values were used to predict vibrational population decay histories by means of Eq. (5.18). There was excellent agreement, which not only demonstrated the low error introduced by the integrated method of rate determination, but more importantly showed that the data can be adequately interpreted in terms of the single quantum collisional transfer reactions employed in the analysis. If the relaxation mechanism were different than assumed, the calculated rate constants need not have properly reproduced the population time histories.

The analysis presented above was developed under the assumption that only single quantum deactivation processes were important. While this assumption should be appropriate for deactivation by O_2 , theoretical arguments have been presented that the deactivation of $NO(v)$ by oxygen atoms proceeds preferentially by multi-quantum processes.^{5,24} Indeed, shock tube studies of $NO(v=1,2)$ relaxation by O-atoms at elevated temperatures have been interpreted in terms of a multi-quantum transfer. In order to gauge the potential importance of this effect the data analysis has been re-examined under the assumption that oxygen atoms completely deactivate $NO(v)$, i.e.:



The decay rates in this limit may be derived in a manner completely analogous to Eqs. (5.15)-(5.18), except that now the quantity $k_0(m)$ in the definition of R_m , Eq. (5.14), must be replaced by the expression:

$$\sum_{n=m}^N k_0(n) a_n / a_m(0) . \quad (5.21)$$

It can immediately be seen that this substitution will in no way compromise the "upper bound" evaluations of $k_{O_2}(v)$ which were deduced under the assumption that the oxygen atom concentration was zero. On the other hand, "lower bound" values could be affected inasmuch as a curvature could now be introduced into the Stern-Volmer plots even if the oxygen atom concentration was invariant, i.e., the ratios $a_n/a_{v,n>v}$, would be expected to vary somewhat with the O_2 concentration. This does not appear to be the case however, inasmuch as the latter correction would be largest for $v=1$ and yet it has been found that our evaluation for k_1 is in excellent agreement with previous studies.

In conclusion, although it clearly would have been useful to have an independent measurement of the oxygen atom concentration in this work, the analysis strongly suggests that the effects of oxygen atom deactivation have not distorted the present determinations of the rate constants for deactivation of $NO(v)$ by O_2 .

It is also of interest to examine the intercepts of the Stern-Volmer plots which represent the contributions of N_2 , O , and $A_{v \rightarrow v-1}$ relaxation at near zero O_2 concentrations. The intercepts are displayed in Fig. 5.6 for $v=1-7$. The error bars indicated contain contributions from the uncertainties in the rates and from the standard deviation of the intercepts from the least squares fits of the Stern-Volmer plots. The measured $k_{N_2}(1)[N_2]$ value and the theoretical NO Einstein coefficients are shown for comparison. At least for $v=1$, O -atoms are felt to represent the dominant additional quenching partner. Coupling the deduced intercept value with the rate constant measurement of Fernando and Smith,^{5,6} the O -atom concentration at low O_2 levels may be estimated to be $\leq 3 \times 10^{13}$ molecules/cm³. This value is in fair agreement with our model predictions which are based on neutral kinetics, electron energy deposition, and gas diffusion times. (If the O -atom quenching is multiquanta, then the estimated O -atom concentration would be 10^{13} molecules/cm³ in poorer agreement with the modeling.) If indeed O -atoms are responsible for the observed intercept relaxation rates, then the observed invariance with vibrational level could be interpreted as meaning that the magnitude of $k_O(v)$ is independent of vibrational level. Because the $v=1$ rate constant is already

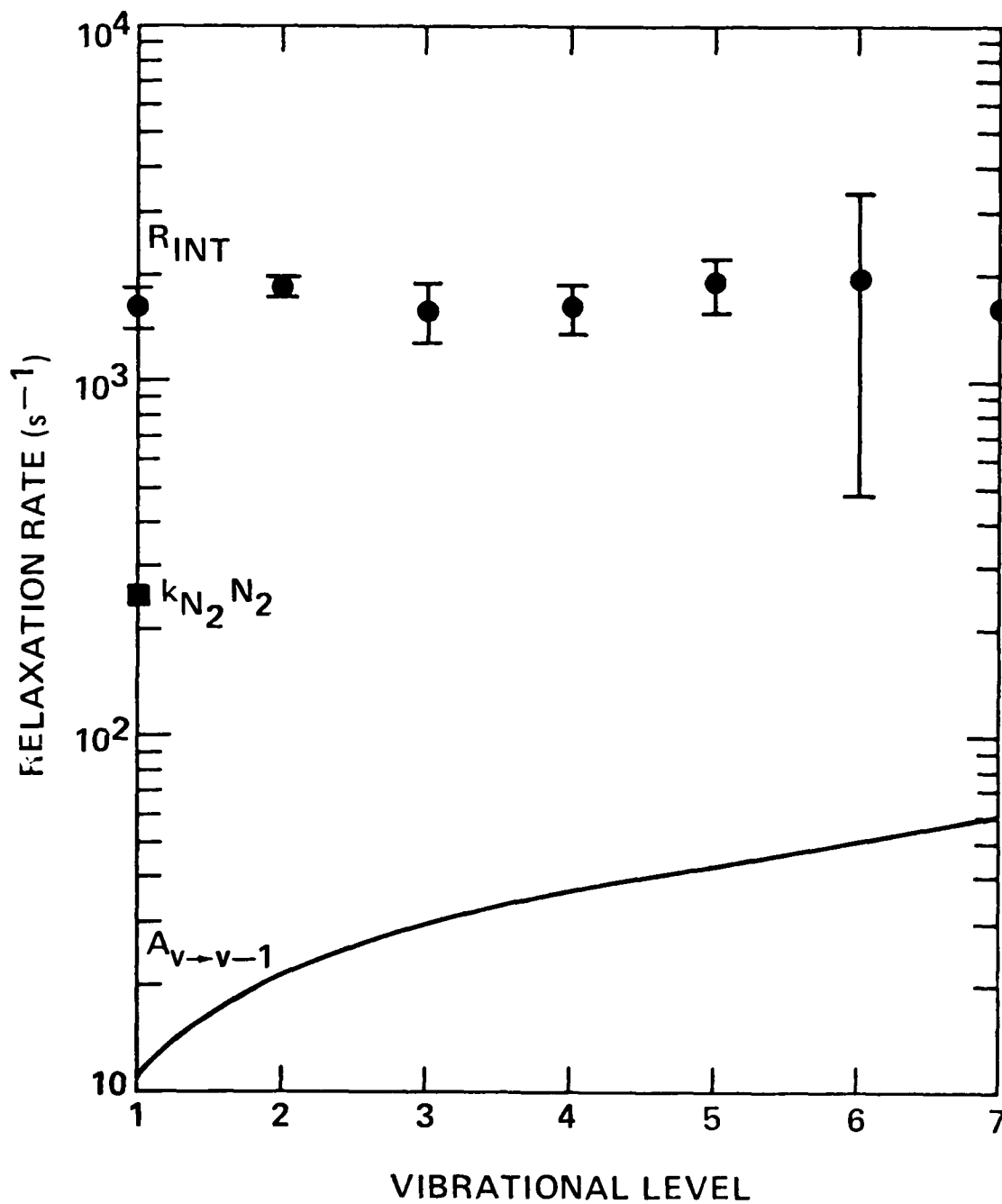


Fig. 5.6 Intercepts of Stern-Volmer plots with expected N_2 relaxation for $v = 1$ and radiative decay rates shown for comparison. It is felt that O-atom relaxation is responsible for the observed decays.

one-third gas kinetic it would not be surprising that these rate constants do not increase with vibrational level. Additionally, the rate constants $k_N(v)$ must scale as:

$$k_{N_2}(v) < vk_{N_2}(1)$$

or they would be larger than the observed intercept rates at the higher vibrational levels.

5.4 Global Kinetic Effects/Computer Modeling

As might be anticipated a large, chemically interactive, number of species can be formed when nitrogen/oxygen mixtures are irradiated by energetic electrons. For example, the species N_2^+ , O_2^+ , N^+ , O^+ , N , O and a number of electronically excited states, including the metastables $N_2(A)$ and $N(^2D, ^2P)$, can be formed directly in collisions between electrons and O_2/N_2 . These species can in turn undergo further reaction. Reactions between ionic species, including electron/ion recombination tend to be rapid and will occur primarily only when the beam is on. These reactions can produce other ionic species, such as NO^+ , as well as other neutral species. The neutral chemistry occurs on a longer time scale and can result in the production of additional species such as NO , NO_2 , NO_3 , N_2O and O_3 . Since the gas residence time is typically much longer than the characteristic time between pulses, the concentrations of these neutral species can build up over time to sizable levels. Indeed, these species concentrations could become sufficiently large so as to effect the fluorescence phenomena under study.

The operating conditions for the NO fluorescence experiments were specifically selected to provide a balance between the simultaneous generation of optimal signal and minimal beam-created species. Nonetheless, species such as N and O , are known to rapidly quench vibrationally excited NO by the reactions:



The room temperature rate constants for these reactions are measured to be $k_{22} \approx 6.5 \times 10^{-11} \text{ cm}^3/\text{s}^{5.6}$ for $v=1$ and $k_{23} \approx 3.4 \times 10^{-11} \text{ cm}^3/\text{s}^{5.25}$ for $v=0$ (anticipated to be the same for higher v). Since these rate constants are several orders of magnitude larger than that for quenching by O_2 , small concentrations of O and N can readily perturb the NO relaxation kinetics. A preliminary investigation of the importance of such effects is provided below.

As the energetic electrons traverse the N_2/O_2 gas mixture, the following global dissociation/ionization reactions will occur:



A number of electronically excited states may be created in a similar manner, indeed even in the dissociative paths shown in reactions (5.24) and (5.25). Ultimately all of the electron energy will be degraded through such collision processes.

In the present effort a computer model developed by Peterson et al.^{5.25} has been used to predict the ultimate allocation of electron energy among the various possible excitation processes. This code utilizes the detailed specification of the energy dependence of all relevant excitation cross-sections to calculate the electron energy degradation (including all contributions due to secondary electrons) in the continuous slowing down approximation. The excitation cross-sections used in these calculations have recently been reviewed by Jackman et al.^{5.27} These are relatively complete with 54 excitation processes included for N_2 and 33 for O_2 . Many of the excited states are Rydberg states, or states sufficiently high lying so that they have finite branching ratios for producing dissociation products. The branching ratios utilized to predict atomic species production rates have been discussed by Porter et al.^{5.28}

The computer model was exercised for a number of N_2/O_2 mixtures with the O_2 mole fraction being varied between 10^{-3} and 0.21 (air). The resulting predicted species production rates per ion pair created are shown in Fig. 5.7. As can be seen, over the full range of O_2 mole fraction studied, the dominant ion formed is N_2^+ , with the production rate for N^+ being a factor of ~ 3.7 lower. As might have been anticipated, the O_2^+ , O^+ production rates scale almost linearly with O_2 mole fraction, again with the molecular ion exhibiting the larger production rate. The production rate for nitrogen atoms is slightly more than one per ion pair, of which approximately half are formed in excited states.^{5.28} The predicted production rate for the $N_2(A^3\Sigma_u^+)$ state is also shown in Fig. 5.7. The characteristic value of this latter quantity is ~ 0.4 /electron and ion pair; this includes the effect of radiative cascade from any higher triplet states which are formed.

Perhaps the most interesting feature of Fig. 5.7 is the non-linear variation of the oxygen atom production rate with oxygen mole fraction. Oxygen atoms are produced in large part through excitation to the $O_2(A^3\Sigma_g^+)$ state and the cross-section for exciting this state tends to peak in an electron energy region where there are no dominant competing loss mechanisms in nitrogen. Thus, since the electron energies cascade quasi-continuously from their initial energies to thermal, an energy "window" exists for oxygen atom

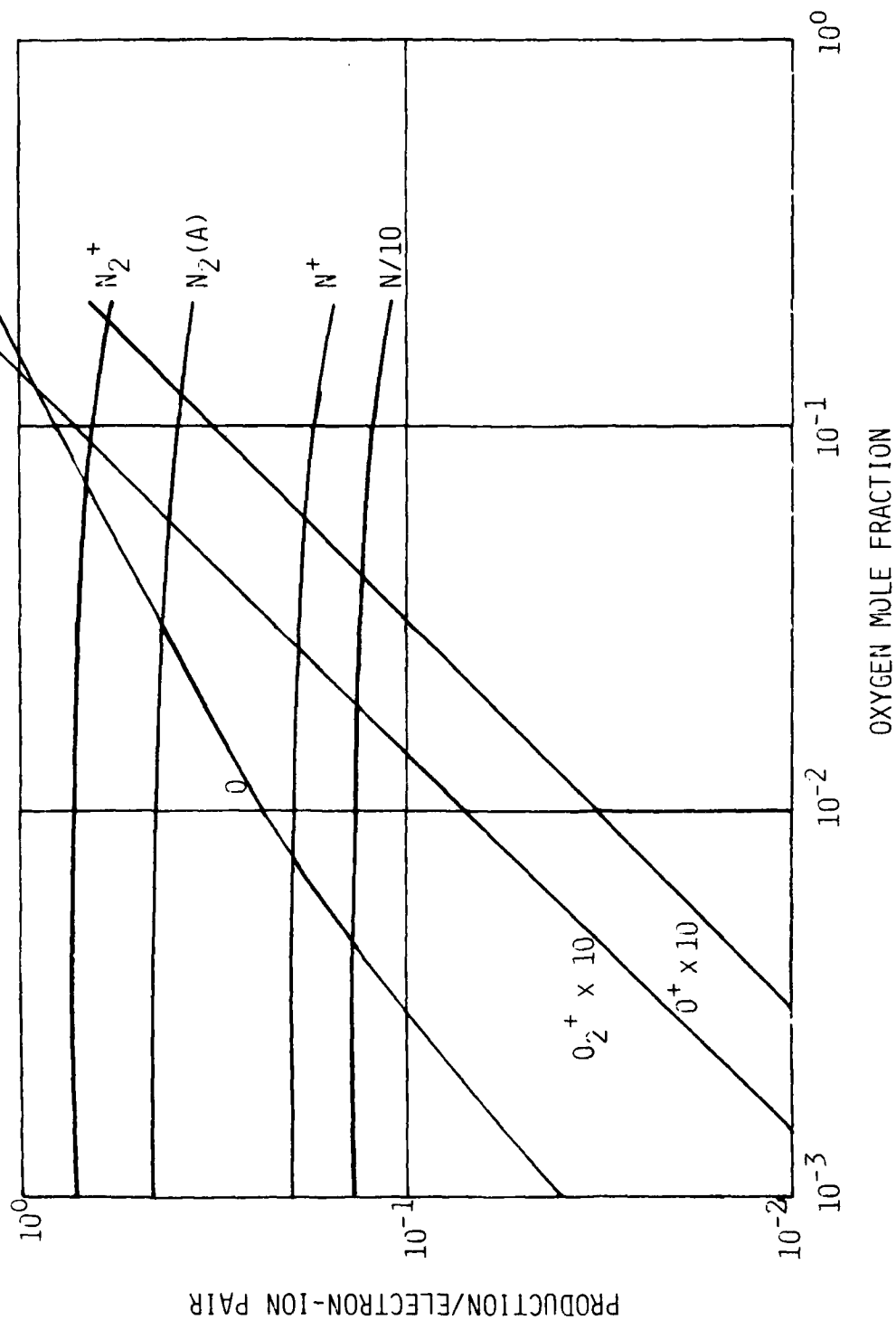


Fig. 5.7 Predicted relative production/electron-ion pair of N_2^+ , $N_2(A)$, N^+ , N , O_2^+ , O^+ , O for various O_2/N_2 mixtures.

production which is only weakly dependent on the oxygen mole fraction. Note that oxygen atom production is relatively efficient; indeed, at air stoichiometry the oxygen and nitrogen atom production rates are nearly equal.

Given the production rates of Fig. 5.7, the next issue to be addressed is the fate of the ionic species created by the beam. The positive ions will ultimately recombine with electrons, however, at the pressures and electron densities of interest in this work a number of ion-neutral reactions will occur prior to recombination. These reactions act primarily to situate the positive charge in that species exhibiting the lowest ionization potential. In the case of unperturbed N_2/O_2 mixtures the apparent dominant ion becomes O_2^+ , through reactions such as:



which have rate constants of 4×10^{-11} , 2.4×10^{-11} and 6×10^{-10} cm^3/s , respectively.^{5,29} The true situation is more complicated, however, in that NO has a lower ionization potential than O_2 . Thus, if there is a sufficient buildup in NO concentration, the reaction:



$k = 4.4 \times 10^{-10}$ cm^3/s ,^{5,29} could occur prior to dissociative recombination of O_2^+ , i.e.,



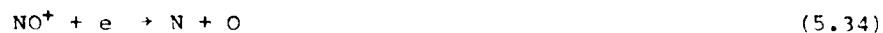
$k_{30} = 1.9 \times 10^{-7} \text{ cm}^3/\text{s}$ for thermal electrons.^{5.30} Note that reaction (5.20) will dominate (5.30) when the ratio NO/e exceeds 500. NO^+ can also be formed by reactions such as:



which have rate constants of 1.2×10^{-10} and $1 \times 10^{-12} \text{ cm}^3/\text{s}$, respectively.^{5.29} Indeed, reaction (5.28) has another potential branch:



which could also form NO^+ . If NO^+ is formed it will recombine via:



with a rate constant of $3.9 \times 10^{-7} \text{ cm}^3/\text{s}$ for the thermal electrons.^{5.30}

The specification of the dominant terminal ion is particularly important in defining the production rate of atomic species. For example, if O_2^+ dominates there will be at least two oxygen atoms produced per electron-ion pair. On the other hand, if NO^+ dominates the O-atom production rate due

to ionic chemistry is reduced to one per electron-ion pair and more importantly ~76% of the nitrogen atoms produced in reaction (5.34) will be formed in the $N(^2D)$ state,^{5.31} which is the precursor for vibrationally NO via:



It can readily be shown for the present experiments that the ionic concentrations are only appreciable while the beam is on; typical ion decay times upon beam termination are ~0.1 ms. Therefore, the primary effect of the beam is to provide a source of ground and excited state nitrogen and oxygen atoms. These atomic species will then react, producing other species, all of which can build up in concentration from pulse to pulse. A kinetic model has been assembled to describe this chemistry and is shown in Table 5.2. The rate constants for the reactions listed have been compiled for the most part through an examination of several recent review articles.^{5.32-5.34} The rate constants for reaction R14 is controversial,^{5.34} and the lower bound has been used in the present work. The symbol N^* refers to the $N(^2D)$ state and the quenching rate constants used for N_2 and O_2 are taken from Refs. 5.9 and 5.11, respectively. Vibrationally excited NO, designated as NO^* , has been included in a qualitative manner. For simplicity it is assumed that the neutral chemistry of NO^* is the same as that for ground state NO. Furthermore, the NO created by reaction R23 is taken to be formed only in $v=1$ and to be quenched only by O_2 and N_2 , with rate constants as determined by Murphy et al.^{5.1}

This kinetic scheme has been used in a computer model to provide a simulation of the buildup of beam-created species. An important input to this model is the local electron-ion pair creation rate within the field of view. At any distance L , downstream of the beam this quantity can be defined by:

TABLE 5.2

NEUTRAL CHEMISTRY FOR N_2/O_2 MIXTURES

	Reaction	Rate Constant (cm^3/s or cm^6/s)
R1	$O + O + N_2 \leftrightarrow O_2 + N_2$	$1.44 \times 10^{-30}/T$
R2	$O + O + O_2 \leftrightarrow O_2 + O_2$	$2.16 \times 10^{-30}/T$
R3	$O + O_2 + M \leftrightarrow O_3 + M$	$1.1 \times 10^{-34} e^{510/T}$
R4	$O + O_3 \leftrightarrow O_2 + O_2$	$1.5 \times 10^{-11} e^{-2218/T}$
R5	$O + N + M \leftrightarrow NO + M$	$1.8 \times 10^{-31}/T^{1/2}$
R6	$N + O_2 \leftrightarrow NO + O$	$4.4 \times 10^{-12} e^{-3220/T}$
R7	$O + NO + N_2 \leftrightarrow NO_2 + N_2$	$4.2 \times 10^{-33} e^{940/T}$
R8	$O + NO + O_2 \leftrightarrow NO_2 + O_2$	$3.0 \times 10^{-33} e^{940/T}$
R9	$C + NO^* + N_2 \leftrightarrow NO_2 + N_2$	$4.2 \times 10^{-33} e^{940/T}$
R10	$O + NO^* + O_2 \leftrightarrow NO_2 + O_2$	$3.0 \times 10^{-33} e^{940/T}$
R11	$O + NO_2 \leftrightarrow NO + O_2$	9.3×10^{-12}
R12	$O + NO_2 + M \leftrightarrow NO_3 + M$	1.0×10^{-31}
R13	$O + NO_3 \leftrightarrow NO_2 + O_2$	1.0×10^{-11}
R14	$N + O_3 \leftrightarrow NO + O_2$	1.0×10^{-15}
R15	$NO + O_3 \leftrightarrow NO_2 + O_2$	$2.3 \times 10^{-12} e^{-1450/T}$
R16	$NO^* + O_3 \leftrightarrow NO_2 + O_2$	$2.3 \times 10^{-12} e^{-1450/T}$
R17	$NO_2 + O_3 \leftrightarrow NO_3 + O_2$	$1.2 \times 10^{-13} e^{-2450/T}$
R18	$N + N + M \leftrightarrow N_2 + M$	$8.3 \times 10^{-34} e^{500/T}$
R19	$N + NO \leftrightarrow N_2 + O$	3.4×10^{-11}
R20	$N + NO^* \leftrightarrow N_2 + O$	3.4×10^{-11}
R21	$N + NO_2 \leftrightarrow N_2O + O$	$2.1 \times 10^{-11} e^{-800/T}$
R22	$NO + NO_3 \leftrightarrow NO_2 + NO_2$	8.7×10^{-12}
R23	$N^* + O_2 \leftrightarrow NO^* + O$	5.2×10^{-12}
R24	$N^* + N_2 \leftrightarrow N + N_2$	$1. \times 10^{-13} e^{-500/T}$
R25	$NO^* + O_2 \leftrightarrow NO + O_2$	2.4×10^{-14}
R26	$NO^* + N_2 \leftrightarrow NO + N_2$	1.7×10^{-16}

$$\dot{x}^+ = \frac{i \left(\frac{1}{\rho} \frac{dE}{dX} \right) \rho L}{2 e w \pi r_{1/2}^2} \quad (5.36)$$

where i is the beam current, ρ is gas density, e is the electronic charge, w is the energy required to create an electronic-ion pair, 34.4 eV in nitrogen,^{5.35} $r_{1/2}$ is the beam radius at position L which encompasses one-half of the beam current, and $1/\rho \, dE/dX$ is the local beam energy deposition rate.

This latter quantity is a function of the product ρL and is dependent upon both the identity of the gas traversed and the initial electron energy. The electron energy deposition for 36 keV electrons traversing N_2 has been evaluated using the ELTRAN Monte Carlo model^{5.36} and the results are shown in Fig. 5.8. Shown for comparison is the quantity $\rho^{-1} \, dE/ds$ taken from the Berger and Seltzer Tables.^{5.37} The quantity s refers to electron path distance and since the electrons do not travel in straight lines, the ELTRAN predictions should be the larger.

The beam half radius has been evaluated using the work of Center.^{5.38} It was shown in this study that, in a "thin" target gas, beam size grows as:

$$r_{1/2} = L \tan \frac{A(NL)^{3/2}}{1 + BNL} \quad (5.37)$$

where N is gas number density and the quantities A and B are specific to the gas target and electron energy. For 36 keV electrons traversing nitrogen, an interpolation of Center's measurements provides $A = 1.22 \times 10^{-28} \, \text{cm}^3$ and $B = 1.56 \times 10^{-18} \, \text{cm}^2$.

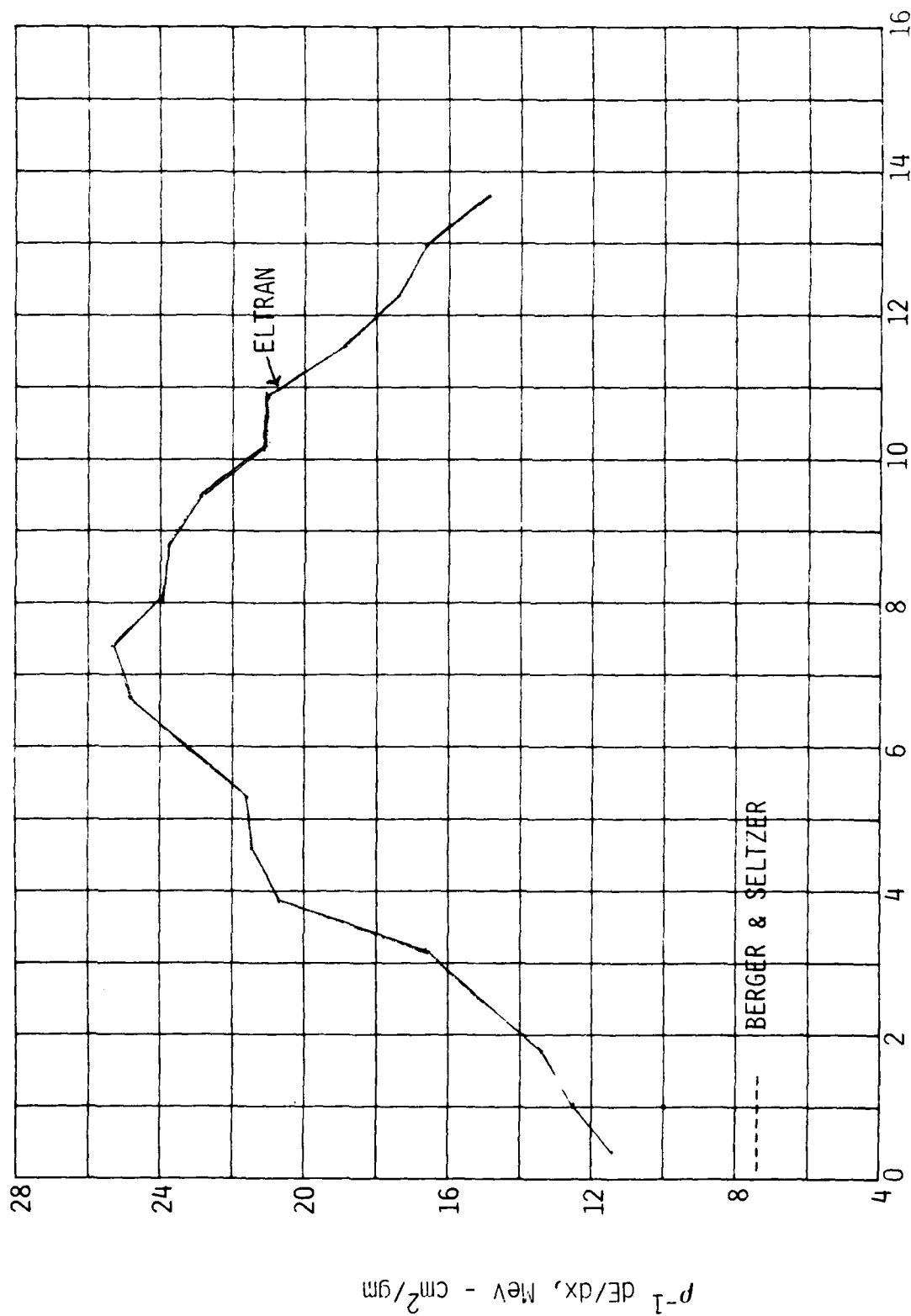


Fig. 5.8 Monte Carlo prediction of electron energy deposition in nitrogen. Initial electron energy is 36 keV.

Equation (5.36) has been evaluated for various pressures and distances using the above two results. It is to be recalled that the field of view is approximately circular, spanning the distance between 4 to 12 cm downstream of the beam entrance. Typical predictions for the local ion pair production rate at several positions within the field of view are shown in Fig. 5.9, a representative beam current of 1 mA was used in this evaluation. One of the more interesting features of this figure is that the ion pair production rate is only weakly dependent on pressure for the conditions considered. Note, however, that there is a significant variation of \dot{x}^+ with position within the field of view. This directly reflects the increase in beam radius with distance downstream. For example, at 50 torr $r_{1/2} = 1.06, 2.22$ and 3.67 cm at $L = 5, 8$ and 11 cm, respectively.

The predictions of Fig. 5.9 may be used in conjunction with previously discussed kinetic considerations to specify the production rates for atomic species in the chemistry calculations. Computer predictions have been provided for a position in the center of the field of view at a nitrogen pressure of 50 torr and at oxygen pressures of 0.2, 0.5 and 2.0 torr. Beam current was taken to be 1 mA, with a pulsing cycle of 1 ms on and 19 ms off. Only neutral chemistry was included in the calculation; from consideration of Fig. 5.7 and the ionic chemistry for pure N_2/O_2 , the relative atom production rates per ion pair of O, $N(^4S)$ and $N(^2D)$ were taken as 2, 0.65 and 0.65, respectively.

The computer model used was of the stream-tube type; therefore, the calculations were carried out only for pulsing sequences where diffusive loss out of the beam did not dominate, i.e., once the beam created species diffuse out of the beam they can no longer affect the NO relaxation kinetics. Characteristic diffusion times were estimated by considering the beam to be a cylinder of radius a , initially having a finite concentration of atoms internally and none externally. It can be shown^{5.39} that, if diffusion is the only loss, the fraction of atoms remaining in the cylinder after time t is:

$$f = \sum_{n=1}^{\infty} \frac{4}{a^2 \alpha_n^2} e^{-D\alpha_n^2 t} \quad (5.38)$$

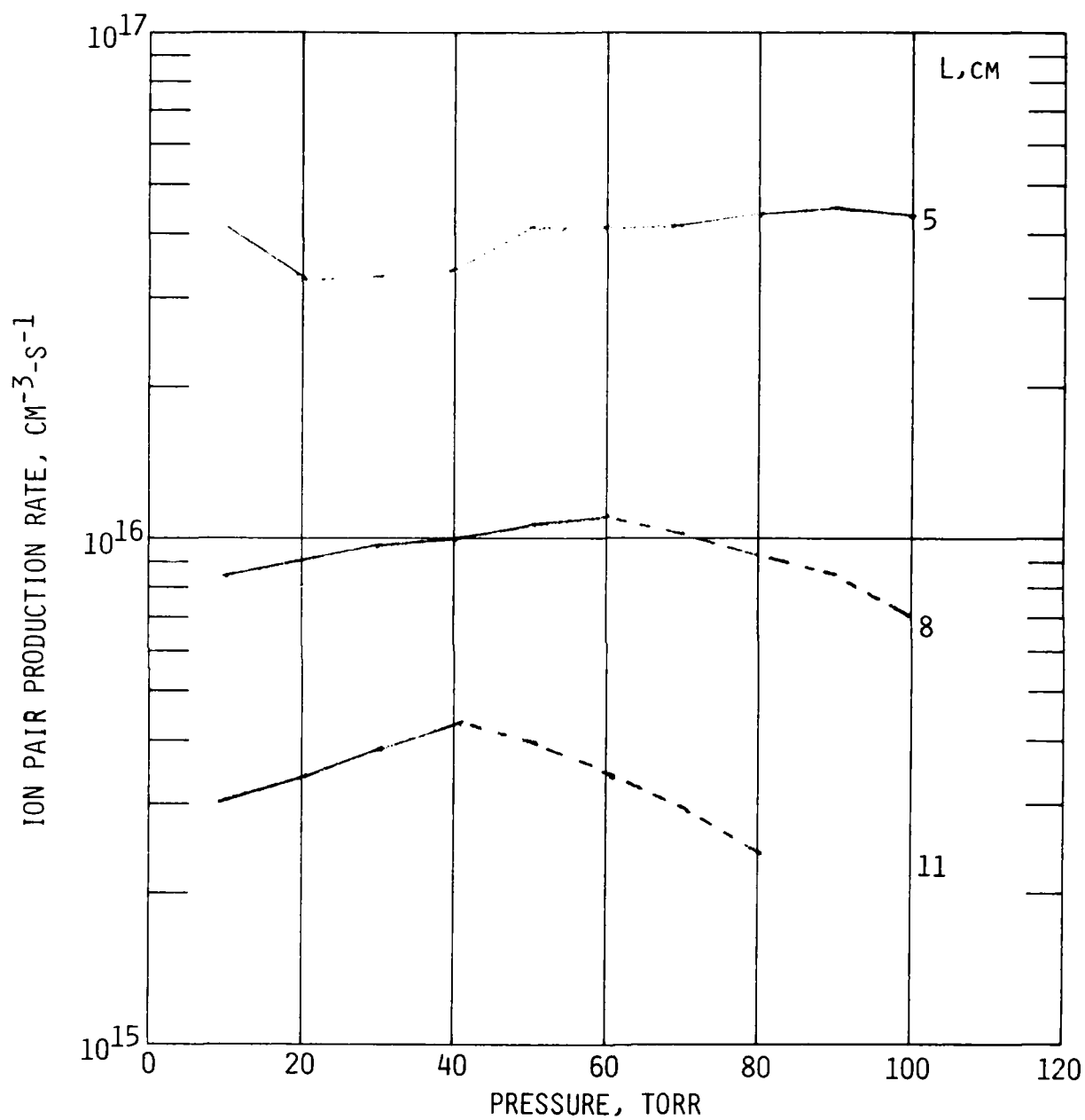


Fig. 5.9 Predicted electron-ion pair production rate vs. pressure for several distances downstream. 36 keV electrons into N₂ at 293 K, $i = 1\text{mA}$. Dashed lines indicate where "thin" target approximation breaks down.

where D is the diffusion coefficient, taken as $270 \text{ cm}^2/\text{s-torr}$ for oxygen atoms,^{5.40} and the α_n 's are defined through the zeros of the zeroth order Bessel function, i.e., from the relationship:

$$J_0(a\alpha_n) = 0 . \quad (5.39)$$

Equation (5.38) has been evaluated for a pressure of 50 torr and a radius of 2.2 cm (corresponding to the center of the field of view) and the results are shown in Fig. 5.10. As can be seen for these conditions, the atomic concentration in the beam falls rapidly within a fraction of a second. For example, after ten pulses (0.2s) less than 20% of the atomic species created by the first pulse will remain within the beam. Although it would take "infinite time" for the atomic species to totally diffuse out of the beam it seems that a duration of 10 pulses is a reasonable choice for defining the diffusion limited domain. For example, the results of Fig. 5.10 can be used to show that the total accumulation of atomic species within the beam after 20 pulses would be less than 20% larger than that after 10 pulses (note again, this neglects the effects of chemical reaction which would further reduce the atomic concentrations).

For this reason, the computer predictions were only carried out for a sequence of 10 pulses. Note that all considerations so far have been for the center of the field of view. At shorter (longer) distances from the beam entrance, the atom production rates are higher (lower) because the beam size is smaller (larger), however, in this instance, diffusion out of the beam will be more rapid (less rapid) and thus the potential variations in concentrations of beam produced species across the field of view will be ameliorated by the diffusion process.

The basic output of the computer predictions are the time histories of the 11 neutral species modeled. A typical result is shown in Fig. 5.11 for the case of $\text{PO}_2 = 0.2 \text{ torr}$. The predicted mole fractions of neutral species

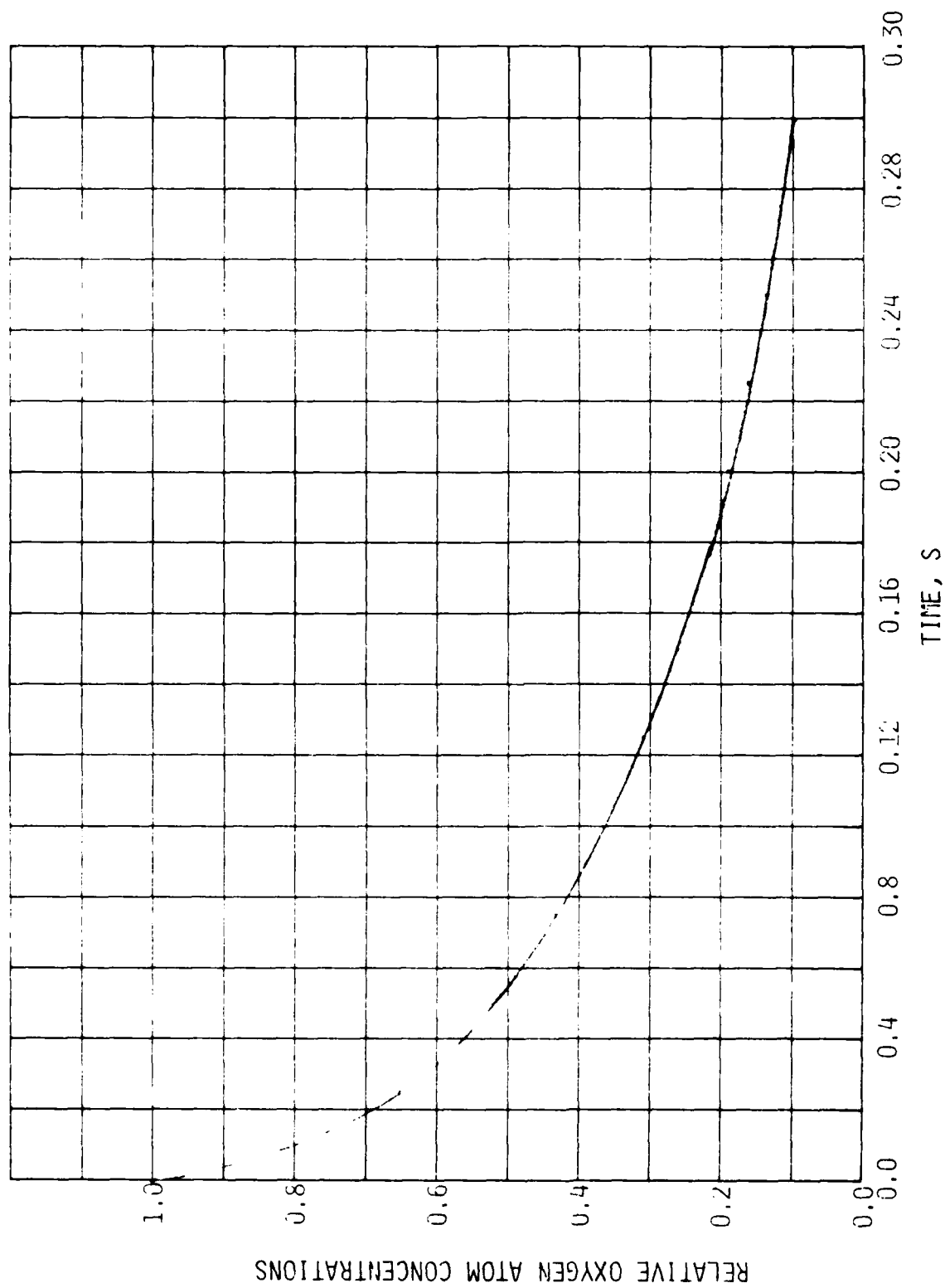


Fig. 5.10 Fraction of oxygen atoms which have not diffused out of a cylinder of radius 2.2 cm. $P = 50$ torr.

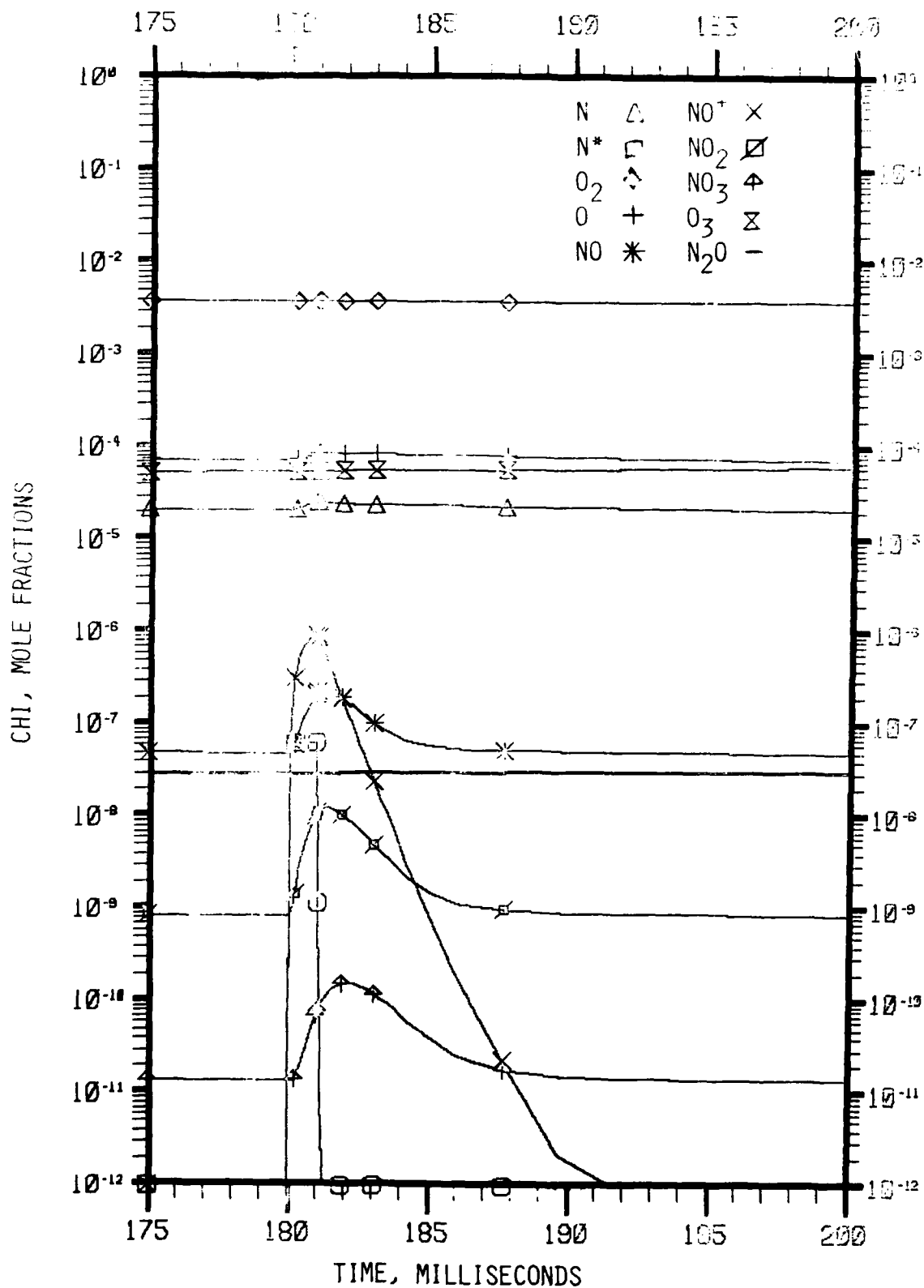


Fig. 5.11 Predicted species mole fraction vs. time for the tenth pulse. $P_{O_2} = 0.2$ torr, $P_{N_2} = 50$ torr, $I = 1$ mA, $L = 8$ cm.

are displayed over a time span corresponding to slightly before the tenth pulse to just prior to the eleventh pulse. As can be seen in this case, many of the species have not yet reached near steady concentrations. The $N(^2D)$ concentration reflects the pulse shape, while the characteristic decay of vibrationally excited NO is of the order of the pulse time. Species such as N, NO and O tend to increase while the beam is on and then decay only slightly, while NO_2 and NO_3 vary considerably over the pulse sequence and N_2O and O_3 steadily, but slowly rise. This latter observation reflects the lack of efficient destruction mechanisms for O_3 and N_2O (recall the uncertainty in R14, however). Note the dynamic range of the mole fractions plotted in Fig. 5.11. Many of these species are predicted to have concentrations well below anticipated gas purity levels. Nonetheless, species such as N, O, NO and O_3 may be present in sufficient quantities to affect either the ionic kinetics or the NO^+ vibrational relaxation and these issues must be investigated further.

Similar results have been obtained at higher O_2 pressures although, in these cases, the neutral chemistry has more completely reached steady state after 10 pulses. This is demonstrated in Fig. 5.12 where the nitrogen and oxygen atom concentrations just prior to (next) pulse initiation are plotted as a function of time for all three cases. As can be seen, the predicted atomic concentrations decrease with increasing oxygen pressure. The predictions for $PO_2 = 2$ torr clearly asymptote within a few pulses and thus, in this instance, the neglect of diffusive losses will be relatively unimportant. On the other hand, it can be seen that the cases corresponding to lower oxygen pressures have not asymptoted within 10 pulses and thus these results are most probably upper bounds. Note the oxygen atom concentrations tend to be significantly larger than those for nitrogen atoms. This is a result both of the higher creation rate of the former and the fact that the available binary reactions which can destroy nitrogen atoms also form oxygen atoms.

It must be noted that these predicted atomic concentrations are at significant levels. At an oxygen pressure of 2 torr vibrational relaxation of NO by O_2 , will dominate the atomic deactivation/destruction reactions:

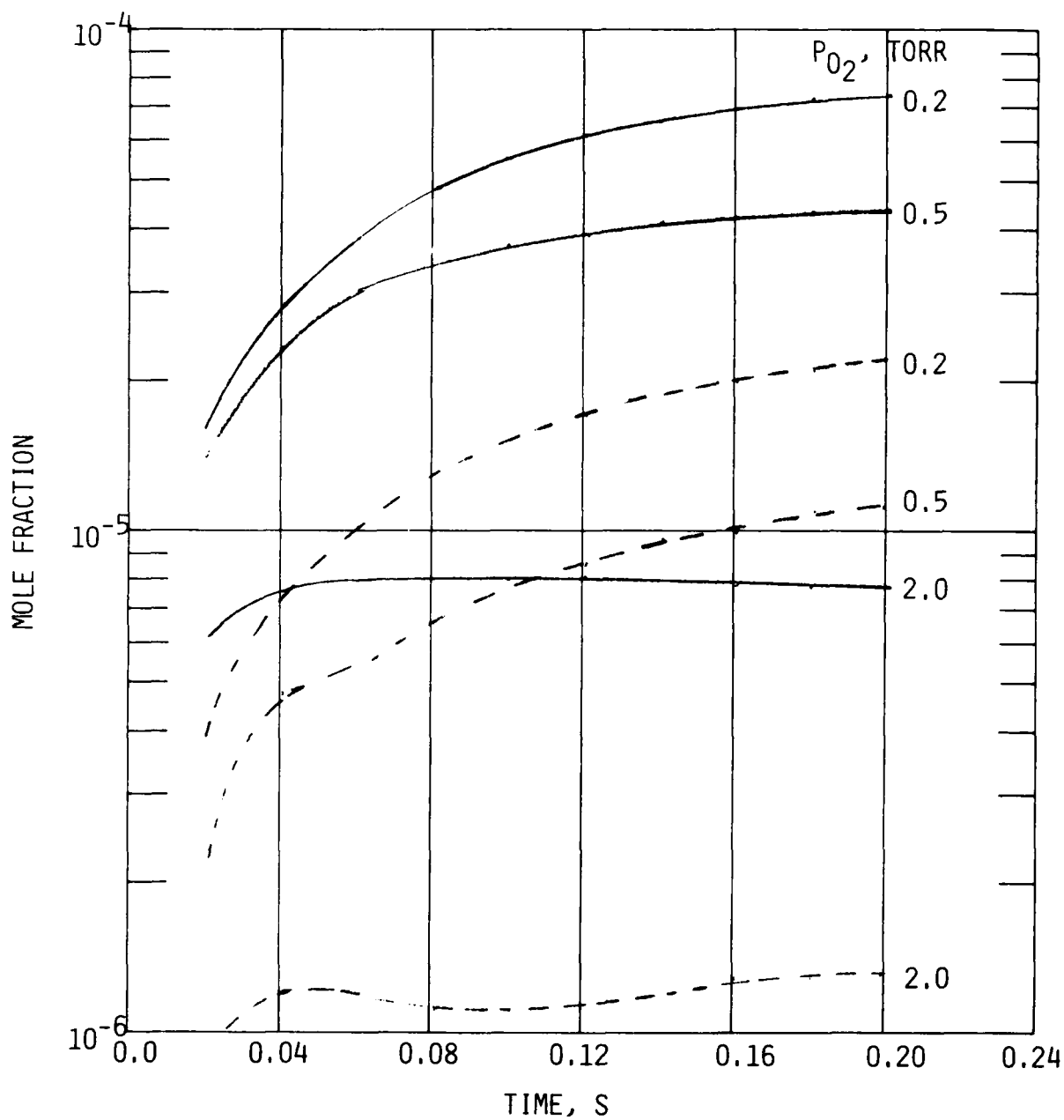


Fig. 5.12 Predicted mole fraction vs. time —, $[O]$; -.- $[N]$. $P_{N_2} = 50$ torr, $i = 1$ mA, pulse on 1 ms off 19 ms. Values shown correspond to just prior to pulse onset.



however, at the lower oxygen pressures the reverse will be true. Furthermore, the fact that the atomic concentrations could vary with oxygen pressure may well invalidate the use of the Stern-Volmer method for deducing kinetic information. There are complications in the analysis, however, particularly in the handling of diffusive effects, and in the neglect of including trace species in assessing the positive ion kinetics. It is clear, however, that supplementary measurements of O/N concentrations in LABCEDE would have been very valuable for assisting in the interpretation of the NO vibrational relaxation data base.

5.5 Summary

Nitric oxide was created in electron irradiated mixtures of N_2 /trace O_2 . The NO is created vibrationally excited at least in part by the reaction between $\text{N}(^2\text{D}) + \text{O}_2$. Time resolved Fourier spectroscopy is used to monitor the spectrally resolved infrared fluorescence. Vibrational distributions during and after the electron beam pulse were determined by spectral fitting of the fluorescence data. These populations were then used to calculate relaxation rates for each vibrational level. Because of reaction zone geometry, the gas in the observation volume is irradiated by more than one pulse and beam created species may occur in sufficient concentrations to affect the kinetics. Computer modeling and visible NO afterglow measurements support the conclusion that quenching by atomic and molecular oxygen are the dominant relaxation mechanisms. The rate constants for relaxation of $\text{NO}(v=1-7)$ by O_2 have been measured using total decay and Stern-Volmer analyses. They are observed to scale roughly as v^2 from a $v=1$ rate constant of $2.6 \pm 0.5 \times 10^{-14} \text{ cm}^3/\text{s}$. This quenching occurs via single quantum transitions. Additionally, measurements at low O_2 concentrations may be interpreted to provide bounds on the vibrational level dependence of the rate constants for quenching of $\text{NO}(v)$ by O and N_2 .

REFERENCES

- 5.1 R. E. Murphy, E. T. P. Lee, and A. M. Hart, "Quenching of Vibrationally Excited Nitric Oxide by Molecular Oxygen and Nitrogen," J. Chem. Phys. 63 (7), 2919 (1975).
- 5.2 J. C. Stephenson and S. M. Freund, "Infrared Laser-Enhanced Reactions: Chemistry of NO(v=1) With O₃," J. Chem. Phys. 65, 4303 (1976).
- 5.3 J. Kosanetsky, U. List, W. Urban, H. Vormann, and E. H. Fink, "Vibrational Relaxation of NO(v=1) Studied by an IR-UV-Double Resonance Technique," Chem. Phys. 50, 361 (1980).
- 5.4 R. P. Fernando and I. W. M. Smith, "Relaxation of NO(v=1) by Radical Species," J. Chem. Soc. Farad, Trans. II 77, 459 (1981).
- 5.5 J. C. Stephenson, "Vibrational Energy Transfer in NO*," J. Chem. Phys. 59, 1523 (1973).
- 5.6 R. P. Fernando and I. W. M. Smith, "Vibrational Relaxation of NO by Atomic Oxygen," Chem. Phys. Lett. 66 (2), 218 (1979).
- 5.7 M. E. Whitson, Jr., L. A. Darnton, and R. J. McNeal, "Vibrational Energy Distribution in the NO Produced by the Reaction of N(⁴S) with O₂," Chem. Phys. Lett. 41 (3), 552 (1976).
- 5.8 D. L. Baulch, D. D. Drysdale, D. G. Horne, and A. C. Lloyd, Evaluated Kinetic Data for High Temperature Reactions. II. Homogeneous Gas Phase Reactions of the H₂-N₂-O₂ System, (Butterworths, London, 1973).
- 5.9 G. T. Black, T. G. Slanger, G. A. St. John, and R. A. Young, "Vacuum UV Photolysis of N₂O. IV. Deactivation of N(²D)," J. Chem. Phys. 51, 116 (1969).
- 5.10 C. L. Lin and F. Kaufman, "Reactions of Metastable Nitrogen Atoms," J. Chem. Phys. 55, 3760 (1971).

REFERENCES (Cont.)

- 5.11 D. Husain, S. K. Mitra and A. N. Young, "Kinetic Study of Electronically Excited Nitrogen Atoms $N(2^2D_J, 2^2P_J)$, by Attenuation of Atomic Resonance Radiation in the Vacuum Ultra-Violet," J. Chem. Soc. Farad. Trans. II 70, 1721 (1974).
- 5.12 A. Rahbee and J. J. Gibson, "Rate Constants for Formation of NO in Vibrational Levels $v=2-7$ from the Reaction $N(^4S)+O_2+NO^*+O$," J. Chem. Phys. 74, 5143 (1981). See Also F. Hushfar, J. W. Rogers and A. T. Stair, "Infrared Chemiluminescence of the Reaction $N+O_2+NO+O$," Appl. Opt. 10, 1843 (1971).
- 5.13 J. P. Kennealy, F. P. DelGreco, G. E. Caledonia, and B. D. Green, "Nitric Oxide Chemi-excitation Occurring in the Reaction Between Metastable Nitrogen Atoms and Oxygen Molecules," J. Chem. Phys. 69 (4) 1574 (1978).
- 5.14 G. E. Caledonia, B. D. Green, and R. E. Murphy, "A Study of the Vibrational Level Dependent Quenching of $CO(v=1-16)$ by CO_2 ," J. Chem. Phys. 71 (11) 4369 (1979).
- 5.15 R. E. Murphy, F. H. Cook, G. E. Caledonia, and B. D. Green, "Infrared Fluorescence of Electron Irradiated CO_2 in the Presence of N_2 , Ar, and He," Air Force Geophysics Laboratory TR-77-0205, Environmental Research Papers, No. 609 (15 Sept. 1977).
- 5.16 R. E. Murphy, F. H. Cook, and H. Sakai, "Time-Resolved Fourier Spectroscopy," J. Opt. Soc. Amer. 65, 600 (1975).
- 5.17 A. Goldman and S. C. Schmidt, "Infrared Spectral Line Parameters and Absorptance Calculations of NO at Atmospheric and Elevated Temperatures for the $\Delta v=1$ Bands Region," J. Quant. Spect. Radiat. Transfer 15, 127 (1975).

REFERENCES (Cont.)

- 5.18 F. P. Billingsley, "Calculated Vibration-Rotation Intensities for $\text{NO}(X^2\Pi)$," J. Molec. Spect. 61, 53 (1976).
- 5.19 D. L. Baulch, R. A. Cox, R. F. Hampson, Jr., J. A. Kerr, J. Troe, and R. T. Watson, "Evaluated Kinetic and Photochemical Data for Atmospheric Chemistry," J. Phys. Chem. Reference Data 9 (2), 295 (1980).
- 5.20 M. Vanpee, K. D. Hill, and W. R. Kinneyko, "Absolute Rate Constant Measurements for the Radiative Combination of Atomic Oxygen with Nitric Oxide," AIAA J. 9 (1) 135 (1971).
- 5.21 A. Fontijn, C. B. Meyer, and H. I. Schiff, "Absolute Quantum Yield Measurements of the NO-O Reaction and Its Use as a Standard for Chemiluminescence Reactions," J. Chem. Phys. 40 (1) 65 (1964).
- 5.22 M. Sutoh, Y. Morioka, M. Nakamura, "Absolute Rate Constant for the Chemiluminescent Reaction of Atomic Oxygen with Nitric Oxide," J. Chem. Phys. 72 (1) 20 (1980).
- 5.23 H. Horiguchi and S. Tsuchiya, "Vibrational Relaxation of $\text{NO}(X^2\Pi)$ in the States of $v=2-10$," Japanese J. Appl. Phys. 18 (7), 1207 (1979).
- 5.24 M. Quack and J. Troe, "Complex Formation in Reactive and Inelastic Scattering: Statistical Adiabatic Channel Model of Unimolecular Processes III," Ber. Bunsenges. Physik. Chem. 79, 170 (1975).
- 5.25 J. H. Lee, J. V. Michael, W. A. Payne and L. J. Stief, "Absolute Rate of the Reaction of $\text{N}(^4\text{S})$ with NO from 196-400 K with DF-RF and FP-RF Techniques," J. Chem. Phys. 69, 3069 (1978).
- 5.26 L. R. Peterson, . Sawada, J. N. Bass and A. E. S. Green, "Electron Energy Deposition in a Gaseous Mixture," Comp. Phys. Comm. 5, 239 (1973).

- 5.27 C. H. Jackman, R. H. Garvey and A. E. S. Green, "Electron Impact on Atmospheric Gases I. Updated Cross-Sections," J. Geophys. Res. 82, 5901 (1977).
- 5.28 H. S. Porter, C. H. Jackman, and A. E. S. Green, "Efficiencies for Production of Atomic Nitrogen and Oxygen by Relativistic Proton Impact in Air," J. Chem. Phys. 65, 154 (1976).
- 5.29 D. I. Albritton, "Ion-Neutral Reaction Rate Constants Measured in Flow Reactors Through 1977," Atomic Data and Nuclear Data Tables 42, 1 (1978).
- 5.30 M. R. Mahdavi, J. B. Hasted, and M. M. Nakshbandi, "Electron-Ion Recombination Measurements in the Flowing Afterglow," J. Phys. B: Atom Molec. Phys. 4, 1726 (1971).
- 5.31 D. Kley, G. M. Lawrence and E. J. Stone, "The Yield of $N(^2D)$ Atoms in the Dissociative Recombination of NO^+ ," J. Chem. Phys. 66, 4157 (1977).
- 5.32 L. G. Anderson, "Atmospheric Chemical Kinetics Data Survey," Rev. Geophys. and Spa. Phys. 14, 151 (1976).
- 5.33 R. F. Hampson, Jr. and D. Garvin, eds. "Chemical Kinetic and Photochemical Data for Modeling Atmospheric Chemistry," NBS Technical Note 866 (1975).
- 5.34 W. B. DeMore et al., eds. "Chemical Kinetic and Photochemical Data for Use in Stratospheric Modeling, Evaluation #2," JPL Publ. 79-27, (April 1979).
- 5.35 G. N. Whyte, "Energy per Ion Pair for Charged Particles in Gases," Rad. Res. 18, 265 (1963).

REFERENCES (Cont.)

- 5.36 F. H. Brittain, "A Description of ELTRAN: An Electronic Deposition Code," Sandia Laboratories Report SC-TM-68-713, 1969, as supplied by Oak Ridge National Laboratory RISC Computer Code Collection.
- 5.37 M. J. Berger and S. M. Seltzer, "Tables of Energy Losses and Ranges of Electrons and Positrons," NASA SP-03012 (1964).
- 5.38 R. E. Center, "Plural and Multiple Scattering of Fast Electrons in Gases," Phys. Fluids 13, 79 (1970).
- 5.39 J. Crank, The Mathematics of Diffusion (Oxford at the Clarendon Press, 1957), p. 56.
- 5.40 F. Kaufman, "Reactions of Oxygen Atoms," in Progress in Reaction Kinetics, I., ed. G. Porter (New York, Pergamon Press, 1961), p. 1.

6. CRYOGENIC LABCEDE SYSTEMS STUDY

6.1 Introduction

The LABCEDE facility, situated at the Air Force Geophysics Laboratory, is a large-scale experimental apparatus developed specifically to study the fluorescence arising from electron irradiated gases. Such studies, although interesting in their own right, are of particular importance in specifying the radiative properties of both aurorally and nuclear-disturbed atmospheres. As will be seen below, LABCEDE is particularly suited for such investigations and indeed, to our knowledge, is the only facility in the nation capable of simulating and measuring auroral (nuclear) excitation processes specific to the long wavelength infrared (LWIR) portion of the spectrum.

In the LABCEDE experiments, well defined and collimated electron beams are used to inject electrons into various target gases held under controlled conditions. As the electrons traverse the target gas they undergo elastic and inelastic collisions with the ambient molecules with the result that the beam both spreads and loses energy. The beam energy loss is the result of direct excitation and ionization of the ambient molecules. The ambient molecules will also undergo excitation by energetic secondary electrons created in the direct ionization process. Furthermore, various gas phase reactions, such as ion-neutral and ion-electron recombination reactions, can provide for additional excitation of the neutral gas molecules. All of these processes can directly or indirectly lead to fluorescence from the various excited states of the target gas. The basic issues of interest in the study of such phenomenology include: (a) identification of fluorescing species and spectral region of fluorescence, (b) determination of the mechanism and efficiency for electron excitation of the various excited states and, (c) the specification of the relaxation phenomena which control the fluorescence.

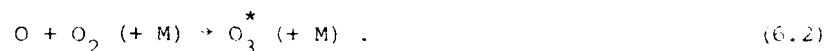
The cryogenically cooled system is designed to examine electron excitation phenomena at pressures $< 100 \mu\text{m Hg}$ and at electron energies of

2-5 keV. The inner walls of this test chamber are held at temperatures near that of liquid nitrogen in order to minimize background radiation so as to allow measurement of LWIR radiation with high sensitivity.

This device may be exploited to provide fundamental information of importance in defining infrared backgrounds relevant to Air Force systems. In particular, the spectral content of electron-irradiated atmospheric gases can be surveyed over the wavelength range of 1-20 μm . Particular systems of interest include NO vibro-luminescence produced by



(see Sections 3 and 5), and O_3 recombination fluorescence, i.e.,



The efficiency for excitation of various CO_2 vibrational bands also requires definition. Other potential infrared radiators such as N_2 Rydberg states, N_2O , NO^+ , OH , etc. could also be investigated. Many of these species have been observed in the disturbed upper atmosphere. The LABCEDE facility allows such molecular systems to be examined under few collisions, low background conditions with a direct electron excitation source. Furthermore, experimental conditions can be varied sufficiently so as to study concomitant relaxation phenomena of specific interest to atmospheric applications. The typical LABCEDE operating pressure range corresponds to altitudes of 60-100 km, and the resulting fluorescence levels from the low pressure irradiated gases are weak. In order to increase signal levels of the fluorescence in this device, the irradiated volume is maximized. The electron beam pathlength is over a meter, and the molecular emission arising from the deposited energy can be observed over this entire pathlength. The apparatus exceeds 4 m in length perpendicular to the beam axis and observation diagnostics are presently located at one end, 2 meters distant from the beam. Because LWIR

emission is of prime concern, system backgrounds are reduced to allow detection of the low density emitters. The cryogenic shroud contained within the device (maintained at 77 K) results in a decrease of the LWIR background level by several orders of magnitude.

The combination of low background levels and large electron irradiated volume makes the LABCEDE cryogenic device a facility singularly suited for the simulation of the disturbed upper atmosphere. During the past year, 1980, Physical Sciences Inc. personnel were asked to perform a system study of the cryogenic LABCEDE facility and to suggest modifications that would improve system performance. In the following sections we will provide a description of the June 1980 status of the cryogenic device, a review of recommended modifications to the system, and a description of the anticipated operating capabilities of the modified device.

6.2 Present System Capabilities

A schematic of the LABCEDE facility is shown in Fig. 6.1. The vacuum tank is nominally 1 m in diameter by 5 m in length. The electron beam enters the tank through a port on the side and irradiates the test gas across the short dimension (Fig. 6.1). Only two optical viewing ports are available: the first is almost directly opposite the e-beam entrance port and, therefore, views the irradiated gas only slightly off axis whereas the second is at one end of the tank and, therefore, views the irradiated gas at right angles to the e-beam path.

Two large diffusion pumps are available to evacuate the tank, but only one is normally used. The usual operating pressure is in the range $1 \times 10^{-6} < p < 100$ mHg. Gas mixtures, such as air, are made external to the tank and brought into the tank through a single line at the top in the same plane as the e-beam. AFGL calculates a nominal flow velocity in the tank at operating pressure of about 15 ft/s.

The entire inner surface of the tank is lined with a metal shroud through which liquid N_2 flows to maintain a nominal wall temperature of 77 K. Various ports are cut into this shroud to provide access to the e-beam, optical

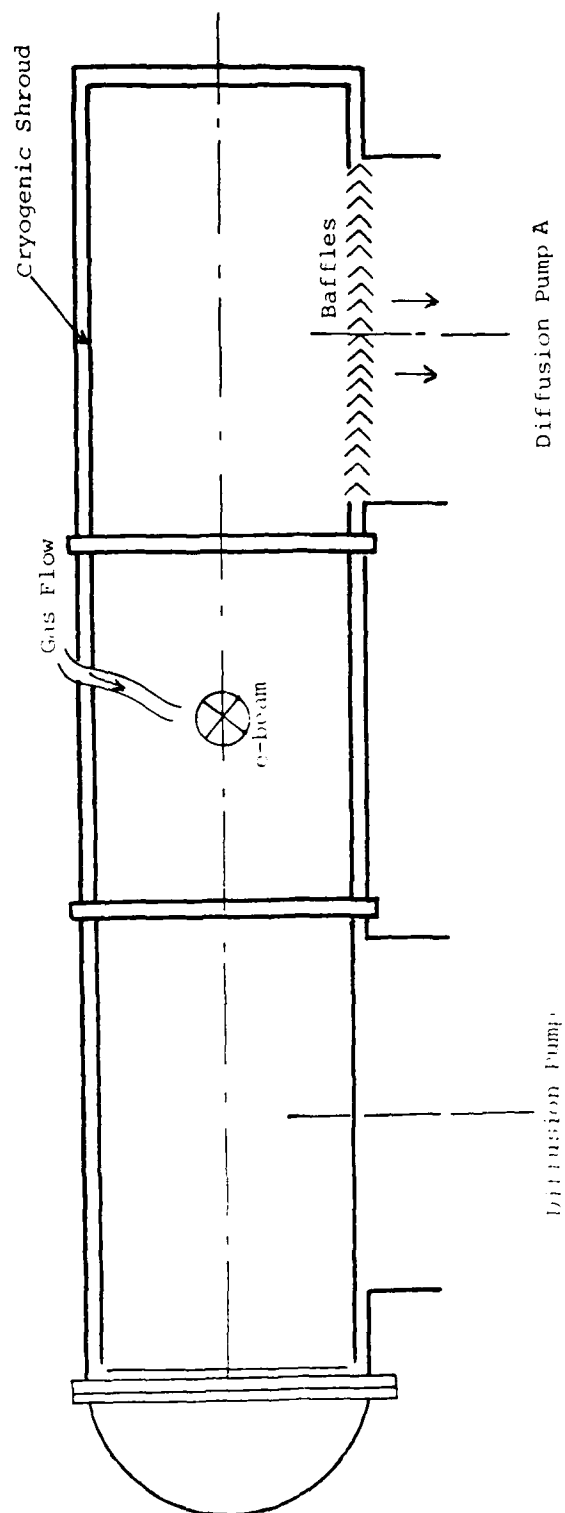


Fig. 6.1 Schematic of cryogenic LABCEDE Facility in its present configuration.

diagnostics, and pumps. Although the shroud is designed to provide a 77 K background for the infrared diagnostics, the presence of various openings, some necessary and some inadvertent, provide a radiation leak, and the measured background is higher, probably more in the range of $90 < T < 150$ K.

The e-beam is designed to produce low energy electrons ($1 < E < 5$ keV) and modest currents ($5 < I < 20$ mA). A nominal operating condition determined at the gun is 5 keV and 15 mA. The beam is collimated as it enters the tank, but is expected to spread due to scattering as it traverses the gas (see sketch in Fig. 6.1). Unfortunately, as there are no beam diagnostics in the tank, the actual energy deposition and beam profile can, at present, only be determined by calculation using the gun parameters. The experimental energy deposition, from which one can calculate ion-pair production, and the spatial extent of this deposition are critical parameters in the design of optimum diagnostics to observe the chemi-excitation and are discussed later.

The primary optical diagnostic used to date has been the radiometer/CVF combination mounted at the end of the tank. This instrument covers the spectral region 2-20 μ with coarse spectral resolution and has a field of view (FOV) at the excitation region of about 15 cm radius. The instrument is optically coupled to the tank through cooled windows to minimize background radiation. A Czerny-Turner spectrometer is also available and could be used to obtain better spectral resolution. However, this instrument is not readily mounted to the tank with the optical ports available, and, because of its small f number (f/7), considerable reduction in signal is anticipated. A cooled interferometer mounted in the tank close to the e-beam path would be an optimum diagnostic, but this approach would require considerable engineering modifications.

6.3 System Study Recommendations

After reviewing the system operating capabilities it was concluded that several modifications were required before definitive measurements could be made on the facility, indeed, before measurements of absolute intensities

and excitation efficiencies could be made in uncontaminated gas mixtures. Suggestions (enumerated below) fall in three areas: electron beam confinement, improvement of irradiated gas composition and flow, and implementation of improved fluorescence diagnostics.

The following are the detailed recommendations of the system study of LABCEDE which form a basis for the planned experimental modifications. It is suggested that the electron beam from the existing electron gun be confined magnetically inside LABCEDE. This will result in an increased energy deposition/cm³, ensuring that all of the energy deposited in the gas will be in the field of view of the detector. Field of view reduction will also result in a reduction of the background emission accepted. There also exists a potential for increasing beam current through confinement of the beam within the gun. It is further suggested that the confined beam be collected in a Faraday cup/trap assembly after passage across the tank. This will permit measurement of unstopped beam current. An initial beam current measurement should also be implemented. If the Faraday cup is separately pumped by a Roots blower or booster diffusion pump, then species sputtered off the trap walls by electron impact will be rapidly removed and not re-enter the chamber at pressures above 1 μ . At present, spectral contaminants complicate the data interpretation. The suggested steps will eliminate emission due to sputtered gases. A schematic of these electron beam system changes is presented in Fig. 6.2.

Beam-created species may also build up with the present flow system in LABCEDE. Additionally, a leak in the liquid nitrogen cooling lines provides a constant background of N₂. Due to the great size of the LABCEDE facility, the shroud cannot be easily removed for repair unless the test chamber is shortened. It was recommended that the test chamber be cut and ~ 1.6 m of length be removed. This will permit ready access to the shortened shroud. The gas flow should be introduced at the shortened end of the tank after precooling by a heat exchanger. If the gas is passed through a diffuser plate to remove its momentum, then a smooth plug flow would occur in the tank. Beam-created species would be swept out of the irradiated volume

in milliseconds and not be recirculated. To insure this directed flow, additional modifications of the shroud would be required. All leaks in the tongue and groove shroud would have to be sealed so as to force gas flow down the tank. Sealing would also be required at the edges of the shroud near ports or at the end of the tank. A better baffling system would have to be designed to permit rapid diffusion pump speeds while blocking 300 K emission. Additionally, to improve pumping speeds in the 3-70 μ pressure region, a throttling system must be designed to permit diffusion pump operation at these elevated pressures. A schematic summary of these modifications is drawn in Fig. 6.3.

The shortened tank will also improve detection system viewing steradiancy. The addition of at least two additional viewing ports is suggested. A cold plate could be mounted behind the electron beam but filling the detector field of view, and a significant reduction in background emission would result. If a second viewport is mounted on the door, then replacement of the cold plate by a mirror will permit absorption measurements to be made. Additional viewports above the beam could be used for monitoring of N_2 electronic transitions such as $N_2(1+)$ and $N_2(1-, 3914 \text{ \AA})$. A possible configuration for these detection system changes, as well as for all the other recommended modifications is presented in Fig. 6.4. The effect of these changes on expected system performance is presented below where we undertake an analysis of the modified system's capabilities.

6.4 System Performance Maps for Refurbished LABCEDE

We now present a first order analysis of the refurbished LABCEDE system capabilities and detection sensitivities. Obviously, a more accurate mapping must wait for the results of the performance of the refurbished system. The time scales for various processes to occur in the cryogenic (90 K) tank are plotted in Fig. 6.5. The times for the quenching of molecular excitation with various cross-sections (gas kinetic, 10^{-2} gas kinetic, and 10^{-4} gas kinetic) and for diffusion out of a certain radius ($r = 5, 15 \text{ cm}$ such as for a field of view, and $r = 50 \text{ cm}$ which corresponds to the walls

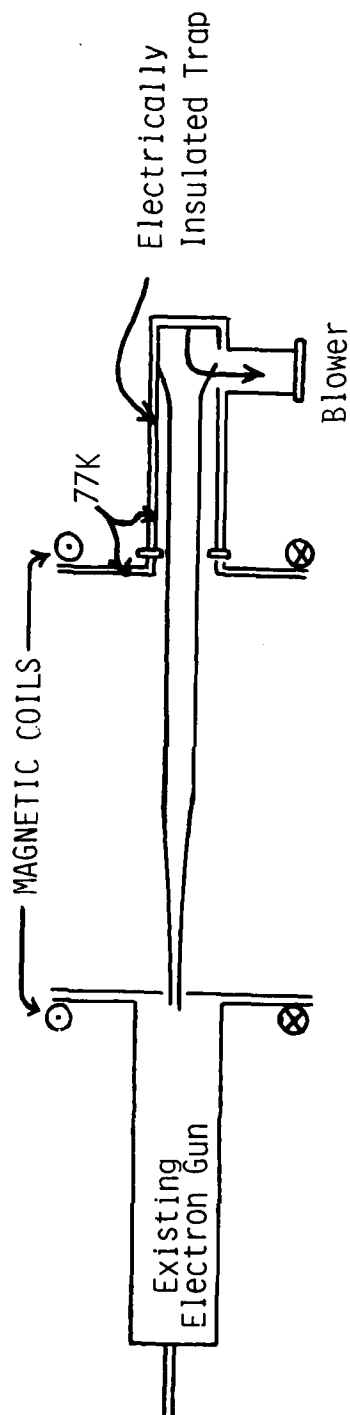


Fig. 6.2 Possible electron beam improvements: the magnetic coils will confine the beam so that all energy is deposited in a thin column; the Faraday cup/trap prevents sputtered species from contaminating the fluorescent emission.

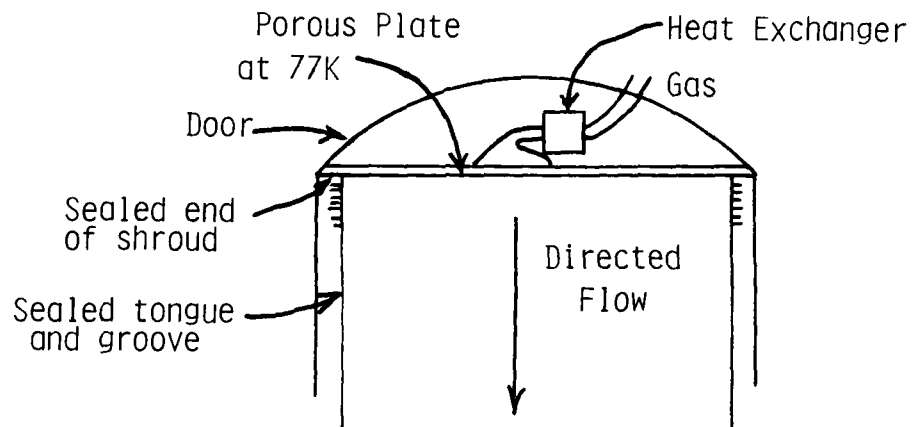


Fig. 6.3 Possible gas flow changes: the porous plate removes momentum so that there is plug flow in the tank; sealing of the shroud directs the flow perpendicular to the electron beam.

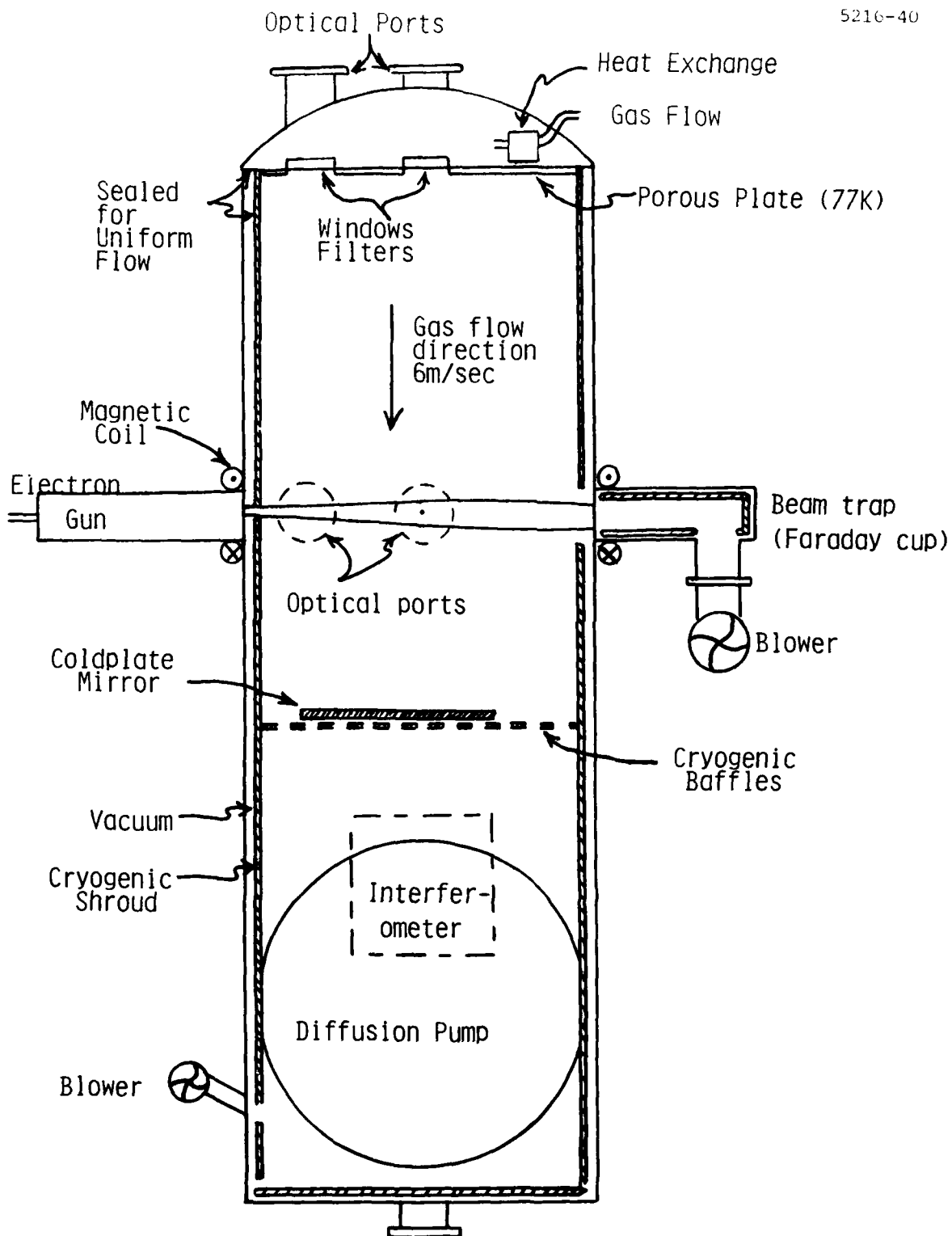


Fig. 6.4 Summary of suggested LABCEDE system changes.

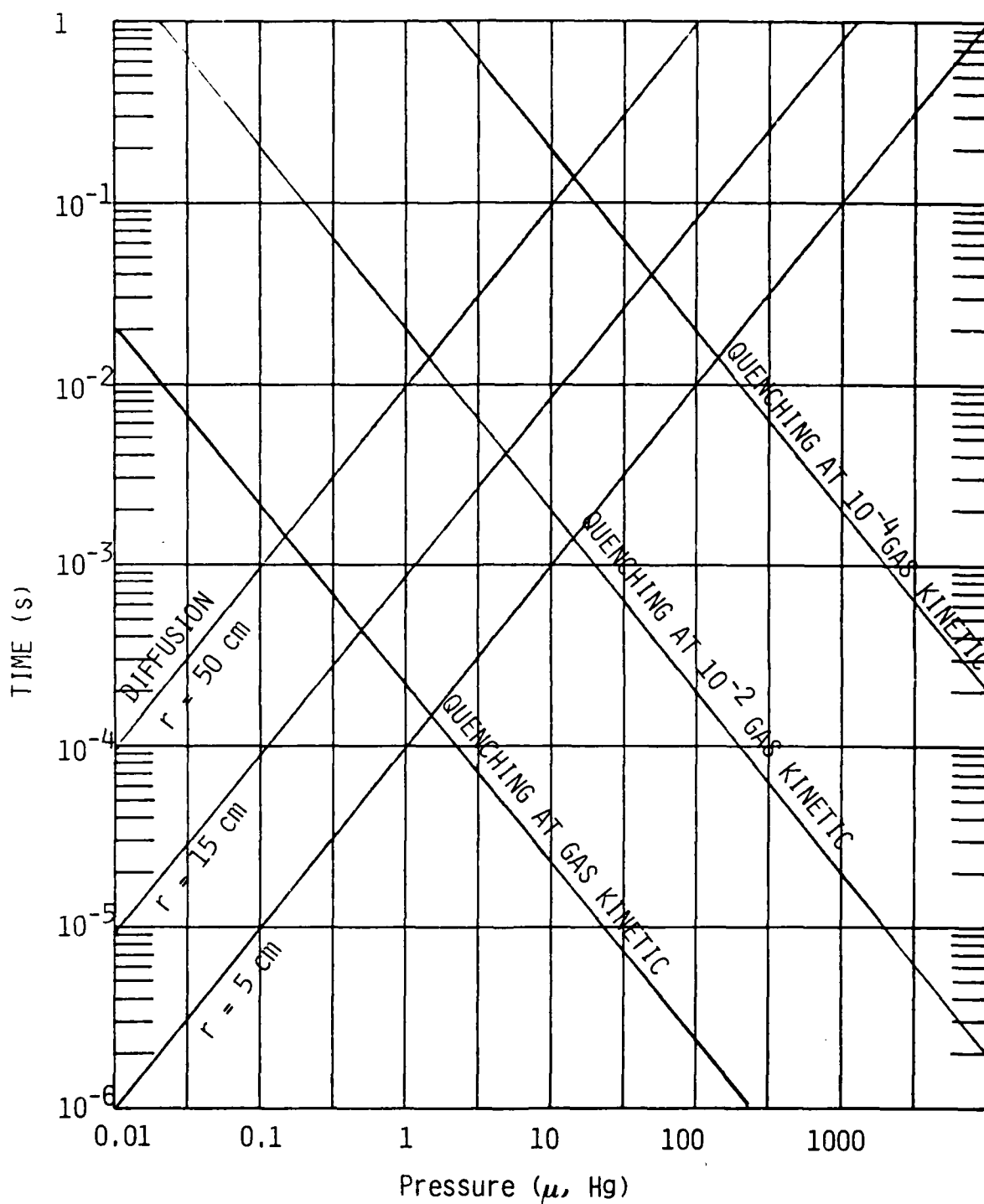


Fig. 6.5 The time scales for diffusion and quenching to occur are plotted as a function of pressure in the cryogenic LABCEDE facility. Quenching times are shown for several rates, as are the diffusion times out of various radii.

of the shroud) are plotted as a function of chamber pressure. As an example, it can be seen that above 1 μ pressure the gas will be quenched before it can diffuse to the walls of the shroud if it is quenched at a rate greater than 10^{-2} gas kinetic.

In Fig. 6.6 the operating region of interest, 0.1-100 μ pressure, is expanded and the radiative lifetimes of selected transitions of interest are listed along the right margin of the graph. Again as an example, it is seen that the lifetime of $O_3(v_3)$ is longer than the diffusion time to the walls at pressures below 10 μ . Additionally, if quenching is rapid, most of the vibrational relaxation will occur via non-radiative channels. This does not mean that no fluorescence will be observed, but that the emission will be reduced due to quenching and diffusion. The fraction of vibrational excitation radiated in the field of view or the quantum yield ϕ , would be given by the formula

$$\phi = \frac{1}{1 + Q\tau_r + D\tau_r} \quad (6.3)$$

where Q and D are the quenching and diffusion rates in s^{-1} and τ_r is the characteristic radiative decay time for the transition. An example for $CO_2(v_2)$ at 100 μ pressure viewed with a 15 cm radius field of view, quenched at 10^{-3} gas kinetic, Eq. (6.3) becomes

$$\phi = \frac{1}{1 + (400 \text{ s}^{-1})(0.31 \text{ s}) + (12.2 \text{ s}^{-1})(0.31 \text{ s})} = 0.008$$

meaning 0.8% of the $CO_2(v_2)$ excitation will appear as fluorescence. The quenching term is seen to dominate and quenching at gas kinetic would reduce the quantum yield to 8×10^{-6} . Thus, emission may be observed in the presence of diffusion and quenching, but determination of excitation efficiencies is restricted by the severe lack of knowledge of the quenching rates, especially at 90 K. Note that this is not a problem for the $N_2(1+)$

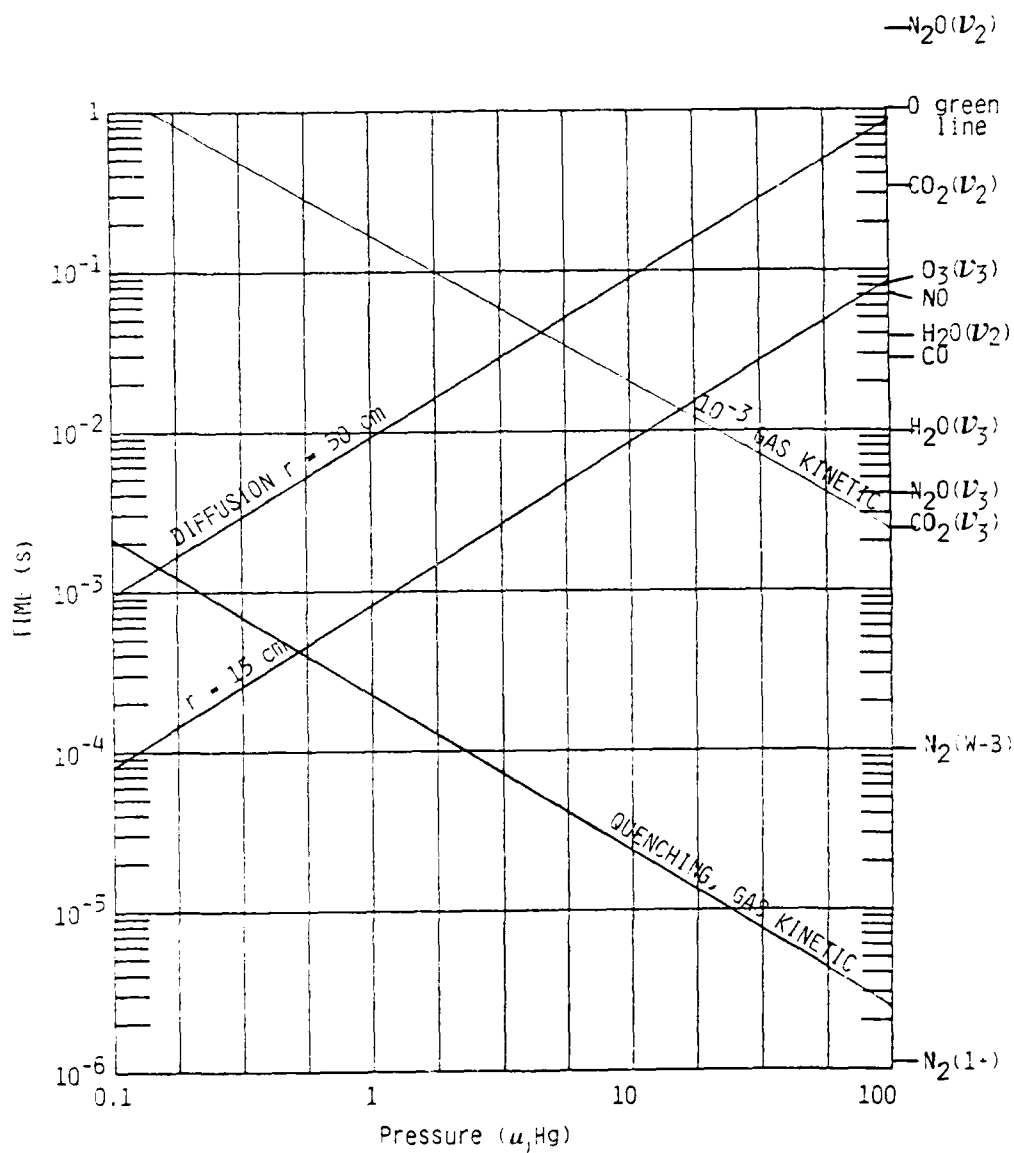


Fig. 6.6 The time scales for diffusion and quenching as in Fig. 6.5. Also shown are the radiative lifetimes of some transitions of interest.

and $N_{\text{eff}}(-)$ electrons is found to be used as energy diagnostics. Operation in a regime where radiative decay is the dominant loss process is necessary for these self-consistent measurements.

[illegible]

Because no measurements of the electron beam spatial shape have been made under LABCEDE conditions, the expected electron beam shape has been modeled by extrapolation. Center^{6.1} measured electron beam shape in thin targets of N₂ and Ar for 20-100 keV electrons and parameterized beam shape in terms of two variables dependent on gas and voltage. The expected beam shape for 5 keV electrons obtained by extrapolation of his measurements is given in Fig. 6.8. Another set of measurements by Cohn and Caledonia^{6.2} were for 2-5 keV electrons but into higher pressure targets. Their results at short ranges where the target was quasi-thin were used to make the second set of predictions in Fig. 6.8. In that figure, the half-power radius of the electron beam is plotted as a function of distance in the tank from the entrance aperture. Half of the electron beam current is contained within this radius. The gas pressure used in these calculations was 30 ... The two

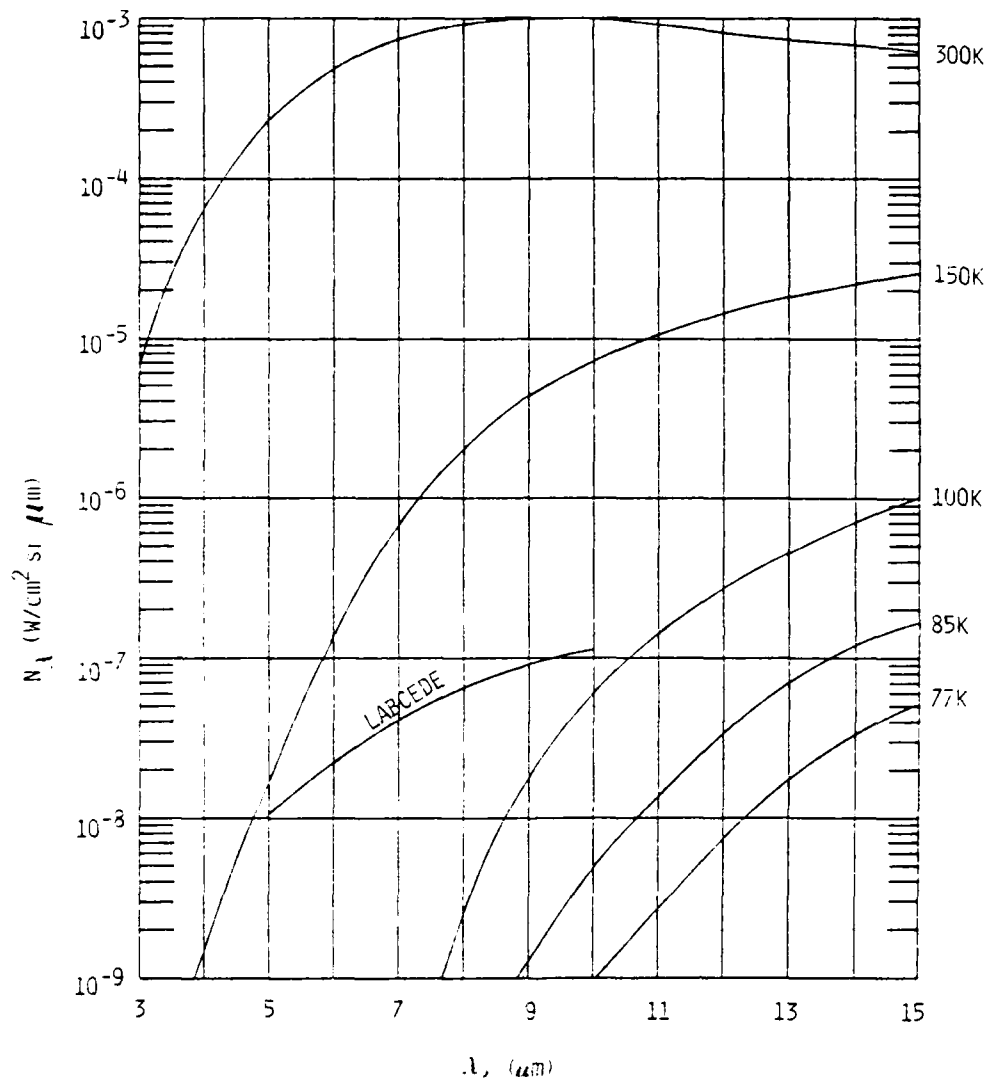


FIG. 6.7 The theoretical blackbody emission curves for several temperatures as a function of wavelength. Also plotted is the estimated current background emission for LABCEDE.

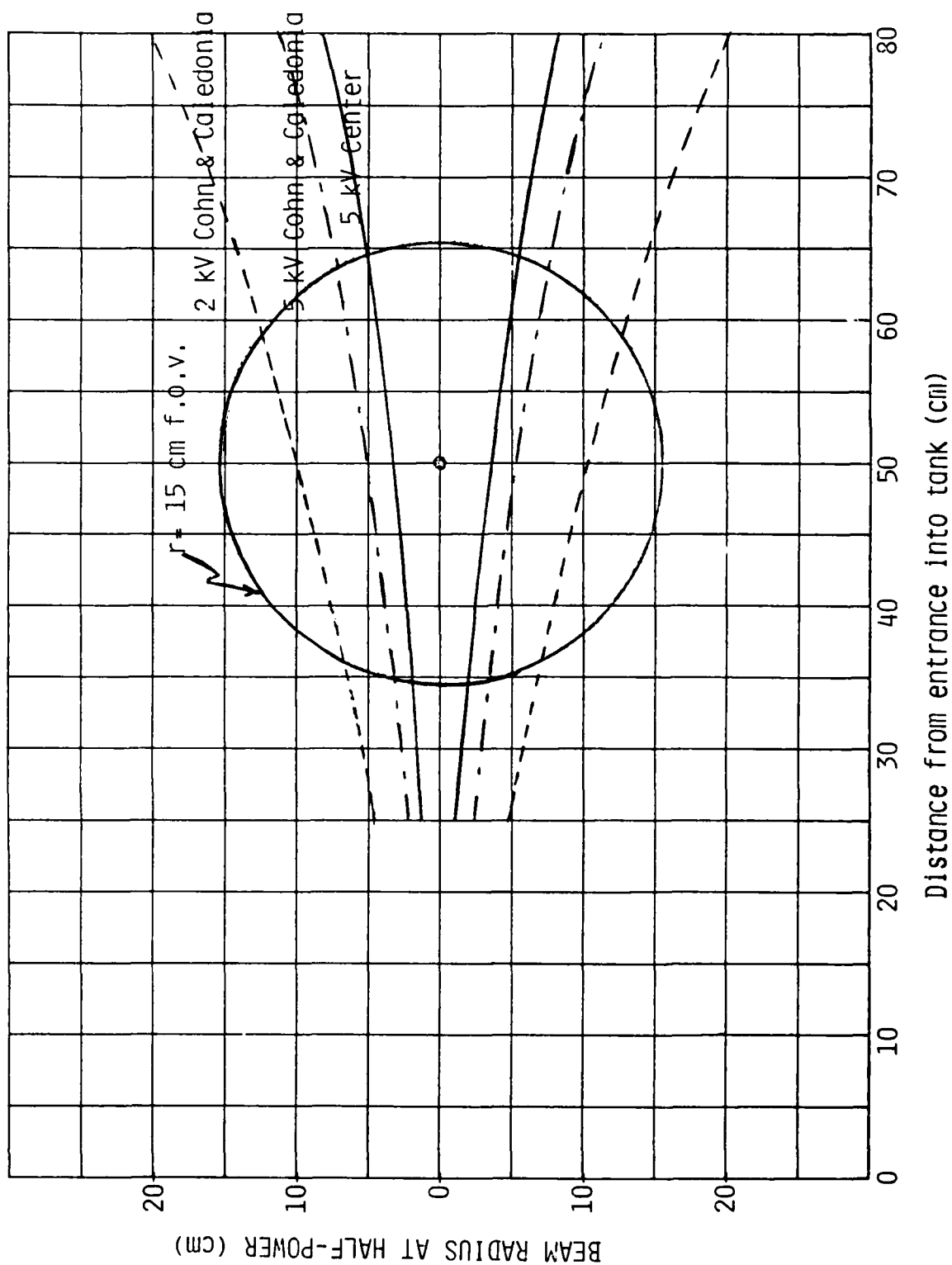


Fig. 6.8 LABCEDE extrapolated beam growth at 30 μ pressure from the two measurements (see text). Total energy deposited is calculated to be 0.1 W/cm.

extrapolations agree well and the observed distribution should be similar to this prediction. It should be noted that for the 2 keV case, only about two-thirds of the total energy deposited in the gas would be within a 15 cm radius field of view at this gas pressure, and the beam would exhibit over a 30 cm radius at the far wall of the shroud. The proposed effort to confine the beam so that all of the energy deposited would be in a 3 cm radius would permit quantitative intensity measurements with a dramatic reduction in the size of the field of view, decreasing accepted background emission.

Several measurements of the total energy deposited exist^{6.2-6.4} and for 2 keV electrons, the expected deposition is 4 mW/cm path- μ pressure. This leads to a prediction of 2×10^{16} ion pairs/s being created in the field of view of Fig. 6.8. Knowing the ion pair creation rate and assuming one molecular excitation per ion pair, parameteric maps of fluorescent intensity as a function of wavelength may be created, as in Fig. 6.9. The fluorescent intensity at 1, 10 and 100 μ pressure are shown for experimental conditions where the radiative lifetime is sufficiently short that quenching and diffusion do not play a role. The wavelength scaling is simply due to the photon energy variation. The 10 μ m curve is an order of magnitude above the 1 μ m curve, deposition scaling linearly with density. The smaller increase above 10 μ m is due to beam growth resulting in deposition outside of the field of view. If the beam is magnetically confined, a linear increase with pressure results. Also displayed on the figure are the background emission intensities in the field of view for two spectral bandpasses. If the molecular emission band were narrow, the spectral bandpass of the detection network could be reduced and still collect all of the molecular emission while decreasing the background level. The plotted background is based on the present LABCEDE emission levels.

A similar plot of fluorescent intensity in W/sr under conditions where the radiative lifetime is long compared to the quenching and diffusion rates is shown in Fig. 6.10. The intensity emitted at all pressures has been greatly decreased. The 1 μ pressure curve is dominated by diffusional losses. At both 10 μ and 100 μ pressure, quenching at 10^{-2} gas kinetic dominates the losses. The 100 μ curve is below the 10 μ curve due to

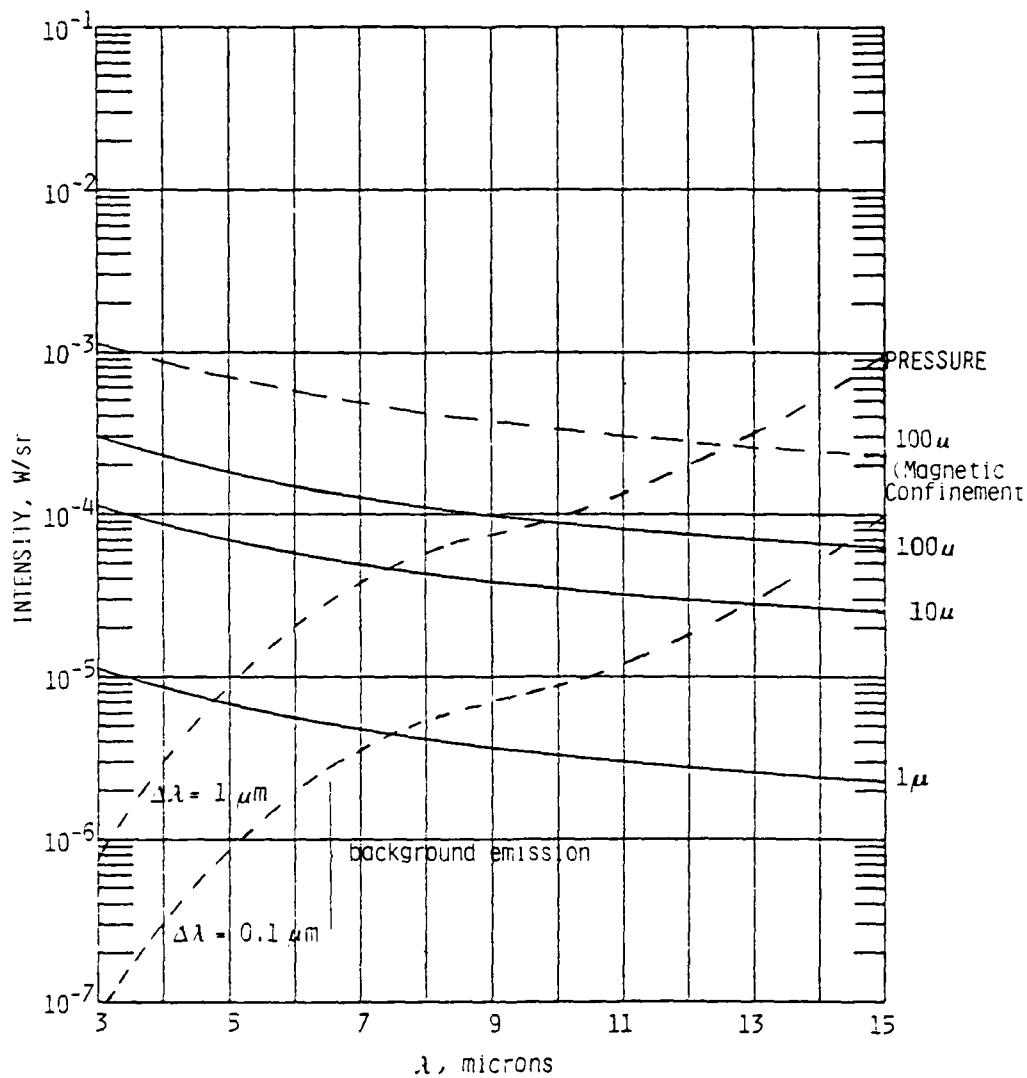


Fig. 6.9 The expected signal and background intensities assuming one photon per ion pair for short lived transitions when diffusion and quenching are unimportant. $V = 2$ keV; backgrounds for two detection system bandpasses are shown.

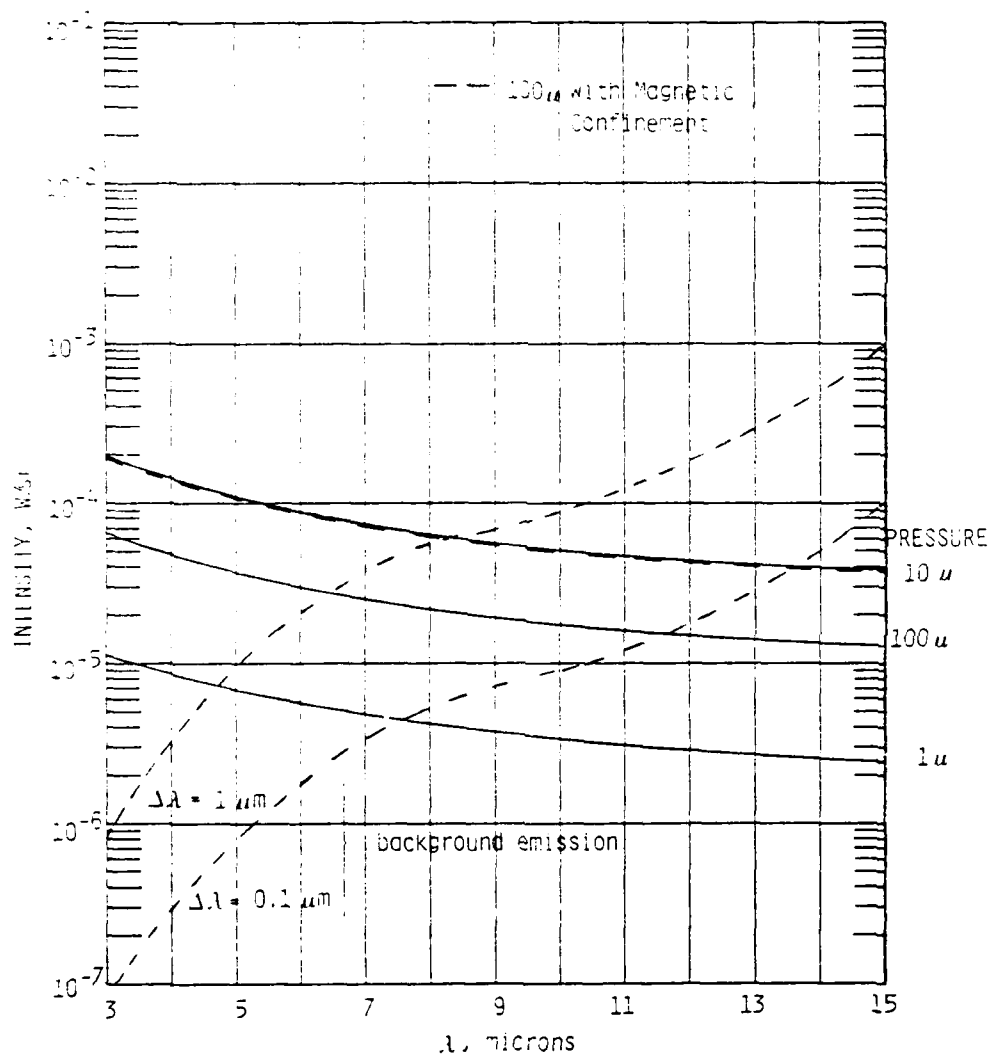


FIG. 6.10 The expected intensities for one photon per ion pair for 2keV electrons assuming quenching occurs at 10^{-2} gas kinetic and a radiative lifetime of 10 ms for a 15 cm field of view.

beam growth as mentioned above. If the beam is confined, the two curves are identical because both deposition and quenching increase linearly with pressure.

Finally, estimates of the signal to noise level can be made for individual molecular bands as a function of pressure. These estimates of the intensity of the detector (in watts) are plotted as a function of wavelength in Fig. 6.11. Numerous assumptions were made in developing Fig. 6.11. The quenching rates were for air stoichiometry at room temperature. One molecular excitation per ion pair is assumed where better theoretical estimates are unavailable. The values of the quenching rates and excitations per ion pair used in constructing Fig. 6.11 are given in Table 6.1. A detection system steradiancy of 2×10^{-2} sr is assumed and a beam duty cycle of 10% is used. The detection system is composed of a HgCdTe 77 K detector looking at the spectrally resolved emission through an 85 K spectrometer. Experimental background is assumed to be the two temperature distribution given above. Noise levels for detection system bandpasses of 1 Hz and 1 kHz are plotted. Any kinetic measurements will require a still larger bandpass. These curves assume a statistical noise dominated by photon flux levels. The fluorescent intensities are easily detectible in the SWIR/MWIR spectral regions. $\text{CO}_2(\nu_2)$ emission should be detectible at the highest pressures. The predicted N_2 Lydberg emission is based on relative intensity measurements from a GE Tempo study.^{6.5} No measurements of this emission exist, however, it would appear to be within the detection limit of the system based on the above assumptions. It must be stressed that a large number of assumptions were required to arrive at Fig. 6.11, and that the conclusions are only approximate. More accurate modeling must wait for a better determination of system operating parameters. Nevertheless, Fig. 6.11 can be instructive as a guide for optimizing the emission of a given species, and as a measure of the relative ease of detection of various emission bands.

The spectrally resolved infrared emission will provide the necessary insight into the gas flow patterns within the facility as evidenced by the irradiation of beam-created species or species sputtered off the wall. The

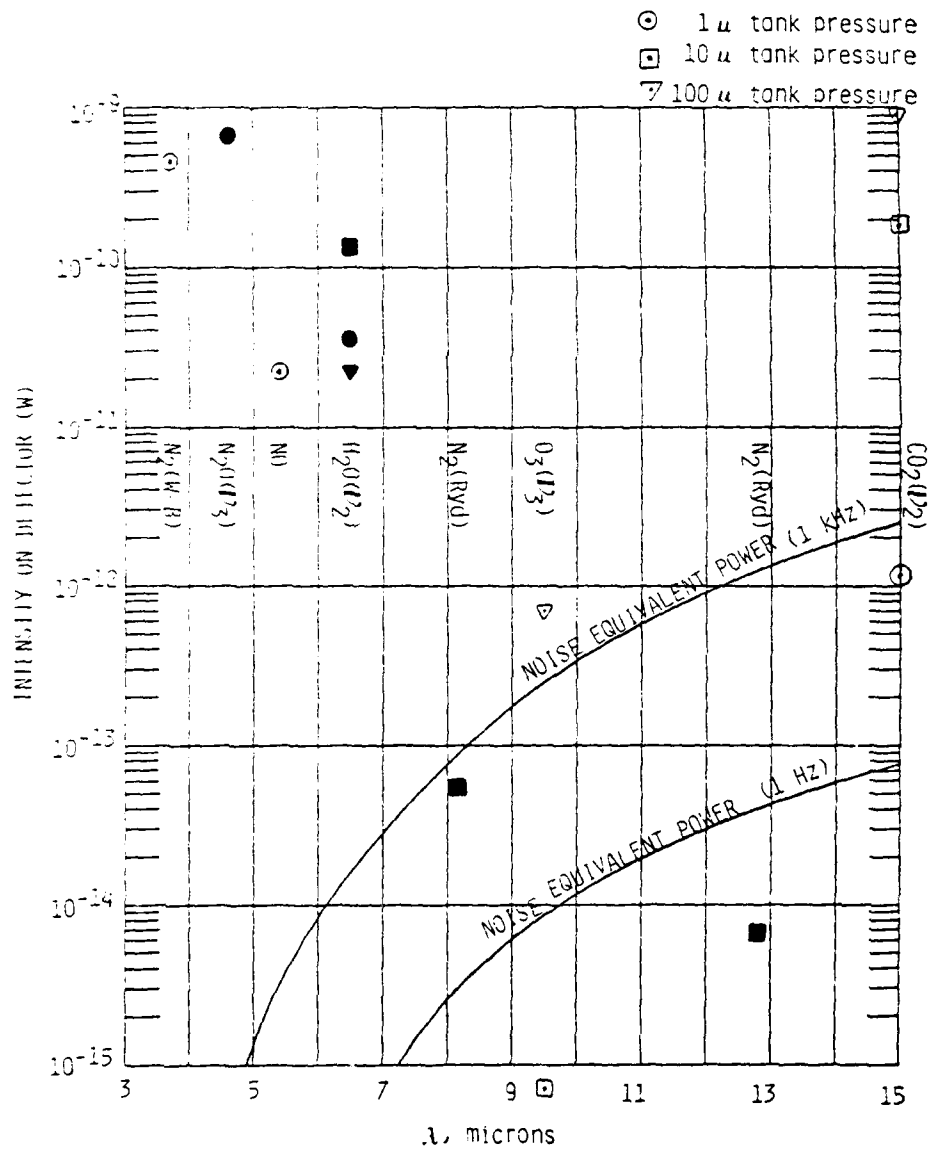


Fig. 6.11 Expected signal and background levels on the refurbished LABCEDE facility. Assumptions used to make this figure are given in the text.

TABLE C.1

QUENCHING RATES BY N_2 , O_2

SPECIES	N_2		O_2		PHOTONS 10 ¹¹ /s
	k_q , cm ³ /s	k_q gas kinetic	k_q , cm ³ /s	k_q gas kinetic	
CO_2	~(-15) 100K	3(-5)	1(-14) v-v	1(-4)	.92
O_3 (λ_3)	2(-14)	3(-4)	2(-14)	3(-4)	*
NO	~0	~0	~2(-14)	3(-4)	1
H_2O (λ_2)	~(-14)	9(-4)	2(-12) v-v	.3	(1)
CO	1(-14) v-v	1(-4)	~0	~0	2.7
H_2O (λ_3)	FAST	1	FAST	1	(1)
N_2 (λ_2)	2(-13) v-v	3(-3)	<10 ⁻¹³	<1(-3)	1
CO_2 (λ_2)	6(-13) v-v	9(-3)	~1(-15)	1(-5)	1.4
$N(^2D)$	6(-16) 100K	1(-5)	6(-12)	.1	1.2
$O(^1D)$	7(-11)	1	7(-11)	1	(1)
$N_2(A)^{low}$	~0	~0	2-6(-12)	.03-.09	
$N_2(B)^{low}$	2(-12)-1(-11)	.03-.15	-	-	.14
$N_2(W)$	est. as $N_2(B)$.03-.15	-	-	.14

* Rates listed are for 300 K unless otherwise noted, and no temperature dependence is assumed. The gas kinetic rate is for 100 K.

* O_3 estimates are for three-body reaction assuming one oxygen atom/ion pair and one photon/ozone molecule. O-atom diffusion and O_3 diffusion and quenching are all included in the estimate of Fig. 6.11.

planned laser radiometric instruments which will be implemented include a magnetic interferometer and spectrometer, and a circular variable filter. These instruments should have sufficient spectral resolution to permit not only discrimination between bands of different emitting species, but also determination of the degree of vibrational excitation in each mode. Finally, calibration of the response of all the diagnostics using lamps or a black-body source will allow the emission to be quantified and absolute excitation efficiencies to be measured as a function of system pressure and beam confinement. To aid in the refurbished system characterization (and later data acquisition), beam diagnostics using spectrometric techniques will be implemented. A phototube sensitive to 391.4 nm $N_2(1-)$ emission (which is proportional to the number of ion pairs created in the gas by the primary electrons) can be used to measure energy deposited and map the spatial distribution of the primary electrons. Emission from either $N_2(1+)$ in the red or $N_2(2+)$ at 337.1 nm could be used to follow the secondary electron distribution. (These electrons are created by collisions of the beam electrons with the tank gas molecules.) It is felt that measurements of excitation efficiencies and surveys of fluorescent emission should be undertaken only after these diagnostics have been implemented, and the system operation parameters have been determined.

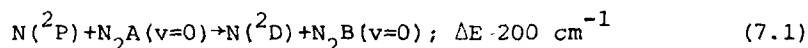
REFERENCES

- 6.1 R. E. Center, "Plural and Multiple Scattering of Fast Electrons in Gases," Phys. Fluids 13, 79 (1970).
- 6.2 A. Cohn and G. E. Caledonia, "Spatial Distribution of the Fluorescent Radiation Emission Caused by an Electron Beam," J. Appl. Phys. 41, 3767 (1970).
- 6.3 A. E. Grün, Z. Naturforsch. A 12, 89 (1957).
- 6.4 J. L. Barrett and P. B. Hays, "Spatial Distributions of Energy Deposited on Nitrogen by Electrons," J. Chem. Phys. 64, 743 (1976).
- 6.5 M. J. Stanton et al., "Nuclear Induced Optical Phenomenology Program (1976-1977) (U)," G. E. TEMP Report GE77TMP-22, August 1977, (SECRET).

7. NEAR IR EMISSION OF N_2/O_2 MIXTURES

7.1 Introduction

In this section the results of a preliminary survey of the emission from pure N_2 , pure O_2 , and their mixtures will be reported. The spectral region between 0.6 and 3 μm was covered using several different detectors. The nitrogen first positive system (N_2 1P) arising from transitions between the $B(^3\Pi_g^-) - A(^3\Sigma_u^+)$ states was the dominant feature observed in pure N_2 . In addition to obtaining the relative intensities for the bands in different series and progressions, the resolution was sufficient to allow branches within a band arising from spin uncoupling to be observed. A theoretical code to predict band intensities, frequencies and shapes was created to aid in spectral analysis. The electron beam not only creates excited molecular nitrogen states, but causes dissociation and some atomic metastable states (2P , 2D) are formed. The N_2 B-A transitions have lifetimes on the order of micro seconds, while metastables have radiative lifetimes of 6s ($^4P \rightarrow ^2D$) and 12 hrs ($^4D \rightarrow ^4S$) respectively,^{7.1} and will exhibit relatively long collisional lifetimes in the LABCEDE chamber. There exists a coincidental energy overlap between the metastable atomic states and the N_2 A and B states such that the reaction



is near resonant. A few microseconds after beam termination only the metastable states will be populated. It should be possible to observe the decay of the $N(^2P)$ concentration by monitoring the long time decay of the N_2 (1P) 0-0 transition if reaction (7.1) occurs.

Molecular oxygen has several weakly allowed infrared bands involving transitions between the $b(^1\Sigma_g^+)$, $a(^1\Delta_g)$, and $X(^3\Sigma_g^-)$ states. The $b \rightarrow a$ transition has previously only been observed by Noxon^{7.2} and in LABCEDE.^{7.3} An anomalous pressure dependence was found in the previous unresolved LABCEDE observations and the preliminary results of spectrally resolved measurements are reported here.

EXPERIMENTAL

Because there is no concern about the effect of beam created species for these measurements, the gases were flowed slowly and the electron beam duty cycle was set to 50% (25 ms period). The electrons were accelerated by 30 keV prior to entering the target chamber. Depending upon chamber pressure 0.3-1.5 mA of current was possible, with the lowest currents occurring at the highest pressures due to beam blowup in the nozzle sections. For the N_2 measurements fluorescence from runs with total pressures between 0.1 and 100 torr was observed. Oxygen pressures of up to 50 torr were used, and A/O_2 mixtures were employed at the lowest oxygen pressures so to increase energy deposition. Fluorescence from irradiated N_2/O_2 mixtures was observed for a variety of O_2 partial pressures ranging from a trace of O_2 to up to 25%.

The fluorescence from the gases was spectrally resolved both with an interferometer and a spectrometer. The interferometer-computer interface was modified so that data points were acquired at every half fringe of the HeNe reference channel, permitting spectral observations down to $0.77 \mu m$ (13000 cm^{-1}). The PbS detector is capable of responding to photons in the visible, but its efficiency is very low. This low responsivity more than offset the throughput advantages of an interferometer and fluorescence below $1.1 \mu m$ could be more efficiently detected using red sensitive phototubes in conjunction with a $1/4 \text{ m}$ spectrometer. The tube housings were incompatible with the interferometer optics. Two tubes were employed: a Hamamatsu R406 phototube with a response similar to S-1, and a high quantum efficiency Varian tube cooled to -60°C . Because it was not easy to switch between interferometer and spectrometer, several measurements out to $\lambda = 2 \mu m$ (spectrometer grating limit) were made using the PbS detector at the exit plane of the spectrometer.

The absolute responses of the three detectors are plotted in Fig. 7.1. These response curves were obtained using an Opto-electronic Laboratories quartz halide calibration lamp with $30 \mu m$ spectrometer slits. The curves represent the combined effects of detector and spectrometer responses.

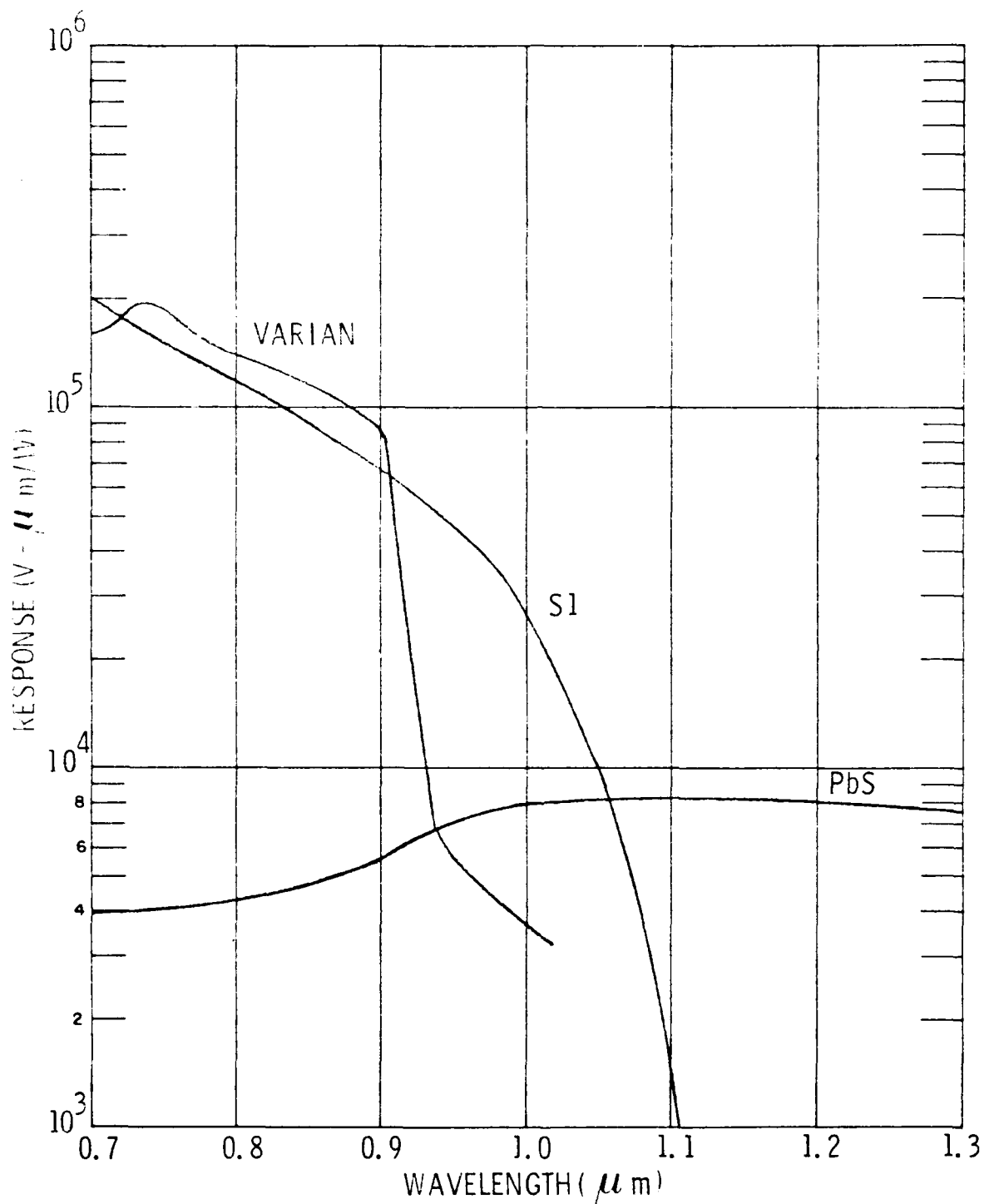


Fig. 7.1 System spectral response of the three detectors when used with the 1/4 m spectrometer. The slits were $30 \mu\text{m}$ for all three, which corresponds to 4 \AA resolution.

The Varian tube is 30-50% more sensitive than the S1 tube in the 700-900 nm region, but has a rapid fall off above 900 nm so that the S1 tube is the most sensitive of the three in the important 0.9-1.06 μm region. At longer wavelengths the PbS is most sensitive, dropping only to $4 \times 10^3 \text{ V}/(\text{W}\cdot\mu\text{m}^{-1})$ at 2 μm . Care was taken with the phototubes to ensure that saturation did not occur either during the runs or calibration. Day to day reproducibility of the detector's spectral response and absolute intensities (detector positioning) was very good. A Corning long pass filter (2-64) was utilized to discriminate grating orders. Its short wavelength cutoff, 650 nm, permits fluorescence in the 0.65-1.3 μm bandpass to be observed unoverlapped. A silicon flat, which becomes transmitting (60%) at wavelengths beyond 1.2 μm is used for the longer wavelength spectrometer observations. Nitrogen (1P) bands were observed using all three detectors on the spectrometer and the interferometer with the PbS detector. The oxygen bands of most concern were the 760 nm (b-X) transition, observed with the spectrometer and Varian tube; the 1.27 μm (a-X) band which was not observed on either optical system due to the relatively poor PbS response; and the 1.9 μm (b-a) band, observed only with the interferometer.

The energy pooling reaction (7.1) was indirectly observed by monitoring the $\text{N}_2(1\text{P})0-0$ transition through a notch filter selected for this transition (5 nm FWHM). The decay of other first positive bands with $v'' = 0$ could be followed using the spectrometer with the sensitive Hamamatsu tube. The decay of these bands was as fast as the electron beam current decay (1/e 6 ns) as expected. Because of the relatively poor system sensitivity at 1.05 μm where the (1P)0-0 band occurs, operation with just a notch filter yielded insufficient signal to obtain accurate decays from an oscilloscope trace even though an integrating sphere was introduced into the chamber to increase the signal. The detector signal was bandpass amplified (PARC 113) and input into a waveform eductor (PARC TDH9). The eductor was triggered by means of a digital delay generator at a time just prior to beam termination. This system allows monitoring of the decay with 10 μs time resolution. The variation of the decay time of the (0-0) band was thus observed as a function of nitrogen (and oxygen) pressure in the target chamber. The results of the three series of measurements are reported in the next part of this section.

7.3 Results and Discussion

7.3.1 Nitrogen First Positive Emission Features

As expected $N_2(1P)$ features were all pervasive across the spectral region monitored. With the spectrometer, emission from transitions in the $\Delta v = v' - v'' = \pm 1, \pm 2, \pm 3$ sequences were observed. Some interesting pressure variations were noted. At the lowest pressures, 0.1-1 torr, the emission intensity scaled as pressure; however, between 1 and 100 torr the variation was less than 50% suggesting that collisional quenching was to a large extent counterbalancing the increased energy deposition. As the pressure was increased from 1 to 10 torr, the $v' = 0, 1$ emission increased, possibly as a result of vibrational relaxation in the B state. Below 10 torr fluorescence from levels $v' \leq 6$ was observed. However, as the pressure was increased further emission from the higher levels increased and at 50 torr $v' = 9$ emission was clearly identified.

The $v' = 0, v'' = 0$ transition band was marginally observable at all pressures. Some degree of spectral overlap between the two measurement systems was achieved: the (0-0) band was barely apparent in the interferometer spectra. More apparent were the (0-1) features at 8100 cm^{-1} , the (1-3) and (0-2) features at 7020 and 6740 cm^{-1} , and the strong (1-4) features at 5700 cm^{-1} . The (0-3) feature was obscured by the atomic lines at $1.9\text{ }\mu\text{m}$. The NO overtone (2 \rightarrow 0) transition was weakly observed, attesting to the fact that there was a small but finite leak rate.

A code for predicting the $N_2(1P)$ emission bands frequencies and intensities was created and used to compute synthetic spectra for comparison with the laboratory data. This code is described in detail in Appendix V. Because of the preliminary nature of this survey, an in-depth analysis of all the spectra was not undertaken. The code frequency predictions matched the data extremely well, and proved invaluable in aiding the analysis of overlapped bands. Only a few runs were made with sufficient resolution to test the code's predictions for a band's spectral intensity distribution. A comparison between the predicted and observed fluorescence from the $v' = 0, v'' = 2$ transition around 6800 cm^{-1} is shown in Fig. 7.2. The experimental spectrum is obtained using the interferometer at 10 cm^{-1} resolution so that

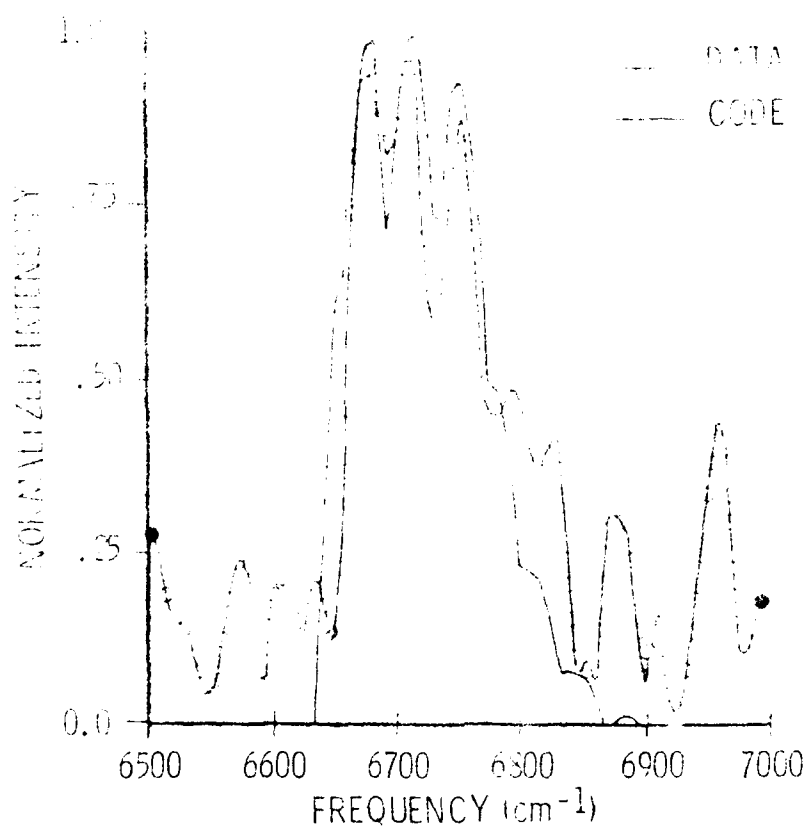


Fig. 1. Comparison of interferometric data and N₂(H) code prediction. The feature in the data is assigned as the ν_{12} , ν_{13} transition. Both frequency and shape of the band are accurately predicted by the code.

the prediction was convolved with the sinc apparatus function. Both frequency and rough spectral distribution are predicted well by the code. The noise level in the data is sizable and detailed comparison is not warranted at this time. A detailed series of measurements with increased signal levels, through use of an integrating sphere in the target chamber, is planned to permit more accurate observations. A significant discrepancy between the observed and predicted $N_2(1P)$ bandshapes would require re-evaluation of the degree of spin uncoupling in the B state. This uncoupling is reflected in the branch separation within the band and largely determines the band shape. (See Appendix V.)

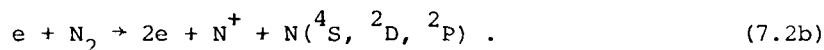
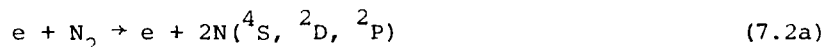
7.3.2 Metastable $N(^2P)$ Decay

Evidence was obtained that may suggest that the energy pooling mechanism, reaction (7.1) was occurring, but several of the observations from the preliminary runs are as yet unexplained. The apparent decay of the total $N_2(1P)$ fluorescence was comparable to the beam pulse decay ($\sim 6 \mu s$) as expected from the B state lifetimes. The measured decays from oscilloscope traces of the Varian output and from the waveform eductor network were in agreement. When the notch filter was positioned in front of the phototube, the beam intensity was reduced by a factor of five. Additionally, the observed decay increased to $100 \pm 10 \mu s$. At a constant N_2 gas flow, the chamber pressure was varied between 10 and 200 torr. The maximum intensity was at 20-60 torr, slowly decreasing on either side. This trend roughly corresponds with the expected beam energy deposition in the field of view. Above 60 torr, the beam is completely stopped by the target chamber gas. The observed decay, on the other hand, remained constant at about 100 μs across this pressure range. Additionally, introduction of oxygen into the chamber has a greater effect on the observed fluorescent intensity than on its decay. Only when the oxygen pressure was comparable to nitrogen did the fluorescence follow the pulse decay ($\sim 6 \mu s$).

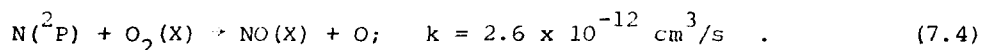
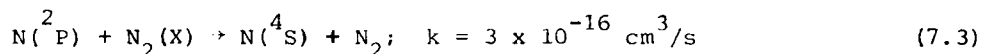
These results are greatly at variance with the unpublished observations of Murphy, where 0.1 torr O_2 in 400 torr N_2 reduced the decay to 10 μs and where a clear inverse dependence on N_2 pressure was observed. The small leak rate into the target chamber would have a constant flow, with

the possible contaminants accordingly having a concentration proportional to the chamber pressure for these constant flow experiments. The decay would be expected to be faster as pressure increased both for contaminant and N_2 quenching of $N(^2P)$. Furthermore, the estimated H_2O impurity concentrations would require faster than gas kinetic quenching rates for all chamber pressures in order to explain the 100 μs decay.

The expected kinetic processes are as follows. While the beam is on direct electron impact dissociation of N_2 is the likely source of $N(^2P)$, i.e.,

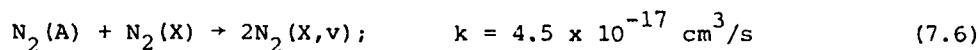
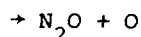
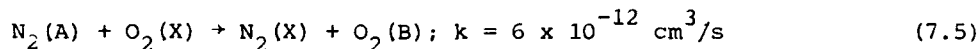


Deactivation of the metastable nitrogen (2P) can occur radiatively ($\tau = 6 s$)^{7.1} by reaction (7.1) or by quenching by ground state N_2 ^{7.4} and O_2 ^{7.5}



From the known and estimated concentrations in the target chamber, the decay times of the $N(^2P)$ concentration due to reaction (7.3) are 11-0.6 ms and reaction (7.4) are 60-3 ms for 10 and 200 torr chamber pressures, respectively, and an estimated upper bound air leak of 100 ppm.

The other reaction partner $N_2(A)$ is also deactivated through phosphorescence ($\tau = 2 s$)^{7.1} or by O_2 ^{7.6} and N_2 ^{7.7} quenching:



The calculated $N_2(A)$ decay times for O_2 quenching are 27-1.3 ms while decay times of 67-3.4 ms would be expected for N_2 . Thus it appears that $N_2(A)$ and $N(^2P)$ will be quenched between pulses and no significant buildup will occur during the gas residence time within the field of view. Quenching of these metastables by the above processes does not occur on the 100 μ s time scale observed in the experiment, however. $N_2(A)$ can also be created after beam termination by $N(^4S)$ recombination.

Quenching due to other contaminant species is unlikely because of the invariance of the observed decay with chamber pressure. The possibility exists that reaction (7.1) itself is the major loss mechanism for $N(^2P)$. The $N_2(1P)$ emission (B state concentration) remained constant over much of the experimental pressure range, and because O_2 quenching will prevent $N_2(A)$ buildup, the $N_2(A)$ concentration may also be roughly constant at all pressures. If the $N_2(A)$ concentration exceeds 10^{13} molecules/cm³, then the observed decay of $N(^2P)$ could possibly be explained by reaction (7.1), proceeding at a less than gas kinetic rate. It is obvious that more experimental work, in addition to modeling with a detailed N_2/O_2 kinetics package, is required to resolve this issue.

7.3.3. Fluorescence from O_2 and N_2/O_2 Mixtures

Relatively few spectral features were observed when oxygen was irradiated. Atomic lines at 777.2 nm and 844.6 nm were observed in a two to one intensity ratio. This agrees well with the measured line strengths which have a three to one ratio.^{7.8} (The upper states for both transitions are within the $2p^3 3p$ manifold.) No evidence of the 557.7 nm atmospheric green line ($2p^4 - 2p^4, ^1D - ^1S$) is observed, but its line strength is only 2% of the 777.2 nm line.^{7.8} Therefore, given the S/N, population of the low lying 1S state cannot be much greater than the $2p^3 3p$ levels. The atmospheric red line ($2p^4 - 2p^4, ^3P - ^1D$) has a very long lifetime (200 s) and is not observed.

The (b-X) atmospheric oxygen bands were observed at 762 nm over a range of pressures, but the fluorescence peaked at 20 torr oxygen pressure. At this pressure the total b-X intensity is 1/10 of the intensity of the

777.2 nm line. The ratio of the bandstrengths of these two transitions are 1:12^{7.1,7.8} and so the $O_2\ b(^1\Delta_g^+)$ is present in roughly the same concentration as the $OI\ 2p^3\ 3p$ state. Using the spectrometer no fluorescence from the (b-a) or (a-X) bands was observed. The integrating sphere was not in the chamber for these measurements, and a factor of six increase can be achieved through its use. The spectrally resolved (b-a) band was observed at several oxygen pressures using the interferometer. Unfortunately the signal was sufficiently weak so that pressure broadening of the (b-a) transition could not be measured in the present configuration. A loose upper bound can be placed on the bandstrength of the b-a transition: it is less than 4% of the 777.2 nm line intensity, which implies that the b state lifetime against transitions to the a state is longer than 150 seconds. This lower bound compares favorably with Noxon's^{7.2} estimate of 400 seconds. Again, utilization of the integrating sphere and recent experimental improvements (see Appendix I) should provide for increased signal levels in future measurements. When N_2/O_2 mixtures were irradiated, the $N_2(1P)$ bands dominated the 0.6-2.0 μm region. The NO overtone and $N_2O(2v_3)$ features at 4400 cm^{-1} were the only additional features observed at all pressures.

7.4 Summary and Future Plans

The near IR fluorescence from several series of measurements of electron irradiated N_2 and O_2 has been observed using detectors spanning the 0.6-3.0 μm region. In nitrogen the many observed transitions of the First Positive (B-A) system were analyzed with the help of a code developed for the prediction of synthetic spectra. Preliminary results demonstrate the excellent predictive capability of the code for the transition frequencies. A discrepancy may exist, however, between the predicted and observed bandshapes and more data is required for comparison. The $N_2(1P)0-0$ band transition was observed to decay an order of magnitude more slowly than the other 1P features. The observed pressure dependence of the decay did not vary inversely with chamber pressure as expected and this behavior is presently not understood. When oxygen was irradiated, the $O_2(b)$ state was created in concentrations comparable to excited atomic oxygen states. As a result, the (b-X) atmospheric oxygen band was easily observed, but due

to system response falloff, the (b-a) Noxon band could only be observed using the interferometer. This band is estimated to be weaker than the (b-x) band with a radiative transition probability of $< 7 \times 10^{-3} \text{ s}^{-1}$.

All of the observations reported in this section are preliminary and will require additional experimental and theoretical investigation before the reactions, bandshapes and transition probabilities of interest can be accurately determined. Recent experimental improvements have yielded substantial increases in signal levels and with the use of the integrating sphere, when appropriate, an order of magnitude gain in the detected fluorescence signal levels should be possible in future measurements.

REFERENCES

- 7.1 Defense Nuclear Agency, Reaction Rate Handbook, 2nd ed., M. H. Bortner and T. Bauser, eds., March 1972.
- 7.2 Noxon, J. F., "Observation of the ($b^1\pi_g - a^1\Delta_g$) Transition in O_2 ," Can. J. Phys. **39**, 1110 (1961).
- 7.3 Rogers, J. W. and Murphy, R. E., unpublished results.
- 7.4 Baulch, D. L., Drysdale, D. D., Horne, D. G. and Lloyd, A. C., Evaluated Kinetic Data for High Temperature Reactions. II. Homogeneous Gas Phase Reactions of the $H_2 - N_2 - O_2$ System. (Butterworths, London, 1973).
- 7.5 Husain, D., Mitra, S. K. and Young, A. N., "Kinetic Study of Electronically Excited Nitrogen Atoms, $N(2^2D_J, 2^2P_J)$, by Attenuation of Atomic Resonance Radiation in the Vacuum Ultra-Violet," J. Chem. Soc. Far. Trans. II, **70**, 1721 (1974).
- 7.6a. Meyer, J. A., Setser, D. W. and Stedman, D. H., J. Phys. Chem. **74**, 2238 (1970).
 - b. Dreyer, J. W., Perner, D. and Roy, C. R., J. Chem. Phys. **61**, 3164 (1974).
 - c. Dunn, O. J. and Young, R. A., Int. J. Chem. Kin. **8**, 161 (1976).
 - d. Young, R. A., Black, G. and Slanger, T. G., J. Chem. Phys. **50**, 303 (1969).
 - e. Slanger, T. G., Wood, B. J. and Black, G., J. Photochem. **2**, 63 (1974).
 - f. Callear, A. B. and Wood, P. M., Trans. Faraday Soc. **67**, 272 (1971).
 - g. Meyer, J. A., Klosterboer, P. H., and Setser, D. W., J. Chem. Phys. **55**, 2084 (1971).
 - h. Meyer, J. A., Setser, D. W., and Clark, W. G., J. Phys. Chem. **76**, 1 (1972).
- 7.7 Dreyer, J. W. and Perner, D., "Deactivation of $N_2(A^3\Sigma_u^+, v = 0 - 7)$ by Ground State Nitrogen, Ethane, and Ethylene Measured by Kinetic Absorption Spectroscopy," J. Chem. Phys. **58**, 1195 (1973).
- 7.8 Wiese, W. L., Smith, M. W. and Glennon, B. M., Atomic Transition Probabilities Vol. I, Hydrogen Through Neon, National Standards Reference Data Series NBS 4, (1966).

8. SURVEYS OF 3-4 μm EMITTERS

The preliminary experiments to detect NO fundamental and overtone radiation simultaneously with a single detector (see Sec. 4) were unsuccessful. The problem was then attacked using two different approaches. Possible sources for spectral noise were investigated and sufficient noise reduction was achieved to permit the measurement to be made. This investigation is reported in Sec. 9. Before the necessary noise reduction was achieved, a search for a spectral radiator detectible by both the PbSe and PbS detectors was instituted. This emission would then be used to obtain a relative calibration between the fundamental and overtone bands.

The spectral response curves of the two detectors narrowly define the optimum wavelength region for spectral emission potentially detectible by both. Approximate response curves for our PbS (at two operational temperatures 77 and 193 K) and PbSe (at 77 K) detectors are plotted in Fig. 8.1. A typical response for an indium antimonide detector is also drawn in that figure. It can be seen that cooling the PbS detector to 77 K results in a decreased response at its peak, but substantially enhanced its response in the 3.5 - 4.3 μm region. The response of the PbSe detector when operated at 77 K is considerably improved at all wavelengths over 193 K operation. The 3.3 - 4.5 μm region was thought to be the most promising for overlap, and gases likely to emit in the 2200 - 3000 cm^{-1} region were viewed with both detectors.

The InSb detector available at the time of these measurements was found to be noisy and did not generate spectra as cleanly as the PbSe (77 K) detector. It was not surprising that the NO fundamental and overtone bands could not be observed using this detector. A new InSb detector was ordered and in the meantime this survey was conducted. When mixtures of N_2 and O_2 were viewed with the noisy InSb detector only the NO fundamental with $v \leq 4$ was observed. (This is due to detector response cut-off at 5.5 μm .) At 100 torr N_2 /2 torr O_2 pressures, however, the N_2O (v_3) band at 2223 cm^{-1} was observed as shown in Fig. 8.2. No other emission (such as NO $\Delta v = 2$)

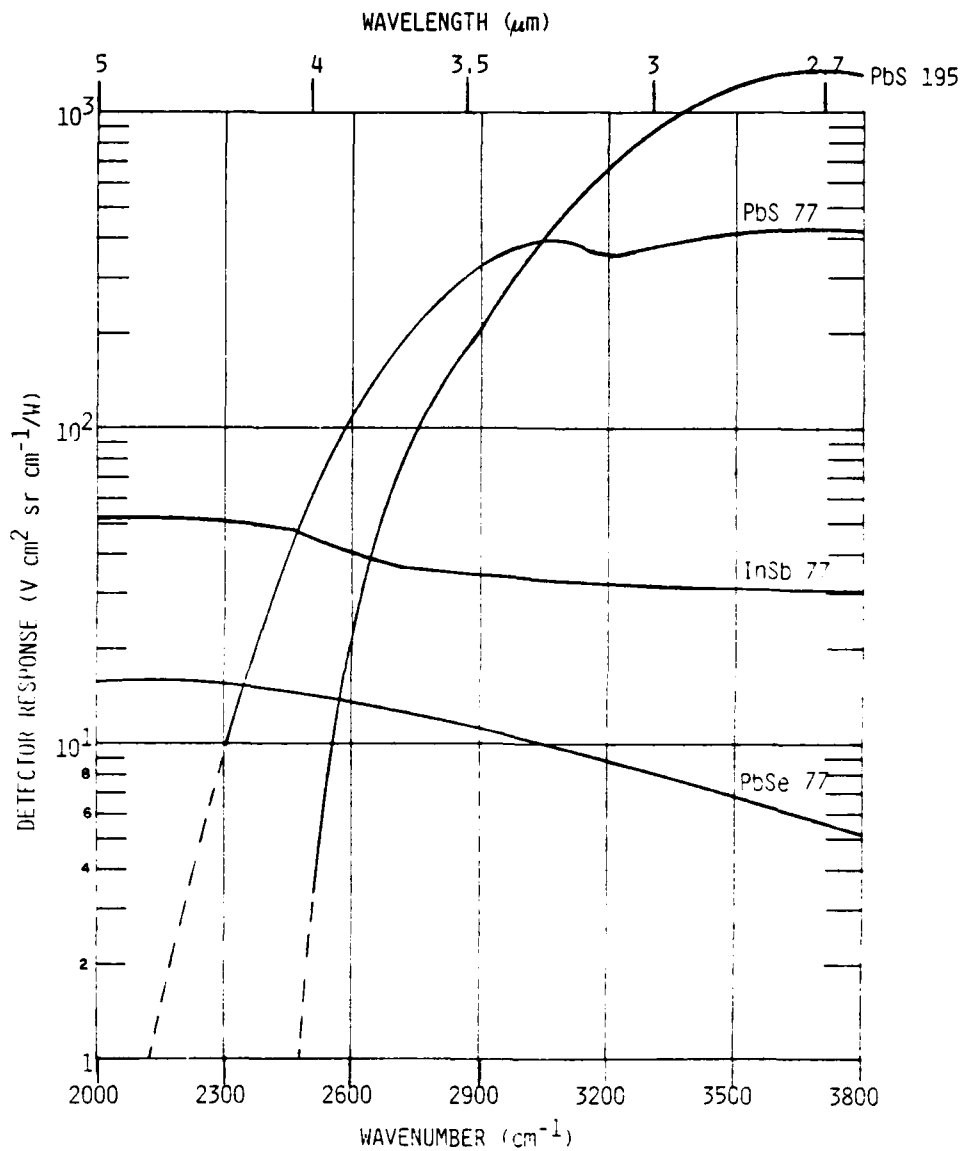


FIG. 8.1 Relative spectral responses of detectors available on LABCEDE for survey runs.

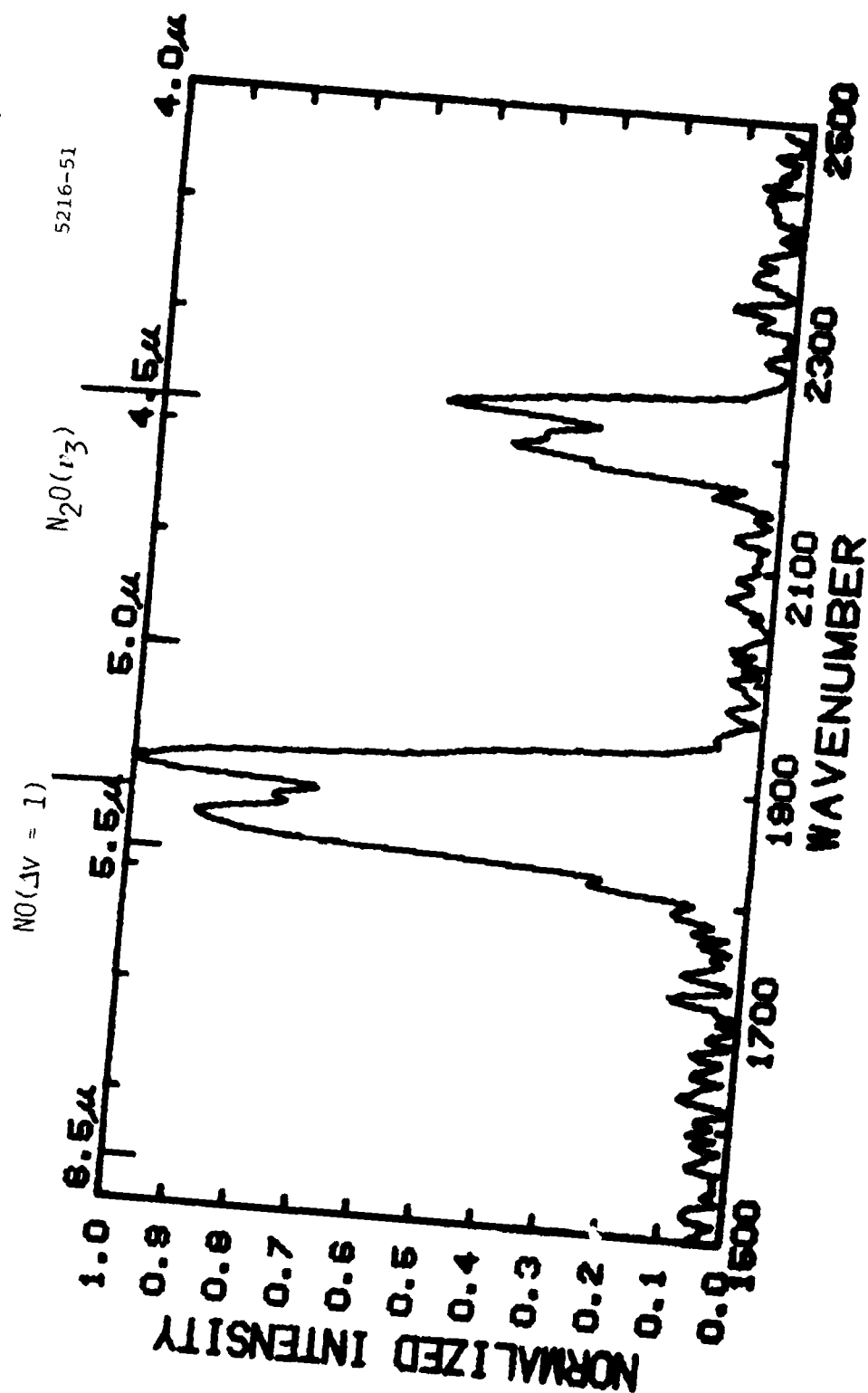


Fig. 8.2 Spectrum from N₂/O₂ mixture at 100 torr/2 torr viewed by a InSb detector. The NO fundamental is limited by bandpass of the detector beyond 5.5 μ m. The N₂O(ν_3) band is optically thin and exhibits branch structure. This spectrum is uncorrected for detector response.

beyond 2500 cm^{-1} was observed. From the discussion and computer modeling of Sec. 5, N_2O and NO_2 are expected to be formed in N_2/O_2 mixtures. The concentration of beam-created species is expected to be much greater here than under the conditions of Sec. 5 due to decreased flow and increased pressure. $\text{NO}_2(\nu_3)$ emission at 1620 cm^{-1} is beyond the response cut-off of this detector but was observed under these conditions with a PbSe detector.

It was initially hoped that the overlap emission could be observed under experimental conditions similar to the NO runs, i.e., same beam current, same N_2 pressure and flow, with just a trace of an additional gas added to provide the emission, so that the beam geometry within the non-uniform field of view of the detector did not vary significantly. As a secondary tactic, if an overlap emission could be found only at higher pressures, it would be viewed by the two detectors under identical experimental conditions and the effect of the differences in beam geometry between these conditions and those of the NO data runs assumed to be small. The NO data runs were confined to low pressure, rapid flow conditions to remove the effects of spectral contaminants such as OH. With these guidelines in mind, the fluorescence from various gas mixtures were observed.

Nitrogen/NO mixtures at 20 torr/4 torr were viewed with the PbSe detector at 77 K. In addition to NO, which appears to have a small electron excitation cross-section, NO_2 and $\text{N}_2\text{O}(\nu_3)$ bands were observed. A spectrum taken under these conditions is shown in Fig. 8.3. Both beam-created species radiate more strongly than the added NO. The small amount of $\text{CO}_2(\nu_3)$ emission is due to atmospheric CO_2 introduced when gas bottles were changed. NO emission was observed only from the lowest levels, indicating either strong quenching of the higher vibrational states or small production rates for those levels. None of these features were observed using the PbS detector at either 77 or 193 K. When N_2O was added to N_2 only $\text{N}_2\text{O}(\nu_3)$ emission was observed. As pressure was increased weak emission from N_2O combination bands could be observed. The spectrum of 90 torr N_2 with 4 torr of N_2O added is displayed in Fig. 8.4. The $\text{N}_2\text{O}(\nu_3)$ band is optically thick with red shifted hot-band emissions dominating the fluorescent features. The other features

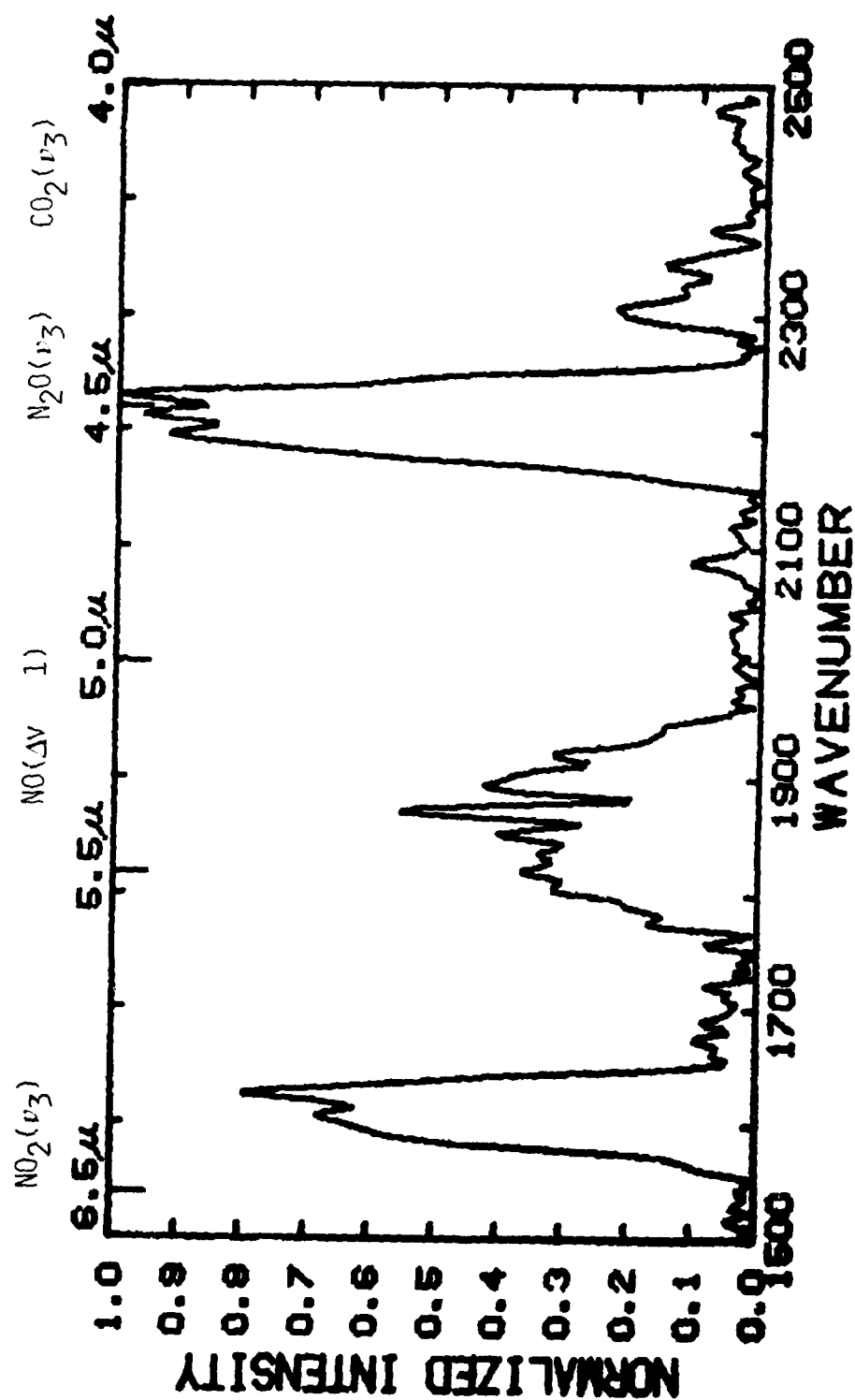


Fig. 8.3 Uncorrected spectrum from 20 torr N_2 , 4 torr NO using a PbSe detector at 77 K. The features are the $\text{NO}_2(\nu_3)$, NO fundamental and the $\text{N}_2\text{O}(\nu_3)$ feature. There is a weak $\text{CO}_2(\nu_3)$ feature at 2320 cm^{-1} due to cylinder changing.

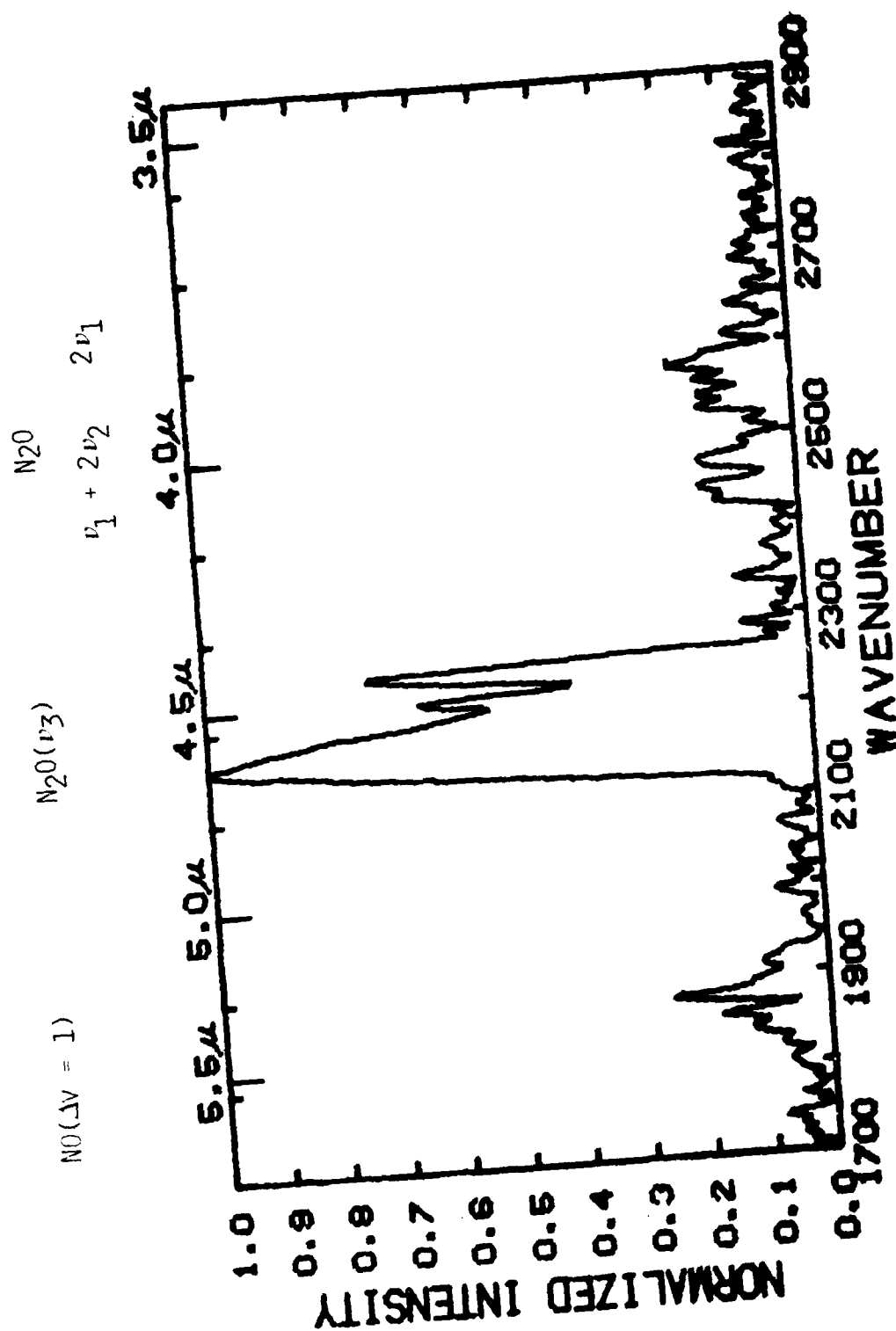
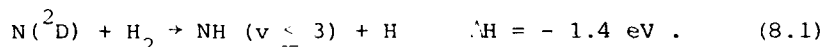


Fig. 1. Uncorrected spectrum of 5 torr N₂O/90 torr N₂ mixture using the PbSe detector at 7 K showing N₂O bands ν_3 , $\nu_1 + 2\nu_2$, and $2\nu_1$ as well as weak NO fundamental.

have been tentatively identified as the first overtone of the ν_1 band at 2560 cm^{-1} and the $\nu_1 + 2\nu_2$ combination band at 2470 cm^{-1} . Unfortunately, these features are so weak they could not be detected by our PbS detector. Interestingly, NO fundamental fluorescence from $v = 1, 2$ can also be weakly observed in Fig. 8.4.

When N_2/He and Ar mixtures were irradiated, atomic lines around $2\text{ }\mu\text{m}$ could be easily observed with the PbS detector, but no weaker lines could be detected further to the red and the PbSe detector was not sensitive enough at $2\text{ }\mu\text{m}$ to observe the atomic lines. Hydrogen was added to N_2 (20 torr) and $\text{NH}(\Delta v = 1)$ emission was observed from levels $v' \leq 3$ as shown in Fig. 8.5. This emission is weak as shown by the poor S/N of the data from our PbS detector at 77 K. The NH formation mechanism in the LABCEDE chamber has tentatively been identified as



The arguments in support of this formation mechanism and the expected formation kinetics and relaxation times will be presented in future reports. The rotational assignments of Fig. 8.5 are based on the previous identifications of Sakai.^{8.1} Emission from vibrational level 1 is curiously weak in these mixtures. The weak NH fundamental, although at a good frequency, could not be observed with the less sensitive PbSe detector at any N_2 pressure, and further studies of formation and relaxation rates of NH were not pursued. When methane was added to N_2 , NH fundamental emission was again observed with the PbS detector at 77 K. In addition, $\text{HCN}(\nu_3)$ fluorescence at 3300 cm^{-1} was observed as shown in Fig. 8.6. The P branch of HCN overlaps the NH emission, but it appears as if NH ($1 \rightarrow 0$) emission is not suppressed here as it was in N_2/H_2 mixtures. Considerable free radical based chemistry is occurring within the LABCEDE test chamber to permit HCN formation. The feature at 3650 cm^{-1} has not been identified. Unfortunately, even the stronger $\text{HCN}(\nu_2)$ feature could not be observed with our PbSe detector. As a cross-check on the possibility of impurities in the CH_4 giving rise to the HCN,

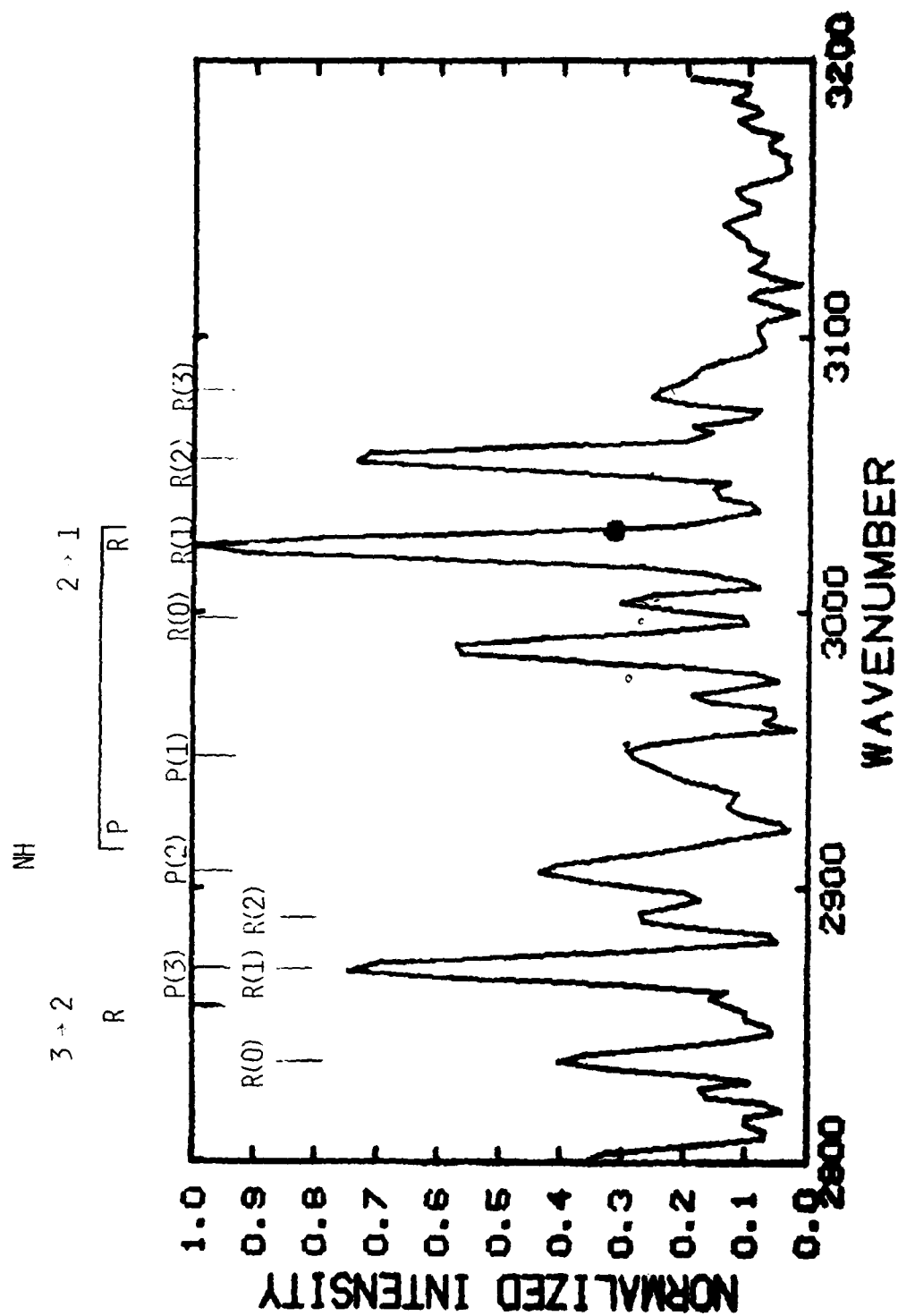


Fig. 8.5 Uncorrected spectrum from N_2 (20 torr)/ H_2 (1 torr) mixture using PbS detector at 77 K. Features have been identified as NH fundamental for $v = 2, 3$.

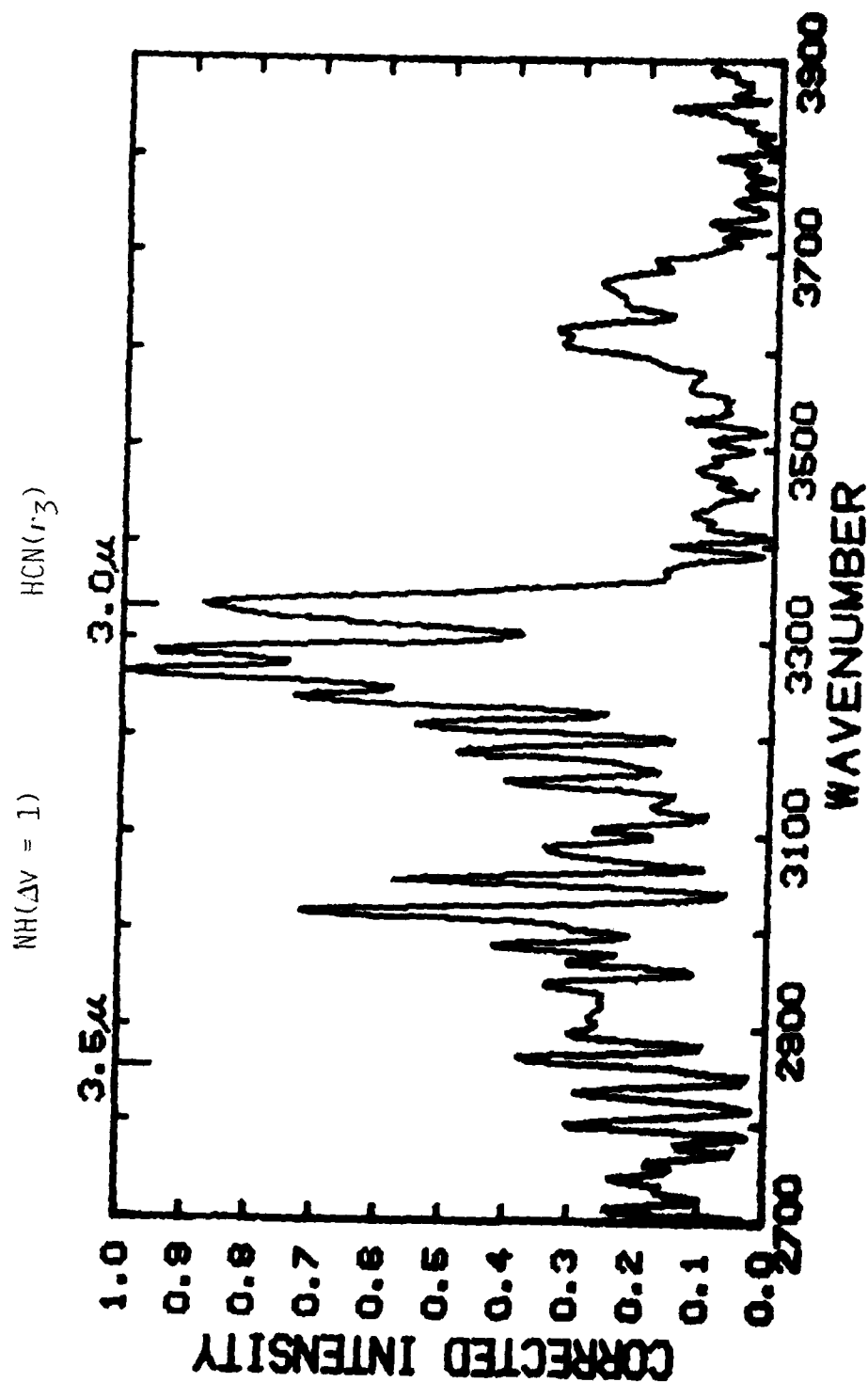


Fig. 8.6 Emission from 0.3 torr CH_4 , 20 torr N_2 mixture. NH, $\text{HCN}(\nu_3)$ features are observed. 3650 cm^{-1} feature is unidentified. Spectrum is corrected for PBS detector response (77 K).

CH₄/Ar mixtures were irradiated and no spectral features were observed with either detector.

The best spectral overlap occurred for CO₂(ν_3) emission when N₂/CO₂ mixtures were irradiated under conditions similar to the NO data runs. The PbSe detector observed the usual CO fundamental and CO₂(ν_3) emission bands. Detector response is relatively flat in this region, but atmospheric CO₂ strongly absorbs the ν_3 emissions.^{8.2} The PbS detector operating at 77 K observes CO overtone emission and the CO₂(ν_3) band. [This suggests a future measurements program for the CO Einstein coefficient ratios.] The response of the PbS detector is falling off rapidly in this region and changes significantly across the CO₂ bandwidth. As a result it was necessary to use the integrated intensity of the ν_3 band rather than comparing peak intensities with the two detectors. This uncertainty coupled with the atmospheric absorption place serious doubts on the accuracy of a relative calibration obtained using the ν_3 emission. Nevertheless, the deduced NO Einstein coefficient ratios based on this calibration agree with Billingsley's^{8.3} values to within 30%. Fortunately, interferometric noise sources were reduced and with the new InSb detector a direct measurement of the NO overtone and fundamental bands was possible, and it was not necessary to rely on the CO₂(ν_3) to provide a relative calibration (see Sec. 4). These survey measurements have not been repeated using the new InSb detector which should give much better signal to noise in the data for emitters in the 3.5 - 5.5 μ m region. Several fascinating observations were made during this survey and it is hoped that more detailed investigations will be possible in the future.

REFERENCES

- 8.1 P. Hansen, H. Sakai and M. Esplin, "Observation of NH Infrared Emission Using Fourier Spectroscopy," Proc. Soc. Photo-Opt. Instrument Eng. Vol. 191, ed. G.A. Vanasse, Aug. 1979, pp. 15-20.
- 8.2 R. E. Murphy, F. H. Cook, G. E. Caledonia, B. D. Green, "Infrared Fluorescence of Electron Irradiated CO₂ in the Presence of N₂, Ar and He," AFGL TR-77-0205, 15 Sept. 1977.
- 8.3 F. P. Billingsley, "Calculated Vibration-Rotation Intensities for NO(X² π)," J. Molec. Spect. 61, 53 (1976).

9. INTERFEROMETRIC NOISE SOURCES

9.1 Introduction

Preliminary experiments in the LABCEDE test chamber revealed that the simultaneous detection of NO fundamental and overtone fluorescence would be difficult. At that time the spectrally resolved overtone band fluorescence was at the spectral noise level. Nearly an order of magnitude improvement in S/N would be required to permit an accurate determination of the $A_{V \rightarrow V-2}/A_{V \rightarrow V-1}$ ratios. Because the peak of the fundamental band was observed to be five to six times as intense as the peak of the overtone, this would require S/N ratios approaching 100 in the fundamental region since noise is fairly uniformly distributed throughout the Fourier transformed spectrum. All attempts to make this measurement using lead selenide and lead sulfide detectors were unsuccessful, although cross-calibration using emission from another radiator observable with both detectors was partially successful (see Section 8).

From the theoretical curves for detector D* (detectivity in $\text{cm Hz}^{1/2}/\text{W}$) we felt that using an indium antimonide detector provided the best chance of observing emission at 5.4 μm and 2.7 μm . The long wavelength response of that detector decreases drastically beyond 5.5 μm . As a result, the entire fundamental band is not observed, only emission from vibrational levels 1-4. Experiments using the existing InSb detector (operating photo-voltaically at 77 K with preamplifier input nulled) revealed that it was far noisier than expected, having a D* two orders of magnitude below typical levels. A new detector was ordered from Infrared Industries in Waltham, and while awaiting its arrival a systematic investigation of other potential noise sources in the observed spectra was conducted. These sources include photon noise, source noise, digitizing noise and sampling errors, in addition to detector noise. We will now discuss each of these noise sources in detail and identify the major spectral noise sources and reductions achievable.

PRECEDING PAGE BLANK-NOT FILLED

9.2 Noise Sources

9.2.1 Detector Noise

The noise on infrared detectors is primarily determined by the fluctuations of the background photons incident on the detector. Detectors are rated while looking at a 295 K blackbody subtending 2π steradian field of view. A reduction in this noise level results if the viewing steradiancy is reduced using a cooled collar or mask. This noise level, however, will be independent of the signal intensity on the detector until the signal level is comparable to the background and its statistical fluctuations contribute to the total noise. Under these conditions an interferometer gains considerably over dispersive techniques, because the emission from all frequencies is simultaneously detected. This multiplex advantage results in a reduction in spectral noise levels over the interferogram noise levels. The detector noise is evenly spread over the transformed spectrum. Thus if emission is occurring at M resolvable frequencies, then^{9.1}

$$\left(\frac{N}{S}\right)_{\text{SI}} \approx M^{-1/2} \left(\frac{N}{S}\right)_{\text{INT}} \quad (9.1)$$

This equation becomes more accurate as M increases and the emission approaches a blackbody. The necessary experimental check on this source of noise is that the detectors are operating near their theoretical capability under our experimental conditions.

The effective Noise Equivalent Power (NEP) for each detector was calculated as follows:

$$\text{NEP} = \frac{\text{noise level (V)}}{\text{resistance (ohms)}} \times \frac{\text{electrons/s}}{A} \times \frac{\text{photons}}{\text{electron}} \times \frac{\text{joules}}{\text{photon}} \quad (9.2)$$

where the noise level measured (on a scope) takes amplification gains into account. As an example for the new indium antimonide detector (operated at 77 K in a photovoltaic mode with preamplifier input voltage nulled)

$$\begin{aligned}
 \text{NEP} &= \frac{1.5 \times 10^{-5} \text{ V}}{10^5 \text{ ohms}} \times \frac{6 \times 10^{18} \text{ e/s}}{\text{\AA}} \times \frac{2.5 \text{ photons}}{\text{e}} \times \frac{4 \times 10^{-20} \text{ J}}{\text{photon}} \\
 &= 9 \times 10^{-11} \text{ W}
 \end{aligned}$$

and

$$D^* = \frac{A_{\text{det}} \Delta f}{\text{NEP}} = 9 \times 10^{10} \text{ cm Hz}^{1/2} \text{ W}^{-1} \quad (9.3)$$

This detector is surrounded by a collar which extends down from the cold finger reducing the detector field of view to ~ 7 steradians. Further steradiancy reductions are not feasible because of the fast f/1 lens used to focus the light onto the detector. Infrared Industries measured the D^* of this detector to be $1.3 \times 10^{11} \text{ cm Hz}^{1/2} \text{ W}^{-1}$ using their own electronics. This is in good agreement with our value, and thus our experimental detection system and amplification network add little noise above the rated detector noise. The indium antimonide detector mentioned previously was found to be bad, but all other detectors tested were within a factor of two of their literature values of D^* . Thus our detector network is operating as well as possible and no significant gains in noise reduction could be achieved in this area.

9.2.2 Source Noise

The interferograms are created by sequentially sampling the detector signal every time the mirror moves $0.63 \mu\text{m}$. The mirror movement is followed by observing the interference pattern created using the monochromatic light from a Helium-Neon laser. The data is gathered every other zero crossing of the laser fringe pattern, about once a second. The detector signals for all electron beam pulses between zero crossings are averaged.^{9.2,9.3} As a result, low frequency variations of the source level will distort the interferogram. These variations could arise from atmospheric turbulence, vibrations of the interferometer, or fluctuations of the source either due to changes in the target chamber operating conditions or electron beam jitter. When source variations are significant there is actually a multiplex disadvantage because emission from all wavelengths is detected at all times, or according to Murphy^{9.1}

$$\left(\frac{N}{S}\right)_{SP} = M^{1/2} \left(\frac{N}{S}\right)_{INT} \quad (9.4)$$

Some obvious remedies included: insuring that the interferometer was well isolated vibrationally - that the isolation table was performing satisfactorily; enclosing the optical path-reducing effects of dust and turbulence; stabilizing the electron beam - adjusting its period to minimize 60 Hz pick-up, optimizing its position in the differential pumping apertures, and discarding runs which suffer long term intensity drifts of more than half a percent. The short term, pulse to pulse, jitter in the beam current was less than 3% typically and since 50 pulses were averaged during an interferogram mirror position, this jitter was effectively reduced to 0.4%. In order to quantify the effects of this noise level on the spectrum, computer simulations were carried out on a Prime 400 computer available at Physical Sciences Inc. to check the validity of Eq. (9.4).

Several interferograms having very low noise levels were digitized, input to the Prime computer and transformed using a Cooley-Tukey algorithm, believed to be similar to the one used on the AFGL PDP-15. There was excellent agreement (better than 99%) between the spectra reduced using the different methods in terms of intensities, spectral frequencies and integrated intensities. Both routines generated spectra which had an effective resolution slightly larger than theoretically possible. This was due to the finite detector size.

The data is sampled at mirror positions separated by $\lambda_{laser} = 0.6328 \mu m$. This means that the maximum wave number emission which can be detected free from spectral overlap is

$$\sigma_{MAX} = \frac{1}{2d} = 7901.4 \text{ cm}^{-1} \quad (9.5)$$

If the data is acquired at 1024 positions (2^{10}) on one side of center (zero path difference between the two arms of the interferometer) then the mirror has moved 0.0648 cm. The spectral resolution, $\delta\sigma$, then is the spectral range divided by the maximum number of resolvable frequencies N, or

$$\delta\sigma = \frac{\sigma_{\text{MAX}}}{N} = \frac{1}{2X} = 7.72 \text{ cm}^{-1} \quad (9.6)$$

Thus the larger the mirror movement, the greater the resolution (or the smaller $\delta\sigma$). For this mirror movement, the resolving power R is as expected

$$R = \frac{\sigma_{\text{MAX}}}{\delta\sigma} = 2X\sigma_{\text{MAX}} = N = 1024 \quad (9.7)$$

In actuality, the observed resolution obtained by viewing an atomic line is $\sim 10 \text{ cm}^{-1}$. The finite size of the detector ($r_{\text{det}} = 0.15 \text{ cm}$) sets the minimum size that a central interference fringe pattern can extend. As the mirror scans out from center, the pattern contracts. The intensity of the interferogram at a given mirror position x is the integrated emission from all frequencies, σ ,

$$dI(x) = \int_0^{\infty} B(\sigma) \cos(2\pi\sigma x) d\sigma \quad (9.8)$$

When off-axis rays of angle α are included in the analysis, Eq. (9.8) becomes

$$dI(x) = \int_0^{\infty} \int_0^{\Omega} B(\sigma) [\cos(2\pi\sigma x \cos\alpha)] d\sigma d\Omega \quad (9.9)$$

where $\Omega = \pi\alpha^2$ is the solid angle subtended. For small values of α , $2\pi\sigma x \cos\alpha \approx 2\pi\sigma x(1 - \alpha^2/2)$. The first zero of the fringe pattern occurs when a phase difference of π exists between the central ray maximum and the minimum point. Then

$$2\pi\sigma x \frac{\alpha^2}{2} = \pi \quad (9.10)$$

or

$$\alpha = \frac{1}{(\sigma x)^{1/2}}$$

Thus the size of the fringe pattern is inversely proportional to the frequency of the emission and the mirror path difference. The detector is either circular (InSb) or has a circular mask (PbSe, PbS) of radius 0.15 cm. The CaF_2 lens has a focal length of 3 cm, so that in the image plane

$$\alpha = \frac{.15}{3} = .05 \text{ rad}$$

Alternately the field of view at the experiment (as limited by the detector aperture) is 3.25 cm at 65 cm or $\alpha = .05$ rad. This field of view is circular and falls off from maximum in a geometric manner based on the fringe intensity pattern.

If the detector angular extent is used to set the minimum fringe pattern size, then

$$\alpha > \frac{\pi}{\sigma_{\text{MAX}} X} \quad (9.11)$$

where X is the maximum path difference. From Eqs. (9.6) and (9.7), we can then solve for the maximum resolution which can be achieved using this detector and lens,

$$\delta\sigma = \frac{\sigma_{\text{MAX}}}{2\pi} = 9.68 \text{ cm}^{-1} \quad (9.12)$$

as measured experimentally. This resolution is determined by the experiment, not by any subsequent apodization or truncation, and as a result both F.F.T. routines (at PSI and AFGL) generated spectra with the same resolution.

In order to observe the effects of source fluctuations on the transformed spectra, random noise was generated (using a random number generator routine) and added to the low noise interferograms. The amplitude of the noise added was a percentage of the interferogram DC level. These new noisy interferograms were then transformed and could be compared to the spectrum from the original interferogram. The spectra with no noise, 1%, 3%, and 10% noise added to the interferogram are shown in Figs. 9.1 - 9.4.

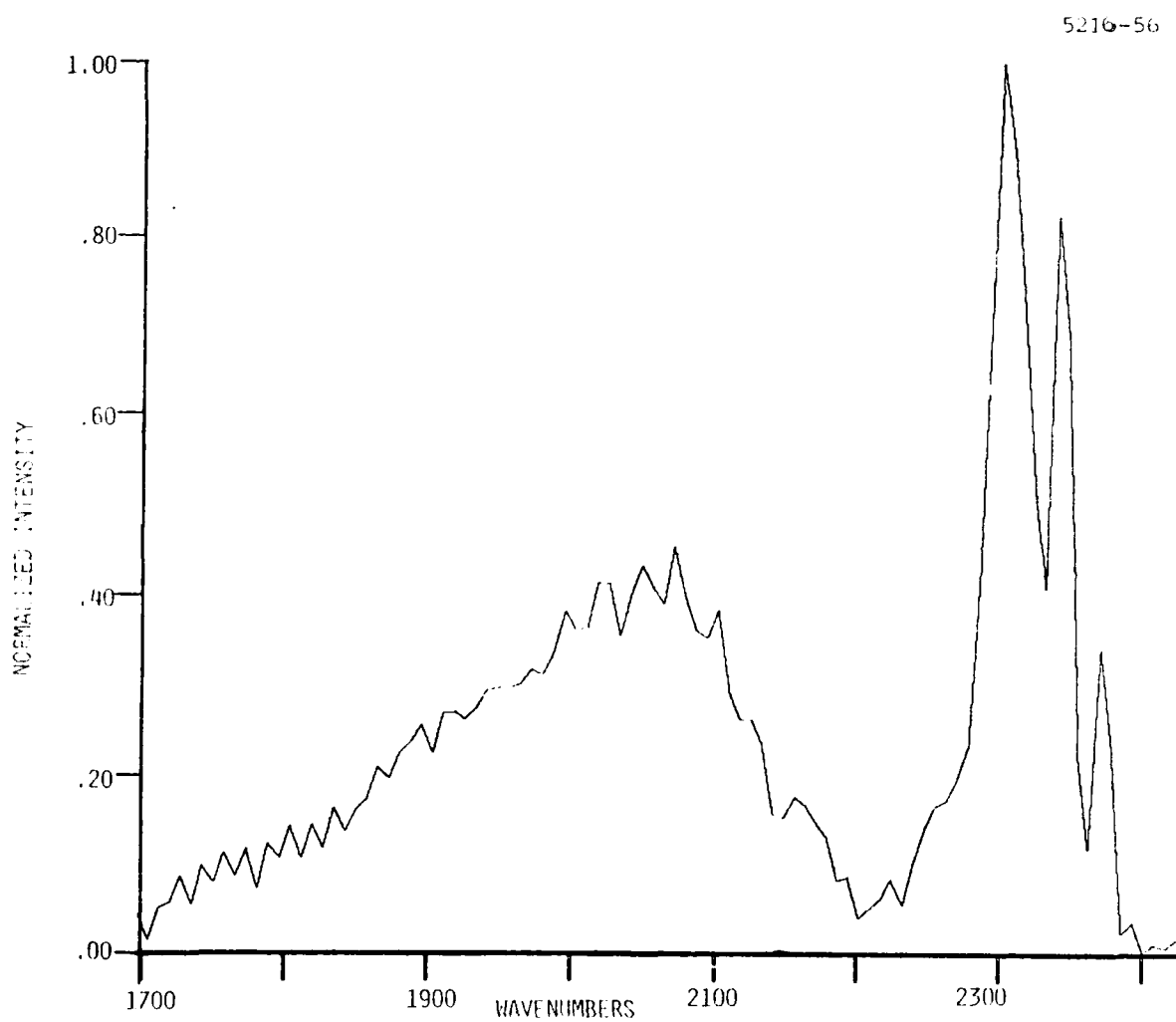


Fig. 9.1 Spectrum from transformed interferogram at beam termination from a 0.14 torr CO₂/8.9 torr Ar mixture. The interferogram has low noise and no additional noise has been added. Maximum intensity is 7.1×10^{-7} W/cm² sr cm⁻¹.

5216-57

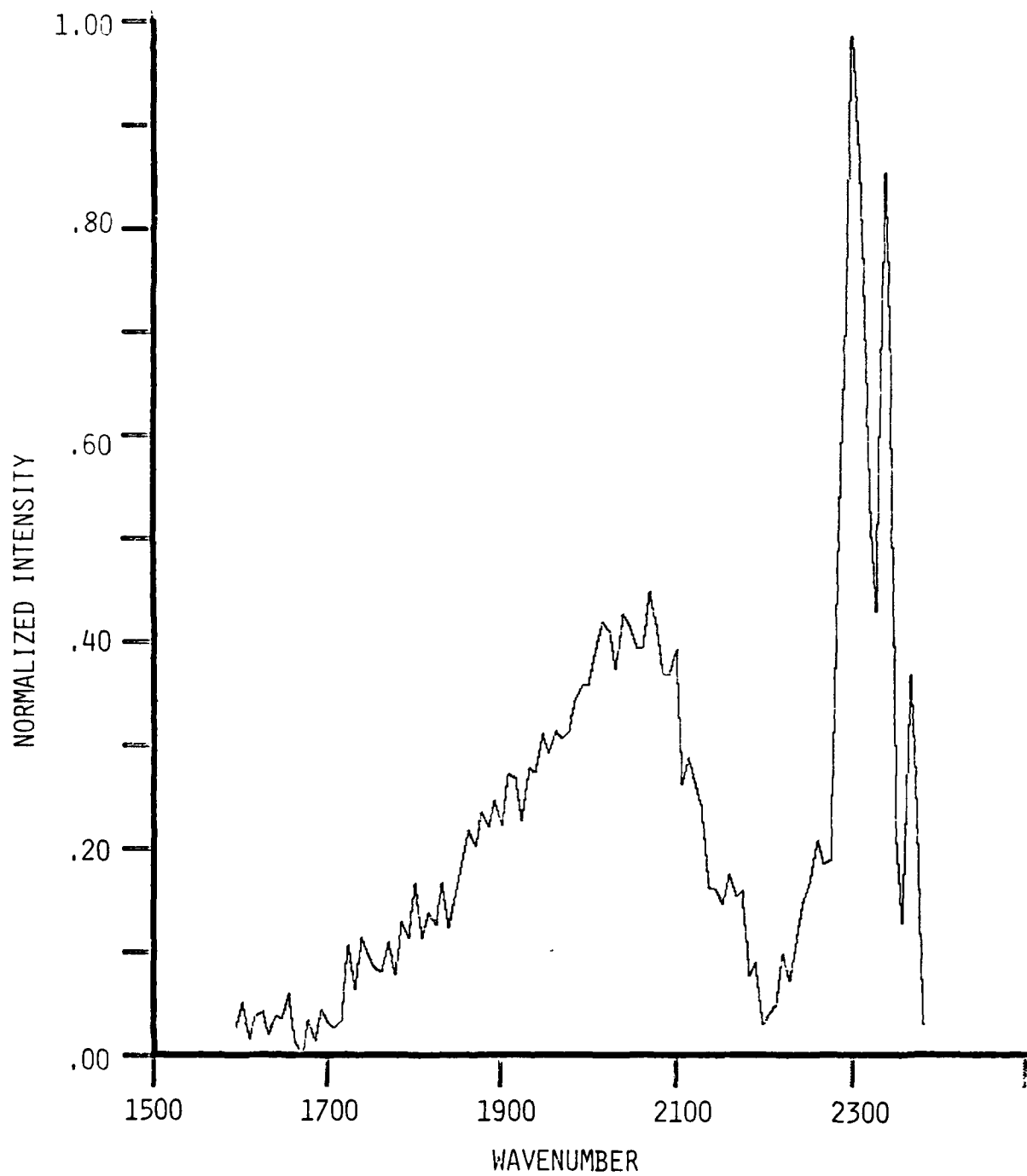


Fig. 9.2 - Spectrum from transformed interferogram with 1% noise added.
Maximum intensity is $7.1 \times 10^{-7} \text{ W/cm}^2 \text{ cm}^{-1} \text{ sr.}$

AD-A114 389

PHYSICAL SCIENCES INC WOBURN MA
LABCEDE STUDIES.(U)

F/G 20/7

UNCLASSIFIED

SEP 81 B D GREEN, G E CALEDONIA, L G PIPER
PSI-TR-261

F19628-78-C-0115

AFGL-TR-82-0060

NL

3-3

21-2-89



END

DATE

FILED

6 82

DTIC

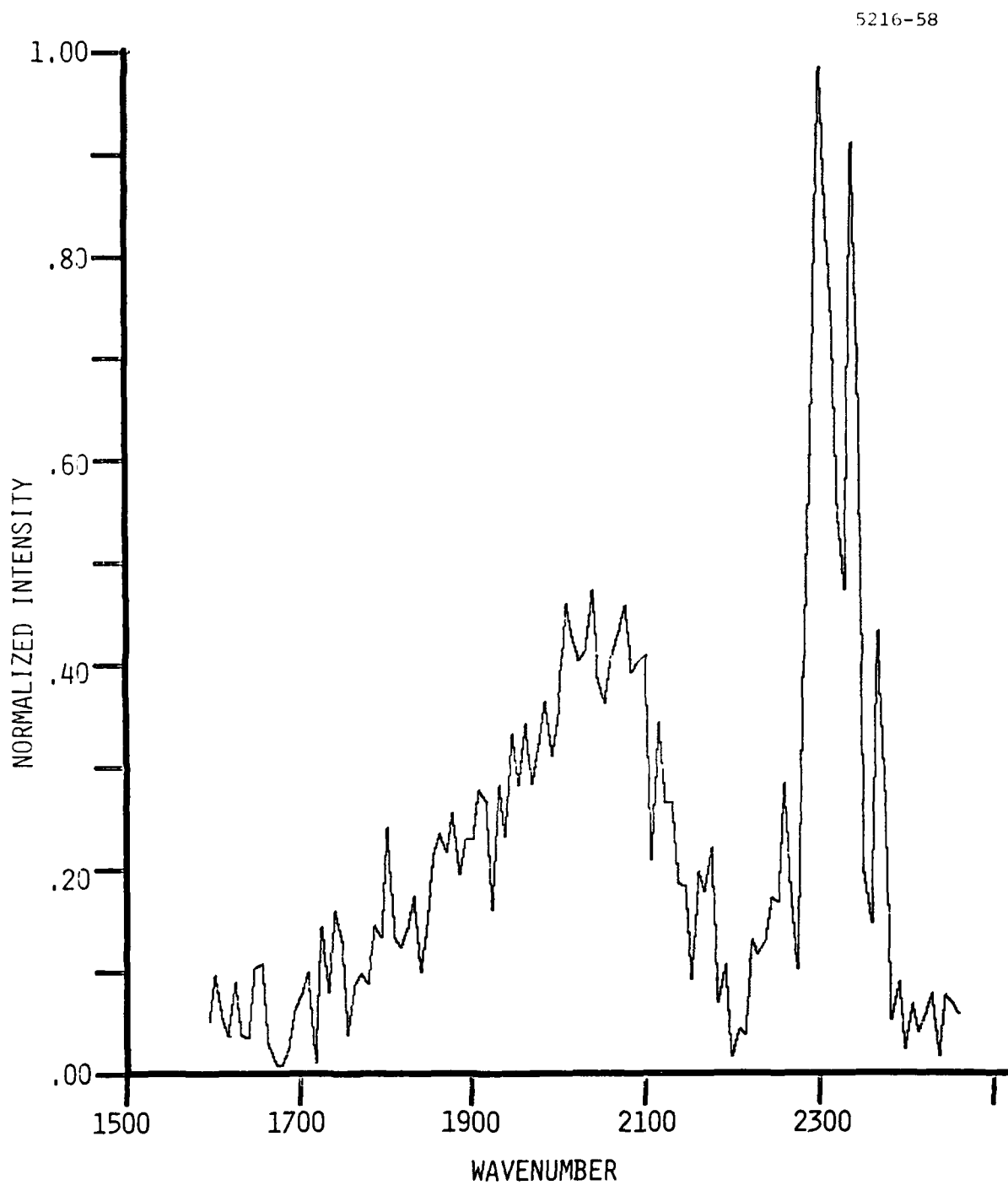


Fig. 9.3 - Spectrum from transformed interferogram with 3% noise added.
Maximum intensity is $7.0 \times 10^{-7} \text{ W/cm}^2 \text{ sr cm}^{-1}$.

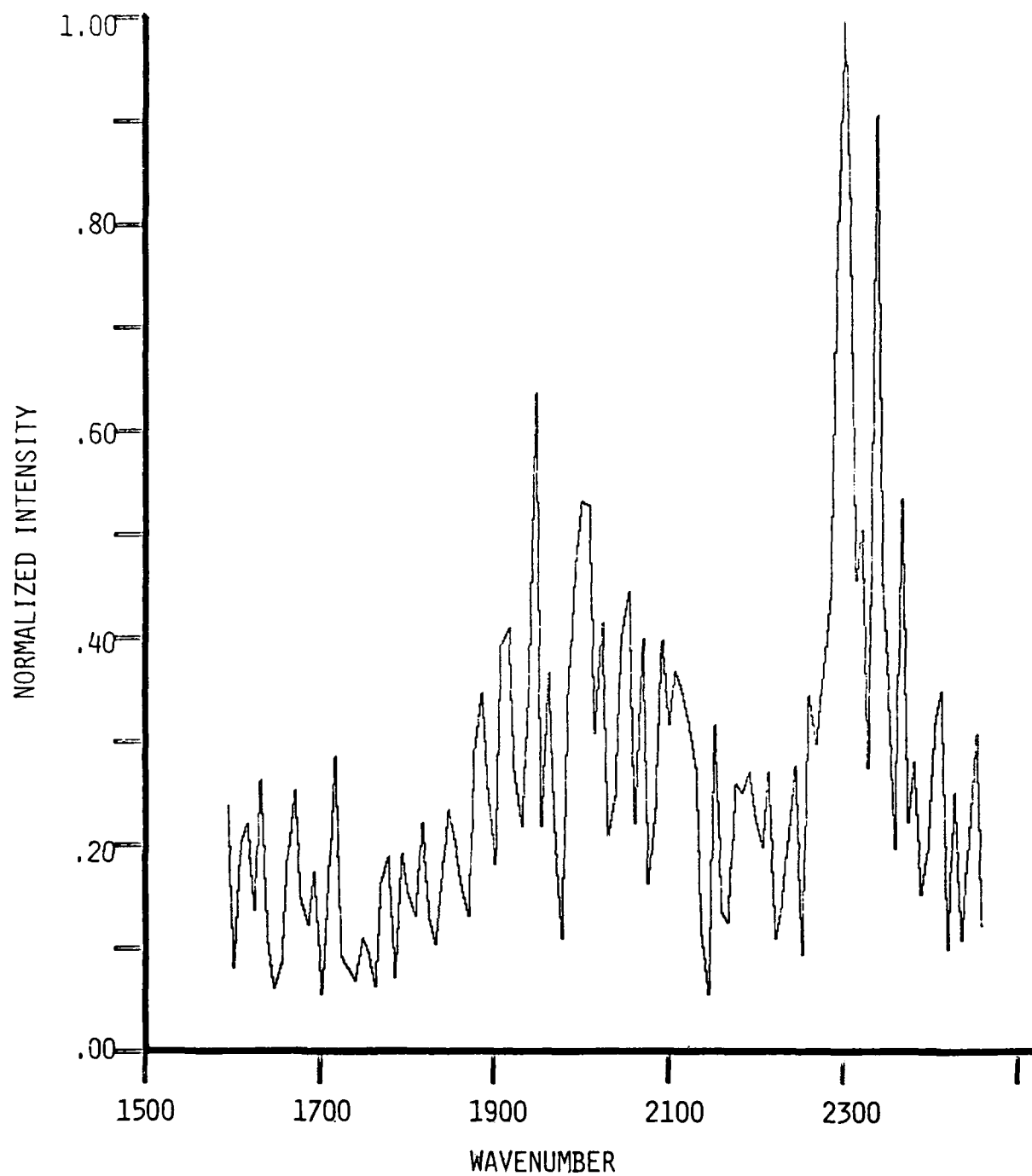


Fig. 9.4 - Spectrum from transformed interferogram with 10% noise added.
Maximum intensity is $8.1 \times 10^{-7} \text{ W/cm}^2 \text{ sr cm}^{-1}$.

The interferograms used in this exercise were from previous CO_2/Ar runs using a PbSe detector. $\text{CO}(v)$ fundamental and $\text{CO}_2(v_3)$ emission contribute to the interferogram. The interferogram used for these calculations corresponds to the signal at beam termination. This data was chosen because of the large S/N level. The conclusions drawn should be equally valid for the NO emission of interest here.

It can be seen that the spectrum rapidly degenerates as the noise level increases. A spectrum from the interferogram with 50% random noise added had no distinguishable spectral features above the noise. It should be noted in Figs. 9.1-9.4 that the envelope of the emission is unchanged as noise is added, the random noise is distributed throughout the transformed spectrum. If these "noisy" spectra are then compared with synthetic spectra using the least-square fitting routine, the effects of source noise on the calculated populations can be observed. The fit populations of CO vibrational levels 1-12 are plotted in Fig. 9.5 for cases when no noise, 1% and 3% random noise was added to the interferogram. The absolute average error in the calculated populations is 11% for the case when 1% noise was added, 40% for the 3% case. Thus it appears as though Eq. (9.4) is an accurate representation - there is a multiplex disadvantage when source noise is the dominant interferometric noise. Moreover, the calculated populations may be less accurate than the spectra. This exercise highlights the importance of source noise reduction. The effective short term jitter (0.4%) may give rise to a 4% error in the calculated fundamental populations, possibly a 20% error in the overtone populations, if the computer modeling accurately represents this noise. Similarly, the long term drifts must be kept as small as possible, preferably 0.5% or smaller.

In the work of Section 4, there were several sets of data taken under conditions when source noise fluctuations were small and the NO overtone and fundamental emission could be satisfactorily observed. As a result, more permanent system changes to reduce source noise were not attempted. Nevertheless, for future work when high signal to noise is desired the following design changes should be considered. The beam pulse should be synchronized

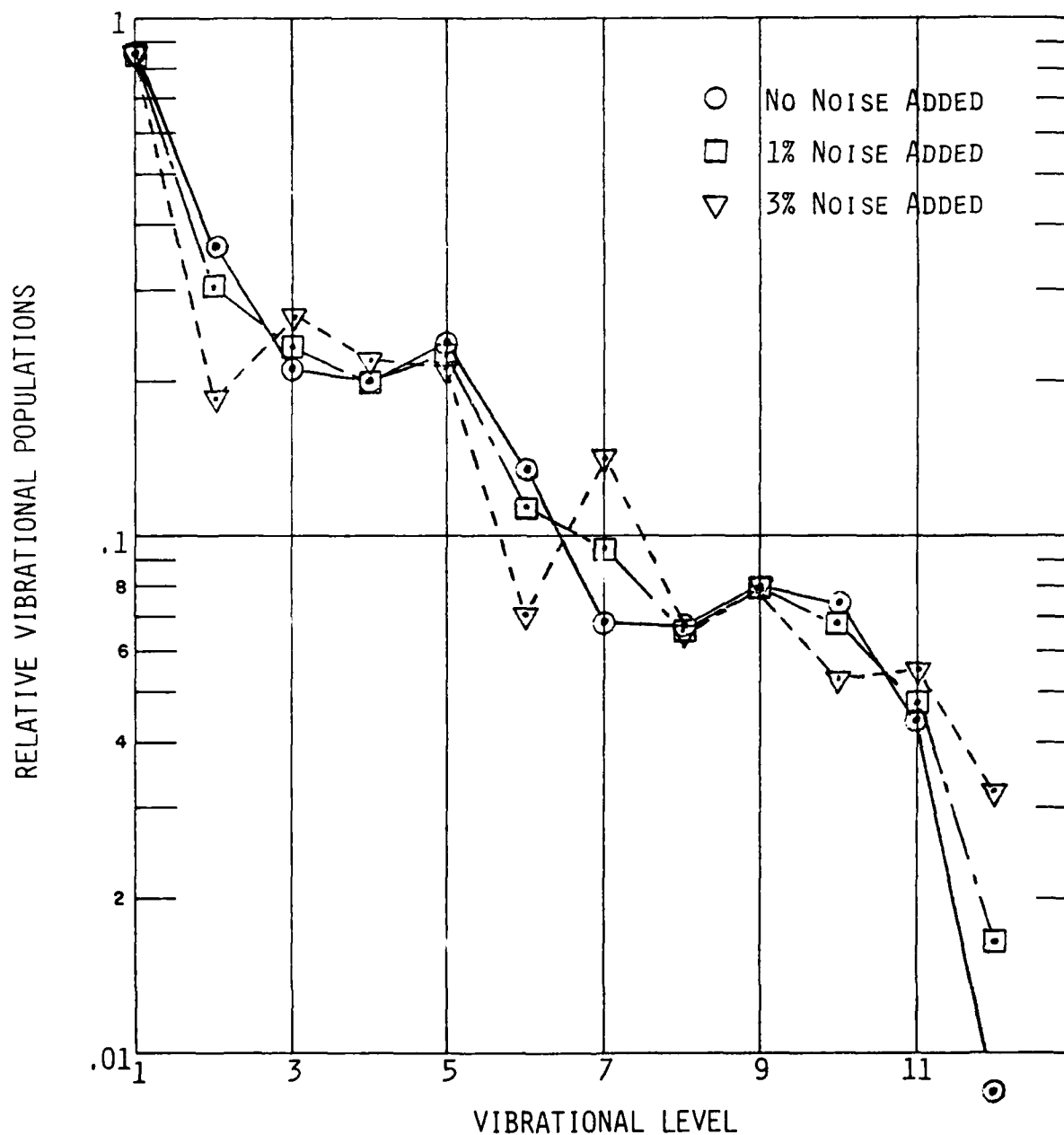


Fig. 9.5 -Vibrational populations calculated from previous spectra with varying amounts of noise added to the original interferogram.

to line frequency. The present ripple in the current detected in the target chamber may be due to pickup in the steering coils. The filament is heated by a regulated DC supply, the pulse network puts out a 40 V pulse free from ripple. The ripple only becomes significant after the beam has passed through the differential pumping nozzles where small variations in beam steering affect the fraction of the beam passing through these tiny apertures. Additionally a feedback network could be constructed to eliminate long term drift due to supply voltage variations.

9.2.3 Digitizing Noise

The analog detector signal is sampled by a 10-bit A/D converter, then stored on magnetic tape. The system dynamic range is thus effectively limited to 10^3 (2^{10}). The error introduced onto the interferogram by the digitizing process will be a variation of the interferogram intensity in a random manner (for non-periodic interferograms). The effect of this noise on the transformed spectra and calculated populations should be similar to the source noise fluctuations discussed above. If the full dynamic range of the A/D converter is utilized, then the error introduced onto the interferogram points is at most 0.1% which would give rise to a 1% error in the populations calculated from the spectra. For the NO data, the full signal on the detector has a large background component, especially for the PbSe detector with excellent long wavelength response. For this detector, and to a certain extent for the InSb detector, some of the 300 K background emission is along the interferometer optical axis and falls within the detector spectral bandpass. As a result, each interferogram contains a contribution from a 300 K blackbody. Subtraction of the interferogram at a reference time effectively removes this contribution from the spectra. However, the raw data interferograms may be dominated by this contribution and the NO fluorescence component of the interferogram will not span the full dynamic range, possibly resulting in significant spectral noise arising from the digitizing. As a check on this, interferograms were simultaneously recorded on paper tape and on the computer. The component of the fluorescence arising from beam irradiation was separated from the background emission using a lock-in amplifier. The output of the amplifier was then sampled

with a digital voltmeter to four significant figures (10^5 dynamic range) and punched onto paper tape. In this manner the NO component of the detector signal was amplified to occupy the full 10^5 dynamic range. This data was transformed and compared with the spectra from the computer-acquired data. No significant difference in noise levels was observed. For these runs the spectral noise level was a few percent of the peak of the fundamental intensity. Thus it can be concluded that the digitizing errors are not the dominant interferogram noise source, but to be certain, care should be taken to fill the entire dynamic range of the A/D converter.

9.2.4 Photon Noise

In the infrared the dominant source of detector noise is the fluctuations or photon noise of the background radiation. As discussed above, interferometric techniques gain over dispersive methods when the source intensity is comparable to the photon noise of the background (multiplexing). If the signal itself is intense enough that its photon noise dominates the detector noise, the multiplex advantage is not realized.^{9.1,9.4} This situation is not felt to apply to the present set of measurements. As an interesting aside, the photon noise is greatest for the intense spectral features. This noise is spread over the entire transformed spectrum when an interferometer is making a measurement.^{9.1} The spectrum from a dispersive instrument exhibits the noise associated with each feature. Thus weak lines or bands (such as the overtone) may be obscured in the distributed noise of the transformed spectrum, and a dispersive technique may be preferable for these types of measurement, if the signal levels are high enough that the throughput advantage is not required.

9.2.5 Sampling Errors

If the actual mirror position at the time of data acquisition is at a slightly different place on the fringe pattern for each sample, then satellite lines having the appearance of noise will be generated in the spectrum. The interferogram intensity for a monochromatic line at any path difference, $I(x)$, is (following the treatment of Sakai)^{9.5}

$$I(x) = B(\sigma) \cos 2\pi \sigma x \quad (9.8)$$

If the sampling occurs with a periodic error, then the path difference at which sampling occurs, x' , is

$$x' = x + \beta \sin 2\pi \epsilon x \quad (9.13)$$

where β is the amplitude and $1/\epsilon$ is the period of the error. Then the measured interferogram is

$$I(x') = B(\sigma) \cos 2\pi \sigma (x + \beta \sin 2\pi \epsilon x) \quad (9.14)$$

and for small amplitudes β

$$I(x') = B(\sigma) [\cos 2\pi \sigma x - \pi \sigma \beta \cos 2\pi (\sigma + \epsilon) x + \pi \sigma \beta \cos 2\pi (\sigma - \epsilon) x] .$$

The satellites are at frequencies $(\sigma + \epsilon)$, and $(\sigma - \epsilon)$ and have heights of $\pi \sigma \beta$ relative to the main feature. Random errors can be written as the sum of periodic terms. For this case

$$I(x') = B(\sigma) \left[\cos 2\pi \sigma x - \sum_{i=1}^K \pi \sigma \beta_i \cos 2\pi (\sigma + \epsilon_i) x + \sum_{i=1}^K \pi \sigma \beta_i \cos 2\pi (\sigma - \epsilon_i) x \right] . \quad (9.15)$$

If the average sampling **error** can be characterized by a standard deviation $\langle \Delta x \rangle$, then the heights of the satellites can also be characterized by a standard deviation,

$$\langle \gamma \rangle = \pi \sigma \langle \beta \rangle = \pi \sigma (\sqrt{K}/\sqrt{N}) \langle \Delta x \rangle \quad (9.16)$$

where N is the number of samples, K the total number of modes excited by errors. If $\langle \gamma \rangle$ is comparable to the spectral noise level from other sources, it contributes to the total noise. This bound places a constraint or tolerance on the acceptable errors $\langle \Delta x \rangle$.

$$\langle \Delta x \rangle = (N/S)_{sp} \left(\frac{\sqrt{L}}{\pi} \right) \frac{1}{\sigma \sqrt{N}} \approx (N/S)_{sp} \left(\frac{\sqrt{L}}{\pi} \right) \frac{\delta \sigma^{1/2}}{\sigma^{3/2}} \quad (9.17)$$

A more careful derivation^{9.4} gives $\sqrt{L}/\pi \sim 6$. Thus it can be seen that for a 1% spectral noise level at 3720 cm^{-1} and 10 cm^{-1} ($N=1024$) resolution, the standard deviation of the sampling errors must be less than 60 \AA or about 1% of the sampling distance. Electronic filtering of the laser fringe pattern is employed to reduce noise levels of the signal. This smoothing would tend to distort the zero crossing position if the mirror was not uniformly scanning. As the cutoff frequency of the low pass filter was increased from 2 to 20 Hz, the spectral noise level for comparable runs was observed to decrease slightly. If the cutoff frequency is too high, noise on the fringe pattern could also give rise to zero crossing errors. Thus care must be taken to optimize the cutoff frequency of the filter on the fringe pattern to prevent spectral noise. An obvious remedy for this situation is the improvement of the laser detector amplification network to reduce noise to negligible levels so that no filtering is necessary.

9.2.6 Summary of LABCEDE Interferometric Noise Sources

As a result of this investigation, we have clearly identified source variations as the major contributor to noise in the transformed spectra of the existing system. Any improvement in source stability will result in significant increases in the observed spectral signal to noise. Possible system modifications mentioned above are recommended if future high signal to noise measurements are planned. An additional noise source was identified to be an average error in the measured zero crossing values. This was remedied by reducing the filtering of the laser fringe pattern. A more satisfactory solution would be improvement of the laser fringe amplification electronics to reduce noise sufficiently so that filtering is not required. This investigation was also valuable because we determined that the detectors and amplification network were operating near their theoretical limits. It was also found that little distortion of the interferogram resulted from digitizing

errors, but that the full range should be employed. Alternately, the number of sampling intervals could be increased to 2^{12} (4096) decreasing the introduced errors by a factor of four.

In light of these conclusions, the system performance was modified sufficiently so that very low noise data could be acquired. Signal to noise levels of 10/1 in the overtone region were obtained, corresponding to a 50/1 signal to noise in the fundamental. Additionally, both fluorescence bands were observed with the InSb detector. The NO populations in the overtone could be determined with sufficient accuracy that the absolute values of the $A_{v \rightarrow v-2}/A_{v \rightarrow v-1}$ ratios for NO could be measured to 10% - 20% accuracy as described in Section 4 of this report.

9.3 Interferometer Optical Misalignment

As part of previous measurements programs, attempts were made to measure absolute intensities of the infrared fluorescence. Significant variations in the calculated values from day to day prompted a thorough investigation of the calibration process. It was discovered that the fundamental Fourier relation was not being satisfied, i.e.,

$$I_{\text{det}}(x) \neq \int_0^{\sigma_{\text{max}}} B(\sigma) \cos 2\pi \sigma x \, d\sigma \quad (9.18)$$

The observed intensity on the detector (volts) at large x was greater than the integrated spectral intensity (V/cm^{-1}). This error exists prior to detector response correction and cannot be associated with the calibration process. Additionally, the FFT program on the PDP-15 produced spectra which accurately matched those generated with the PSI transform routine (see Section 9.2.2). As a result, we decided that this effect might be associated with interferometer optical alignment due to excellent reproducibility within a single day's data, but poor agreement between data acquired months apart.

Two sets of data were acquired viewing a blackbody through a notch filter with two bandpasses at 2100 cm^{-1} and 4900 cm^{-1} . For one run the interferometer was severely misaligned (1-1/2 complete fringe shifts would occur as the observer's eye swept across the detector plane); for the other run the interferometer was carefully aligned so that a fringe shift of less than 1/4 fringe occurred. The transformed spectra acquired from these runs are displayed in Figs. 9.6 and 9.7 for the misaligned and aligned runs, respectively. Misalignment decreased the value of $\int B(\sigma) d\sigma$ calculated. For the aligned case the ratio of $\int B(\sigma) d\sigma$ to I_{det} was 1.025/1 when all frequencies were integrated. When just the emission in the bandpasses was considered, their ratio was 0.89/1. Additionally the ratio of the intensities in the two bands was 0.87/1. These results are summarized in the table below. When the interferometer was misaligned, the total intensity on the detector was unchanged but only 84% of this value appeared as spectral intensity anywhere: 70% appeared in the two bandpasses. Moreover, the two bandpasses were now of comparable intensity.

TABLE 9.1
COMPARISON OF SPECTRAL INTENSITIES

	Aligned	Misaligned
I_{det}	$2.6 \times 10^{-4} \text{ v}$	$2.8 \times 10^{-4} \text{ v}$
$\frac{\int_0^{\sigma_{\text{MAX}}} B(\sigma) d\sigma}{I_{\text{det}}}$	1.025	0.84
$\frac{\int_{1900}^{2500} B(\sigma) d\sigma + \int_{4600}^{5100} B(\sigma) d\sigma}{I_{\text{det}}}$	0.89	0.70
$\frac{\int_{1900}^{2500} B(\sigma) d\sigma}{\int_{4600}^{5100} B(\sigma) d\sigma}$	$\frac{1.08 \times 10^{-4}}{1.24 \times 10^{-4}} = 0.87$	$\frac{1.00 \times 10^{-4}}{9.8 \times 10^{-5}} = 1.02$

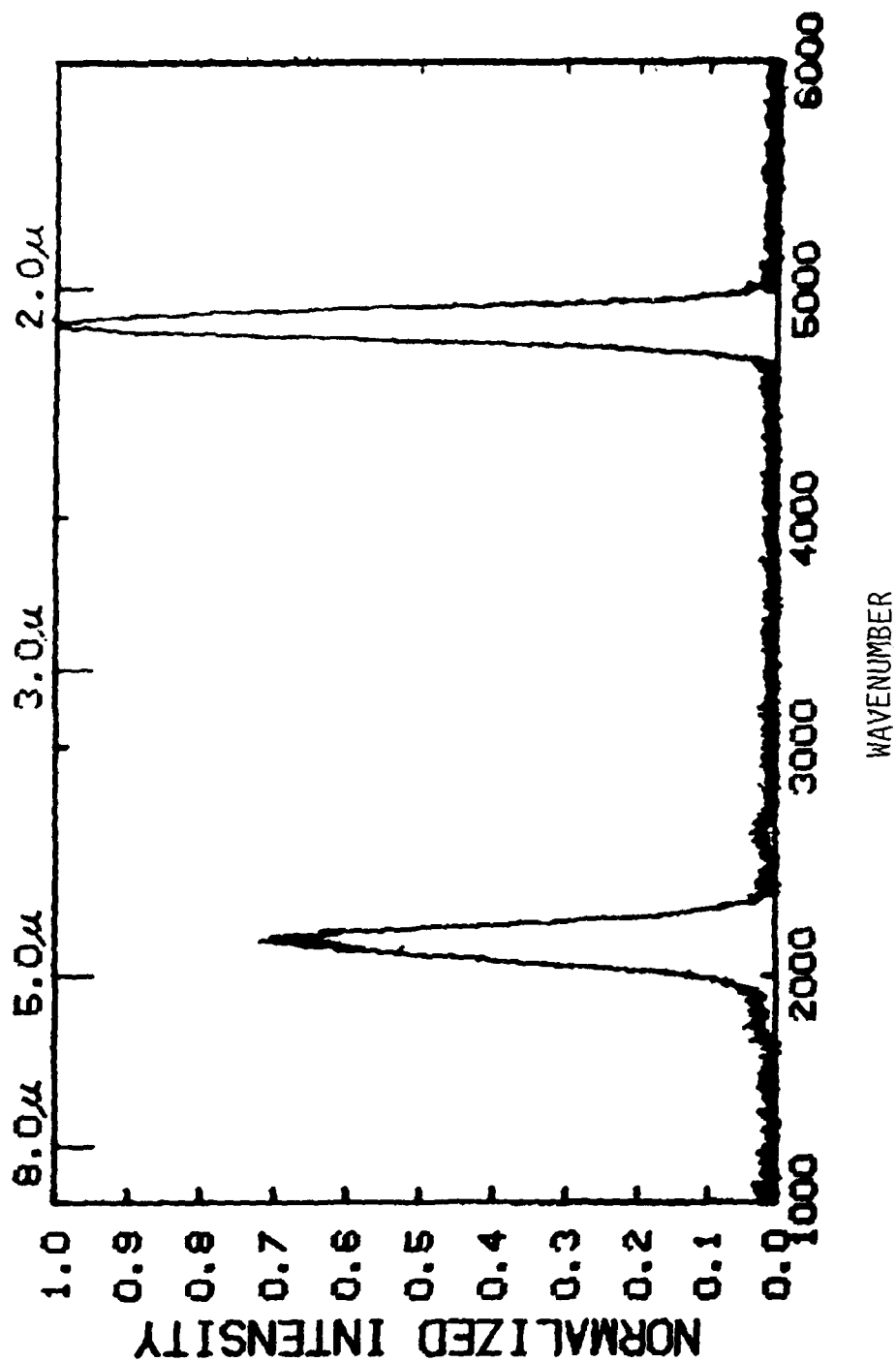


Fig. 9.6 - Spectrum of blackbody (1173 K) viewed through a filter with a PbSe detector at 77 K. The interferometer was carefully aligned prior to the run. The uncorrected maximum intensity is $7.9 \times 10^{-7} \text{ V-cm at } 4850 \text{ cm}^{-1}$.

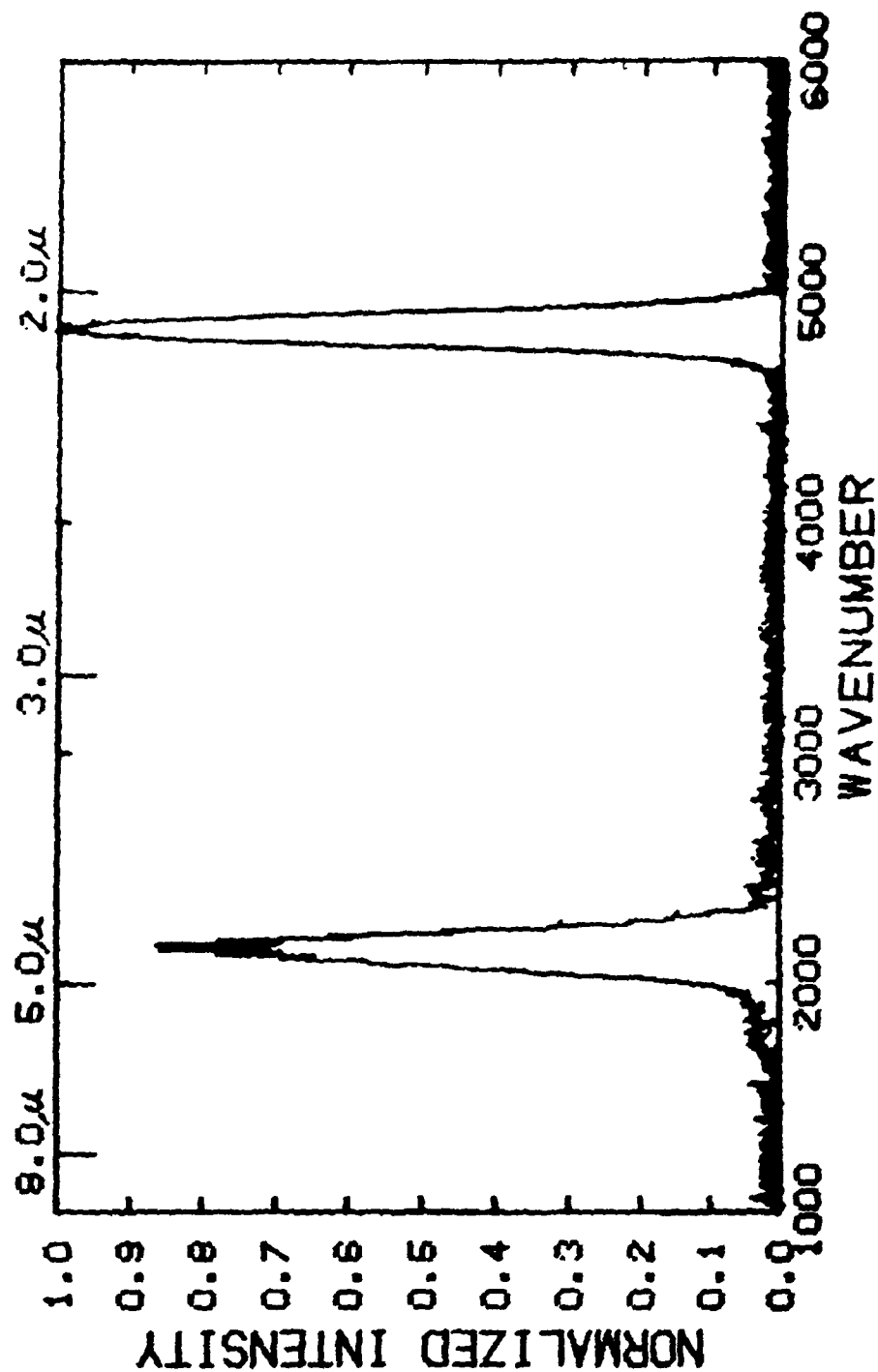


Fig. 9.7 - Spectrum of blackbody viewed under the same conditions as Fig. 9.6, except interferometer was poorly optically aligned for this run. The uncorrected maximum intensity is 6.1×10^{-7} V-cm at 4850 cm^{-1} .

The misalignment had a much more dramatic effect on the intensity of the large wavenumber bandpass; the 2100 cm^{-1} /feature was relatively unaffected by the process. The larger wavenumber emission forms a more compact fringe pattern at the detector than the $5 \text{ }\mu\text{m}$ radiation. It is felt that this smaller fringe pattern will be more sensitive to optical misalignment and thus will decrease more rapidly in intensity as misalignment increases. The effect has seriously hampered past measurements of absolute intensity, and a computer program has been written which calculates the quantity $\int B(\sigma) d\sigma$ on the PDP-15.

This program will provide a daily check on the interferometer alignment, and permit the misalignment to be observed and corrected prior to data acquisition rather than after several weeks of calibration and data reduction at PSI. The fact that the $\int B(\sigma) d\sigma$ can be made to equal the detector intensity when the interferometer is aligned completes the last link relating target chamber fluorescence to calibrated spectral intensities and calculated excited state population densities.

REFERENCES

- 9.1 Murphy, R. E., "Measurements of Infrared Transient Phenomena" in Spectrometric Techniques, Vol. I, G. A. Vaneese, Ed, (Academic, New York, 1977).
- 9.2 Caledonia, G. E., Green, B. D., and Murphy, R. E., "A Study of the Vibrational Level Dependent Quenching of CO($v = 1-16$) by CO₂," J. Che. Phys. 71 (11) 4369 (1979).
- 9.3 Murphy, R. E., Cook, F. H., and Sakai, H., "Time-Resolved Fourier Spectroscopy," J. Opt. Soc. Amer. 65, 600 (1975).
- 9.4 Sakai, H. "Consideration of the Signal-to-Noise Ratio in Fourier Spectroscopy" in the Proceedings of the Aspen International Conference on Fourier Spectroscopy, 1970, Air Force Cambridge Research Laboratories Special Report No. 114, AFCRL-71-0019.
- 9.5 Sakai, H., "High Resolving Power Fourier Spectroscopy," in Spectrometric Techniques, Vol. I. op. cit.

APPENDIX I

EXPERIMENTAL APPARATUS MODIFICATIONS

In addition to the replacement of components which failed (the Helium-Neon Laser, electron gun filaments) several modifications were made to the experimental apparatus in order to gain signal intensity and stability. The effort can be divided into three areas: electron source stabilization, target chamber flow characterization, and improvements in data acquisition and reduction.

Arcing on the high voltage table has been a persistent problem resulting in large signal spikes which transform as spectral noise. A sheet of polyethylene sheeting (1 mm) was placed under all the components on the table in an effort to reduce possible arcing to the standoff transformer or table supports. New ground cables were made, a new line regulator and a new filament supply (Kepco 30A, 6V) was integrated into the system. As a result of these measures breakdown now occurs only in very humid weather. A variable voltage and current supply was employed to power the magnetic steering coils, permitting wider tunability of the focused beam. Nevertheless, it was observed that the current reaching the chamber was slowly decreasing in amplitude even though the filament current remained constant. The filament position was adjusted over the range 2.43-2.54 cm (its prescribed position is 2.51 cm) height. The anode cup is at 2.54 cm. Little variation in the beam current in the chamber was observed. Apparently the filament position is much more sensitive to side to side position beneath the hole in the anode cup than height. It was observed that the end of the gun was drooping. The acrylic spacers between acceleration stages of the gun had slipped sufficiently that a fraction of the current leaving the cathode did not enter the acceleration zone, but was skimmed off. Efforts to gradually shim the cathode end of the gun back into position were only moderately successful. Current for the runs had dropped as low as 0.25 ma. Shimming restored this to 0.6 ma, still far below the previous 1.5 ma level. A new electron gun was installed.

In order to obtain accurate values of chamber residence time (necessary for estimates of beam created species concentrations) the chamber volume and flow and leak rates were measured. The chamber volume of 10 liters and a total system volume of 31.2 ± 0.9 liters were determined by expanding a known volume into the system and observing the pressure change using a Wallace-Tiernan gauge. This gauge was also used to calibrate the alphasatron and new thermocouple gauges at several positions in the system. At several times during the reporting period, the total leak rate was measured consistently to be 10^{-2} torr/minute, which corresponds to 1.7×10^{17} molecules/s. In most of the runs used for analysis, the gas flow was greater than 5 standard l/minute (or 2.2×10^{21} molecules/s) and the fractional concentration due to the leak is less than 8×10^{-5} . Efforts to reduce the level of this leak are continuing.

Three flow meters were integrated into the gas handling system: a Manostat 1045M model for 1-20 s \dot{m} flows, a Matheson R-2-25D #72 tube useful in the 20-500 sccm flow range, and a Matheson 1/16" tri-flat tube covering the 2-300 sccm range. Each flowtube was calibrated by monitoring the system pressure rise resulting from a metered flow for a measured time. These calibrations were made for CO₂, O₂ and air for the small flowtubes, and N₂, O₂, and argon in the large flowmeter. Corrections for gas density and buoyancy were applied. The calibrations accompanying each flowtube were found to be fairly accurate, and the flow scaled as expected with gas density.

The interferometer cover was removed and the internal optics observed. The total path from the front aperture, through the compensating beamsplitter, to either the rear moving mirror or fixed bottom mirror, and finally through the lens to the detector element was measured at 17.9 cm. The active areas of the elements (lens 2.22 cm, mirror 2.54 cm, aperture in faceplate 2.86 cm) did not restrict the field of view, and the mask on the detector surface is the limiting aperture. The As₂S₃ lens was found to be inverted; when the convex surface faces the detector, coma and spherical aberration was greatly reduced for this high index material. The focusing lens increases the signal by a factor of 250 over the level with the lens removed. The total signal level

did not change upon inversion; nor was detector field of view non-uniformity reduced. It was found, however, that the field of view asymmetry rotated when the lens was rotated; the lens was deformed. A new calcium fluoride lens was ordered to permit extension of the interferometer scans into the near IR. The optical system had a more uniform response across the field of view with this lens. Additionally, the transmission of the CaF_2 lens was about 90% for wavelengths less than 7 μm . For this reason a CaF_2 flat was also purchased to replace the chamber window, giving a net transmission gain of the optical system of a factor of four.

Further signal increases were obtained by using a sensitive Santa Barbara Research Corporation PbSe detector. This detector has excellent long wavelength response and a low noise level. When mounting the detectors, a thin film of RTV was used to attach the detector to the Dewar cold finger. If the RTV is not cured properly it will creep across the detector face during subsequent operation causing absorptions at 1700, 2000, and 2700 cm^{-1} . Variation of the detector bias voltage and load resistor yielded operating conditions for each detector which have a maximum signal/noise level: PbSe 90 V, 400 $\text{k}\Omega$; PbS 90 V, 2 $\text{M}\Omega$.

Previously, the interferometer system and detector position was aligned using a blackbody standard and then rotated 90° to view the experiment. It was found that the interferometer did not rotate in a plane, and that a 50% increase in signal level could be gained by optimizing the detector position on the peak of the fluorescence from the chamber. Finally, the radiation detected when the blackbody was observed was found to arise both from the 1173 K aperture (1 mm^2) and the front plate (200 cm^2) which was at a temperature of ~ 330 K. To remedy this, aluminized Mylar® was used to cover the front plate and an iris was positioned midway between the source and the detector.

The total improvement achieved by all the above changes is a factor of 20 in signal to noise. Implementation of the new electron gun increased this still further.

Three computer programs were written to aid in data reduction on the PDP15 computer. The first speeds tape re-ordering prior to transformation. The function of program URTR3 is to convert LABCEDE data that is stored on magnetic tape #2. The tape contains a maximum of 2150 data points, each containing information at many times during the pulse period. Conversion of the data involves choosing the Ith time dependent element from each of the 2150 records, subtracting off the first element, and creating an interferogram by placing this Ith element of each record in an array of maximum dimension 2150. All of the data reading from tape #2 takes place in a MACRO-15 subroutine called RTWRT2.

Originally, URTR3 converted the data by calling RTWRT2 within 2 loops, the outermost "I" loop incrementing by 1 from starting time to the maximum time desired. The inner loop started from data point #1 to point 2150. RTWRT2 was called with a list of 5 arguments: ITR(J), the time dependent element of data point J; NUMINT, the number of time elements; I, the time element index; J, the data point index; and INTSUB, the element to subtract. Previously RTWRT2 proceeded to read through each point, picked off one Ith time element, subtracted off the value of INTSUB, and passed the resulting value back to URTR3. It continued the process for each of the 2150 points storing each element in array ITR(J). This array was written onto magnetic tape #1, tape #2 was rewound, and the "I" loop was incremented. This process took about 2 minutes to create an interferogram at one time.

Modifications were made to URTR3 so that 9 time elements are read from tape #2 simultaneously. First the I loop containing the call to RTWRT2 was modified by changing the time increment from 1 to 9. The second loop over the number of data points, J, remains the same. Subroutine RTWRT2 is still called; however, argument ITR(J) is changed to JTR(J) which is the array of 9 elements that RTWRT2 passes back to URTR3. The argument NINE was added to specify the number of time elements picked off tape #2. This extra argument corresponds to NVAL in the subroutine. RTWRT2 was modified so that NVAL is

loaded into the accumulator, its two's complement is taken, and this quantity is deposited into the accumulator. The section of the code where one element from each data point is picked off and stored in the accumulator for subtracting was made into a loop NPASS. This was done by adding a counter, INC, taking its two's complement, and adding a jump statement so that NPASS is executed 9 times.

The following section of the code where IIISUB is subtracted from the first time element at each data point was changed into loop INCLOC. In this loop, a counter INCL is used in the same manner as in NPASS in order to facilitate the subtraction of IIISUB from each of the 9 elements.

In UTR3 8 different arrays [ITRA(J), ITRB(J), ITRC(J), ITRD(J), ITRE(J), ITRF(J), ITRG(J), ITRH(J)] were added in addition to the original ITR(J) array, each dimensioned to 2150. The first element of the JTR array is stored in element 1 of ITR(J), second element of JTR array is stored in element 1 of ITRH(J). This process continues until all 2150 records are exhausted and takes approximately 3 minutes.

Lastly, all 9 interferograms are written onto magnetic tape #1. Previous to these modifications, only one interferogram was written onto tape #1 for each read from tape #2. As a result, the time required for tape re-ordering is reduced by a factor of six. Only 9 arrays of maximum dimension of 2150 are stored in the code because of the limited memory capacity of the PDP-15.

The second program is used to reduce the number of tapes required for data storage. Previously, the data from each run was stored on a separate tape, using only ~ 15% of the available storage capability. The program CONTAP, STACK, CONDEN, TAPRD is used to stack the many sets of data onto a single tape. The input tape is on MT1, the storage tape on MT2. After writing the file onto storage, a control P will continue operation when a new tape (MT1) has been loaded. All header information is stored with each file, but

the total number of files is not stored internally and the tape must be accurately labeled. To remove any file from storage, the program URTAPE, UNSTAK, CONDEN, TAPRD2 sequentially reads through the data files (MT1) displaying the header information. When the desired file is accessed, it will be written onto MT2. This output tape is then compatible with all other data reduction programs used on the unstored data files.

A third program (INTEG) was created to permit the integrated spectral intensity (in volts) to be quickly determined to check for interferometer alignment (see Chapter 9). A wavenumber region is chosen and integrals can be calculated for all times of interest.

APPENDIX II

FIELD OF VIEW CALCULATIONS

The development of an absolute calibration for the LABCEDE test chamber was complicated because neither the interferometer response function nor the electron beam energy deposition was uniform across the system field of view (see Sec. 3, main text). The details of a computer model, developed to properly account for these features, are described below.

Figure 3.1 of the main text shows the field of view, beam origin and its expansion as the beam propagates. If x is measured along the beam axis, the electron beam expands in y - z plane as x is increased. For thin argon and nitrogen targets, it has been found that the beam current distribution is Gaussian about the beam axis.¹ Consequently, if $j(x, y, z)$ is the current density at a point (x, y, z) , then

$$j(x, y, z) = J(x) e^{-(r/a)^2} \quad (\text{II.1})$$

where $J(x)$ is the current density at the beam axis and $a = a(x)$. Now we define $r_{1/2}$ as the beam radius measured from the beam axis, at which one-half of the total beam current is encompassed. If I is the total current, then

$$\int_0^{2\pi} \int_0^{r_{1/2}} j(x, y, z) r dr d\theta = \frac{I}{2} . \quad (\text{II.2})$$

From the conservation of total current I , we get,

$$\int_0^{2\pi} \int_0^{\infty} j(x, y, z) r dr d\theta = I . \quad (\text{II.3})$$

Solving Eqs. (II.2) and (II.3) simultaneously and using Eq. (II.1), we obtain the following

$$J(x) = \frac{I}{\pi a^2(x)} \approx \frac{I}{4.53 r_{1/2}^2(x)}$$

$$a = 1.2 r_{1/2}$$

$$j(x, y, z) = J(x) e^{-(r/a(x))^2} \quad (II.4)$$

The electron beam radius $r_{1/2}$ is related to half-angle $\theta_{1/2}$ by the following relation:

$$r_{1/2} = x \tan \theta_{1/2} + r_b \quad (II.5)$$

where x is measured from the beam origin and r_b is the initial beam radius. It is this half-angle $\theta_{1/2}$ which has been obtained empirically for N_2 and argon in Ref. II.1. This angle is measured from the beam origin and is defined as the angle at which one-half of the total current is encompassed. In terms of the target number density N , $\theta_{1/2}$ is given as,^{II.1}

$$\theta_{1/2} = \frac{A(Nx)^{3/2}}{1 + B(Nx)} \quad (II.6)$$

where A and B are constants which are a function of electron energy only. The ratio A/B may be calculated from,^{II.1}

$$\text{Nitrogen } \frac{A}{B} = \frac{2.7 \times 10^{-9}}{V(1 - 10^{-3}V)} \quad (II.7a)$$

$$\text{Argon } \frac{A}{B} = \frac{4.4 \times 10^{-9}}{V(1 - 10^{-3}V)} \quad (\text{II.7b})$$

where V is in units of keV.

The values of the quantities A and B , as determined by Center in Ref. II.1, are shown in Table II.1. These values are plotted in Fig. II.1. In order to obtain values of A and B at other electron energies, interpolation and extrapolation techniques have been used such that Eq. (II.7a) is satisfied for N_2 and Eq. (II.7b) is satisfied for argon. For argon, since only two data points are available, a curve similar in shape to that of N_2 is drawn through the two data points and then extrapolation is carried out. With the above described procedure, the values of A and B that have been generated are shown in Table II.2.

Now we may write down the rate of production of electron beam excited species, $i(x, y, z)$ as follows:

$$i(x, y, z) = \frac{j(x, y, z) N L(E)}{eW} \quad (\text{II.8})$$

where

W = Average energy required to produce an ion pair

$L(E)$ = loss function which depends upon the electron energy E

e = Electronic charge.

Substituting Eq. (II.4) in Eq. (II.8) and noting that $r^2 = y^2 + z^2$ we get

$$i(x, y, z) = \frac{INL(E)}{4.53 \times 10^{12} eW} \exp \left\{ \frac{-y^2}{1.44 r_{1/2}^2} \right\} \exp \left\{ \frac{-z^2}{1.44 r_{1/2}^2} \right\} \quad (\text{II.9})$$

since the field-of-view function of the detector is in the $x - y$ plane, we may integrate Eq. (II.9) over z .

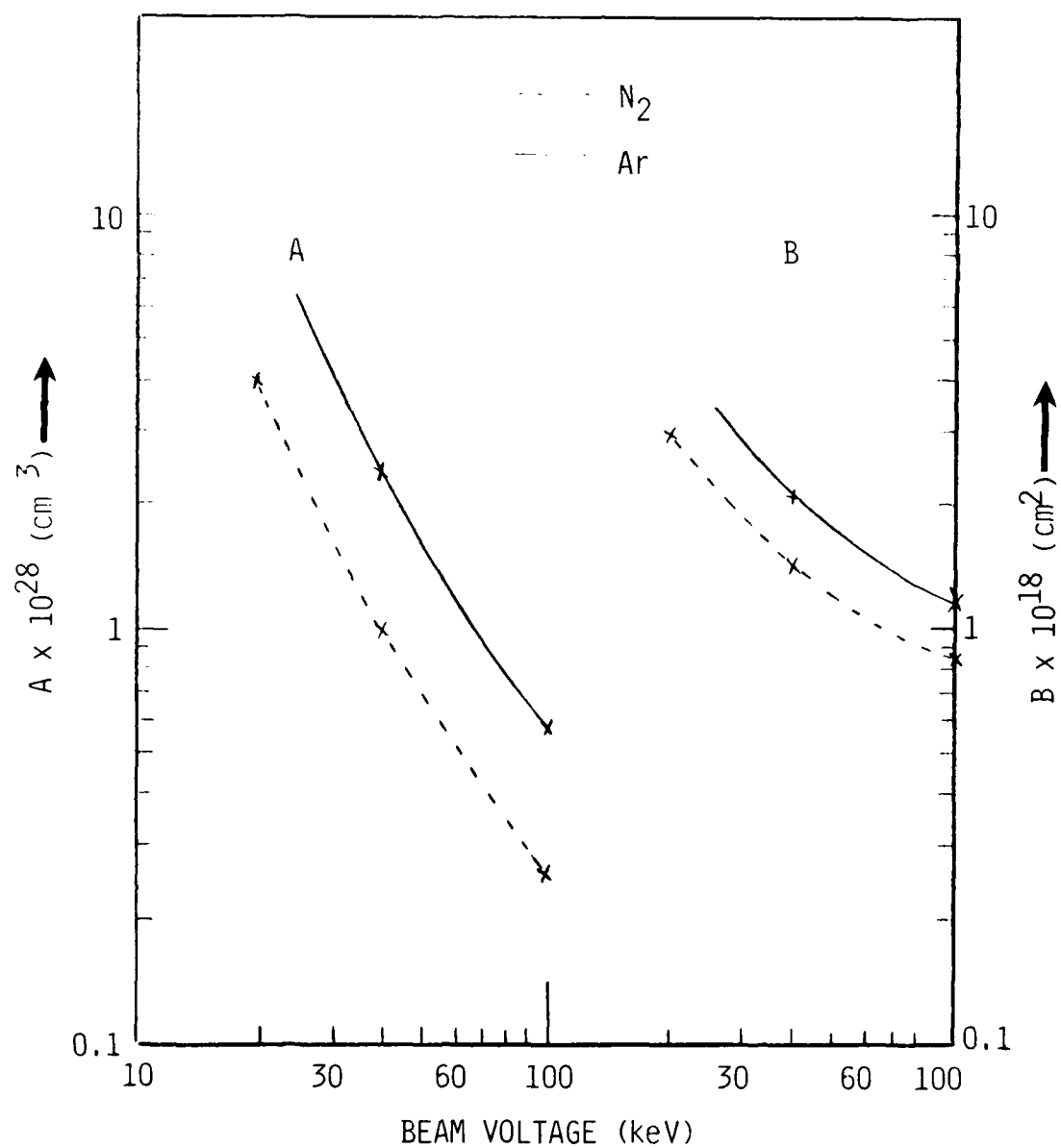


Fig. II.1 Beam growth parameters A and B.

BEAM GROWTH PARAMETERS

TABLE II.1

	N ₂		Ar	
Beam Voltage kV	A x 10 ²⁸ cm ³	B x 10 ²⁸ cm ²	A x 10 ²⁸ cm ³	B x 10 ¹⁸ cm ²
20	4.00	2.94	----	----
40	1.00	1.43	2.36	2.08
100	0.262	0.87	0.58	1.19

TABLE II.2

	N ₂		Ar	
Beam Voltage kV	A x 10 ²⁸ cm ³	B x 10 ¹⁸ cm ²	A x 10 ²⁸ cm ³	B x 10 ¹⁸ cm ²
25	2.5	2.25	6.32	3.5
30	1.72	1.85	4.20	2.78
35	1.28	1.60	3.05	2.35
40	1.00	1.43	2.36	2.08
20	4.00	2.94	11.00	4.9

$$\alpha(x, y) = \frac{INL(E)}{2.13 r_{1/2} eW} \exp \left\{ \frac{-y^2}{1.44 r_{1/2}^2} \right\} . \quad (II.10)$$

If the field-of-view function of the detector is denoted by $Fov(x,y)$, we can obtain INT, the quantity which is proportional to the total fluorescence intensity measured by the detector as follows:

$$INT = \int_{x_{min}}^{x_{max}} \int_{y_{min}}^{y_{max}} Fov(x,y) \alpha(x,y) . \quad (II.11)$$

It should be noted that in all the relations which are developed here, x is measured from the origin of the electron beam. In the computer program, however, x is measured from the field-of-view center which is located 8 cm from the origin of the electron beam.

In Table II.3 we show that field-of-view function for $PbSeLN$, 4 mm square, masked 3 mm round. It can be seen from this table that the field-of-view function is very asymmetric with respect to both x and y . The details of the code are listed in Table II.4.

TABLE II.3

FIELD-OF-VIEW FUNCTION

(PbS LN₂ 4 mm sq. masked 3 mm round, 4/24/78)

$\frac{x}{y}$	-4.5	-4.0	-3.5	-3.0	-2.5	-2.0	-1.5	-1.0	-0.5	0	0.5	1.0	1.5	2.0	2.5	3.0	3.5	4.0
4.5	0	0	0.122	0.128	0.137	0.139	0.151	0.176	0.184	0.186	0.161	0.142	0.134	0.120	0.099	0.097	0.093	0
4.0	0.116	0.123	0.136	0.139	0.163	0.197	0.268	0.321	0.328	0.326	0.291	0.237	0.181	0.135	0.109	0.096	0.093	0
3.5	0.116	0.138	0.137	0.174	0.242	0.330	0.417	0.465	0.486	0.477	0.445	0.372	0.281	0.181	0.111	0.093	0.088	0
3.0	0.116	0.123	0.153	0.228	0.344	0.453	0.534	0.605	0.644	0.639	0.593	0.507	0.384	0.237	0.130	0.088	0.069	0
2.5	0.114	0.135	0.198	0.302	0.438	0.558	0.666	0.739	0.773	0.767	0.723	0.628	0.488	0.307	0.161	0.089	0.077	0
2.0	0.107	0.144	0.221	0.344	0.515	0.639	0.759	0.832	0.841	0.832	0.820	0.749	0.587	0.372	0.184	0.074	0.051	0
1.5	0.097	0.146	0.254	0.383	0.571	0.693	0.814	0.872	0.884	0.884	0.884	0.883	0.841	0.662	0.446	0.193	0.051	0
1.0	0.101	0.146	0.260	0.407	0.584	0.702	0.849	0.893	0.912	0.910	0.922	0.872	0.683	0.414	0.178	0.035	0.023	0
0.5	0.098	0.144	0.253	0.400	0.578	0.697	0.854	0.935	0.966	0.981	0.973	0.949	0.653	0.395	0.146	0.004	0	0.039
0	0.095	0.139	0.240	0.383	0.514	0.655	0.790	0.883	0.968	1.0	0.903	0.837	0.645	0.377	0.0604	0	0	0
-0.5	0.095	0.138	0.207	0.321	0.453	0.609	0.727	0.883	0.887	0.925	0.877	0.779	0.592	0.309	0.071	0	0	0
-1.0	0.095	0.116	0.189	0.279	0.384	0.518	0.665	0.756	0.808	0.832	0.787	0.674	0.587	0.232	0.058	0	0	0
-1.5	0.095	0.104	0.140	0.228	0.316	0.414	0.505	0.593	0.654	0.674	0.630	0.516	0.360	0.186	0.047	0	0	0
-2.0	0.093	0.097	0.129	0.163	0.229	0.314	0.378	0.442	0.479	0.500	0.465	0.402	0.285	0.151	0.066	0	0	0
-2.5	0.081	0.093	0.108	0.137	0.141	0.228	0.282	0.325	0.353	0.356	0.329	0.285	0.211	0.116	0.071	0.046	0.046	0
-3.0	0.051	0.069	0.082	0.093	0.110	0.137	0.144	0.181	0.194	0.209	0.194	0.181	0.122	0.088	0.064	0.046	0.039	0

TABLE II.4

FIELD-OF-VIEW COMPUTER CODE

Constants Used

e = Electronic charge = 1.602×10^{-19} [C]
 u = Atomic mass unit = 1.66×10^{-24} [g]

Input Parameters

I = Total current [A]
 r_b = Initial radius of e-beam [cm]
 N = Medium density [# of particles/cm³]
 W = Average energy to produce an ion pair [eV]
 M = Molecular weight of the gas
 A = Empirical parameter [cm³]
 B = Empirical parameter [cm²]
 LFX = Loss function, two options are available
 LF = 0, LFX is a constant independent of x [MeV - cm²/g]
 LF = 1, LFX is read as a table vs. x (x is taken from the field-of-view center)
 FOV = Field-of-view function, 4 options are available
 FOVO = 1, FOV = 1 for $(x^2 + y^2)^{1/2} \leq R$
 = 0 for $(x^2 + y^2)^{1/2} > R$
 FOVO = 2, FOV is an analytical function in x and y
 FOVO = 3, FOV is a function of $R = (x^2 + y^2)^{1/2}$ in a table form
 FOVO = 4, FOV is a function of x and y in table form
 $\theta_{1/2}$ = Half angle of electron beam measured from the beam origin,
 two options are available
 ITH = 0, $\theta_{1/2} = 0$ for all x
 = 1, $\theta_{1/2}$ is calculated from Center's formula

TABLE II.4 (Cont.)

FIELD-OF-VIEW COMPUTER CODE

Output QuantitiesGas density (ρ) = NUM [g/cm³]

$$\text{INT} = \int_{y_{\min}}^{y_{\max}} \int_{x_{\min}}^{x_{\max}} \alpha(x,y) \text{ FOV}(x,y) \, dx dy \, [\text{s}^{-1}]$$

Here x is measured from the field-of-view center and not from the origin of the electron and $\alpha(x,y)$ is given as

$$\alpha(x,y) = \frac{I_e L (8 + x) 10^6}{2.13 r_{1/2}(x) \text{ ew}} \exp \left(\frac{-y^2}{1.44 r_{1/2}^2(x)} \right) [\text{cm}^{-2} \text{ s}^{-1}]$$

APPENDIX II - REFERENCES

1. R. E. Center, "Plural and Multiple Scattering of Fast Electrons in Gases," Phys. Fluids 13, 79-88 (1970).

APPENDIX III

RADIATIVE TRAPPING OF ELECTRONICALLY EXCITED ARGON

A portion of the electron energy transferred to the Ar/CO₂ gas mixture (cf, Sec. 3) is allocated to electron excitation of argon atoms. In the case of Ar metastable states the dominant decay mechanism is collisional quenching by CO₂. On the other hand, optically active states may radiatively decay. The purpose of this appendix is to examine the fate of the optically active Ar* in terms of radiative trapping and associative ionization.

Using a Beer's law distribution we can calculate the average distance, ℓ , that a photon will travel before being absorbed. This average distance or step size will be useful in calculating the time needed for the photon to escape the gas using a random walk treatment. The Beer's law distribution is given by

$$I/I_0 = e^{-\alpha x} \quad (III.1)$$

Normalizing the distribution we have

$$N^2 \int_0^{\infty} e^{-2\alpha x} dx = 1 \quad (III.2)$$

with $N = \sqrt{2\alpha}$. Since Beer's law is a weighting factor for the distance into the gas that a photon will travel before being absorbed, we can find the average value for this distance with:

$$\langle \ell^2 \rangle = 2\alpha \int_0^{\infty} x^2 e^{-2\alpha x} dx, \quad (III.3)$$

leading to

$$\langle \ell^2 \rangle = \frac{1}{2\alpha^2}. \quad (III.4)$$

Alternatively, we could have defined $\langle \ell^2 \rangle$ as the value of x^2 when $I/I_0 = 1/2$, i.e.,

$$0.5 = e^{-\alpha x}$$

leading to

$$x = \frac{\ln(2)}{\alpha} \text{ or } x^2 = \frac{.48}{\alpha^2} \quad (III.5)$$

We note that both approaches give nearly identical results. For future reference we note that the minimum possible step size is simply the distance between atoms. For typical test conditions of $Ar = 3 \times 10^{17}$ molecules/cm³ we have $\langle \ell^2 \rangle_{\min} = 2 \times 10^{-12}$ cm². In the above expressions $\alpha = \sigma \cdot N$ where σ is the cross section and N the number density. Oscillator strengths were taken from Ref. 1 for the transitions of interest in Ar*. The oscillator strength (f) is an integral in frequency over the cross section for a particular line. The peak oscillator strength for a doppler broadened line is given by

$$\sigma(\nu_0) = 2.64 \times 10^{-2} \times f \times \frac{\sqrt{\ln 2}}{\sqrt{\pi} W_D c} \quad (III.6)$$

where W_D is the half width at half maximum which we take to be 0.1 cm^{-1} and c is the speed of light. Thus

$$\sigma(\nu_0) = 4.14 \times 10^{-2} \times f, \text{ cm}^2 \quad (III.7)$$

Using the expression $\langle \ell^2 \rangle = \frac{1}{2\alpha^2}$ with $\alpha = \sigma \cdot N$, coupled with a random walk formula, $\bar{t} = \frac{R^2}{\langle \ell^2 \rangle}$, we can determine which Ar* transitions are radiatively trapped. In the latter formula \bar{t} is the time needed to travel the distance R if the average step size is $\langle \ell^2 \rangle$ and the frequency of steps is ν^{-1} .

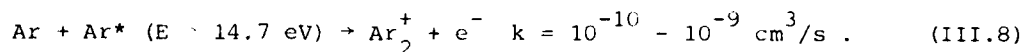
For ν' we use the inverse of the lifetime of the upper state and for R we use the radius of the field of view (4 cm). So, for the $1S \rightarrow (4s, 3/2)$ $J = 1$ transition in Ar we have $N_{Ar} = 3 \times 10^{17} \text{ cm}^{-3}$, $\sigma = 2.5 \times 10^{-13} \text{ cm}^2$, with $\alpha = 7.5 \times 10^4 \text{ cm}^{-1}$. Thus, $\langle \ell^2 \rangle = \frac{1}{2\alpha^2} = 8.7 \times 10^{-11} \text{ cm}^2$. For ν' we have $1.19 \times 10^8 \text{ s}^{-1}$ and $\bar{t} = 25.8 \text{ mins.}^1$ Therefore this transition is radiatively trapped. Below is a sampling of transitions:

TRANSITION	$\langle \ell^2 \rangle (\text{cm}^2)$	$\nu (\text{s}^{-1})$	$\bar{t} (\text{mins})$
$1S \rightarrow (4s, 3/2) J = 1$	8.7×10^{-11}	1.19×10^8	25.7
$1S \rightarrow (4s', 1/2) J = 1$	5.0×10^{-12}	5.1×10^8	104.5
$1S \rightarrow (3d, 3/2) J = 1$	3.7×10^{-11}	2.70×10^8	26.7
$1S \rightarrow (3d', 3/2) J = 1$	2.9×10^{-11}	3.13×10^8	29.4
$1S \rightarrow (5s, 3/2) J = 1$	4.5×10^{-10}	0.77×10^8	7.7
$1S \rightarrow (5s', 1/2) J = 1$	2.3×10^{-9}	0.350×10^8	3.3

Therefore, all of the states given above are radiatively trapped (i.e., $\bar{t} > 1 \text{ ms}$).

The highest energy of the states listed above is 14.25 eV. We will now address the lifetimes of more energetic states.

Consider very high Rydberg states with, for example, $n = 10$. Using a hydrogenic approximation (see Bethe and Salpeter²) we take roughly $\sigma = 10^{-16} \text{ cm}^2$. This gives $\alpha = \sigma \cdot N = 30$ and $\langle \ell^2 \rangle = 5.6 \times 10^{-4}$ with $\bar{t} = 2.29 \text{ ms}$. Therefore, Rydberg states as high as $n = 10$ will be radiatively trapped, although higher Rydberg states will not. However, for states of Ar^* with $E > 14.7 \text{ eV}$, associative ionization will be the dominant loss mechanism,^{3,4} i.e.,



Taking $\text{Ar} = 3 \times 10^{17} \text{ cm}^{-3}$, the e-fold time for reaction (III.8) will be $< 3 \times 10^{-8} \text{ s}$. None of the transitions listed in Ref. 1 corresponding to upper state with energies $> 14.7 \text{ eV}$ have lifetimes this short. Therefore,

all Ar* (both metastables and allowed transitions) with $E > 14.7$ eV (except for possibly some allowed transitions to the ground state not tabulated in Ref. 1) will disappear via associative ionization.

We have seen that ground state transitions of optically active states with energies below 14.7 eV will be radiatively trapped. Transitions between states above ground level will occur, however these will lead to population of lower excited states which, in turn, will be radiatively trapped. Thus although we have not traced the fate of all possible excited states of argon, it appears that the electron energy deposited in argon excitation will not be radiated away, but rather will be available for further reaction, perhaps ultimately leading to creation of excited CO.

REFERENCES (APPENDIX III)

1. Wiese, W. L., Smith, M. W. and Miles, B. M., Atomic Transition Probabilities, Volume II, Sodium through Calcium, U. S. Department of Commerce, NBS 22, October 1969.
2. Bethe, H. A. and Salpeter, E. E., Quantum Mechanics of One- and Two-Electron Atoms, Academic Press Inc., New York, 1957.
3. N. T. Holcombe and F. W. Lampe, "Pulsed Mass Spectrometric Study of Associative Ionization in Argon-Nitric Oxide and Argon Acetylene Mixtures," J. Chem. Phys. 56, 1127 (1972).
4. Y.-J. Shiu and M. A. Biondi, "Dissociative Recombination in Argon: Dependence of the Total Rate Coefficient and Excited-State Production on Electron Temperature," Phys. Rev. A 17, 868 (1978).

APPENDIX IV

NO + O AFTERGLOW STUDIES

IV.1 Introduction

Measurements in the LABCEDE apparatus on the deactivation of vibrationally excited NO by O₂ have shown a deactivation rate when the molecular oxygen concentration is reduced to zero that is larger than can be explained by deactivation by radiative decay or by molecular nitrogen quenching (see Section 5, main text). The available evidence indicates that this excess deactivation might come from atomic oxygen in the reactor. In order to assess this hypothesis further, it seemed useful to make an independent determination of the atomic oxygen number density, and to determine how the atomic oxygen number density varied as the number density of molecular oxygen was changed. We made some measurements in the LABCEDE facility to try to learn about atomic oxygen in N₂/O₂ mixtures.

There are essentially three techniques commonly used to measure O-atom number densities: vacuum ultraviolet absorption or resonance fluorescence on the 130.4 nm triplet of atomic oxygen;^{1,2} recombination of atomic oxygen with a concomitant heat release upon the surface of a catalytic probe;^{3,4} and air afterglow intensity measurements.⁵⁻⁷ The vuv absorption or resonance fluorescence techniques have the advantage that they are specific to atomic oxygen and do not interfere with the kinetic processes taking place in the reactor. However, they suffer from the rather great disadvantage that they could not be implemented without significant modification of the apparatus. Catalytic probe techniques suffer from the disadvantages that they are non-species specific (any atom recombination process generates heat), and that the insertion of a probe into the reactor could seriously alter the kinetic processes going on inside the reactor. The air afterglow technique is specific to atomic oxygen and requires no modifications to the present set up of the LABCEDE apparatus. The major disadvantage of the air afterglow technique is that the addition of NO to the reactor, which is required for the O-atom detection, could seriously alter the kinetics

inside the reactor. We opted for the air afterglow technique as being easy to implement, and hoped that we might be able to assess the potential kinetic interferences by adding varying amounts of NO to the reactor and looking for changes in behavior.

IV.2 Basic Technique of Air Afterglow Calibrations

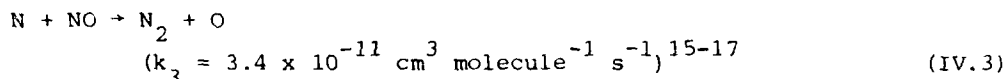
When atomic oxygen and nitric oxide are mixed, a continuum emission is observed between 400 and 3500 nm,^{5,6,8-14} the intensity of which is directly proportional to the number densities of O and NO, but independent of total pressure:

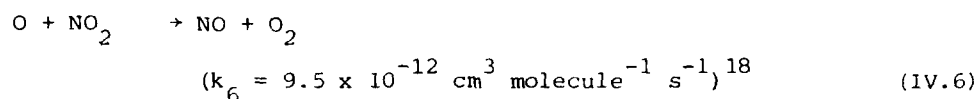
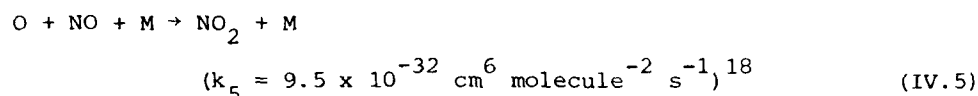
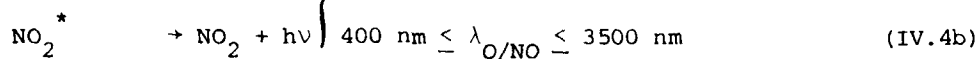
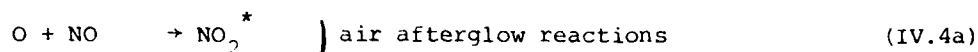
$$I_{O/NO} = \kappa [O] [NO] , \quad (IV.1)$$

where κ is a constant which incorporates such factors as viewing geometry, detection sensitivity and the absolute air-afterglow rate constant.⁸⁻¹⁴ If the constant κ is known for a particular apparatus and wavelength, atomic oxygen number densities can be determined by measuring the air-afterglow intensity as a function of added known amounts of NO, i.e.,

$$[O] = \frac{I_{O/NO}}{\kappa [NO]} . \quad (IV.2)$$

In general, κ can be determined by air afterglow intensity measurements when known amounts of O and NO are added to the reactor. The easiest technique for preparing known number densities of atomic oxygen is to titrate atomic nitrogen with excess NO.⁷ The reactions important to air-afterglow calibrations are summarized as follows:





In a low pressure apparatus ($P \sim 1$ torr, $t < 10\text{-}20$ ms), reaction (IV.5) is quite slow for normal number densities of O and NO ($\leq 10^{14}$ molecules cm^{-3}). Thus, neither the O nor the NO is consumed, and the number densities of O and NO are straightforward to determine because reaction (IV.3) is both quantitative and fast. At higher pressures ($P > 10$ torr), reaction (IV.5) becomes more significant, and the atomic oxygen is removed from the system. Reaction (IV.6) is quite rapid and serves to further reduce the atomic oxygen number density, as well as to regenerate NO. The overall effect of reactions (IV.5) and (IV.6) is to reduce atomic oxygen with an effective rate constant of twice that given by k_5 , while maintaining a constant NO number density.

In the limit that reactions (IV.5) and (IV.6) are not particularly important, the air afterglow intensity which obtains in the presence of excess nitric oxide is given by

$$I_{\text{O/NO}} + k[\text{O}][\text{NO}] \approx k[\text{N}]_0 ([\text{NO}]_{\text{added}} - [\text{N}]_0) \quad (\text{IV.7a})$$

$$\approx k[\text{N}]_0 [\text{NO}]_{\text{added}} - k[\text{N}]_0^2, \quad (\text{IV.7b})$$

where $[\text{N}]_0$ is the initial number density of atomic nitrogen in the reactor prior to reaction with NO, and $[\text{NO}]_{\text{added}}$ is the number density of NO which would have obtained in the reactor in the absence of atomic nitrogen. Thus,

a measurement of $I_{O/NO}$ as a function of $[NO]_{\text{added}}$ will be linear in $[NO]_{\text{added}}$ beyond the titration end point, i.e., where $[NO]_{\text{added}} \geq [N]_0$. The air afterglow calibration factor, κ , can then be determined by dividing the square of the slope of a plot of $I_{O/NO}$ vs. $[NO]_{\text{added}}$ by the intercept on the ordinate. The initial atomic nitrogen number density is given by the ratio of the intercept to the slope.

The problems in applying this technique to the LABCEDE apparatus are that atomic oxygen is rapidly consumed by reactions (IV.5) and IV.6) because of the 50 torr operating pressure in the apparatus, so that one must extrapolate measurements of $I_{O/NO}$ versus time to an initial intensity; the atomic oxygen consumption is sufficiently rapid that significant amounts of atomic oxygen are consumed during the 1 ms that the e-beam pulse is operating, so that the extrapolation mentioned above is not straightforward; and the addition of NO to the reactor might affect the ion chemistry which leads to the formation of atomic nitrogen in the reactor. This latter point requires a fairly extensive modeling effort to resolve, and this modeling has not as yet been done. The extrapolation to an initial intensity does seem to be possible, and the procedure used is described in the next section.

IV.3 Air Afterglow Calibration in LABCEDE

IV.3.1 Experimental Set Up

The room temperature LABCEDE facility has been described in detail previously^{19,20} so that only the modifications for making spectral observations between 500 and 900 nm will be described. The apparatus as used in these studies is shown schematically in Fig. IV.1. Various gas mixtures containing N_2 , O_2 and NO are irradiated by a beam of electrons with a current of about 2 mA and an energy of 36 kV. The e-beam is pulsed at a repetition rate of 50 Hz with a pulse duration of 1 ms.

Fluorescence excited by the electron beam exits the observation chamber through a CaF_2 window normal to the e-beam axis and is collected by a glass lens of 50 mm diameter and 65 mm focal length situated approximately 25 cm from the e-beam axis. The radiation is focused upon the entrance

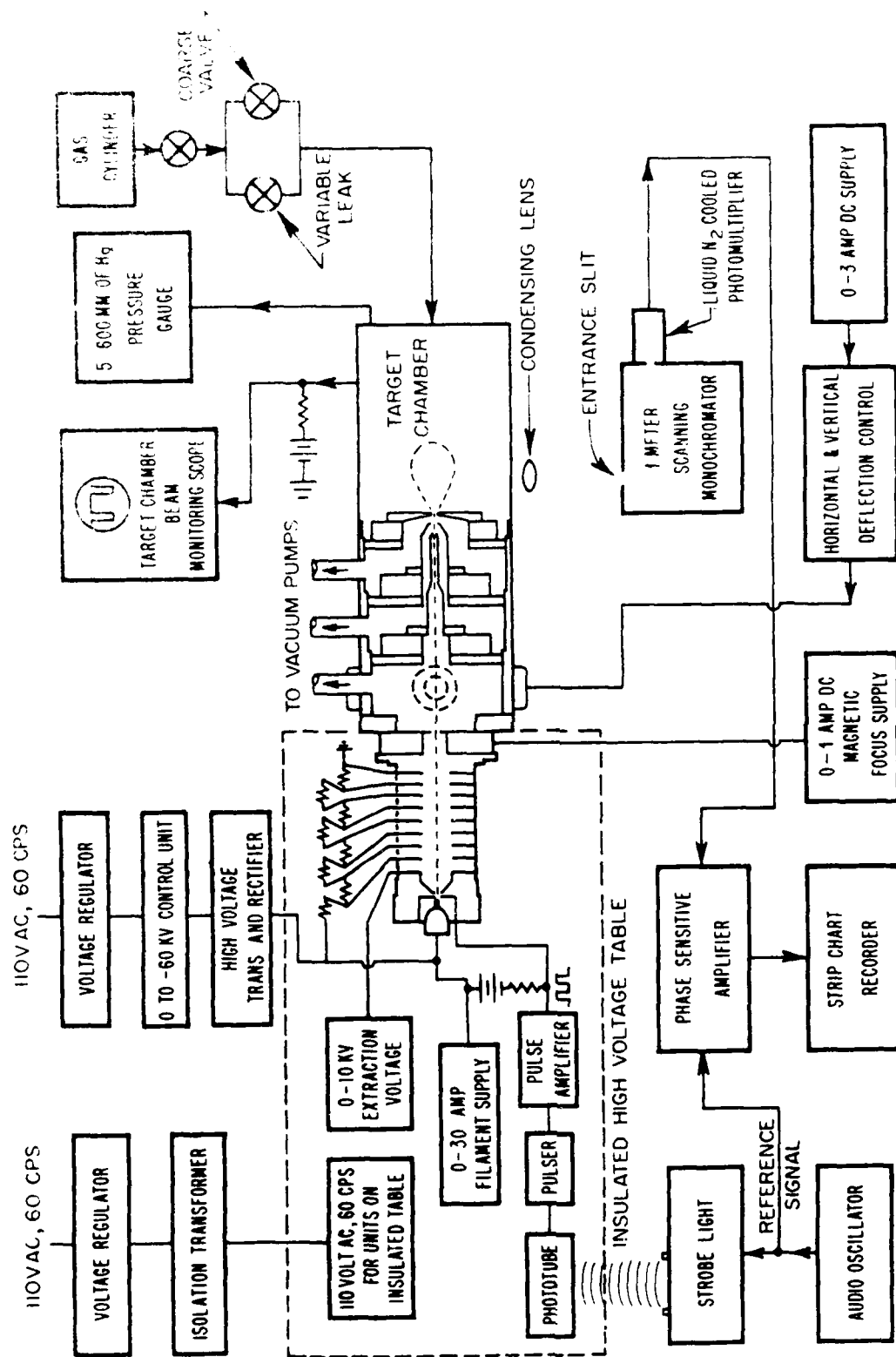


Fig. IV.1 Block diagram of experimental system.

slit of a 0.3 m monochromator (McPherson 218) which is approximately 8.6 cm from the lens. This gives an effective viewing region across the fluorescent region of a rectangular parallelepiped whose length is determined by the width of the fluorescent region as viewed along the axis of the e-beam, and whose cross sectional area is a three-fold magnification of the monochromator entrance slit which was usually 0.2 cm x 1.0 cm. Radiation entering the monochromator was dispersed by a grating blazed at 500 nm and detected photo-electrically using an HTV R955 photomultiplier which has an extended S-20 spectral response. A Corning CG3-69 short wavelength cut off glass filter is placed at the entrance of the monochromator to ensure that only first order radiation is observed ($\lambda \geq 525$ nm). The current from the photomultiplier was shunted to ground through a 60 k Ω load resistor. The voltage drop across the load resistor was amplified by a factor of 100 by a PARC 113 pre-amplifier, and then measured using a box car integrator (PARC 160), the gate of which was normally scanned temporally between 1.6 and 20 ms after the beginning of the e-beam pulse. Some spectral scans were taken at a fixed delay time after termination of the e-beam pulse. In order to avoid current saturation of the photomultiplier resulting from the strong fluorescence during the e-beam pulse, it was necessary to reduce drastically the gain of the photomultiplier. This reduced gain was restored by the preamplifier in the detection train. To avoid saturation of the box-car amplifiers during the e-beam pulse, it was necessary to operate on a scale range such that afterglow signals were typically only about 1-5% of full scale. In order to obtain measurable signal levels, therefore, it was necessary to display the output of the box-car on a strip-chart recorder (Heath SR-205) operating on a full scale sensitivity which was only a small fraction of the nominal full scale output of the box-car.

Reagent gases flowed through traps at dry ice temperature prior to introduction into the reaction cell. Reagent-gas flow rates were measured on rotameters which had been calibrated for air. It was assumed that the calibrations for the gases used, N₂, O₂, and NO, would differ little from the air calibrations. The consistency of our kinetic results with other measurements in the literature confirms this assumption.

Typical conditions consisted of flow rates of 5100 atm-cm³ min⁻¹ for N₂, 0-200 atm-cm³ min⁻¹ for O₂, and 0-20 atm-cm³ min⁻¹ for NO, and a total pressure of 50 torr.

IV.3.2 Identification of O/NO Afterglow

Before making the calibrations to determine the O-atom number density in LABCEDE it was necessary to ensure that reasonable number densities of atomic nitrogen could be made in the apparatus in the absence of added NO, and that the air afterglow would obtain upon the addition of NO to the irradiated nitrogen. Fig. IV.2 shows a spectrum of the first positive bands of nitrogen approximately 5 ms after termination of the e-beam. The spectrum shows enhancement of emissions from vibrational levels 12-10 and 6 which is typical of first positive emission excited by the three-body recombination of atomic nitrogen. Figure IV.3 shows the spectrum which obtains upon the addition of NO to the reactor. Although some banded structure is evident, the spectrum is predominantly a continuum emission. The intensity distribution of this continuum with wavelength does not look like the typical air afterglow continuum that one normally sees in the laboratory with a grating monochromator blazed at 500 nm and an S-20 photomultiplier.²¹ One would normally expect a more uniform increase in intensity from 500 nm to a peak closer to 600 nm that observed here. The effective leveling off of the spectrum between 540 and 600 nm especially looks strange. It is possible that this anomaly can be explained by a reduced transmission of the optical system between 550 and 600 nm due perhaps to color centers in the CaF_2 cell window or to Wood's anomalies in the grating. This reduction in intensity around 580 nm is also apparent in the spectrum of the nitrogen first positive bands shown in Fig. IV.2. Under normal circumstances the intensity of the $\Delta v=4$ bands peaked on the 11, 7 transition is roughly a factor of two times more intense than the $\Delta v=3$ peak centered on the 11,8 transition.²¹ The spectrum shown in Fig. IV.2 on the other hand shows that the 11,7 intensity is actually weaker than that of the 11,8 band.

Given the unusual intensity distribution of the continuum spectrum shown in Fig. IV.3, we wanted to perform an experiment to satisfy ourselves that we were indeed observing the air afterglow emission. We, therefore, monitored the decay in a portion of this continuum (700 ± 5 nm) as a function of time after termination of the e-beam and as a function of number density of NO added to mixtures of N_2 and O_2 at total pressures of 50.7 and 21.1 torr.

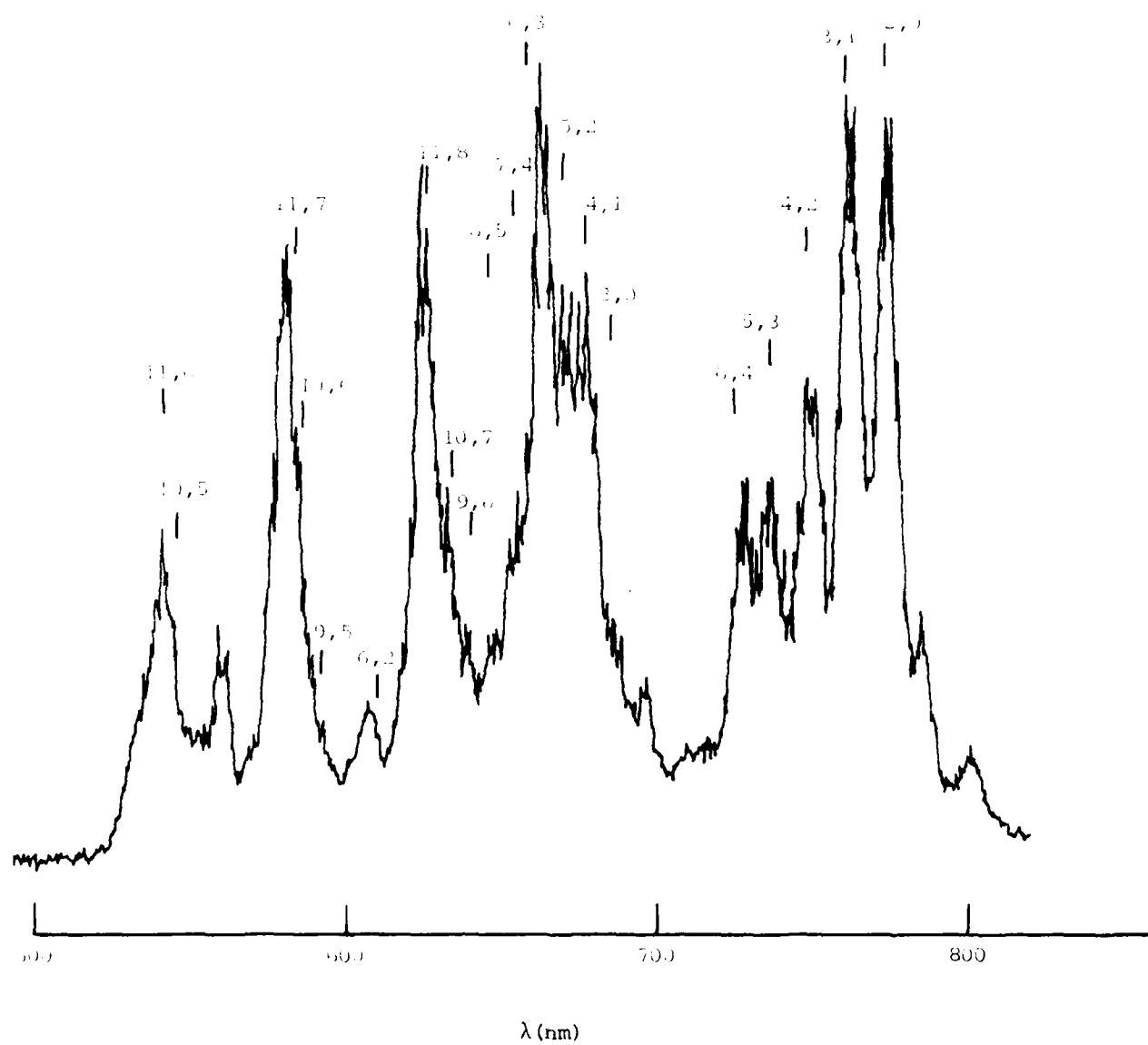


FIG. IV.2 N $1s$ spectrum from N-atom recombination in 50 torr of N_2 6 ms after termination of α -beam pulse, $\lambda_0 = 5.2$ nm



Fig. IV.3 Air afterglow spectrum in N_2/NO mixtures, 4 ms after e-beam termination. $[NO] = 7.7 \times 10^{14}$ molecules cm^{-3} . $\Delta\lambda = 5.2$ nm.

We expect that the dominant processes for atomic oxygen removal in the reactor will be reactions (IV.5) and (IV.6). Given that assumption, the differential equation which describes the rate of O-atom removal with time is

$$\frac{d[O]}{dt} = -2k_5 [O] [NO] [N_2] \quad , \quad (IV.8)$$

which under pseudo-first-order conditions ($[NO] \gg [O]$) has the solution

$$\ln \frac{[O]}{[O]_0} = -2k_5 [NO] [N_2] \quad . \quad (IV.9)$$

Equation (IV.2) shows that the atomic oxygen density is directly proportional to the intensity of the air afterglow. Thus, if the emission we observe is indeed the air afterglow, its intensity should decay as indicated in Eq. (IV.9). Figure IV.4 shows some typical semi-log decay plots of the emission at 700 nm at several different number densities of NO. The slopes of these lines along with similar slopes for other NO number densities when plotted against NO number density should give linear plots whose slopes will equal $2k_5$. Such plots are shown in Fig. IV.5 for two different total pressures. The rate constant derived at both pressures is $1.8 \times 10^{-31} \text{ cm}^6 \text{ molecule}^{-2} \text{ s}^{-1}$. The literature value for $2k_5$ is $1.9 \times 10^{-31} \text{ cm}^6 \text{ molecule}^{-2} \text{ s}^{-1}$ for $M = N_2$, in excellent agreement with the determination made here. These results confirm that our observations are indeed of the air afterglow, and in addition confirm the accuracy of the flow meter calibrations for the gases used.

IV.3.3 Kinetic Model for Analyzing Air Afterglow Calibration Experiments

In order to obtain a value for the calibration constant, K , in Eq. (IV.1), it is necessary to make air afterglow intensity measurements in N_2/NO mixtures as a function of NO number density. Because the O-atom number density decays rapidly upon the addition of NO, the air afterglow intensities must be measured as a function of time and appropriately extrapolated

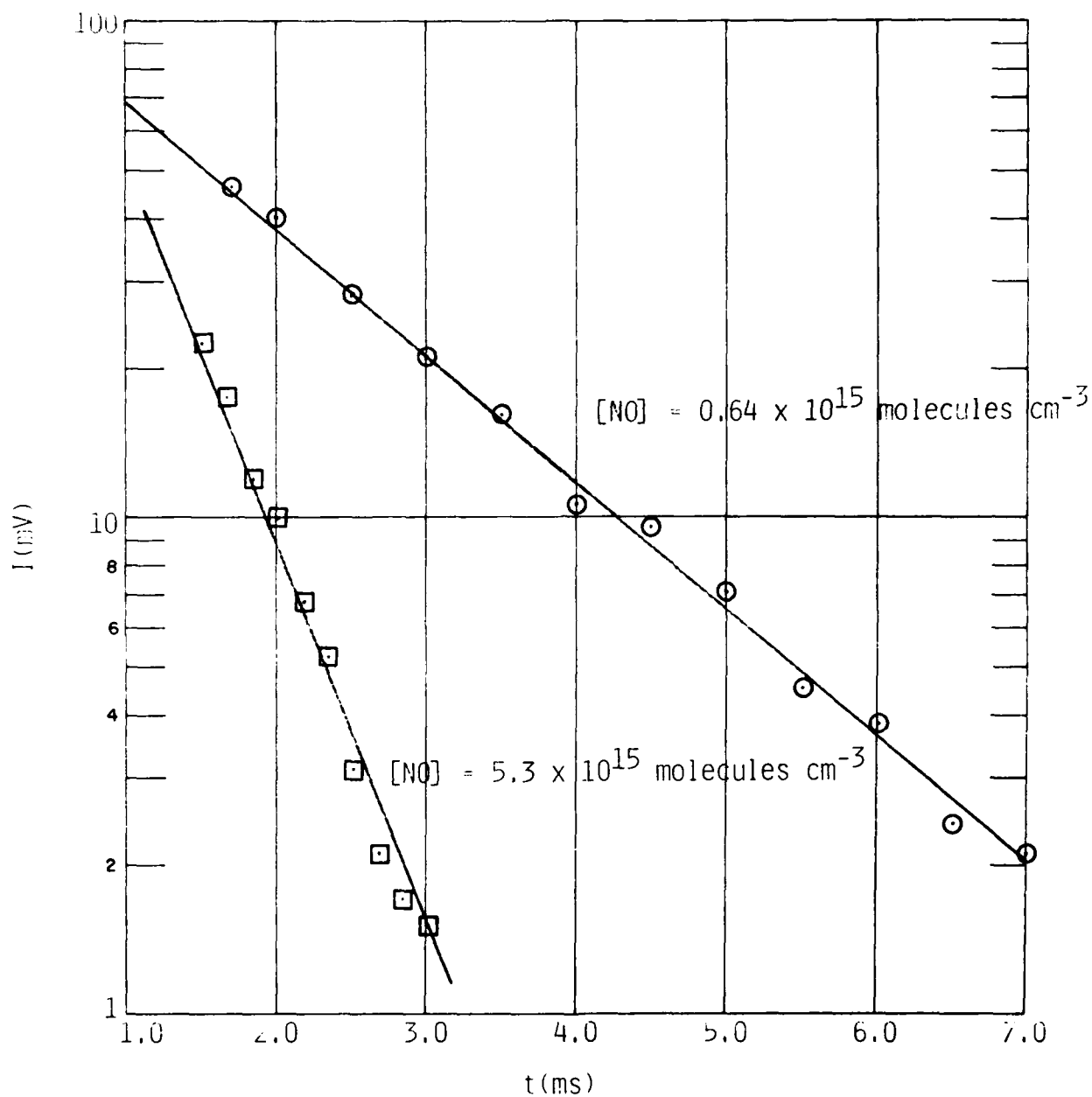


Fig. IV.4 Decay of emission at 700 nm in $N_2/O_2/NO$ mixtures. $[O_2] = 6.5 \times 10^{16} \text{ molecules cm}^{-3}$, $P = 50.7 \text{ torr}$.

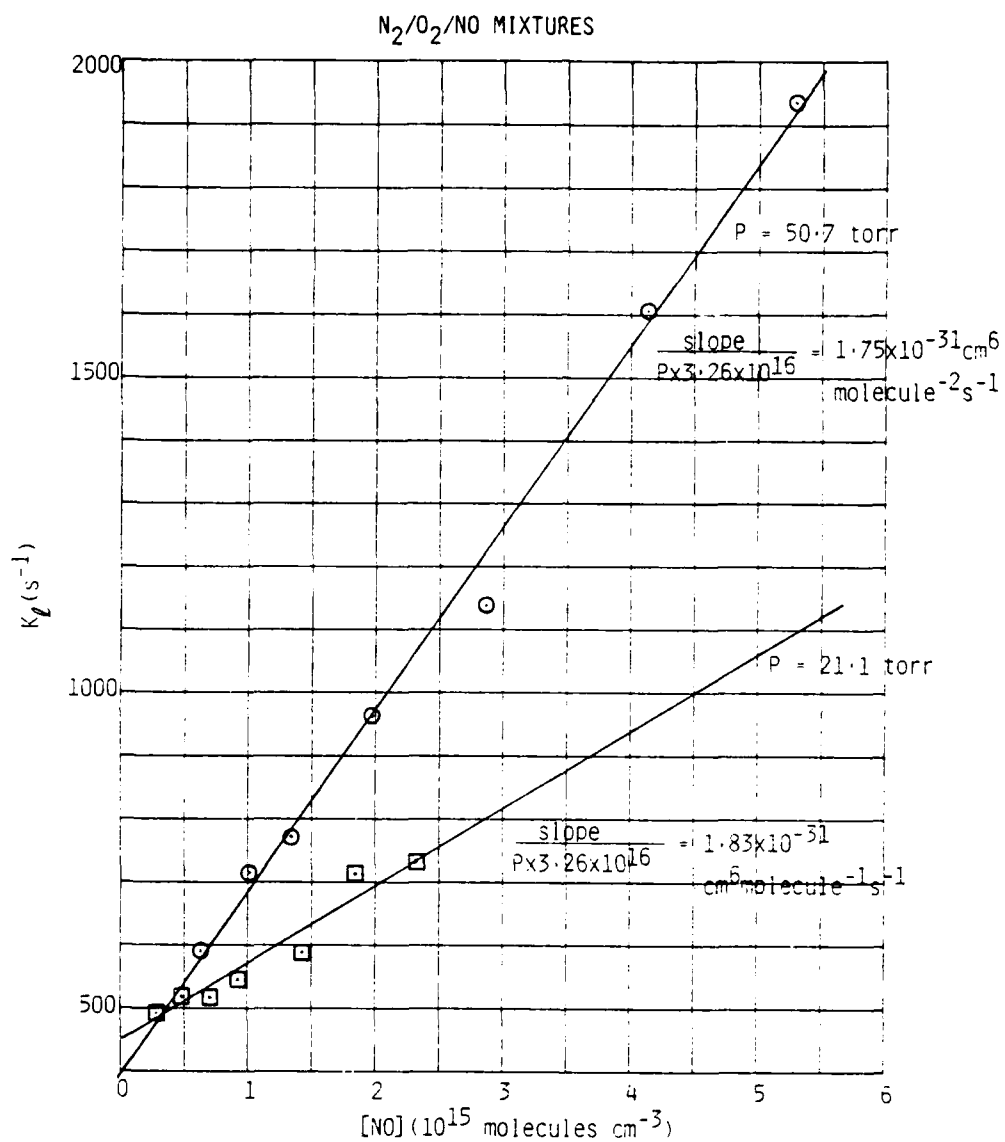


Fig. IV.5 Decay rates of 700 nm emission as a function of $[\text{NO}]$ at two different total pressures in $\text{N}_2/\text{O}_2/\text{NO}$ gas mixtures.

to some initial value. In developing the kinetic model used in this extrapolation, we have assumed that the e-beam creates only atomic nitrogen in its interaction with the gas mixture, and that all atomic oxygen is created through reaction (IV.3) and destroyed in reactions (IV.5) and (IV.6). We further assume that the rate of atomic nitrogen production is constant during the e-beam pulse and zero after the pulse is shut off. We must therefore consider the kinetics during the e-beam pulse as well as those after pulse termination. Actually, it is not crucial that reaction (IV.3) be the only pathway for the production of atomic oxygen. The critical assumption is that one oxygen atom is created for each NO molecule destroyed. This production can occur, therefore, equally well through dissociative electron recombination with NO^+ . Such processes do not alter the subsequent development.

After pulse termination, the atomic oxygen decays as indicated in Eq. (IV.8). Thus the number density of atomic oxygen is given by

$$[\text{O}] = [\text{O}]_{t=t_{\text{off}}} e^{-K_0(t-t_{\text{off}})} \quad (\text{IV.10})$$

where $[\text{O}]_{t=t_{\text{off}}}$ is the atomic oxygen number density at beam termination, t_{off} is the time that the e-beam terminates, zero time starting on the leading edge of the e-beam pulse, and K_0 , the pseudo first-order decay rate, is equal to $2k_5[\text{NO}][\text{N}_2]$.

During the e-beam pulse, the rate of change in atomic nitrogen number density is given by

$$\frac{d[\text{N}]}{dt} = \alpha - k_3[\text{N}][\text{NO}] , \quad (\text{IV.11})$$

where α is the N-atom production rate. This equation can be solved under pseudo first-order conditions $[\text{N}] \ll [\text{NO}]$ to give

$$(\text{IV.12})$$

$$[N] = \frac{\alpha}{K_f} (1 - e^{-K_f t}) \quad (\text{IV.12})$$

where K_f is just the product $k_3[NO]$.

The rate of change in atomic oxygen number density with time during the e-beam pulse is given by

$$\frac{d[O]}{dt} = K_f[N] - K_\ell[O] \quad (\text{IV.13})$$

Inserting the result from Eq. (IV.12) and rearranging slightly gives

$$\frac{d[O]}{dt} + K_\ell[O] = \alpha (1 - e^{-K_f t}) \quad (\text{IV.14})$$

Equation (IV.14) has the solution

$$[O] = \frac{\alpha}{K_\ell} (1 - e^{-K_\ell t}) + \frac{\alpha}{K_\ell - K_f} (e^{-K_\ell t} - e^{-K_f t}) \quad (\text{IV.15a})$$

which can be simplified further to give

$$[O] = \frac{\alpha}{K_\ell} (1 - e^{-K_\ell t}) \quad (\text{IV.15b})$$

because the ratio $K_f/K_\ell = 108$ at 50 torr. Substitution of Eq. (IV.15b) at $t=t_{\text{off}}$ into Eq. (IV.10) gives an expression for the atomic oxygen number density in the afterglow:

$$[O] = \frac{\alpha}{K_\ell} e^{-K_\ell t} (e^{K_\ell t_{\text{off}}} - 1) \quad (\text{IV.16})$$

This equation can then be used to describe the temporal behavior of the air afterglow intensity after beam termination,

$$I_{O/NO} = \kappa [O] \{ [NO]_{\text{added}} - [N]_0 \} \quad (\text{IV.17a})$$

$$= \frac{\kappa \alpha}{K_\ell} e^{-K_\ell t} (e^{K_\ell t_{\text{off}}} - 1) \{ [NO]_{\text{added}} - \alpha t_{\text{off}} \}, \quad (\text{IV.17b})$$

where we have incorporated the fact that in the absence of reaction (IV.3), $[N]_0 = \alpha t_{\text{off}}$. Equation (IV.17b) can be equated to the experimentally derived temporal behavior of the air afterglow intensity.

$$I_{O/NO} = b e^{-K_\ell t}, \quad (\text{IV.18})$$

where b is the intercept of the experimental semi-log plots of intensity versus time, to give

$$\frac{K_\ell b}{e^{K_\ell t_{\text{off}}} - 1} = \kappa \alpha [NO]_{\text{added}} - \kappa \alpha^2 t_{\text{off}}. \quad (\text{IV.19})$$

Equation (IV.19) is the calibration equation which is equivalent to Eq. (IV.7b) which obtains under steady-state conditions. A plot of the right hand side of Eq. (IV.19) versus $[NO]_{\text{added}}$ should be linear, with the slope and the intercept of the plot giving the important parameters:

$$r = \frac{(\text{slope})^2 t_{\text{off}}}{\text{intercept}}$$

and

$$r_1 = \frac{\text{intercept}}{\text{slope} \times t_{\text{off}}}.$$

IV.3.4 Results of O/NO Calibration with N₂/NO Mixtures

Figure IV.6 shows some typical first-order decay plots of the I_{O/NO} in N₂/NO mixtures. The decay rates are plotted against NO number density in Fig. IV.7. The negative intercept indicates that some of the NO is consumed in reaction (IV.3), so that the actual NO number density in the afterglow is somewhat reduced from what would have obtained in the absence of reaction (IV.3). The curvature at low [NO] indicates a breakdown in the pseudo first-order approximation. The rate constant obtained from these data is $1.55 \times 10^{-31} \text{ cm}^6 \text{ molecule}^{-2} \text{ s}^{-1}$ slightly lower than the value expected for $2k_5$. This reduction is probably an indication that reaction (IV.6) is not participating completely in the catalytic removal of O by NO as outlined in reactions (IV.5) and (IV.6), due to lower NO number densities and therefore lower NO₂ product number densities from reaction (IV.5).

The calibration plot of Eq. (IV.19) is shown in Fig. IV.8. The linearity is excellent. The results from two separate experiments gave $\kappa = (4.8 \pm 1.7) \times 10^{-28} \text{ mV cm}^6 \text{ molecule}^{-2}$ and $\alpha = (3.9 \pm 1.0) \times 10^{-17} \text{ molecules cm}^{-3} \text{ s}^{-1}$. The value obtained for α is about an order of magnitude larger than was expected from the kinetic modeling of N₂/O₂ mixtures, and probably indicates some problems either in the kinetic analysis used to extract the values of α and of κ , or else the presence of NO in the gas mixture drastically alters the ion chemistry. In either case, the problem will be resolved only by kinetic modeling of the LABCEDE operation including full NO ion chemistry.

IV.4 Air Afterglow Measurements in N₂/O₂/NO Mixtures

IV.4.1 Kinetic Model for N₂/O₂/NO Mixtures

The kinetic model used for the analysis of the air afterglow intensity measurements in the N₂/O₂/NO mixtures is quite similar to that used previously in the analysis of the N₂/NO mixtures. In this case, we assume that atomic oxygen can be produced only during the e-beam, either directly through dissociation of O₂ or NO, and dissociative electron recombination with O₂⁺ or NO⁺, or indirectly through production of atomic nitrogen followed

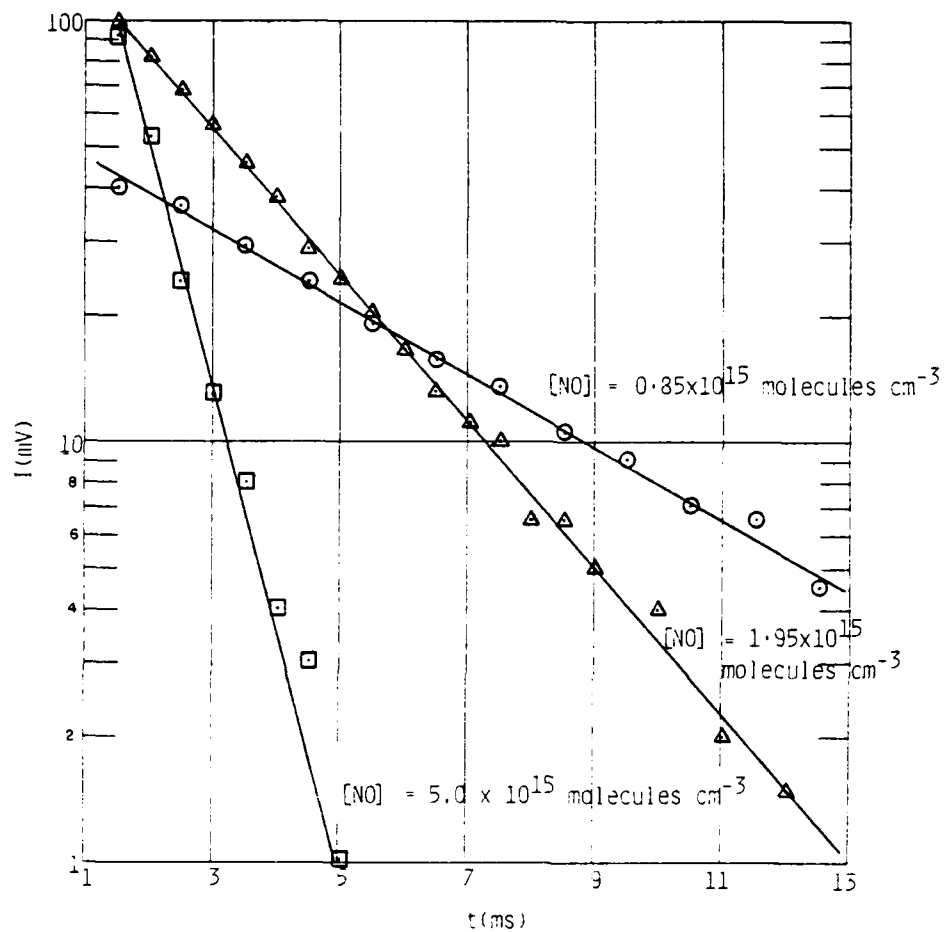


Fig. IV.6 Decay of emission at 700 nm as a function of time for N_2/NO mixtures.
 $P = 49.5$ torr.

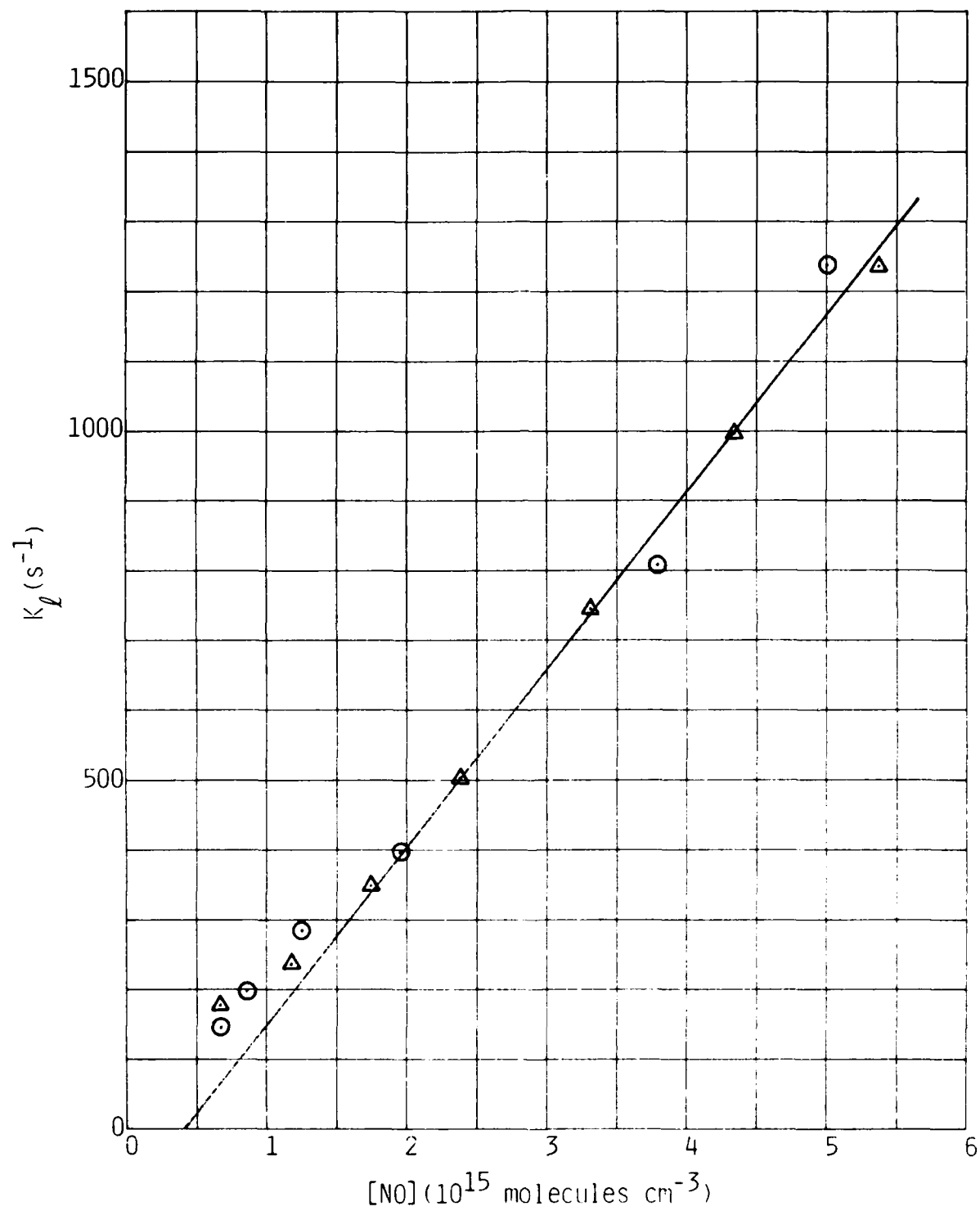


FIG. IV. Decay rates of 700 nm emission as a function of $[NO]$ for N₂/NO mixtures.

N₂/NO DATA

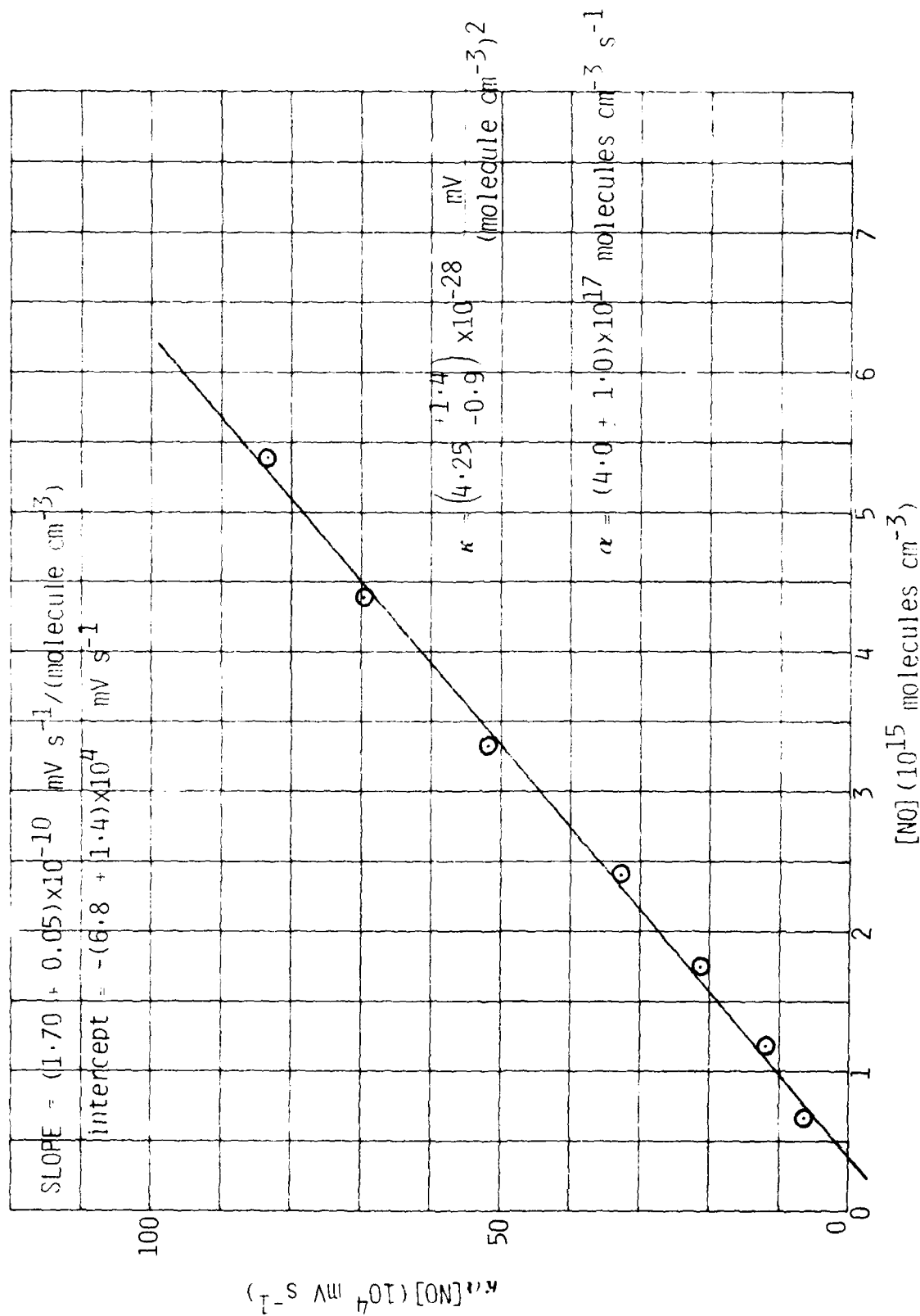


Fig. IV.8 Air afterglow calibration plot after Eq. (IV.19).

by reaction (IV.3). For the NO number densities used in this study, $\geq 10^{15}$ molecules cm^{-3} atomic oxygen production via reaction (IV.3) can be considered to be instantaneous upon the production of a nitrogen atom by the electron beam. The loss mechanisms for atomic oxygen are reactions (IV.5) and (IV.6) as before, but also include the following



$$(k_{20} = 5.5 \times 10^{-34} \text{ cm}^3 \text{ molecule}^{-1} \text{ s}^{-1}; \text{M} = \text{N}_2)^{22}$$



$$(k_{21} = 1.7 \times 10^{-14} \text{ cm}^3 \text{ molecule}^{-1} \text{ s}^{-1})^{23}$$

The NO_2 formed in reaction (IV.21) will further remove an oxygen atom through reaction (IV.6). Thus we expect that the rate of removal of atomic oxygen by molecular oxygen will show an effective rate constant of $2k_{20}$. Reaction (IV.22),



$$(k_{22} = 8.3 \times 10^{-15} \text{ cm}^3 \text{ molecule}^{-1} \text{ s}^{-1})^{22}$$

could also be a step for some atomic oxygen removal, but is not expected to be significant in $\text{N}_2/\text{O}_2/\text{NO}$ mixtures because of the much faster rate of reaction (IV.21) resulting from the added NO.

The differential equation for the rate change in $[\text{O}]$ with time during the e-beam pulse is

$$\frac{d[\text{O}]}{dt} = k_1 - \{2k_5[\text{NO}][\text{N}_2] + 2k_{20}[\text{O}_2][\text{N}_2]\} [\text{O}], \quad (\text{IV.23})$$

where β is the rate of O formation. This equation can be solved under the pseudo first-order approximation to give

$$[O] = \frac{\beta}{K_2} (1 - e^{-K_2 t}) , \quad (IV.24)$$

where $K_2 = 2k_5[NO][N_2] + 2k_{20}[O_2][N_2]$. In the afterglow, the atomic oxygen number density is described in Eq. (IV.10). Inserting Eq. (IV.24), evaluated at $t=t_{\text{off}}$ into Eq. (IV.10) and then inserting the resultant expression into Eq. (IV.1) gives the temporal behavior of the air-after glow emission intensity subsequent to beam termination,

$$I_{O/NO} = \frac{\kappa \beta [NO]}{K_2} e^{-K_2 t} (e^{K_2 t_{\text{off}}} - 1) . \quad (IV.25)$$

Equating this expression with the experimentally observed expression given in Eq. (IV.18) results in an expression which relates the experimental intensity observations to the desired rate of formation of atomic oxygen,

$$\beta = \frac{K_2 b}{\kappa [NO] (e^{K_2 t_{\text{off}}} - 1)} . \quad (IV.26)$$

The issues to be addressed then are what the magnitude of β is and whether β varies significantly with molecular oxygen number density.

IV.4.2 Results of Studies in $N_2/O_2/NO$ Mixtures

We will discuss first the results of the kinetic measurements in the $N_2/O_2/NO$ mixtures, and then discuss what the intensity information says about atomic oxygen number densities and how they change with changes in molecular oxygen density.

A typical box car decay is shown in Fig. IV.9, and semi-log plots of air afterglow intensity decays as a function of time are shown in Fig. IV.10. A plot of decay rates as a function of molecular oxygen number density for three different values of nitric oxide number density is shown in Fig. IV.11. The three lines are parallel, indicating that changes in decay rate with $[O_2]$ are independent of $[NO]$. The average of the three slopes gives an effective deactivation rate constant of $(2.4 \pm 0.1) \times 10^{-33} \text{ cm}^6 \text{ molecule}^{-2} \text{ s}^{-1}$. This value is a factor of four larger than the currently accepted value of k_{20} . We would have expected an effective rate constant of $2k_{20}$ because of the participation of reactions (IV.21) and (IV.6) in the decay mechanism. We are at a loss to explain the extra factor of two.

The intercepts of the three lines in Fig. IV.11 result from removal of O by NO in reactions (IV.5) and (IV.6). The effective rate constant will be the ratio of the intercept to the product $[NO][N_2]$. The average of the three intercepts gives an effective rate constant of $(2.0 \pm 0.2) \times 10^{-31} \text{ cm}^6 \text{ molecule}^{-2} \text{ s}^{-1}$, in excellent agreement with the expected value, $2k_5$.

The effective O-atom production rate, β , as calculated from Eq. (IV.26) is plotted against $[O_2]$ in Fig. IV.12 for three different initial values of $[NO]$. The intercept represents the effective O-atom production rate in the limit of no molecular oxygen addition to the reactor. The value obtained is $(3.4 \pm 0.2) \times 10^{17} \text{ molecules cm}^{-3} \text{ s}^{-1}$ and does not appear to be dependent upon the initial NO number density. This value agrees quite well with the value obtained above from the analyses of the N_2/NO mixtures.

The slope of Fig. IV.12 represents the increase in O-atom production rate with increasing molecular oxygen number density and also does not appear to be strongly dependent upon the initial NO number density. The numerical value of the slope, $2.5 \pm 0.4 \text{ s}^{-1}$, indicates that the effective O-atom production rate doubles in raising the molecular oxygen number density to 4 torr. Actually, the observed effective increase in β with increasing $[O_2]$ does not necessarily result from increased O-atom production. All that we are really able to measure is the product $[O][NO]$, so that all we can really tell is that this product appears to increase slightly with

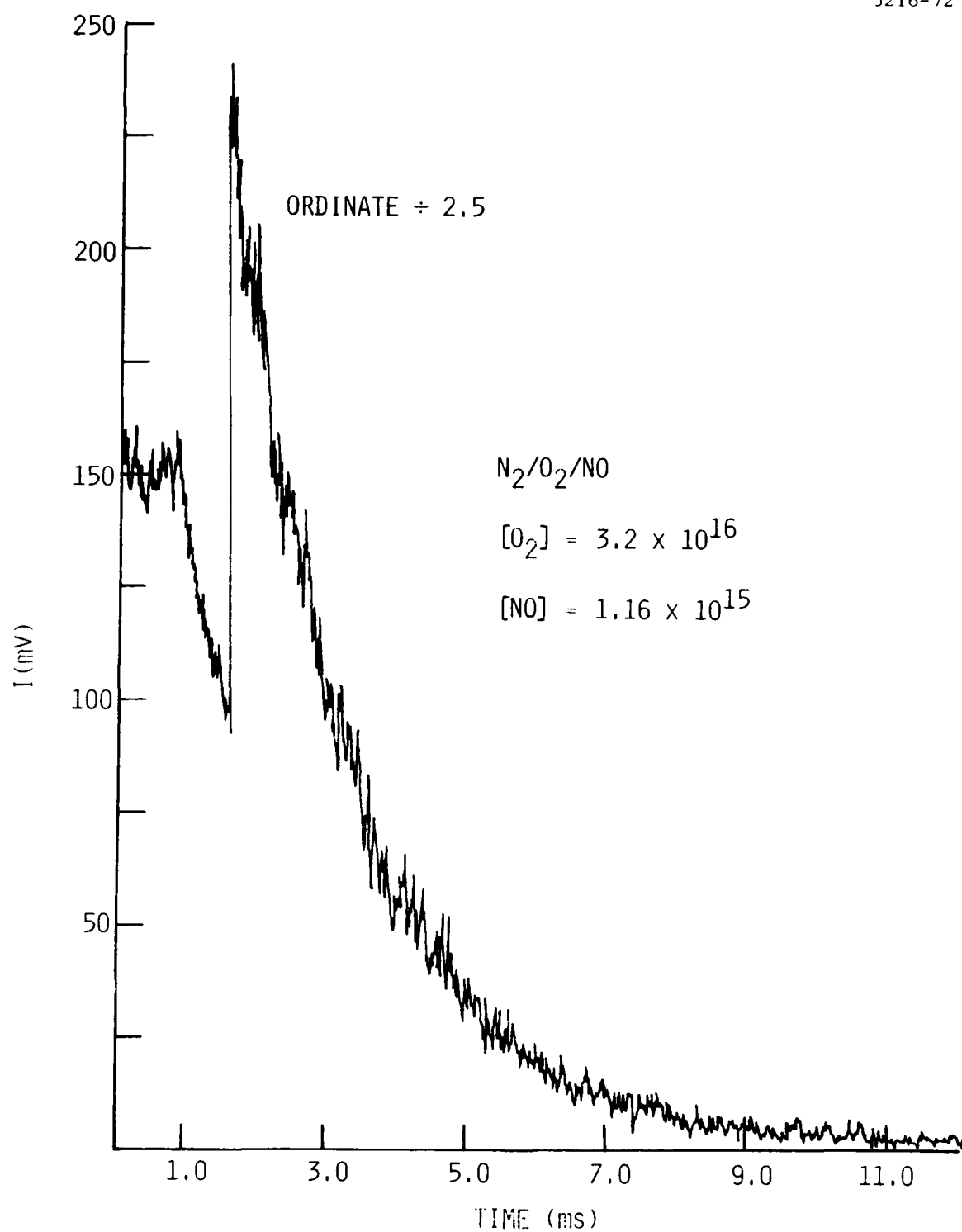


Fig. IV.9 Decay of emission at 700 nm as a function of time. $N_2/O_2/NO$ mixtures: $[O_2] = 3.2 \times 10^{16}$ molecules cm^{-3} $[NO] = 1.16 \times 10^{15}$ molecules cm^{-3} , $P = 51$ torr.

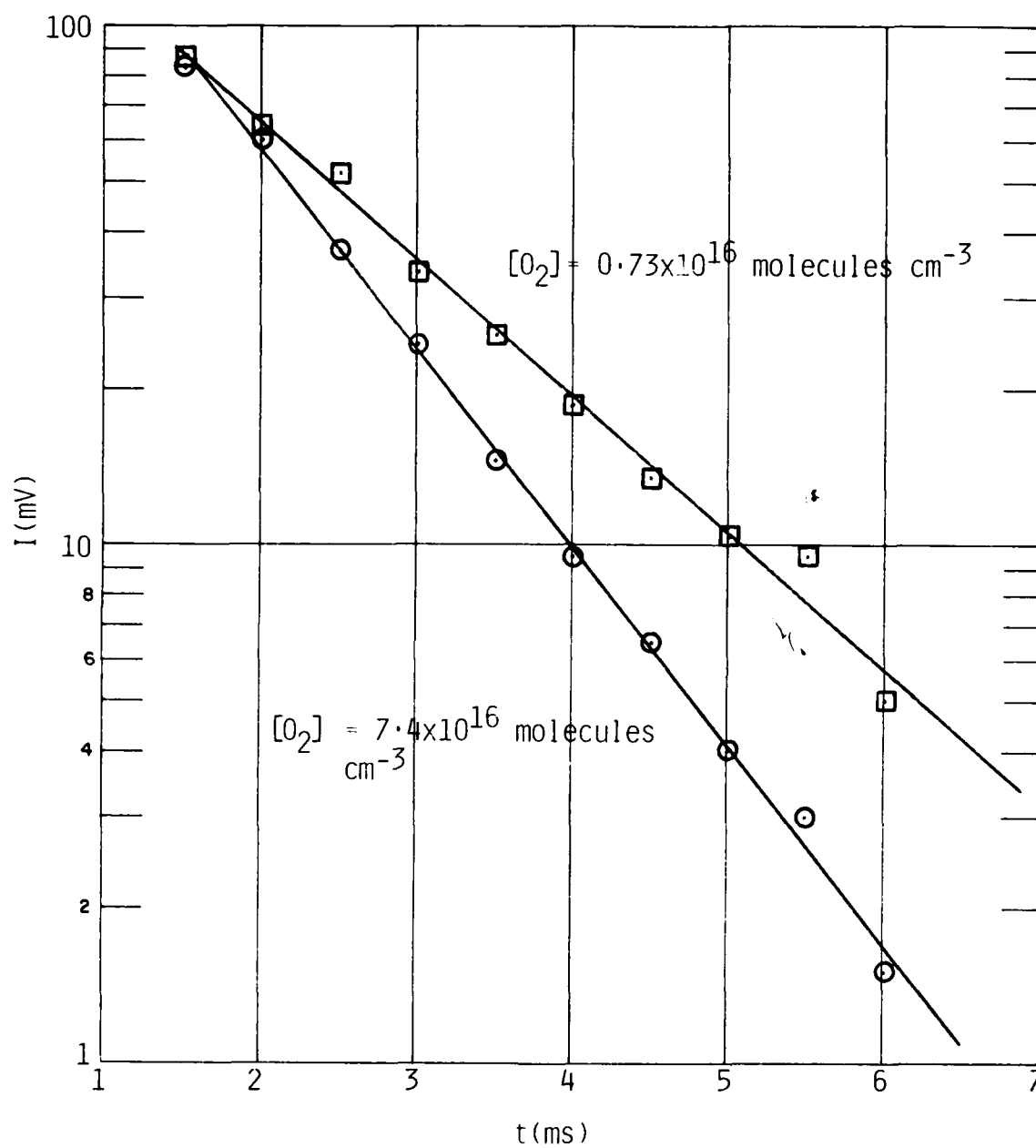


Fig. IV.10 Decay of emission at 700 nm as a function of time for $N_2/O_2/NO$ mixtures. $[NO] = 1.97 \times 10^{15} \text{ molecules cm}^{-3}$. $P = 52 \text{ torr}$.

$N_2/NO/O_2$ MIXTURES

5216-74

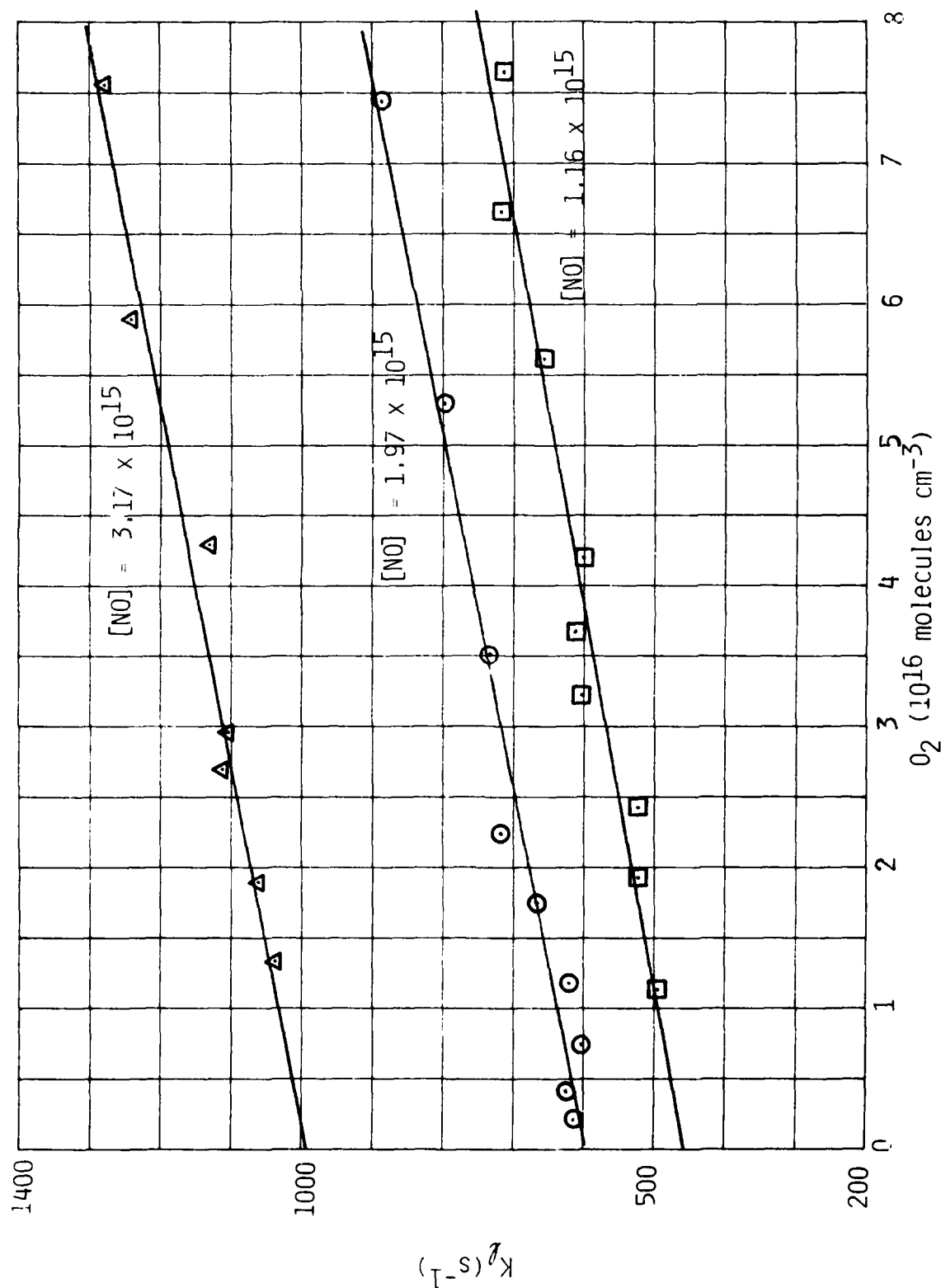


Fig. IV.11 Decay rates at 700 nm as a function of $[O_2]$ for different $[NO]$ in $N_2/O_2/NO$ mixtures. $P = 51$ torr.

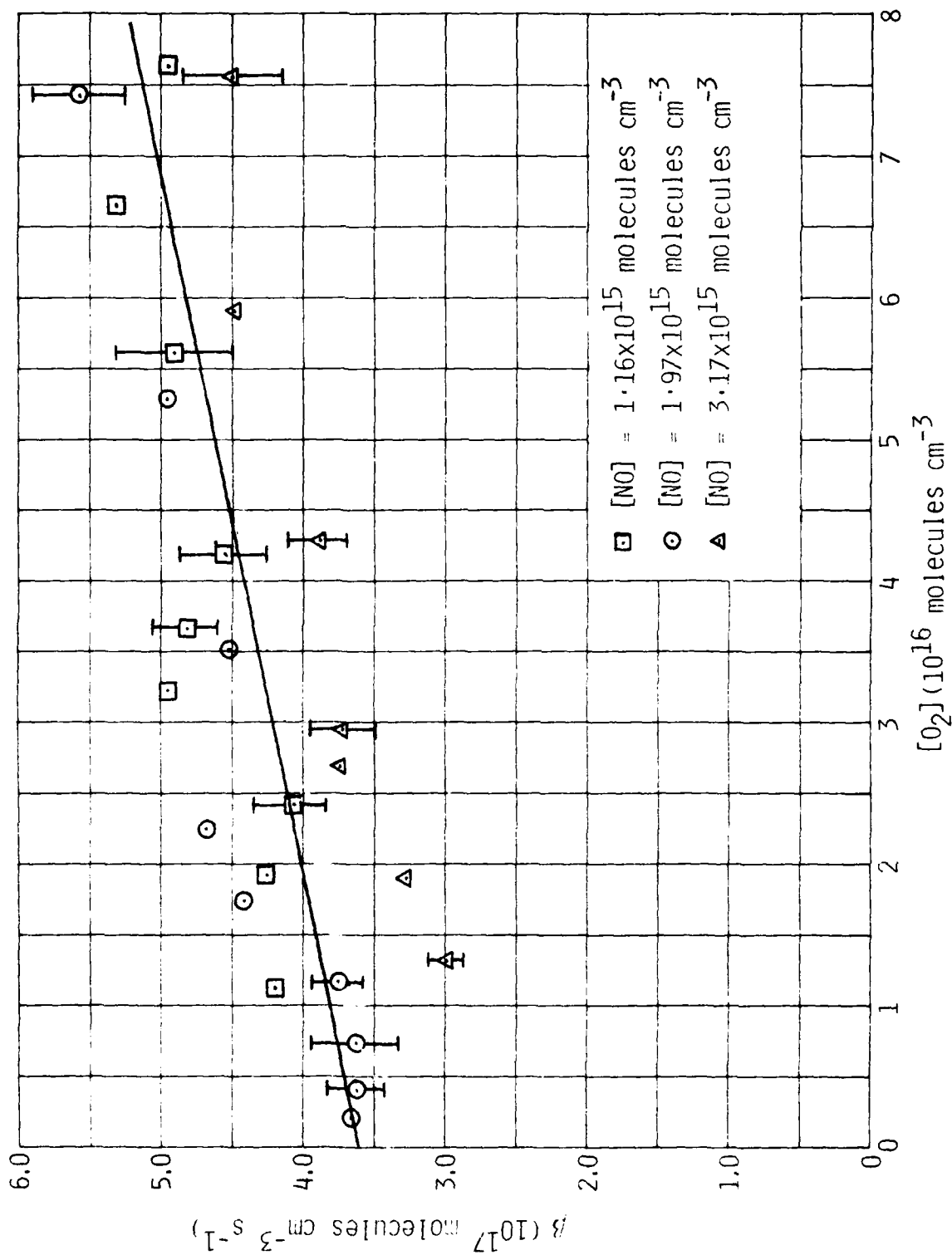


Fig. IV.17 \circ production rates as a function of $[\text{O}_2]$ for different values of $[\text{NO}]$ in $\text{N}_2/\text{O}_2/\text{NO}$ mixtures. $P = 51$ torr.

increasing $[O_2]$ in the $N_2/O_2/NO$ mixtures. Thus it would be possible to have the O-atom production rate decrease slightly, while at the same time having the NO number density increase sufficiently so that the product $[NO]$ increases as $[O_2]$ decreases.

IV.5 Observations in N_2/O_2 Mixtures

IV.5.1 N_2/O_2 Mixtures with $O_2 > 1.5$ Torr

Even in the absence of added NO some emission is observed at 700 nm, which presumably comes from the air afterglow. A spectrum of the emission with relatively large amounts of O_2 added to the reactor looks somewhat similar to that shown in Fig. IV.3, although the absolute intensity is much weaker without added NO. At low O_2 number densities, the spectrum is dominated by banded emission at 760 and 660 nm, but there is also evidence of continuum emission throughout the spectral region of interest. The kinetics of the emission decay are somewhat different at high $[O_2]$ compared to low $[O_2]$, so that data in each regime will be discussed separately.

At partial pressures of O_2 above 1.5 torr, the emission at 700 nm appears to decay via a single exponential. A plot of the rates of decay in the emission as a function of O_2 is shown in Fig. IV.13. If the decay is assumed to result from the removal of atomic oxygen in a three body reaction with O_2 , reaction (IV.20), with a steady-state number density of NO remaining essentially constant, then the slope of the line in Fig. IV.13 should equal k_{20} . The expected steady-state number densities of NO and O_3 are expected to be sufficiently small that reactions (IV.21) and (IV.22) do not take place to any significant extent, and thereby do not increase the observed effective O-atom removal rate constant above k_{20} . The slope of the line in Fig. IV.13 divided by the total reactor number density gives an O-atom removal rate constant of $(5.2 \pm 0.7) \times 10^{-34} \text{ cm}^6 \text{ molecule}^{-2} \text{ s}^{-1}$. This agrees well with the literature value of k_{20} .

The intercept in Fig. IV.13 is quite large and indicates some background removal process for atomic oxygen. It is not clear what this process is, since the species expected to have significant steady-state concentrations in the reactor, such as N and O_3 do not react particularly rapidly

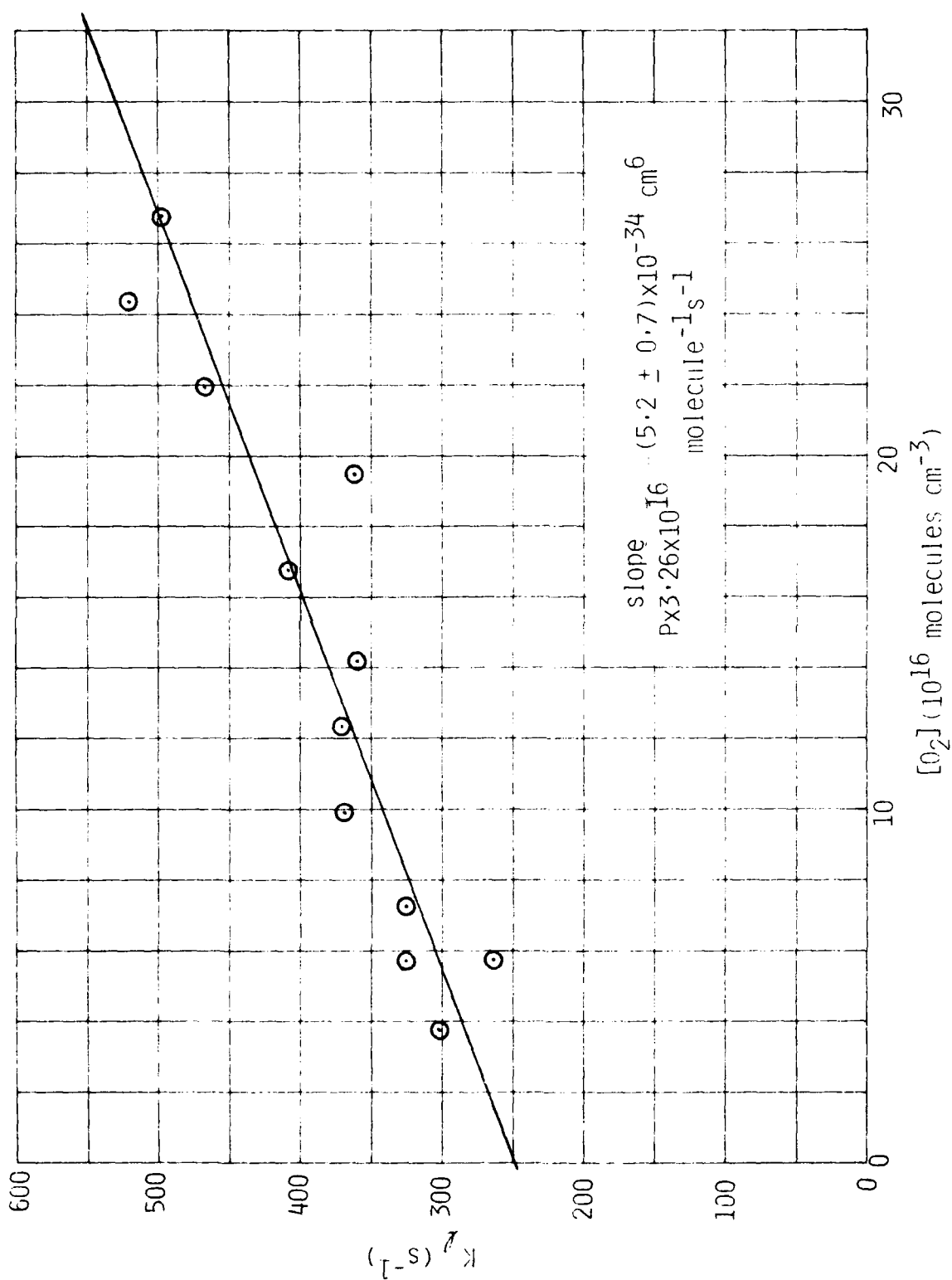


Fig. IV.13 Decay rates of emission at 700 nm as a function of $[O_2]$ in N_2/O_2 mixtures. $p = 51$ torr.

with atomic oxygen. Of course, since we are measuring only the product $[O][NO]$ it could be that the observed decay is a composite decay of the two species. The composite decay will equal the sum of the decays of the individual components.

Under the assumption that the extrapolation procedure given in Eq. (IV.26) is valid, the product $[O][NO]$ can be determined as a function of O_2 number density. This dependence is shown in Fig. IV.14. The intercept of the plot, when divided by the calibration constant κ , as determined above, gives the product $\delta[NO] = 3.1 \times 10^{31} \text{ molecules}^2 \text{ cm}^{-6} \text{ s}^{-1}$. Because the electron-beam pulse time is 1 ms, the initial $[O][NO]$ product is $3 \times 10^{28} \text{ molecules}^2 \text{ cm}^{-6}$. The LABCEDE kinetic modeling (see Section 5, main text), obtained the result $[O][NO] = 1.2 \times 10^{26} \text{ molecules}^2 \text{ cm}^{-6}$. This two order of magnitude discrepancy is consistent with the earlier experimental results which indicated species production rates a factor of ten greater than predicted in the modeling.

The slope from Fig. IV.14 is $(3.5 \pm 0.7) \times 10^{-14} \text{ molecules cm}^{-3} \text{ s}^{-1}$ and indicates that the product $[O][NO]$ will double upon increasing the molecular oxygen partial pressure to 13 torr.

IV.5.2 N_2/O_2 Mixtures With $p_{O_2} < 0.75 \text{ Torr}$

At very low partial pressures of molecular oxygen, the intensity at 700 nm showed a very marked bimodal decay which when analyzed as bi-exponential decay, gave fast decays on the order of 600 s^{-1} and slow decays about an order of magnitude less. Figure IV.15 shows a box car trace from one of the N_2/O_2 experiments. In this series of experiments, the signal levels were so low that it was difficult to determine exactly where the baseline was. This results in quite a lot of scatter in the data analysis. Figure IV.16 shows a plot of the decay rates of the fast and slow components plotted against molecular oxygen number density. The fast decays may be increasing somewhat at the lowest O_2 partial pressures, while the slow decay component appears to increase slightly with increasing O_2 number density. The kinetic modeling which has been done indicates that at low $[O_2]$, the atomic oxygen number density is essentially constant from one pulse to the

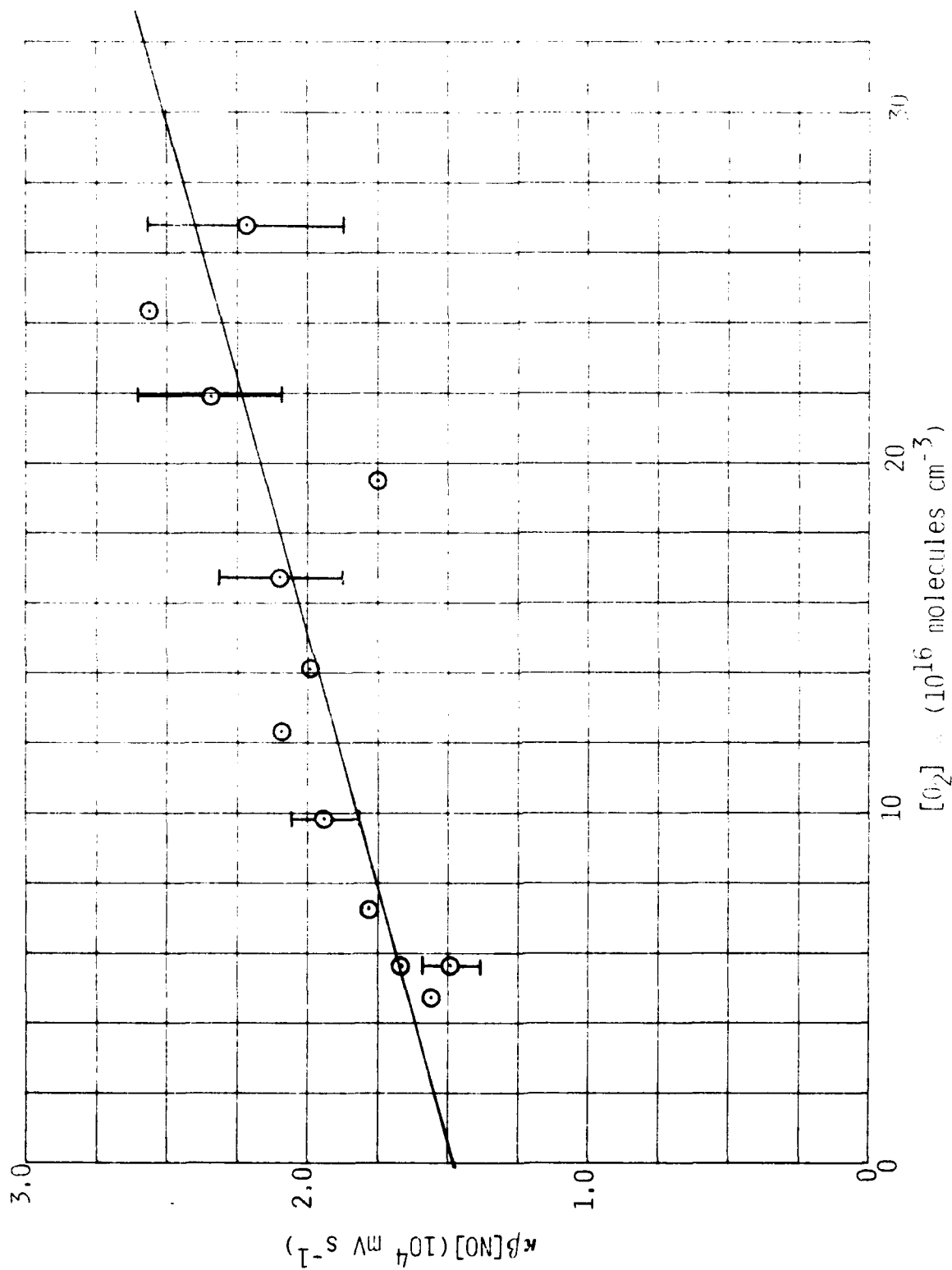


Fig. IV.14 700 nm emission zero-time intercepts as a function of $[O_2]$ for N_2/O_2 mixtures. $P = 51$ Torr.

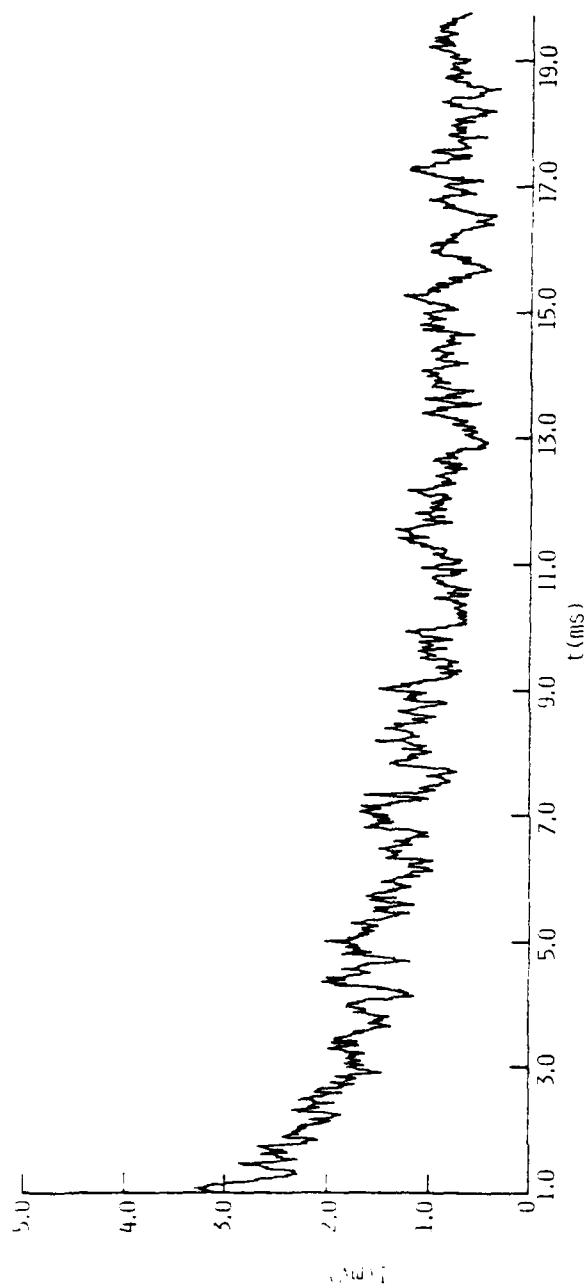


Fig. IV.15 Variation in emission intensity at 700 nm with time in N_2/O_2 mixtures. $[O_2] = 8.8 \times 10^{15}$ molecules cm^{-3} . $P = 50$ torr.

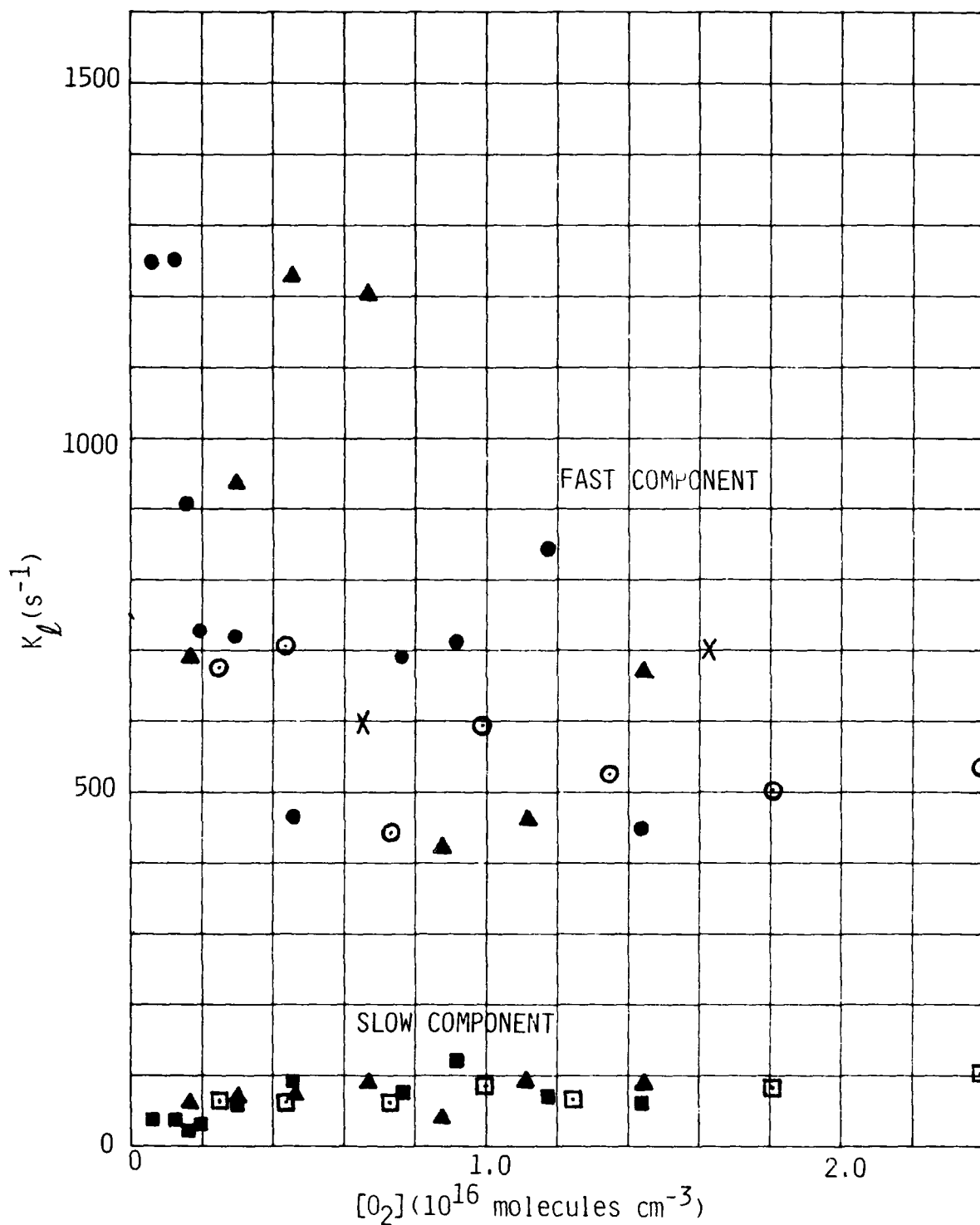


Fig. IV.16 Decay rates at 700 nm as a function of $[\text{O}_2]$ for small $[\text{O}_2]$ in N_2/O_2 mixtures. $P = 50$ torr.

next, whereas the NO number density is enhanced significantly just after the e-beam pulse with a rapid decay — on the order of a few milliseconds — to a somewhat lower steady-state value. The data are consistent with this modeling prediction. The points marked with x's in Fig. IV.16 show the initial NO decay rates determined from the kinetic modeling predictions. They are in excellent agreement with our experimental observations.

The slow decay results from removal of atomic oxygen in reactions such as (IV.20) and (IV.22) as well as with impurities in the reactor, and in addition diffusion to the reactor walls and volumetric removal resulting from pumping gas out of the reaction chamber.

Using Eq. (IV.26) to extrapolate the intensities of the fast decay components to an initial value of $k\beta[\text{NO}]$ (Fig. IV.17), shows that the product $[\text{O}][\text{NO}]$ is approximately $1 \times 10^{28} \text{ molecules}^2 \text{ cm}^{-6}$, and essentially independent of $[\text{O}_2]$. This value is about two orders of magnitude larger than the results of the modeling calculations which gave 0.5 and $2.3 \times 10^{26} \text{ molecules}^2 \text{ cm}^{-6}$ at 0.2 and 0.5 torr O_2 , respectively.

The intensities of the slow decay components at $t=0$ are plotted in Fig. IV.18. Because the decay is so slow, there is little point in using a more elaborate extrapolation procedure. The intensities displayed are proportional to the product $[\text{O}][\text{NO}]$ and it is clear from Fig. IV.18 that this product is independent of $[\text{O}_2]$. The average value obtained for $[\text{O}][\text{NO}]$ is $2 \times 10^{27} \text{ molecules}^2 \text{ cm}^{-6}$ which again is about two orders of magnitude larger than the model calculations which obtained $1.0 \times 10^{25} \text{ molecules}^2 \text{ cm}^{-6}$ at 0.2 and 0.5 torr O_2 , respectively.

IV.6 Summary

The O/NO air afterglow has been positively identified in the LABCEDE apparatus by spectral characterization, a study of the kinetics of the afterglow decay in the presence of nitric oxide, and by a study of the intensity dependence as a function of added nitric oxide. The kinetic studies give rate constants for various O-atom removal processes by NO and O_2 in excellent agreement with rate constant values published in the literature.

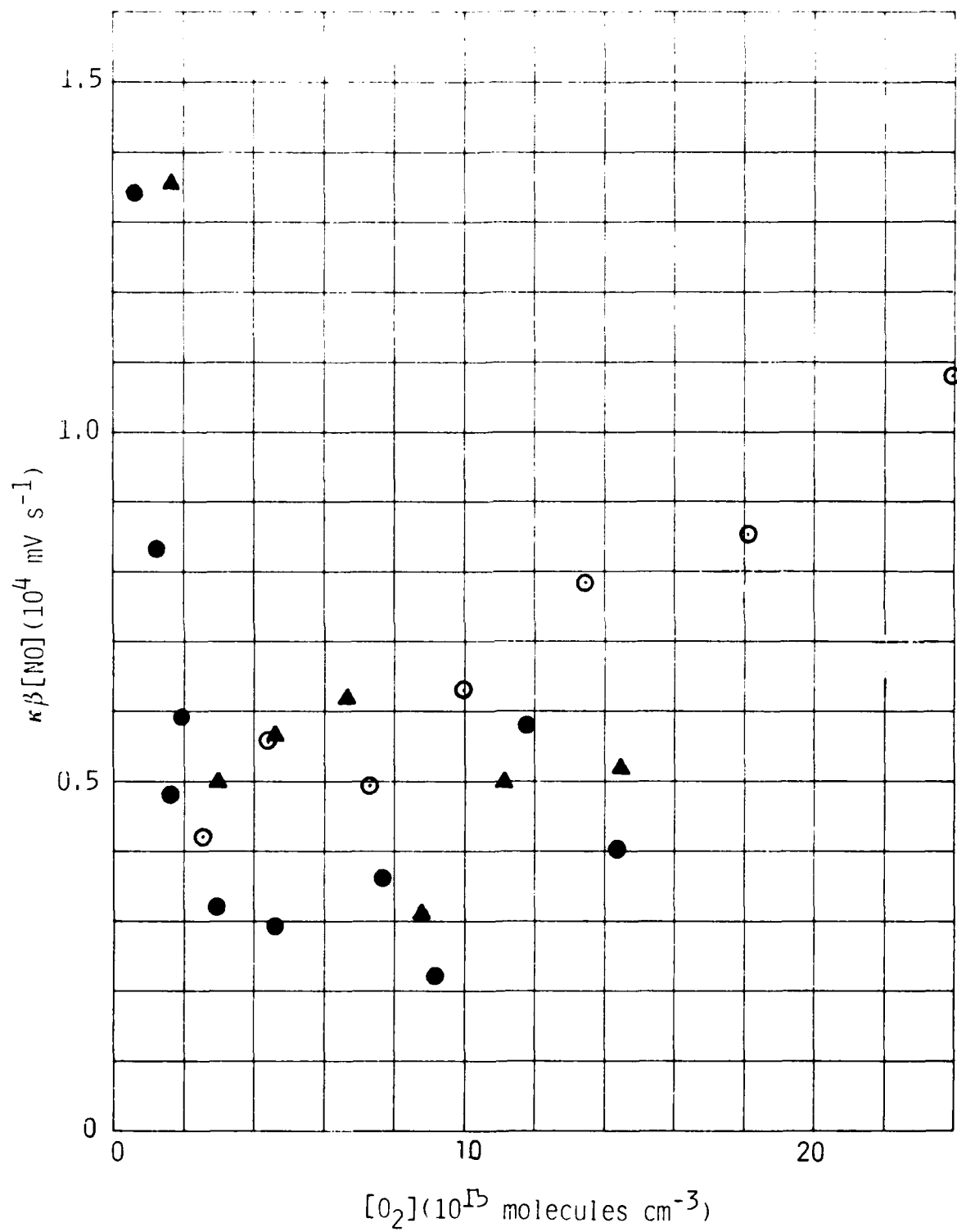


Fig. IV.17 700 nm intensity intercept of last decay component in N_2/O_2 mixtures at low $[\text{O}_2]$. $P = 50 \text{ torr}$.

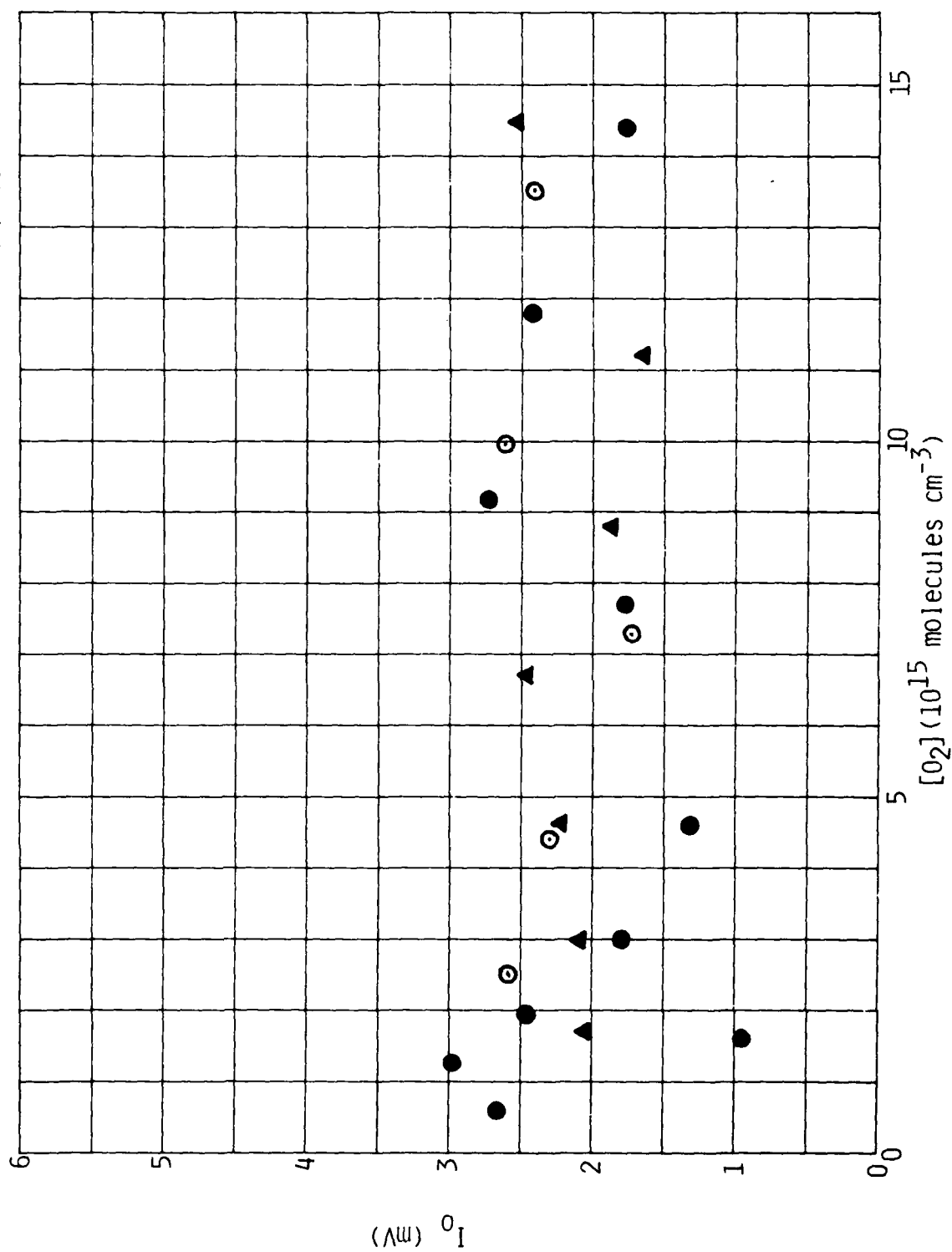


Fig. IV.18 Intensity of slow decay component as a function of $[O_2]$ in N_2/O_2 mixtures at low $[O_2]$. $P = 50$ torr.

The absolute calibration of the spectral system using the titration of atomic nitrogen by excess nitric oxide leads to estimated species number densities an order of magnitude larger than expectations, or in the case of studies where the product of two number densities was determined, the discrepancy is two orders of magnitude above expectations. This may be a result of some faulty assumptions made in the analysis required to obtain the air afterglow titration plot of Fig. IV.8. The assumption that one oxygen atom is created for each nitric oxide molecule destroyed is the one assumption which, if erroneous, is most likely to result in a resolution between experimental observations and modeling predictions, but only in the event that the ratio $[O]_{\text{produced}}/[NO]_{\text{destroyed}}$ is about 0.1. We are at a loss at present to find reactions involving nitrogen and oxygen species where this situation is likely to hold. Only a complete kinetic modeling involving NO ion chemistry can fully resolve this issue.

In summary, the experimental observations on the air afterglow intensity show good qualitative agreement with the kinetic modeling predictions, and the kinetic observations show excellent quantitative agreement both with modeling predictions and with the well established values for the rate constants of the important reactions in the system.

APPENDIX IV - REFERENCES

1. Bermand, P. P. and Clyne, M. A. A., "Atomic Resonance Fluorescence Spectrometry for Rate Constants of Rapid Bimolecular Reactions, Pt. 3 - Oxygen Atom Resonance $O^3S_1 - ^3P_{2,1,0}$," JCS Faraday II 69, 1643 (1973).
2. Clyne, M. A. A. and Piper, L. G., "Kinetic Spectroscopy in the Far Vacuum Ultra-Violet Pt. 3 - Oscillator Strengths for the 3s, 4s and 5 s $^3S - 2p^4\ ^3P_2$ Transition in Atomic Oxygen," JCS Faraday II 72, 2178 (1976).
3. Kaufman, F., "Reactions of Oxygen Atoms," Prog. React. Kinet. I 3, (1961).
4. Elias, L., Ogryzlo, E. A. and Schiff, H. I., "The Study of Electrically Discharged O_2 by Means of an Isothermal Calorimetric Detector," Can. J. Chem. 37, 1680 (1959).
5. Kaufman, F., "The Air Afterglow and its Use in the Study of Some Reactions of Atomic Oxygen," Proc. Roy. Soc. (London) A 247, 123 (1958).
6. Kaufman, F., "The Air Afterglow Revisited, Chemiluminescence and Bioluminescence," M. J. Cormier, D. M. Hercules, and J. Lee, eds. pp. 83-100 (1973).
7. Piper, L. G., Rawlins, W. T., and Caledonia, G. E., "COCHISE Studies," PSI TR-233, under Air Force Contract #F19628-77-C-0089 (1980).
8. Fontijn, A., Meyer, C. B., and Schiff, H. I., "Absolute Quantum Yield Measurements of the NO - O Reaction and Its Use as a Standard for Chemiluminescent Reactions," J. Chem. Phys. 40, 64 (1964).
9. Vanpee, M., Hill, K. D., and Kineyko, W. R., "Absolute Rate Constant Measurements for the Radiative Combination of Atomic Oxygen with Nitric Oxide," AIAA Journal 9, 135 (1971).
10. Golde, M. F., Roche, A. E., and Kaufman, F., "Absolute Rate Constant for the O + NO Chemiluminescence in the Near Infrared," J. Chem. Phys. 59, 3953 (1973).
11. Golomb, D. and Borwn, J. H., "The Temperature Dependence of the NO - O Chemiluminous Recombination. The RMC Mechanism" J. Chem. Phys. 63, 5246 (1975).
12. Woolsey, G. A., Lee, P. H., and Slafer, W. D., "Measurement of the Rate Constant for NO - O Chemiluminescence Using a Calibrated Piston Source of Light," J. Chem. Phys. 67, 1220 (1977).

APPENDIX IV - REFERENCES (Cont.)

13. Sutoh, M., Morioko, Y., and Nakamura, M., "Absolute Rate Constant for the Chemiluminescent Reaction of Atomic Oxygen with Nitric Oxide," J. Chem. Phys. 72, 20 (1980).
14. Pravilov, A. M. and Smirnova, L. G., "Spectral Distribution of the Chemiluminescence Rate Constant in the $O + CO(+M)$ and $O + NO(+He)$ Reactions," Kinet. and Catal. 19, 202 (1978).
15. Husain, D. and Slater, N. K. H., "Kinetic Study of Ground State Atomic Nitrogen, $N(2^4S_{3/2})$ by Time-Resolved Atomic Resonance Fluorescence," JCS Faraday II 76, 606 (1980).
16. Lee, J. H., Michael, J. V., Payne, W. A., and Stief, L. J., "Absolute Rate of the Reaction of $N(4S)$ with NO from 196-400 K with DF-RF and FP-RF Techniques," J. Chem. Phys. 69, 3069 (1978).
17. Clyne, M. A. A. and McDermid, I. S., "Mass Spectrometric Determinations of the Rates of Elementary Reactions of NO and NO₂ with Ground State N^4S Atoms," JCS Faraday I 71, 2189 (1975).
18. Baulch, D. L., Drysdale, D. D., Horne, D. G., and Lloyd, A. C., Evaluated Kinetic Data for High Temperature Reactions. II. Homogeneous Gas Phase Reactions of the $H_2 - N_2 - O_2$ System. (Butterworths, London, 1973).
19. O'Neil, R., and Davidson, G., "The Fluorescence of Air and Nitrogen Excited by Energetic Electrons," American Science and Engineering Inc. report ASE1602 under Air Force Contract AF19(628)-4080 (1968).
20. Davidson, G. and O'Neil, R., "Optical Radiation from Nitrogen and Air at High Pressure Excited by Energetic Electrons," J. Chem. Phys. 41, 3946 (1964).
21. Piper, L. G., unpublished results (1978).
22. Arnold, J. and Comes, F. J., "Temperature Dependence of the Reactions $O(^3P) + O_3 \rightarrow 2O_2$ and $O(^3P) + O_2 + M \rightarrow O_3 + M$," Chem. Phys. 42, 231 (1979).
23. Clough, P. N. and Thrush, B. A., "Mechanism of the Chemiluminescent Reaction between Nitric Oxide and Ozone," Trans. Faraday Soc. 63, 915 (1967).

APPENDIX V

NITROGEN FIRST POSITIVE SPECTRUM SYNTHESIS

V.1 Theory

The emission intensity for the $N_2(1^+)$ transition ($B^3\pi \rightarrow A^3\Sigma$) can be written as

$$I_{v' \rightarrow v''} = hc \nu_{v' \rightarrow v''} N_{v'} A_{v' \rightarrow v''}$$

$$= \frac{64 \pi^4}{3h} hc \nu_{v' \rightarrow v''}^4 N_{v'} \left| R_{v' \rightarrow v''} \right|^2 \quad (V.1)$$

where v' and v'' , respectively, refer to the vibrational states of upper electronic level ($B^3\pi$) and lower electronic level ($A^3\Sigma$), $A_{v' \rightarrow v''}$ denotes the Einstein coefficient for $v' \rightarrow v''$ transition and $R_{v' \rightarrow v''}$ the matrix element. If we assume that the matrix element is independent of the rotational quantum numbers J' , J'' , then the emission intensity for a rotation-vibration-electronic transition is given as

$$I_{v' \rightarrow v'', J' \rightarrow J', J' \pm 1} =$$

$$= \frac{64 \pi^4}{3h} hc \nu_{v' \rightarrow v'', J' \rightarrow J', J' \pm 1}^4 N_{v', J'} \left| R_{v' \rightarrow v''} \right|^2 \left(\frac{S_{J'}}{2J' + 1} \right) \quad (V.2)$$

where $S_{J'}$ is the Hönl London factor. For $B^3\pi \rightarrow A^3\Sigma$ transition in N_2 , $\Delta\Lambda = +1$ and the Hönl London factors for P, Q, R branches are given as follows:¹

$$S_{J'}^P = \frac{J'}{4}$$

$$S_{J'}^Q = \frac{2J' + 1}{4}$$

$$S_{J'}^R = \frac{J' + 1}{4}$$

$$S_{J'} = \frac{2J' + 1}{2} \quad (V.3)$$

There is a splitting of each rotational line of $B^3\pi$ state because it is a $\Lambda = 1$ transition. Consequently, there are twice as many transitions to the $A^3\Sigma$ state. However, this splitting is typically on the order of a fraction of a wavenumber. Since the resolution in the experiment is expected to be approximately 10 cm^{-1} , the two split states can be assumed to be of the same energy. Consequently,

$$I_{v' \rightarrow v'', J' \rightarrow J', J' \pm 1} = \frac{2hc \nu_{v' \rightarrow v'', J' \rightarrow J', J' \pm 1}^4}{(2J' + 1) \nu_{v' \rightarrow v''}^3} A_{v' \rightarrow v''} N_{v', J'}(S_{J'}) \quad (\text{V.4})$$

Due to spin uncoupling, each rotational level is split into three components for a $B^3\pi$ state. These components have energy differences on the order of the resolution of the instrument which is approximately 10 cm^{-1} . Therefore, these components have to be considered separately.

The population of the i^{th} component associated with rotational level J' and the vibrational level v' can be written as

$$N_{v', J', i} = N_{v', (2J' + 1)} \left[\frac{\exp(-F_{v', J', i} hc/kT)}{\sum_{J=0}^{\infty} \sum_{i=1}^3 (2J + 1) \exp(-F_{v', J', i} hc/kT)} \right] \quad (\text{V.5})$$

where

$$i = 1, 2, 3$$

$$F_{v', J', 1} = B_{v'} \left[J'(J' + 1) - \sqrt{Z_1} - 2Z_2 \right] - D_{v'} \left(J' - \frac{1}{2} \right)^4$$

$$F_{v', J', 2} = B_{v'} \left[J'(J' + 1) + 4Z_2 \right] - D_{v'} \left(J' + \frac{1}{2} \right)^4$$

$$F_{v', J', 3} = B_{v'} \left[J'(J' + 1) + \sqrt{Z_1} - 2Z_2 \right] - D_{v'} \left(J' + \frac{3}{2} \right)^4$$

$$Z_1 = Y(Y - 4) + \frac{4}{3} + 4J' (J' + 1)$$

$$Z_2 = \frac{1}{3Z_1} \left[Y(Y - 1) - \frac{4}{9} - 2J' (J' + 1) \right]$$

$$Y = A/B_v$$

In Eq. (V.5) it has been assumed that the particles in a given vibration-rotation level are divided into the split up components according to their energies.

Now, we can write the expression for absolute intensity for P, Q, and R branches as follows:

P-branch

$$I_{v' \rightarrow v'', J' \rightarrow J' + 1, i} = \frac{2hc A_{v' \rightarrow v''} v_{v' \rightarrow v'', J' \rightarrow J' + 1, i}^4 N_{v', J', i} \frac{J'}{4}}{(2J' + 1) v_{v' \rightarrow v''}^3} \quad (V.6a)$$

Q-branch

$$I_{v' \rightarrow v'', J' \rightarrow J', i} = \frac{2hc A_{v' \rightarrow v''} v_{v' \rightarrow v'', J' \rightarrow J', i}^4 N_{v', J', i}}{4 v_{v' \rightarrow v''}^3} \quad (V.6b)$$

R-branch

$$I_{v' \rightarrow v'', J' \rightarrow J' - 1, i} = \frac{2hc A_{v' \rightarrow v''} v_{v' \rightarrow v'', J' \rightarrow J' - 1, i}^4 N_{v', J', i} \left(\frac{J' + 1}{4} \right)}{(2J' + 1) v_{v' \rightarrow v''}^3} \quad (V.6c)$$

In order to calculate the frequencies, we note that, in wavenumbers, the frequency corresponding to the vibrational transition $v' \rightarrow v''$ is the difference in energy of vibrational level v' and v'' .

$$\nu_{v' \rightarrow v''} = E_{v'} - E_{v''}$$

where $E_{v'}$ and $E_{v''}$ can be calculated from²

$$E_v = E_e + \omega_e \left(v + \frac{1}{2}\right) - \omega_e x_e \left(v + \frac{1}{2}\right)^2 + \omega_e y_e \left(v + \frac{1}{2}\right)^3 + \omega_e z_e \left(v + \frac{1}{2}\right)^4$$

Now we can write the expression for frequency corresponding to the split up components of a vibration-rotation-electronic transition as follows:

P-branch

$$\nu_{v' \rightarrow v'', J' \rightarrow J' + 1, i} = E_{v'} - E_{v''} + F_{v', J', i} - F_{v'', J' + 1} \quad (V.7a)$$

Q-branch

$$\nu_{v' \rightarrow v'', J' \rightarrow J', i} = E_{v'} - E_{v''} + F_{v', J', i} - F_{v'', J'} \quad (V.7b)$$

R-branch

$$\nu_{v' \rightarrow v'', J' \rightarrow J' - 1, i} = E_{v'} - E_{v''} + F_{v', J', i} - F_{v'', J' - 1} \quad (V.7c)$$

where

$$F_{v'', J''} = B_{v''} (J'' + 1) J'' - D_{v''} J''^2 (J'' + 1)^2$$

V.2 Computer Program

The computer program to generate nitrogen first position spectra has been made in two parts. In the first part, the data compiled in Ref. 2 has been used to calculate frequency and emission intensity for all the possible transitions as discussed in the theory part of this write up. These frequency-intensity pairs are then stored on a magnetic tape as a function of v' , $\Delta v (\Delta v = v'' - v')$, J' , $\Delta J (\Delta J = J'' - J')$ and $i (i = 1, 2, 3)$. For P, Q, and R branch transitions, ΔJ is +1, 0 and -1, respectively. However, in the code, P, Q, and R branch transitions correspond to $\Delta J = 1, 2$, and 3, respectively.

The computer program is based upon the assumption that there is a complete rotational equilibrium. For a given rotational temperature, the code automatically calculates the maximum number of rotational levels that should be taken into account. This number is chosen such that the emission intensity associated with this level is a given fraction of the maximum emission intensity.

The computer code has been made sufficiently flexible so that $N_2(1P)$ spectrum in any wavelength region could be generated with ease. For a particular input data file, the first part of the program is run only once to store all the required information on the tape. Once this has been completed, in the second part, the magnetic tape is attached to the disc and scanning is done to pick up the desired frequency-intensity pairs for spectrum synthesis in the appropriate wavelength region.

Input to Part 1

T = Translational temperature in K
 E', E'' = Electronic energy of $B^3\Pi$ and $A^3\Sigma$ levels [cm^{-1}]
 ω_e', ω_e'' = Potential parameters for $B^3\Pi$ and $A^3\Sigma$ levels
 $\omega_e'x_e', \omega_e''x_e''$ = Potential parameters for $B^3\Pi$ and $A^3\Sigma$ levels
 $\omega_e'y_e', \omega_e''y_e''$ = Potential parameters for $B^3\Pi$ and $A^3\Sigma$ levels
 $\omega_e'z_e', \omega_e''z_e''$ = Potential parameters for $B^3\Pi$ and $A^3\Sigma$ levels

$B_{v'}, B_{v''}$ = Rotational constants for B $^3\Pi$ and A $^3\Sigma$ levels
 $D_{v'}, D_{v''}$ = Rotational constants for B $^3\Pi$ and A $^3\Sigma$ levels
 $A_{v'}$ = Spin coupling parameters for B $^3\Pi$ state [cm^{-1}]
 $A_{v' \rightarrow v''}$ = Einstein coefficient for transition $v' \rightarrow v''$ [s^{-1}]
 IR = Ratio of maximum intensity to the intensity corresponding to highest rotational level

Output of Part 1

Frequency and emission intensity corresponding to each v' , Δv , J' , ΔJ and i .

Input to Part 2

$(\omega_n)_{\min}$ = The smallest frequency in wavenumber to be considered for the spectrum
 $(\omega_n)_{\max}$ = The largest frequency in wavenumbers to be considered for the spectrum
 T = Temperature in [K]
 Res = Resolution of the spectrum [cm^{-1}]
 $\text{Sinc}(x)$ = The slit function of the instrument
 $N_{v'}$ = Population of vibrational level v' [$\#/\text{cm}^3$]
 $\Delta\omega_n$ = The range over which line averaging is performed [cm^{-1}] (in general $\text{Res} > 2 \Delta\omega_n$).

Output of Part 2

The output is the plot of relative intensity vs. frequency in wavenumbers. The absolute intensity plot can also be obtained if desired.

TABLE V.1

INPUT DATA (cm^{-1})

$$E' = 58443.6519$$

$$E'' = 49027.93049$$

$$\omega_e' = 1733.391$$

$$\omega_e'' = 1460.638$$

$$\omega_e' x_e' = 14.1221$$

$$\omega_e'' x_e'' = 13.8723$$

$$\omega_e' y_e' = -0.05688$$

$$\omega_e'' y_e'' = -0.01030$$

$$\omega_e' z_e' = 3.612 \times 10^{-3}$$

$$\omega_e'' z_e'' = -1.965 \times 10^{-3}$$

$$A_v' = 42.0$$

TABLE V.2
ROTATIONAL CONSTANTS (CM⁻¹)

v	B _{v'}	B _{v''}	D _{v'}	D _{v''}
0	1.63	1.4459	6.15 x 10 ⁻⁶	6.15 x 10 ⁻⁶
1	1.6105	1.4271	6.15 x 10 ⁻⁶	6.15 x 10 ⁻⁶
2	1.5922	1.4089	6.15 x 10 ⁻⁶	6.15 x 10 ⁻⁶
3	1.5737	1.3907	6.15 x 10 ⁻⁶	6.15 x 10 ⁻⁶
4	1.5551	1.3720	6.15 x 10 ⁻⁶	6.15 x 10 ⁻⁶
5	1.5368	1.3529	6.15 x 10 ⁻⁶	6.15 x 10 ⁻⁶
6	1.5179	1.3338	6.15 x 10 ⁻⁶	6.15 x 10 ⁻⁶
7	1.4990	1.3152	6.15 x 10 ⁻⁶	6.15 x 10 ⁻⁶
8	1.4794	1.2954	6.15 x 10 ⁻⁶	6.15 x 10 ⁻⁶
9	1.4602	1.2756	6.15 x 10 ⁻⁶	6.15 x 10 ⁻⁶
10	1.4412	1.2500	6.15 x 10 ⁻⁶	6.15 x 10 ⁻⁶
11	1.4213	1.2300	6.15 x 10 ⁻⁶	6.15 x 10 ⁻⁶
12	1.4015	1.2100	6.15 x 10 ⁻⁶	6.15 x 10 ⁻⁶
13	1.3800	1.1900	6.15 x 10 ⁻⁶	6.15 x 10 ⁻⁶

THE SPECTRUM OF MOLECULAR NITROGEN

287

TABLE V. 3

 Table 96. Absolute transition probabilities of the N_2 First Positive System

$v'' \backslash v'$	0	1	2	3	4	5	6	7	8	9	10	11	12	13	$f_{v'' \leftarrow v'}$	Extrap- olated
0	10469.0	12316.6	14894.5	18739.1	25082.9	37522.0									1.12+5	1.12+5
	6.25+4	3.56+4	1.12+4	2.47+3	3.97+2	4.24+1										
1	8883.4	10179.0	11878.1	14201.7	17569.3	22882.0	32503.7								1.28+5	1.29+5
	8.72+4	4.12+2	1.85+4	1.48+4	5.69+3	1.40+3	2.27+2									
2	7732.0	8695.3	9905.7	11470.9	13572.1	16538.8	21039.8	28671.4	44417.6						1.42+5	1.43+5
	4.44+4	6.17+4	1.25+4	2.68+3	1.05+4	7.29+3	2.71+3	6.39+2	6.87+1							
3	6858.3	7605.8	8516.0	9647.7	11092.0	12997.4	15624.1	19475.2	25648.7	37156.2	66089.9				1.54+5	1.54+5
	1.07+4	7.73+4	2.17+4	2.85+4	7.97+2	3.88+3	6.33+3	3.69+3	1.24+3	2.57+2	2.54+1					
4	6173.1	6772.1	7484.4	8344.7	9403.8	10738.4	12470.6	14806.6	18124.8	23202.8	31932.9	50431.6			1.62+5	1.64+5
	1.29+3	3.02+4	8.36+4	1.54+3	2.94+4	7.84+3	1.93+2	1.52+3	3.74+3	1.94+3	5.44+2	9.03+1				
5	5621.6	6114.1	6688.7	7367.5	8181.0	9172.9	10407.7	12885.9	16071.2	16951.5	21182.2	27993.4	40756.3		1.72+5	1.73+5
	7.42+1	5.08+3	5.26+4	6.86+4	3.02+3	1.91+4	1.52+4	1.10+3	1.72+3	2.81+3	2.13+3	8.95+2	2.24+2			
6	5581.6	6036.7	6663.0	7255.0	8024.4	8953.8	10097.6	11538.2	13405.9	15920.7	19483.8	24914.0	34170.0		1.78+5	1.81+5
	3.71+2	1.19+4	7.09+4	4.38+4	1.58+4	7.10+3	1.76+4	5.11+3	---	1.40+3	1.93+3	1.17+3	4.24+2			
7	5542.7	6007.9	6529.7	7146.5	7874.4	8745.6	9806.0	11123.1	12800.7	15007.4	18035.1	22434.2	28434.2		1.81+5	1.88+5
	1.07+3	2.14+4	8.10+4	2.03+4	2.88+4	5.09+2	1.49+4	9.39+3	1.12+3	2.31+2	1.26+3	1.22+3				
8	5504.9	5946.7	6453.9	7011.8	7730.4	8547.4	9531.1	10736.9	12247.4	14191.7	16781.1				1.82+5	1.95+5
	2.34+3	3.25+4	8.15+4	4.94+3	3.50+4	1.38+3	8.11+3	1.15+4	3.73+3	9.33+1	4.62+2					
9	5092.2	5468.0	5893.9	6380.3	6940.5	7592.1	8358.3	9271.4	10376.4	11739.1	13456.6				1.84+5	2.01+5
	7.77+1	4.29+3	4.38+4	7.31+4	---	3.28+4	7.66+3	2.44+3	1.01+4	6.47+3	1.17+3					
10	5068.2	5432.0	5842.5	6308.8	6842.6	7458.9	8177.6	9025.3	10038.9	11268.9					1.78+5	2.07+5
	1.59+2	6.92+3	5.38+4	5.86+4	3.99+3	2.44+4	1.54+4	---	6.96+3	7.95+3						
11															1.65+5	2.13+5
12															1.60+5	2.18+5

Data from Shemansky and Broadfoot [572].

 λ (Å) and $A_{v'' \leftarrow v'}$ are given for each $v'' \leftarrow v'$.

This table is taken directly from reference 2.

REFERENCES (APPENDIX V)

1. G. Herzberg, Spectra of Diatomic Molecules, Van Nostrand Reinhold Company, New York, p 208 (1950).
2. A. Lofthus and P. H. Krupenie, "The Spectrum of Molecular Nitrogen," J. Phys. and Chem., Ref. Data 6, pp. 113-307 (1977).

DATE
ILME